The kinetics of Fe(II)-carbonate precipitation



A Thesis
Presented to the University of Oxford
in Candidacy for the Degree of
Doctor of Philosophy

By

Clancy Zhijian Jiang
Linacre College
Oxford

Under the guidance of: Nicholas J. Tosca

Revised: 22nd October 2020

Short abstract

The kinetics of Fe(II)-carbonate precipitation

Clancy Zhijian Jiang

University of Oxford

This thesis investigates the processes, products, and rates of Fe(II)-carbonate precipitation using two experimental approaches. The first was to constrain the requisite critical supersaturation for homogeneous/spontaneous nucleation directly from solution, and to understand the mineralisation pathway of Fe(II)-carbonate once nucleated. The second set of experiments was designated to correlate the kinetic behaviour of siderite growth and solution chemistry, and to implement established rate laws to better understand the microscopic mechanisms that underpin crystal growth. This knowledge, in turn, allowed a further investigation into kinetic fractionation of carbon isotopes, enquiring how the isotopic composition reflects the kinetics of siderite growth and the chemistry of the parent solution.

Nucleation experiments revealed that a precursor amorphous Fe(II)-carbonate (AFC) phase played a critical role in the homogeneous precipitation of Fe(II)-carbonate. Results indicate that, once the requisite critical supersaturation is surpassed, pervasive nucleation AFC rapidly decreases the solution saturation, and the nucleation rate behaves as an exponential function of solution saturation. The nucleated AFC subsequently crystallises into chukanovite ($Fe_2(OH)_2CO_3$) or siderite ($FeCO_3$) in days, depending on the availability and the ratio between Fe^{2+} and CO_3^{2-} ions; a mineralisation pathway that is more intricate than previously appreciated.

Growth experiments yielded a complete data set of the kinetic behaviour during siderite growth from near-nucleation (with respect to AFC) to near-equilibrium (with respect to siderite). These results delineate a chemical affinity-based kinetic model that predicts growth rate limited by the transport of dissolved species to the mineral surface at high solution saturation, but limited by the rate of surface reactions when the system approaches equilibrium. These observations are analogous to calcite precipitation studies, only that, siderite grows nearly 7 orders of magnitude slower than calcite at room temperature. The comparable growth mechanisms but contrasting growth rates between calcite and siderite can be attributed to the physiochemical difference between hydrated Ca^{2+} and Fe^{2+} ions. Due to the smaller ionic radius of Fe^{2+} (0.078 nm) than that of Ca^{2+} (0.1 nm), a higher activation energy is required to dehydrate the more densely charged Fe^{2+} ion on the crystal surface to form an-

hydrous $FeCO_3$, thus siderite precipitate significantly slower than calcite and often involve the formation of hydrous/hydroxylated metastable phases.

Isotopic analyses of both the solution and the precipitate indicate that siderite precipitated from supersaturated solution exhibit significant discrimination against ^{13}C. Though information is still lacking, the observed isotopic compositions in precipitated siderite are satisfactorily explained with a kinetic fractionation model, which indicates the maximum kinetic isotope effect of C in abiotic siderite growth can be as much as $10^3 \ln \alpha_{sid-\mathrm{DIC}} = -12.13$ ‰. On the basis of the kinetic constraint on siderite growth, experimental results presented in this thesis suggest that significant accumulations of abiotic siderite in the sediments require a considerable supersaturation to achieve an appreciable precipitation rate within the time frame of early diagenesis; inevitably, displays a negative $\delta^{13}C$ signature.

Geochemical constraints arising from this thesis prompt a re-evaluation on the palaeoenvironmental reconstruction based on ferruginous sediments, notably, late Archaean iron formation. Incorporating recent advances in high-resolution petrography, experimental geochemistry, and modelling studies of Fe-minerals, this study presents an updated understanding of the Fe cycle on early Earth, in which the deposition of ferruginous sediments was a direct response to enhanced Fe(II) influxes (e.g., hydrothermal venting), where Fe(II)-silicate nucleation was the dominant mechanism that attenuated hydrothermal Fe(II) fluxes to seawater, and Fe(II)-carbonate precipitation served as the ultimate sink of a comparatively small seawater Fe(II) reservoir.

Long abstract

The kinetics of Fe(II)-carbonate precipitation

Clancy Zhijian Jiang

University of Oxford

This thesis investigates the processes, products, and rates of Fe(II)-carbonate precipitation using two experimental approaches. The first was to constrain the requisite critical supersaturation for homogeneous/spontaneous nucleation directly from solution, and to understand the mineralisation pathway of Fe(II)-carbonate once nucleated. The second set of experiments was designated to correlate the kinetic behaviour of siderite growth and solution chemistry, and to implement established rate laws to better understand the microscopic mechanisms that underpin crystal growth. This knowledge, in turn, allowed a further investigation into kinetic fractionation of carbon isotopes, enquiring how the isotopic composition reflects the kinetics of siderite growth and the chemistry of the parent solution.

Nucleation experiments revealed that a precursor amorphous Fe(II)-carbonate (AFC) phase played a critical role in the homogeneous precipitation of Fe(II)-carbonate. Results indicate that, once the requisite critical supersaturation is surpassed, pervasive nucleation AFC rapidly decreases the solution saturation, and the nucleation rate behaves as an exponential function of solution saturation. The nucleated AFC subsequently recrystallises into chukanovite ($Fe_2(OH)_2CO_3$) or siderite ($FeCO_3$) in days, depending on the availability and the ratio between Fe^{2+} and CO_3^{2-} ions; a mineralisation pathway that is more intricate than previously appreciated.

Growth experiments yielded a complete data set of the kinetic behaviour during siderite growth from near-nucleation (with respect to AFC) to near-equilibrium (with respect to siderite). These results delineate a chemical affinity-based kinetic model that predicts growth rate limited by the transport of dissolved species to the mineral surface at high solution saturation, but limited by the rate of surface reactions when the system approaches equilibrium. These observations are analogous to calcite precipitation studies, only that, siderite grows nearly 7 orders of magnitude slower than calcite at room temperature. The comparable growth mechanisms but contrasting growth rates between calcite and siderite can be attributed to the physiochemical difference between hydrated Ca^{2+} and Fe^{2+} ions. Due to the smaller ionic radius of Fe^{2+} (0.078 nm) than that of Ca^{2+} (0.1 nm), a higher activation energy is required to dehydrate the more densely charged Fe^{2+} ion on the crystal surface to form anhydrous $FeCO_3$, thus siderite precipitate significantly slower than calcite and often

involve the formation of hydrous/hydroxylated metastable phases.

Isotopic analyses of both the solution and the precipitate indicate that siderite precipitated from supersaturated solution exhibit significant discrimination against ^{13}C. Though information is still lacking, the observed isotopic compositions in precipitated siderite are satisfactorily explained with a kinetic fractionation model, which indicates the maximum kinetic isotope effect of C in abiotic siderite growth can be as much as $10^3 \ln \alpha_{sid-\mathrm{DIC}} = -12.13$ ‰. On the basis of the kinetic constraint on siderite growth, experimental results presented in this thesis suggest that significant accumulations of abiotic siderite in the sediments require a considerable supersaturation to achieve an appreciable precipitation rate within the time frame of early diagenesis; inevitably, displays a negative $\delta^{13}C$ signature.

Geochemical constraints arising from this thesis prompt a re-evaluation on the palaeoenvironmental reconstruction based on ferruginous sediments, notably, late Archaean iron formation. Incorporating recent advances in high-resolution petrography, experimental geochemistry, and modelling studies of Fe-minerals, this study presents an updated understanding of the Fe cycle on early Earth, in which the deposition of ferruginous sediments was a direct response to enhanced Fe(II) influxes (e.g., hydrothermal venting), where Fe(II)-silicate nucleation was the dominant mechanism that attenuated hydrothermal Fe(II) fluxes to seawater, and Fe(II)-carbonate precipitation served as the ultimate sink of a comparatively small seawater Fe(II) reservoir. More specifically:

1. The transient maximum Fe^{2+} concentration in a ferruginous water body resembling the chemistry of late Archaean ocean was not controlled by homogeneous precipitation of Fe(II)-carbonate but by Fe(II)-silicate.

2. Micritic siderite facies in many Precambrian iron formations bear morphological and textural evidence for and settling direct precipitation (homogeneous nucleation) from the water column. The simplest explanation of water column precipitation of siderite was caused by hydrothermal-seawater mixing, where the requisite critical supersaturation for AFC nucleation was surpassed.

3. Rapid nucleation of Fe(II)-carbonate and -silicate at the hydrothermal-seawater mixing zone supplied nanoparticles of nuclei/seeds to the sediment and drew down the concentration of Fe^{2+} in the bottom water via crystal growth until equilibria are reached. This dynamic process disentangles the deposition of ferruginous sediments from the equilibrium state of the ambient seawater, in the sense that the abundance of ferruginous sediments in the late Archaean does not imply a prolonged oversaturation of the ambient seawater with respect to these minerals.

4. Crystal growth of the nucleated Fe(II)-carbonate and -silicate in the sediment pile would have further attenuated dissolved Fe^{2+} in the deepwater until chemical equilibrium with respect to these two mineral groups was reached.

5. Because siderite is nearly 2 orders of magnitude less soluble and precipitates 7 orders of magnitude slower than that of calcite, at a given pH-pCO_2 condition, siderite supersaturation varies significantly in response to Fe flux, which implies a more dynamic and episodic precipitation process than previously appreciated. In this light, the enhanced Fe flux caused by hydrothermal input in

the late Archaean oceans might have allowed siderite precipitation to temporarily surpass calcite growth as the major sink of DIC. This possibility deserves more investigation from a theoretical and experimental point of view.

6. Microbial activity, namely the dissimilatory Fe(III) reduction, has been suggested to generate the negative $\delta^{13}C$ signature in iron formation-associated siderite facies, which in turn, necessitated Fe(III) fluxes that were provided by microbial Fe(II)-oxidation or photosynthetic oxidation. Aside from Fe(II)-bearing carbonate facies (including ankerite) that clearly show metamorphic overprints, texturally primary siderite exhibits $\delta^{13}C$ signatures that are consistent with abiotic precipitation fractionation from a hydrothermal-seawater mixing fluid and/or growth at an elevated solution saturation (causing kinetic isotope fractionation). This prompts a re-evaluation of how biological processes might have controlled the formation of siderite in the geologic record.

Nullius in Verba.

-Quintus Horatius Flaccus

Dedication

To my parents and my sister.

Declaration

I declare that this thesis, which I submit to the University of Oxford for examination in consideration of Doctor of Philosophy in Earth Sciences is entirely my own work except where otherwise indicated. This thesis has not been submitted, either partially or in full, either for this Honour School or qualification or for another Honour School or qualification of this University, or for a qualification at any other institution. I have clearly indicated the presence of all material I have quoted from other sources, including any diagrams, charts, tables or graphs. I have clearly indicated the presence of all paraphrased material with appropriate references. I have acknowledged appropriately any assistance I have received in addition to that provided by my adviser.

Acknowledgement

I dedicate my most sincere gratitude to my doctorate advisor, Nicholas J. Tosca, for his critical scientific insight and foresight, encouragement and enlightenment, and his inexhaustible effort in substantiating and elaborating my ideas.

To the same extent, I express my gratitude to Benjamin Tutolo for in-depth discussions on the theoretical development, utilisations, and limitations regarding the thermodynamics of aqueous electrolyte systems. I thank him for his hospitality during my academic visit to the University of Calgary, and his substantial assistance in this doctorate project.

I express my appreciation to Rosalie Tostevin, for her immeasurable patience and devotion that set me on the course of rigorous experimentation; for the help and care she provided when I started stumbling around in the aqueous geochemistry lab.

With all sincerity, I am thankful to my peers and friends, for the support, inspiration, and delight they provided in both my professional and personal development: Ritwika Sengupta, Sascha Holland, Brooke Johnson, Lucy Kissick, Raphael Pietzsch, Katherine Clayton, Sam Cornish, and Tomas Jonathan; Sumner A. R. Braund, Lucia Bucciarelli, and Claudia M. H. Haindl.

In memory of Danielle Kondla.

Contents

1 Introduction **1**
- 1.1 The chemistry of ferruginous Precambrian ocean 2
  - 1.1.1 Genesis of iron formations: traditional models 5
  - 1.1.2 New constraints on the origin of late Archaean/early Palaeoproterozoic iron formation: petrographic studies . . . 7
  - 1.1.3 A new depositional and diagenetic model for Archaean iron formations 14
- 1.2 The atmospheric CO_2 levels on early Earth 17
- 1.3 Thesis layout 21

2 Homogeneous nucleation of Fe(II)-carbonate **23**
- 2.1 Introduction 25
- 2.2 Experimentation 27
  - 2.2.1 Analytical technique and procedure 30
- 2.3 Analytical results 32
- 2.4 Discussion 38
  - 2.4.1 Mineralisation pathway 38
  - 2.4.2 Homogeneous precipitation kinetics 40
  - 2.4.3 Could Fe(II)-carbonate have precipitated from anoxic ferruginous seawater? 42
  - 2.4.4 Constraints on the origin of siderite in late Archaean/early Palaeoproterozoic iron formations 46
- 2.5 Conclusion 50
- 2.6 Supplementary material 53
  - 2.6.1 Thermodynamic calculation 53
  - 2.6.2 Carbonate speciation in Fe(II)-carbonate precipitation. . 55
  - 2.6.3 Fe^{2+} concentration and Fe(II)-carbonate saturation. . . . 57

3 Growth kinetics of siderite **59**
- 3.1 Introduction 62
- 3.2 Methodology 64
  - 3.2.1 Apparatus and reagent preparation 64
  - 3.2.2 Siderite seed synthesis 65
  - 3.2.3 Growth and reprecipitation experiments 66
  - 3.2.4 Analytical procedures 68
- 3.3 Results 71
  - 3.3.1 Solution chemistry evolution 71
  - 3.3.2 Solid characterisations 74

3.4 Discussion . . . 82
3.4.1 Chemical affinity-based rate laws . . . 82
3.4.2 Siderite growth kinetics . . . 86
3.4.3 Comparison with previous siderite kinetic studies . . . 91
3.4.4 Comparison with Ca- and Mg-carbonate growth . . . 95
3.5 Conclusion . . . 98
3.6 Supplementary information . . . 101
3.6.1 Thermodynamic calculations . . . 101
3.6.2 Carbonate speciation calculation . . . 105

4 Kinetic isotope effect of carbon in siderite growth at 25 °C and 1 bar 107
4.1 Introduction . . . 107
4.2 Theoretical treatment . . . 109
4.2.1 Microscopic processes at mineral-water interface . . . 109
4.2.2 Fractionation by diffusion: α_d . . . 111
4.2.3 Fractionation by surface reaction: α_{sr} . . . 115
4.3 Experimental and analytical method . . . 118
4.4 Results and discussion . . . 119
4.4.1 Product isotopic composition of precipitated siderite . . . 119
4.4.2 Kinetic fractionation model of C isotopes during siderite growth . . . 122
4.4.3 Backward reaction rate r_b . . . 128
4.5 Conclusion . . . 129

5 The Iron cycle on early Earth 131
5.1 Summary of Fe(II)-mineralisations . . . 131
5.1.1 Fe(II)-carbonate system . . . 131
5.1.2 Fe(II)-$SiO_2(aq)$ system . . . 135
5.1.3 Green rusts . . . 139
5.2 The Archaean iron cycle: merging sedimentological and geochemical constraints . . . 142
5.2.1 Hydrothermal effluent-seawater mixing and the origin of iron formation . . . 143
5.2.2 Early diagenetic Fe(II)-carbonate precipitation as a deep water sink for Fe^{2+} . . . 148
5.3 Summary . . . 155

Supplementary chapters 159
S.1 Siderite solubility determination . . . 160
S.1.1 Thermodynamic properties of Fe(II) carbonate. . . . 160
S.1.2 Speciation schemes. . . . 162
S.1.3 Siderite solubility product. . . . 164
S.1.4 Conclusion. . . . 169
S.2 Thermodynamics of aqueous electrolyte systems . . . 171
S.2.1 Introduction . . . 171
S.2.2 Activity, activity coefficient, and ionic strength . . . 172
S.2.3 Debye-Hückel equation . . . 175

S.2.4 Conclusion 182

List of Tables

2.1 Thermodynamic properties and constants for activity coefficient calculation 55

3.1 Starting solution compositions of growth and reprecipitation experiments 68
3.2 Evolution of solution chemistry of growth experiments 87
3.3 Evolution of solution chemistry of reprecipitation experiments . 88
3.4 Thermodynamic properties and constants for activity coefficient calculation 102
3.5 A shortlist of reported values of siderite solubility product . . . 104

4.1 Initial solution chemistry, measured $\delta^{13}C_{sid,exp}$, and Modelled ($\delta^{13}C_{sid,mod}$) of each growth experiment. 122

S.1 A shortlist of reported siderite solubility product $\log K_{sp}$ 163

List of Figures

1.1 Temporal evolution of ocean oxidation state, atmospheric O_2 and CO_2, and Fe tonnage in iron formations 3
1.2 Examples of post-depositional alteration and generation of fine-grained secondary haematite 9
1.3 Greenalite-rich laminae and chert, Wittenoon Formation, Hamersley Group. 11
1.4 Examples of post-depositional alteration and oxidation of siderite 12
1.5 Schematic diagram for the formation of magnetite-rich bands in Hamersley Group iron formation. 15

2.1 Evolution of solution [Fe(II)] (ICP-OES analysis) in the Fe(II)-carbonate and Fe(II)-carbonate-silicate systems 33
2.2 logpCO_2-pH space of closed-system synthesis of Fe(II)-carbonate in two different matrices 34
2.3 XRD diffractograms of precipitated Fe(II)-carbonate 36
2.4 FT-IR transmittance spectra of precipitates from Fe(II)-carbonate system and Fe(II)-carbonate-silicate system. 36
2.5 SEM images of precipitated materials from Fe(II)-carbonate system. 37
2.6 amorphous Fe carbonate (AFC) precipitation rate as a function of solution saturation. 43
2.7 Fe(II)-carbonate-silicate system controlled by greenalite solubility 45
2.8 Compilation of $\delta^{13}C$–$\delta^{18}O$ from reported siderite facies in banded iron formations. 48

3.1 Experimental apparatus for siderite seed synthesis 66
3.2 pCO_2-pH space of closed-system syntheses of siderite 69
3.3 Evolution of solution [Fe(II)] (ICP-MS analysis) in the growth and the reprecipitation experiments 72
3.4 The evolution of solution saturation and the cumulative Fe(II) consumption (in moles) of growth experiments 73
3.5 Powder X-ray diffractograms of seed and harvested solids 76
3.6 FT-IR transmittance spectra of seed and harvested solids 77
3.7 SEM images of siderite seed and harvested solids from growth experiments 80
3.8 SEM images of harvested solids from reprecipitation experiments 81
3.9 An illustration of microscopic mineral-water processes a schematic of kinetic behaviour 84
3.10 Kinetic behaviours of siderite growth 89

3.11 Comparison of siderite growth rates with previous studies 95
3.12 Comparison of growth kinetics between siderite and calcite. . . . 97

4.1 Illustration of microscopic processes at mineral-water interface with associated kinetic fractionation 110
4.2 Measured isotopic composition $\delta^{13}C$ (‰; VPDB) of siderite from growth experiments plotted against (A) initial solution saturation and (B) initial growth rate. 121
4.3 (A) Modelled evolution of solution saturation and (B) corresponding instantaneous $\delta^{13}C_{sid}$ in precipitated siderite of growth experiments. 125
4.4 (A) Modelled isotopic composition ($\delta^{13}C_{sid,mod}$; ‰) after 46 days according to the kinetic fractionation model compared to the measured isotopic composition ($\delta^{13}C_{sid,exp}$) from growth experiments. (B) Modelled initial fractionation factor plotted at the initial siderite growth rate. 126

5.1 Solubility diagram for the Fe^{2+}-SiO_2-H_2O system at 25 °C. . . . 137
5.2 Experimentally determined nucleation-dominated greenalite precipitation rate as a function of solution saturation. 138
5.3 Reaction path modelling of the mixing between hydrothermal effluent and anoxic seawater. 146
5.4 Homogeneous vs heterogeneous precipitation of siderite, theoretical comparison. 152
5.5 Relationship between siderite supersaturation and Fe concentration as a function of pCO_2 levels estimated for the late Archaean. 153
5.6 Schematic of the Fe cycle before the oxygenation of the oceans and atmosphere. 156
S.7 Debye length (κ_D) of monovalent ion as a function of stoichiometric ionic strength. 181
S.8 Mean activity coefficient of NaCl solution as a function of hypothetical $\mathring{a}$ 182

Chapter 1

Introduction

Our understanding of the surface biogeochemistry on early Earth relies heavily on geochemical and isotopic proxies preserved in the sedimentary record. Comparing the surface of the early Earth with that of the modern, two aspects of chemistry stand out among many. First, before the rise of atmospheric $O_2(g)$, the anoxic oceans likely featured higher fluxes of hydrothermally-sourced cations in reduced states, notably Fe^{2+}, which ultimately entered the marine sedimentary record (the Fe^{2+}-rich condition is referred to as ferruginous; see review by Poulton and Canfeld 2011). Secondly, the early Earth atmosphere likely contained elevated greenhouse gases (e.g., CO_2, CH_4) that counter-balanced a reduced solar luminosity at the early stage of star evolution (the faint young Sun paradox; Sagan and Mullen 1972), thus, maintained a surface temperature for liquid water (e.g., Gough 1981; Kasting 1993; Sagan and Mullen 1972) (Fig. 1.1). These conditions favoured the formation of ferrous carbonate—siderite ($FeCO_3$). In fact, owing to its widespread abundance in sedimentary rocks, siderite has been frequently used as a palaeoenvironmental proxy in reconstructing the levels of Fe^{2+} and pCO_2 in the Precambrian. For example, the abundance of siderite in Precambrian iron formation led to the interpretation that siderite equilibrium represents a reasonable upper limit for the concentration of Fe^{2+} in the ferruginous oceans (Holland 1984; Raiswell et al. 2011). Conversely, the absence of siderite in the 2.2 Ga palaeosols led

to the argument that $p\mathrm{CO_2}$ at the time of deposition was too low to maintain a surface temperature above freezing (Rye et al. 1995), prompting hypotheses that invoke other greenhouse gases like $\mathrm{CH_4}$ (Kasting 2013; Kasting et al. 2001).

Although the widespread occurrence of siderite has motivated thermodynamic studies for most of the last century (since Smith 1918), the kinetic behaviours relating to the nucleation and crystal growth of Fe(II)-carbonate remain poorly understood. In what follows, a brief introduction is provided regarding these two aspects of palaeoenvironmental reconstruction that centralised on the thermodynamics and precipitation kinetics of siderite. Though this thesis has to limit its scope to the marine sedimentary record, a broad overview of atmospheric $\mathrm{CO_2}$ evolution provides the context of using terrestrial siderite as a $p\mathrm{CO_2}$-proxy.

1.1 The chemistry of ferruginous Precambrian ocean

The chemical conditions of the Precambrian ocean were inextricably linked to the redox evolution of the ocean-atmosphere system (Canfield 2005; Holland 1984; Lyons et al. 2014; Raiswell et al. 2011; Walker 1985). A lack of atmospheric $\mathrm{O_2}$ and vigorous hydrothermal input probably sustained the anoxic and ferruginous conditions that persisted through much of the Archaean and Palaeoproterozoic (Holland 1984; Isley 1995; Isley and Abbott 1999; Kump and Seyfried 2005) (Fig. 1.1). This chemistry is most conspicuously archived by iron formations, an iron- and silica-rich chemical sedimentary rock that peaked in sedimentary abundance as it was deposited on late Archaean-Palaeoproterozoic continental margins (see reviews by Beukes and Gutzmer 2008; James 1954; Klein 2005; Pufahl 2010; Simonson 2003, and references therein) (Fig. 1.1). Most studies agree that the Fe contained in iron formations was primarily sourced from hydrothermal activities and/or seafloor basaltic volcanism (e.g., Derry and Jacobsen 1990; Jacobsen and Pimentel-

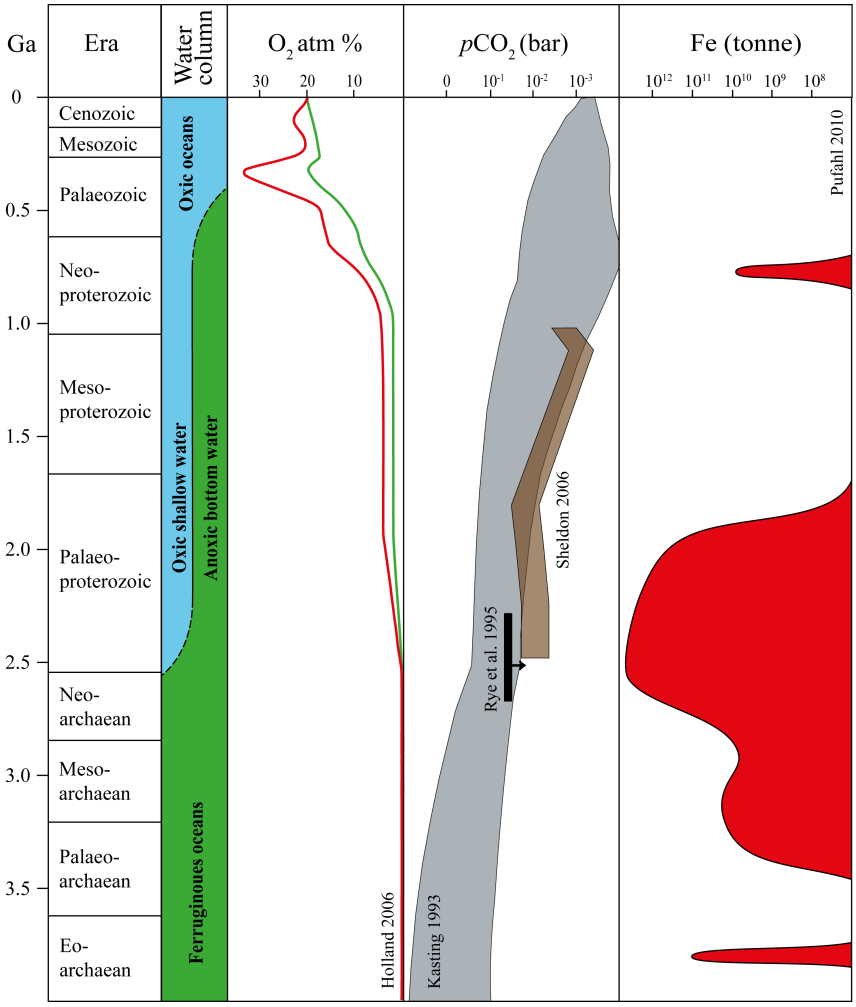


Figure 1.1: Temporal evolution of ocean oxidation state, atmospheric O_2 and CO_2, and Fe tonnage in iron formations. Evolution of atmospheric O_2 is summarised by Holland (2006, and references therein) with the red and green lines represent the upper and lower boundaries of estimations, respectively. pCO_2 evolution reconstructed by Kasting (1993) (grey area) based on an one-dimensional climate model that mitigates a reduced solar luminosity in the past (Sagan and Mullen 1972), with the upper and lower boundaries set by ocean-covered and ice-covered Earth, respectively. Rye et al. (1995) proposed $pCO_2 < 10^{-1.4}$ (black bar) based on the absence of siderite in four pre-2.2 Ga palaeosols, by assuming greenalite-siderite equilibrium behaviour. Sheldon (2006) employed a mass-balance weathering model (brown area) focuses on cation-loss in six palaeosol profiles and constrained pCO_2 levels that were insufficient in keeping a liquid-water surface temperature on early Earth. Fe tonnage in Precambrian iron formations is summarised by Pufahl (2010, and references therein), based on deposit age and resource estimates.

Klose 1988; Krapež et al. 2003; Simonson 2003). Although some are strongly overprinted by post-depositional oxidation, these successions show that alongside amorphous silica, Fe was ultimately deposited as greenalite (Fe(II)-silicate; $Fe_3Si_2O_5(OH)_4$) and siderite, in turn reflecting a distinct Fe cycle that persisted for much of Earth history before the oxygenation of deepwater (Beukes et al. 1990; Holland 2007; Klein 2005; Rasmussen et al. 2016, 2017; Tosca et al. 2016, 2019).

Surprisingly, however, gaps still persist in our understanding of the pathways and products of Fe-based chemical sedimentation from early oceans. In part, these arise from two research challenges. The first involves developing a more quantitative understanding of reaction rates and products involving ferrous iron and applying this understanding to aid in the interpretation of mineralogical, chemical, and isotopic signatures recovered from ancient rocks. Because these data were largely unavailable at the time, early views of the Fe cycle relied instead upon thermodynamic predictions of important reactions thought to have taken place in the water column or sediment pore waters (Drever 1974; Eugster and Chou 1973; Holland 1973, 1984). Together these calculations mark a critical starting point, and have shaped our current view of iron cycling on the early Earth. For example, citing the widespread occurrence of sideritic carbonates in the geologic record, Holland (1984) inferred that the late Archaean oceans would have been poised at both calcite and siderite saturation. Following from this, several authors have suggested that siderite equilibrium itself represents a reasonable upper limit for Fe^{2+} concentration (e.g., Halevy et al. 2017; Raiswell et al. 2011).

A second challenge arises from the probability that ancient sedimentary successions have been metamorphosed or otherwise altered after deposition. Although chemical sediments are preserved in a number of Archaean successions, their extensive post-depositional history commonly features multiple generations of diagenesis and/or mineral transformation (Beukes et al. 1990; Kaufman 1996; Kaufman et al. 1990; Klein and Beukes 1989; Klein 2005).

A correct interpretation of ancient sedimentary rocks, therefore, requires deconvolving primary (i.e., marine) mineral products from those that are largely post-depositional in origin. Our view of the chemical state of Precambrian oceans thus hinges on understanding the behaviour of Fe^{2+} in seawater and sedimentary pore water.

Petrographic studies indicate that many of the Precambrian BIF-associated cherts were formed by direct silica precipitation at or just below the seabed in the form of silica gel (which lacks ghosts or inclusions of precursors and show fine-scale grain fracturing from syneresis; Maliva et al. 2005; Rasmussen et al. 2015a), suggesting a dissolved silica concentration likely at or above the equilibrium solubility with respect to opal-CT and possibly also to amorphous silica (or opal-A; Holland 1984; Maliva et al. 2005; Siever 1992). Therefore, constraining Fe^{2+} concentrations in the Precambrian oceans requires an understanding of the competitive precipitation of Fe(II)-silicates and/or Fe(II)-carbonate (Holland 2007; Raiswell et al. 2011). Although recent work has investigated the kinetics of Fe(II)-silicate precipitation (Tosca et al. 2016), a more comprehensive understanding of Fe(II)-carbonate precipitation kinetics has persisted as a major obstacle in exploiting Fe(II)-carbonate as a useful palaeoenvironmental indicator, and in understanding ferruginous seawater chemistry more broadly.

In what follows, a brief summary is given on the traditional deposition model for some Precambrian iron formations, as well as merging new models based on recent advance in petrographic and geochemical studies (reproduced with permission from Tosca et al. 2019).

1.1.1 Genesis of iron formations: traditional models

Archaean sedimentary rocks, long recognised by geologists as conspicuously enriched in iron, offer an unusually accessible record of the early iron cycle. Several workers have emphasised compositional differences between Archaean and post-Archaean clastic sedimentary rocks (Garrels and Mackenzie 1971;

McLennan 1982; Taylor and McLennan 1985), but Kump and Holland (1992) further examined secular patterns in Fe enrichment. They showed that Fe was added to marine siliciclastic sediments at a flux (relative to the total deposition rate) that increased the average bulk Fe content by a factor of two compared to younger equivalents. How, and in what form (i.e., particulate or dissolved) was this Fe delivered to Archaean marine sediments? Although clastic sedimentary rocks provide clear evidence for secular change in bulk Fe enrichment, chemically-precipitated sedimentary rocks have yielded the most important constraints on Fe delivery mechanisms. In particular, iron formation, a chemical sedimentary rock deposited through much of the Archaean (and specific intervals at the beginning and end of the Proterozoic; Bekker et al. 2010) (Fig. 1.1), serves as our most important archive of the mineral products that entered precursor sediments.

Early models for the origin of iron formation centred mainly on the origin of haematite ($Fe(III)_2O_3$), the oxidised Fe-mineral principally responsible for imparting the distinctive red colour to many (but not all) of the most iconic deposits (i.e. James 1954). Depositional and diagenetic models have long hypothesised that the finest-grained (or "dusty") haematite, commonly trapped in early diagenetic chert, might represent minerals formed directly from seawater (Ayres 1972; Beukes and Gutzmer 2008; Dimroth and Chauvel 1973; Spencer and Percival 1952; Sun et al. 2015). This inference, based predominantly on small particle size (i.e., following criteria established by LaBerge 1964), along with thermodynamic calculations that appeared to reconcile the co-existence of haematite, siderite ($Fe(II)CO_3$), and pyrite ($Fe(II)S_2$) in modern and ancient sediments (Krumbein and Garrels 1952), led to a general acceptance that the dusty haematite represented a primary precipitate from Archaean seawater (see Rasmussen et al. 2016 for historical context). This, in turn, prompted models for the origin of haematite through oxidation of soluble Fe^{2+} via iron-oxidising photosynthesis or reaction with $O_2(aq)$ produced from cyanobacteria (first suggested by Cloud 1973). Other ideas for the origin

of oxidised Fe-phases in iron formation included UV photolysis (Braterman et al. 1983), though Konhauser et al. (2007) later suggested that photolysis rates were probably too slow to account for apparent depositional rates of iron formation.

As a consequence, genetic models for iron formation, developed over the last several decades, have posited that much of the haematite was derived from the dehydration of Fe(III)-oxides that initially entered iron formation precursor sediments (Ayres 1972; Beukes and Gutzmer 2008; Dimroth and Chauvel 1973; Konhauser et al. 2017; Spencer and Percival 1952; Sun et al. 2015). This oxidised Fe is generally hypothesised to have served as a source of electron acceptors for dissimilatory iron reduction during early diagenesis (Konhauser et al. 2005; Walker 1984). In this view, reduced Fe(II)-bearing phases would be predominantly diagenetic in origin, formed through the reduction of Fe(III) in combination with various dissolved pore water components to generate magnetite ($Fe(II)/Fe(III)_2O_4$), siderite, and Fe(II)-silicates (Walker 1984). A supporting line of evidence for this hypothesis comes from the negative carbon isotopic composition (expressed as $\delta^{13}C$) of many iron formation carbonates, which was originally suggested to reflect the influence of microbial iron reduction coupled to organic matter oxidation (Walker 1984). More recent isotopic investigations have inferred that such processes may also be recorded by iron isotopes because iron formation carbonates and magnetite feature depleted $\delta^{56}Fe$ values that correlate with negative $\delta^{13}C$ (Johnson et al. 2008a, 2005, 2013; Yamaguchi et al. 2005).

1.1.2 New constraints on the origin of late Archaean/early Palaeoproterozoic iron formation: petrographic studies

Given that traditional optical microscopy was the principal tool available to early investigators of iron formation, the advent of high-resolution electron microscopy has increased the effective spatial resolution at which observations can be made by 4 orders of magnitude. This has offered a new opportunity to

re-examine iron formation successions and re-assess paragenetic relationships between minerals. With this goal in mind, Rasmussen and colleagues, in a series of recent studies, applied a combination of transmission/reflected light microscopy, backscattered electron imaging, and high angle annular dark-field STEM and TEM microscopy on focused ion beam (FIB)-milled specimens of iron formation (Rasmussen et al. 2014, 2013, 2015b, 2016, 2017). The examination of several hundred thin sections, sampled from well-preserved drill core through the 2.63–2.45 Ga Hamersley Group, Australia, led Rasmussen et al. (2014, 2016, 2017) to conclude that much of the finest-grained (so called "dusty") haematite is consistent with a secondary, or post-depositional, origin. This conclusion is supported by the following groups of observations (Fig. 1.2):

1. Haematite dust is concentrated along grain boundaries, cleavage planes and within altered grains of diagenetic/metamorphic Fe(II)-carbonate and Fe(II)-silicates.

2. Transition zones from green to red chert are commonly observed along individual sedimentary laminae; these are discordant to sedimentary bedding. These observations are not immediately compatible with hypotheses arguing for the precipitation of both Fe(II)-silicates (primarily responsible for green pigmentation) and Fe(III)-oxide/-hydroxides (responsible for red/orange pigmentation) from the same water column.

3. Replacement of Fe(II)-silicate by haematite is commonly observed along hairline fractures that cross-cut laminated chert.

4. Cavities are commonly observed to contain Fe(II)-silicate which sometimes occurs with haematite in the same cavity. These cavities are inferred to represent dissolution/precipitation processes associated with mineral replacement reactions that created nano-pore space eventually filled or replaced by haematite.

5. Relict Fe(II)-silicate nanoparticles are abundant and commonly found

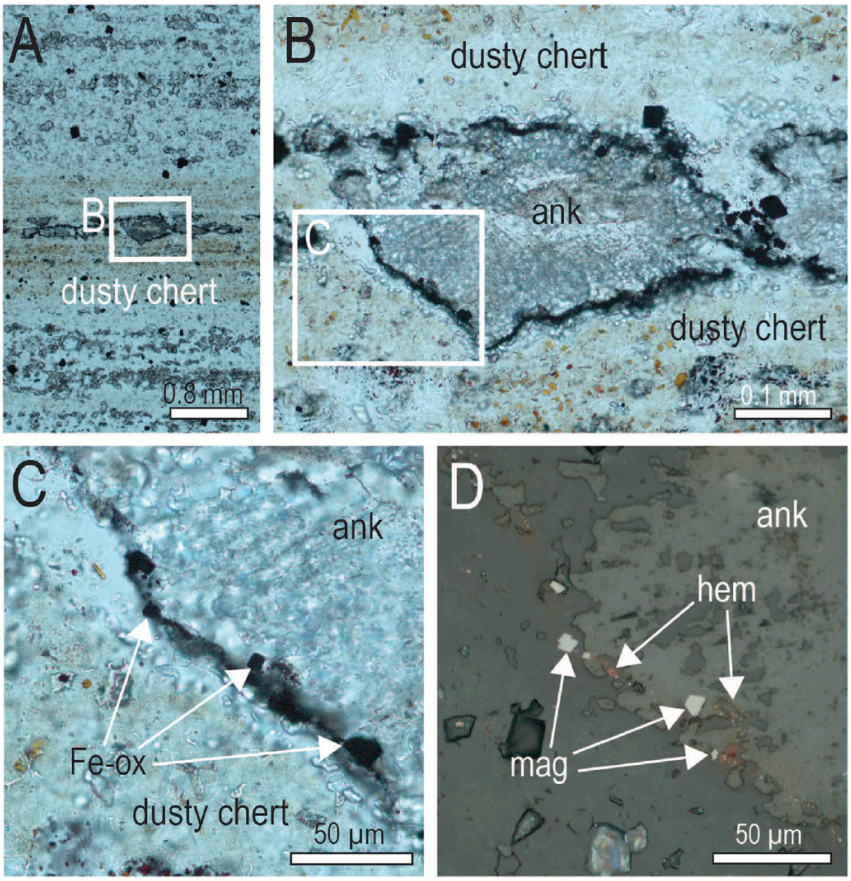


Figure 1.2: Examples of post-depositional alteration and generation of fine-grained secondary haematite. Drill-hole ABDP9, 222.1-0.19m (Mt Sylvia Formation, Hamersley Group). (A) and (B). Transmitted light images of diagenetic ankerite (ank) in dusty chert. (C). Transmitted light image of fine-grained magnetite and haematite (Fe-ox) concentrated at the edges of coarse-grained diagenetic ankerite. (D). Reflected light image of fine-grained magnetite (mag) and haematite (hem) concentrated at the edges of coarse-grained diagenetic ankerite.

preserved in otherwise red cherts.

Perhaps the most important conclusion drawn from high-resolution petrographic studies of Archaean iron formation is that the mineral phases displaying the clearest evidence for a primary origin are Fe(II)-silicates, specifically greenalite ($Fe_3Si_2O_5(OH)_4$) and possibly stilpnomelane ($(K,Ca,Na)(Fe,Mg,Al)_8(Si,Al)_{12}(O,OH)_{36} \cdot nH_2O$) (Rasmussen et al. 2014, 2013, 2015b, 2016, 2017). A primary origin is supported by pervasive Fe(II)-silicate nanoparticles trapped in early diagenetic chert (Fig. 1.3), formed via silicification at or below the seafloor during or shortly after the re-working and accumulation of Fe(II)-silicate muds (Rasmussen et al. 2014, 2013, 2015b, 2016, 2017). In fact, sedimentological and petrographic evidence of silica-rich horizons in Archaean iron formation that show that silicified Fe(II)-bearing muds were subsequently re-worked into intraformational sandstones, indicating that Fe(II)-silicate deposition and silicification occurred syndepositionally (i.e. Rasmussen et al. 2015a). More recent investigations of iron formation successions from the late Archaean Transvaal Supergroup lead to a similar conclusion. Here, Fe(II)-silicates appear to represent the dominant depositional phase, also commonly preserved in chert (Rasmussen et al. 2017). Like the Hamersley Group, Fe(II)-silicate-rich horizons of iron formation in the Transvaal Supergroup are commonly replaced by coarser grained Fe(III)-oxide, Fe-silicate (i.e., minnesotaite) and Fe-carbonate minerals (Rasmussen et al. 2017).

These high resolution petrographic and microscopic investigations have also shown that magnetite, a common mineral in nearly all Archaean iron formation deposits, may also owe its origins to secondary replacement processes (Rasmussen and Muhling 2018; Fig. 1.4). Rasmussen and Muhling (2018), focusing again on Hamersley Group iron formation, reached this conclusion based on the following groups of observations:

1. The identification of lateral transitions from siderite-rich Fe(II)-silicate bands into magnetite-rich bands.

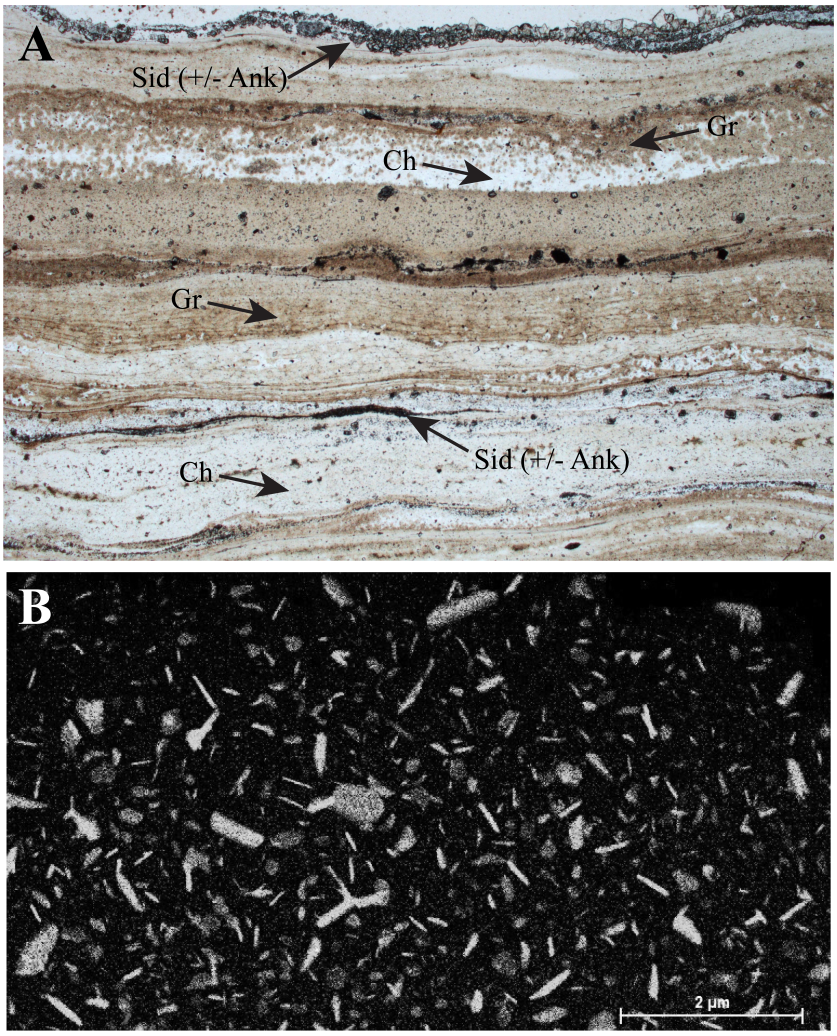


Figure 1.3: (A). Greenalite-rich laminae and chert (Drill hole ABDP9, 288.23-0.36m (Wittenoom Formation, Hamersley Group). Ch=chert; Sid=siderite; Ank=ankerite; Gr=greenalite. (B). Transmission electron microscopy image of greenalite nanoparticles trapped in chert (Drill hole ABDP9, 37 m).

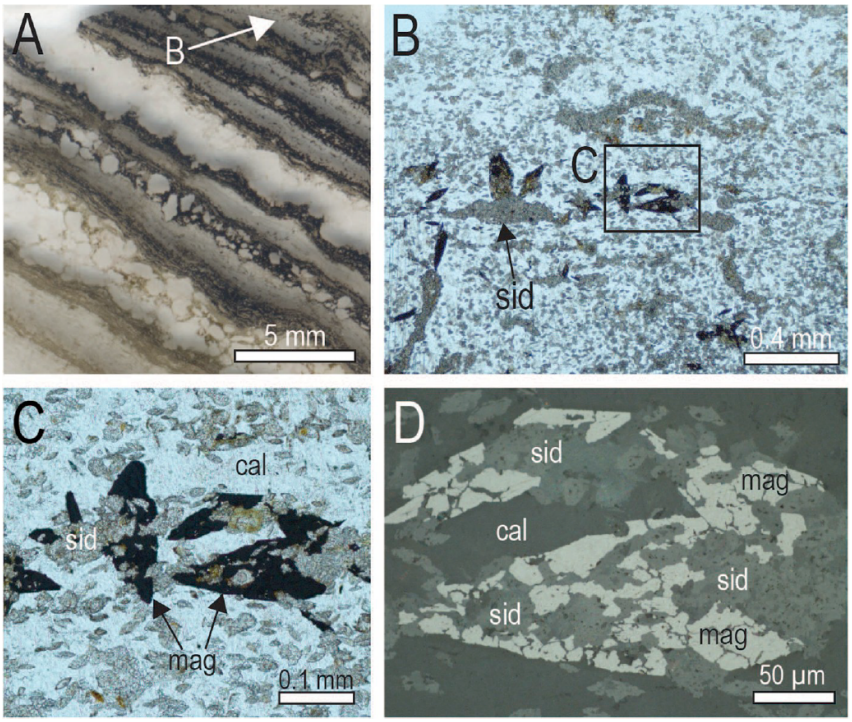


Figure 1.4: Examples of post-depositional alteration and oxidation of siderite. Drillhole Mitchell-2, 311.0m (Dales Gorge Member, Brockman Iron Formation, Hamersley Group). (A-C). Transmitted light images of laminated Fe-oxides and chert. (D). Reflected light image of alteration textures of magnetite over-growths including and overprinting finely crystalline siderite with coarser, crystalline fabric.

2. Minute magnetite (and haematite) crystals along corroded grain boundaries and within partially altered grains of Fe(II)-carbonate and silicates. This suggests that dissolution-reprecipitation reactions were the dominant emplacement mechanism.

3. The association of magnetite with minute haematite particles surrounding altered mineral grains.

4. The development of scalloped and irregular boundaries between magnetite and reacting minerals such as ankerite and siderite. In these cases, magnetite also contains siderite and/or ankerite inclusions, consistent with a secondary origin.

5. Dissolution pits and cavities in siderite crystals adjacent to replacive magnetite.

6. Magnetite precipitation post-dates differential compaction, suggesting replacement occurred after significant burial and the establishment of overburden.

New observational constraints on the origin of magnetite in these deposits support two major conclusions. The first is that magnetite is dominantly replacive in Hamersley Group iron formation, and, given its close spatial association with siderite, likely originated through thermal decomposition reactions upon burial and metamorphism (Rasmussen and Muhling 2018). For example, experimental studies on the thermal decomposition of siderite have shown that in the presence of water, siderite breaks down to form magnetite, liberating CO_2 and H_2 in the process (Milesi et al. 2015). This occurs at temperatures $\approx$ 200–350 °C, which corresponds to metamorphic temperatures experienced by much of the Hamersley Group (Rasmussen and Muhling 2018). The second conclusion is that siderite appears to have commonly precipitated in, and/or along the surfaces of, greenalite-rich laminae before significant compaction took place, pointing to a dominantly early diagenetic origin (Rasmussen and

Muhling 2018).

1.1.3 A new depositional and diagenetic model for Archaean iron formations

Together, the observations summarised above tightly constrain the principal depositional and diagenetic processes that generated late Archaean and Palaeoproterozoic iron formation as well as their relative timing. As summarised by Rasmussen and Muhling (2018), these processes commenced with prolific deposition of Fe(II)-silicate-rich muds (Fig. 1.5A). These highly porous muds were commonly silicified on the seafloor before compaction (Fig. 1.5B), yielding well-preserved greenalite nanoparticles trapped in chert (commonly referred to as "dusty chert"), and non-silicified greenalite-rich sediments, The precipitation of siderite on the surfaces of, and within, Fe(II)-silicate-rich laminae commonly occurred soon after initial deposition but, in many cases, before significant compaction (Rasmussen and Muhling 2018; Fig. 1.5C). Post-depositional transformation of siderite to fabric-destructive and/or replacive magnetite yields variably magnetite-enriched intervals among silicified sediments (Fig. 1.5D). Together, Fe(II)-silicate precipitation, in combination with variable amounts of seafloor silicification, were likely instrumental in generating alternating bands of silica-rich and iron-rich composition (Rasmussen et al. 2017). Post depositional interaction with repeated generations of fluid flow linked to the ca. 2.2 Ga collision or accretion of the Glenburgh Terrane with the Pilbara Craton, known as the Ophthalmian Orogeny, would have driven the secondary formation of haematite (i.e. Rasmussen et al. 2014), consistent with independent geochemical evidence for the appearance of oxygen-rich groundwaters during and shortly after the great oxidation event (i.e. Rybacki et al. 2016). Post-depositional deformation and fluid flow would also have promoted siderite replacement by magnetite via thermal decomposition.

These observations in turn invite new models for how the dominant mineralogical building blocks of iron formation, the Fe(II)-silicates, were initially

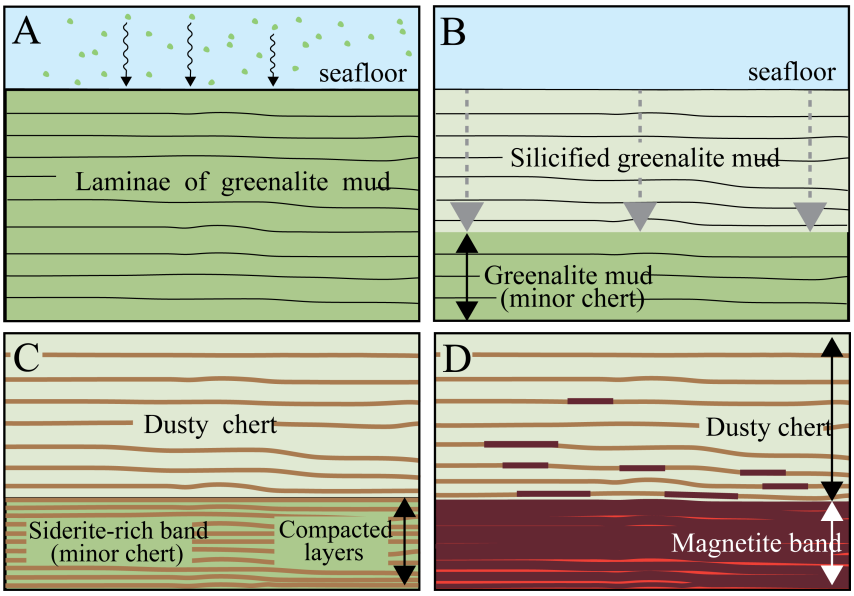


Figure 1.5: Schematic diagram for the formation of magnetite-rich bands in Hamersley Group iron formation (Rasmussen and Muhling 2018). (A). Precipitation of greenalite nanoparticles and micro-granules in the water column, forming laminae of porous, greenalite mud. (B). Silica cementation of greenalite mud prior to compaction forming tabular beds. (C). Compaction of non-silicified greenalite mud. Growth of siderite in greenalite mud and along laminae surfaces. (D). Replacement of siderite and greenalite in compacted iron-rich bands by magnetite and haematite during fluid alteration.

precipitated. Rasmussen et al. (2017), for example, suggested that mixing between hydrothermal effluent and ambient seawater might have triggered the precipitation of Fe(II)-silicate. This hypothesis finds support from sedimentological and stratigraphic studies indicating that iron formation intervals of the Hamersley Group are best interpreted as re-worked chemical sediments deposited on the flanks of submarine volcanoes rather than pelagites derived from chemical sedimentation from the water column (Krapež et al. 2003). In this model, the physical and chemical interaction of two fundamentally different fluid types would have modified local water column chemistry, commonly triggering the deposition of Fe(II)-silicate-rich muds.

The model proposed by Rasmussen et al. (2017) contrasts markedly with previous models for the origin of iron formation in that dissolved oxygen is not required at the time of iron formation deposition. By extension, the role of anoxygenic photosynthesis in generating a flux of oxidised iron to precursor sediments is not easily reconciled with the observations outlined above, or with new micro-analytical constraints indicating that greenalite preserved in iron formation chert contains little structural Fe(III) (Johnson et al. 2018). In addition, a dominantly post-depositional origin for magnetite suggests that the involvement of microbial processes in modifying initial iron formation mineral assemblages during early diagenesis may not be as clearly recorded in these successions as previously thought (Rasmussen and Muhling 2018).

The new model advocated by Rasmussen et al. 2017 also raises a number of questions regarding the early iron cycle and how it was structured before the GOE. Specifically, if Fe(II)-silicate minerals were indeed the primary building blocks of late Archaean/early Palaeoproterozoic iron formation successions, what processes triggered their precipitation, and how might this have influenced marine Fe^{2+} concentrations? Just as important, what processes triggered early diagenetic siderite precipitation in iron formation sediments, and why, in many instances, was it concentrated along Fe(II)-silicate-rich laminae? More broadly, how do these deposits constrain the nature of chemical

interactions between Fe^{2+}, $SiO_2(aq)$, and dissolved inorganic carbon?

1.2 The atmospheric CO_2 levels on early Earth

Physical models suggest a reduced solar luminosity in the early history of our Solar System (the Faint Young Sun theory) that would have left the surface temperature on Earth below the freezing point of seawater at the dawn of life (e.g., Kasting 1993; Rye et al. 1995; Sagan and Mullen 1972; Walker 1985). For example, the average surface temperature would only rise to 0 °C around 2.3 Ga, based on calculations of ≈ 70 % of current luminosity (Sagan and Mullen 1972). Estimated higher mantle temperature in the Archaean (≈ 1500-1600 °C compared to modern ≈ 1350 °C; Herzberg et al. 2010) would have contributed to higher geothermal heat flow and may have allowed life to emerge at hydrothermal hotspots. However, a different atmospheric composition with an elevated greenhouse effect is still needed to explain the hydraulic sedimentation in the geologic record (e.g., mudcracks and ripple marks in the 3.2 Gyr old Swaziland Supergroup; Ramsay 1963).

CO_2 and CH_4 were the leading candidates among the suggested greenhouse gases in mitigating the reduced solar luminosity (e.g., Kasting 2005; Shaw 2008; Walker 1985; Zerkle et al. 2012), with others including H_2O, H_2, CO, and N_2O. On Earth today, CH_4 is mostly of biological origin, and rapidly converted into CO_2 in reaction with O_2. Abiotically, CH_4 is mainly produced at hydrothermal vents via serpentinisation, and at a somewhat limited capacity (<4.1 ppmv simulated under $pCO_2 = 0.1$ bar; Guzmán-Marmolejo et al. 2013). Despite the fact that CH_4 might be able to last longer in an anoxic atmosphere, its steady state concentration would have been subject to efficient photolysis (into CO_2) under a considerably higher solar Lyman alpha radiation in the absence of an ozone layer (Kasting 2014, and references therein). Therefore, unless CH_4 was paired with a productive biosphere, its role in regulating the surface temperature on a geological time scale was probably supplementary to CO_2

(Zahnle 2006).

A high-CO_2 (tens of bars) atmosphere on early Hadean (4.5–4.0 Ga) Earth was a potential consequence of intense volcanic out-gassing (Rubey 1955) and impact degassing of incoming planetesimals (Ahrens et al. 1989). The ultimate sink for CO_2 was likely the subduction of carbonatised ultramafic oceanic crust into the mantle (Zahnle and Sleep 2002). Because the primitive crust was predominantly ultramafic, it has been argued that the pervasive carbonatisation (if subducted into the mantle) would have scrubbed CO_2 from the atmosphere and left a bitterly cold late Hadean world (Zahnle and Sleep 2002; Zahnle 2006). However, the estimated higher mantle temperature implies an absence of modern-style deep subduction into the mantle until the Neoproterozoic (Cawood and Hawkesworth 2014; Herzberg et al. 2010; Sizova et al. 2010). With no evidence of stable continental platforms in the Hadean (Isley and Abbott 1999), on which carbonates could have accumulated, carbonate rocks would instead have stagnated on a heated crust where they would have been unstable and released most of the sourced CO_2 back into the atmosphere. Therefore, the rate and capacity of CO_2 removal by seafloor carbonatisation is undercon-strained at present .

In contrast with the Hadean, Archaean (4.0–2.5Ga) atmospheric CO_2 was arguably controlled by surface processes due to the gradual cratonisation of the crust (Cawood et al. 2013, and references therein). As a solution to the still faint Sun ($\approx$ 75 % at 3.8 Ga; Gough 1981), Walker et al. (1981) proposed that high atmospheric CO_2 levels could be maintained by the carbonate-silicate cycle operating at the Earth's surface via a negative feedback mechanism over geologic timescales. The temperature-dependent silicate weathering would be ineffective on a cold surface and permitted CO_2 to rise, eventually warming the planet until the corresponding increase in silicate weathering rates counterbalanced CO_2 rise. If the surface temperature dropped below freezing, the consequent ice-coverage would have virtually halted both the silicate weathering on the continent (no rainfall) and the carbonatisation of the ultramafic sea-

floor (no gas-exchange), leaving CO_2 to accumulate in the atmosphere without a sink (Walker et al. 1981). On the other hand, silicate weathering is also a process that is physically dictated by the relief of the landmass. For example, the tectonic uplift of the Tibetan plateau during the Himalayan orogeny forcefully enhanced silicate weathering to draw down pCO_2 and contributed to Cenozoic glaciations (Raymo and Ruddiman 1992). Therefore, the thin Archaean continental crust (Cawood et al. 2013, and references therein) casts doubts on the overall effectiveness of the continental silicate-carbonate cycle on regulating Archaean pCO_2.

The sparsity of Precambrian geologic records leaves much of our understandings of the early atmosphere subject to speculation. Considerable efforts have been made in modelling atmospheric pCO_2 in deep time because of its crucial role in theoretical treatments of Earth's surface temperature (e.g., Hessler et al. 2004; Paris et al. 2008), shallow water pH conditions (e.g., Blättler et al. 2017; Halevy and Bachan 2017, and implications for the early biosphere (e.g.,Zerkle et al. 2012).

The framework of the current discussions on early atmospheric pCO_2 was mainly constructed by Kasting (1993), using a one-dimensional climate model, in which CO_2 was assigned as the sole greenhouse gas to maintain the surface temperature above freezing (Fig. 1.1). The wide estimates for pCO_2 proposed by Kasting (1993) sparked intense debates on reconciling the model with the geologic record, where sedimentary minerals that are dependent on the availability of CO_2 became the fundamental point-constraints. For instance, based on the studies of four pre-2.2Ga palaeosols, Rye et al. (1995) argued that siderite did not precipitate and was absent from the original assemblage, leaving Fe^{2+}-Fe^{3+}-silicate to dominate the Fe-mineralogy. Hence, through thermodynamic calculations of the greenalite-siderite phase stability, Rye et al. (1995) proposed $pCO_2 < 10^{-1.4}$ bar, under which siderite would be unstable (Fig. 1.1). Such a low pCO_2 value, however, was apparently insufficient in maintaining a surface temperature above freezing, and necessitates the presence of additional

greenhouse gases (Kasting 2013, 2014, 2004). A similar conclusion was reached in a constitutive mass-balance study by Sheldon (2006) that focused on the cation-loss during silicate weathering of six palaeosol profiles throughout the Proterozoic (Fig. 1.1).

In contrast, Ohmoto (2004) used the same greenalite-siderite phase stability relationship to argue that $p\mathrm{CO}_2 > 10^{-1.5}$ bar accounted for the abundance of siderite in pre-1.8 Ga iron formations. However, this attracted criticisms relating to the reliability of using deepwater facies like BIFs (e.g., Beukes and Gutzmer 2008, and references therein) to reflect the chemical composition of the atmosphere, as the CO_2 budget of deepwater should have been much larger, not least because deepwater was significantly influenced by hydrothermal venting (e.g., Bekker et al. 2013; Beukes and Gutzmer 2008; Isley and Abbott 1999; Krapež et al. 2003; Veizer et al. 1989).

Such climate controversies extend beyond Earth to our rusty terrestrial neighbour, Mars. Mineralogical studies conducted by Curiosity (NASA's Mars Science Laboratory rover) on the fluvio-lacustrine sequences at Aeolis Mons (Gale crater) indicate the abundance of authigenic Fe-minerals, apart from siderite (Bristow et al. 2017). A reaction-transport model that simulated the observed mineralogy, by coupling mineral equilibria with carbonate precipitation kinetics and rates of sedimentation, implies an atmospheric $p\mathrm{CO}_2$ in the range of 10s mbar at the time of deposition (3.5 Ga; Bristow et al. 2017); an insufficient value for existing climate models to explain a Martian surface for liquid water. Unlike Earth, a high CH_4 atmosphere could not be applied to Mars in a similar manner due to the lack of tectonics and life. Therefore, either the existing climate models still lack an essential component, or the $p\mathrm{CO}_2$ values were misinterpreted from our incomplete understanding of the origins of Fe-mineral assemblages.

This brief review on atmospheric $p\mathrm{CO}_2$ is incomplete and inconclusive, as the topic encompasses the evolution of tectonic activities, oxidation state of the mantle, structural evolution of the atmosphere, and the chemical evolution

of the atmosphere-ocean system as a whole. Addressing this grand challenge in our understanding of solar and planetary evolution is beyond the scope of this thesis, the readers are referred to a recent summary book *Atmospheric Evolution on Inhabited and Lifeless Worlds* by Catling and Kasting (2017).

1.3 Thesis layout

In what follows, this thesis investigates the processes, products, and rate of Fe(II)-carbonate precipitation using two experimental approaches. The first was to constrain the requisite critical supersaturation for homogeneous nucleation directly from solution (Chapter. 2). The second experimental approach was designated to investigate the kinetic behaviour of siderite growth as a function of solution chemistry (Chapter. 3). Based on the knowledge derived from these experimentations, kinetic fractionation of carbon isotopes during siderite growth was investigated as a function of growth rate (Chapter. 4). Each chapter is accompanied by a more specific introduction and conclusion. The conclusion chapter summarises the use of Fe(II)-carbonate system as a palaeoenvironmental proxy with a specific focus on the genesis of Precambrian iron formations.

In addition, this thesis includes two review chapters dedicated to (1) the experimental determination of siderite solubility, and (2) the developmental history of the thermodynamics of aqueous electrolyte systems. Even though the widespread occurrence of siderite has motivated thermodynamic studies for the most of the last century (since Smith 1918), the frequently cited siderite solubility product in the contemporary literature can be nearly an order of magnitude different. A review of the experimental methods and calculation schemes employed in the previous studies allows an evaluation of the most suitable value to be used in experimental design. A review on the developmental history of our understanding and modelling of aqueous electrolyte system complements the rationale beyond the choice of calculation schemes presented in

this thesis. The review chapter states the key parameters in the conceptualisation, generalisation, and adaptation of thermodynamic activity, ionic strength, and activity coefficient; discloses the applicability and limitations related to the thermodynamic calculations in this study.

Chapter 2

Homogeneous nucleation of Fe(II)-carbonate

Reproduced with permission from publication:

Fe(II)-carbonate precipitation kinetics and the chemistry of anoxic ferruginous seawater

on

Earth and Planetary Science Letters 506(2019) 231-242,

doi:10.1016/j.epsl.2018.11.010

by

Clancy Zhijian Jiang*, Nicholas J. Tosca

Earth Sciences Department, University of Oxford, OX1 3AN, England, United Kingdom.

Abstract

The chemical evolution of anoxic seawater through time is chronicled in part by the abundance of sedimentary Fe minerals. Our view of the chemical state of the oceans throughout much of Earth's history, therefore, hinges on understanding the behaviour of Fe^{2+} in seawater and sedimentary pore water. However, the formation pathways and precipitation rates of a number of sedimentary Fe(II)-minerals are poorly understood. For example, because siderite is widely distributed in Precambrian rocks, it is frequently assumed that seawater Fe^{2+} concentrations would have been poised at siderite equilibrium. Yet a variety of studies indicate that siderite precipitation would have been strongly controlled by kinetic processes rather than equilibrium behaviour, prompting a reconsideration of the Precambrian Fe cycle and those element cycles to which it was connected. To address this issue, we experimentally investigated spontaneous (or homogeneous) precipitation of Fe(II)-carbonate across a range of pH and pCO_2 conditions, and in the presence/absence of $SiO_2(aq)$. Our data show that the formation of siderite directly from seawater is initiated by the formation of precursor amorphous Fe carbonate (AFC). The precursor, once formed, rapidly transforms into either siderite or chukanovite ($Fe_2(OH)_2CO_3$; metastable with respect to siderite), dependent on the availability of carbonate ions. Precipitation rates estimated from our experiments reveal a strong exponential dependence of AFC precipitation rate on the saturation state of the solution, consistent with theoretical predictions. This relationship, in turn, delineates a critical supersaturation threshold for homogeneous Fe(II)-carbonate precipitation from anoxic and ferruginous water. Incorporation of our experimental data with constraints on the ocean-atmosphere carbon system shows that significant accumulations of siderite in Precambrian sedimentary rocks require an origin from fluids that were distinct from seawater in equilibrium with the ocean-atmosphere inorganic carbon reservoir. In addition, these data show that the maximum transient Fe^{2+} concentration in Precambrian oceans was

controlled by Fe(II)-silicate precipitation and not by Fe(II)-carbonate, consistent with the sedimentary record of Fe-rich Precambrian rocks. More broadly, these results contribute to a quantitative framework that underpins the utility of Fe(II)-carbonate as a sensitive palaeoenvironmental proxy for ferruginous systems where CO_2 may have been present.

2.1 Introduction

Sedimentary Fe-bearing minerals provide a detailed record of the chemical evolution of Earth's oceans through much of their early history. Iron formation, an iron- and silica-rich chemical sedimentary rock that peaked in sedimentary abundance as it was deposited on late Archaean-Palaeoproterozoic continental margins, provides the most conspicuous expression of dominantly anoxic and ferruginous seawater chemistry, in particular during the prelude to the great oxidation event (GOE; see reviews by Beukes and Gutzmer 2008; Klein 2005; Simonson 2003 and references therein). Most studies agree that the Fe contained in iron formations was primarily sourced from hydrothermal activity and/or seafloor basaltic volcanism (Derry and Jacobsen 1990; Jacobsen and Pimentel-Klose 1988; Krapež et al. 2003; Simonson 2003). Although some are strongly overprinted by post-depositional oxidation, these successions show that alongside amorphous silica, Fe was ultimately deposited as greenalite and siderite, in turn reflecting a distinct network of biogeochemical cycles established long before the appearance of atmospheric oxygen (Beukes et al. 1990; Holland 2007; Klein 2005; Krapež et al. 2003; Rasmussen et al. 2016, 2017).

Our view of the chemical state of Precambrian oceans thus hinges on understanding the behaviour of Fe^{2+} in seawater and sedimentary pore water. Nevertheless, we have a relatively poor grasp of the formation pathways and rates of Fe(II)-mineral precipitation. For example, citing the widespread occurrence of sideritic carbonates in the geologic record, Holland (1984, 2007) inferred that the steady-state late Archaean oceans would have been poised

at both calcite and siderite ($FeCO_3$) saturation. Following from this, several authors have suggested that siderite equilibrium itself represents a reasonable upper limit for Fe^{2+} concentration (e.g., Halevy et al. 2017; Raiswell et al. 2011). However, a number of observations support the notion that siderite precipitation would have been strongly controlled by kinetic processes rather than equilibrium behaviour. First, hydrochemical studies have shown that many anoxic water bodies are commonly supersaturated with respect to siderite (e.g., Postma 1982), consistent with experimental work suggesting that substantial supersaturation is required for direct precipitation of siderite from water (herein referred as homogeneous nucleation; Dideriksen et al. 2015; Jimenez-Lopez and Romanek 2004; Sel et al. 2012). Secondly, recent work on siderite precipitation suggests that its mineralisation pathways and products are more variable than previously appreciated. For example, similar to the non-classical/novel nucleation mechanism developed for homogenous $CaCO_3$ precipitation (Gebauer et al. 2008), a growing body of literature suggests that the homogeneous nucleation of siderite may involve the formation of amorphous Fe carbonate (AFC; Dideriksen et al. 2015; Montes-Hernandez and Renard 2016; Sel et al. 2012), which in turn crystallises to either chukanovite ($Fe_2(OH)_2CO_3$) or siderite. Solubility determinations indicate that chukanovite is metastable with respect to siderite (Azoulay et al. 2012), leaving open the possibility that some siderite preserved in the geologic record may, in fact, reflect a multi-step mineralisation pathway (AFC, chukanovite, and siderite are collectively referred as Fe(II)-carbonate herein).

Together, these data suggest that the assumption of equilibrium behaviour with respect to siderite requires re-examination, in particular for Precambrian marine systems. In addition, petrographic studies indicate that many the Precambrian BIF-associated cherts were formed by direct silica precipitation at or just below the seabed in the form of silica gel (lack ghost or inclusions of precursors and show fine-scale grain fracturing from syneresis; Maliva et al. 2005; Rasmussen et al. 2015a), suggesting a dissolved silica concentration

likely at or above the equilibrium solubility with respect to opal-CT and possibly also to amorphous silica (or opal-A; Holland 1984; Maliva et al. 2005; Siever 1992). Therefore, constraining steady-state Fe^{2+} concentrations in the Precambrian oceans requires an understanding of the competitive precipitation of Fe(II)-silicate and/or Fe(II)-carbonate (Holland 2007; Raiswell et al. 2011). Although recent work has investigated the kinetics of Fe(II)-silicate precipitation (Halevy et al. 2017; Tosca et al. 2016), a more comprehensive understanding of Fe(II)-carbonate precipitation kinetics has persisted as a major obstacle in exploiting Fe(II)-carbonate as a useful palaeoenvironmental indicator, and in understanding ferruginous seawater chemistry more broadly.

To address these problems, we experimentally examined the mineralisation pathway specific to homogeneous Fe(II)-carbonate precipitation in a variety of solution compositions relevant to anoxic and ferruginous Precambrian systems. In what follows, we describe experimental protocols, observations on the pathways and products of homogeneous Fe(II)-carbonate nucleation, and develop kinetic expressions for precipitation behaviour. Finally, we discuss constraints on palaeoenvironmental conditions surrounding the origin of some siderite-rich Precambrian rocks, constrain the abiotic reactions that would have limited the maximum transient Fe^{2+} concentration in Precambrian seawater and consider the broader palaeoenvironmental implication of our results.

2.2 Experimentation

All experiments were conducted in 1 L borosilicate glass reaction vessels wrapped in Al-foil (to prevent photo-oxidation) within a strictly anoxic Coy polymer glovebox. The glovebox was filled with 4% H_2/96% N_2 gas and maintained at anoxic conditions by two pairs of palladium catalysts and anhydrous $CaSO_4$ desiccants. The palladium catalysts scrubbed O_2 in the glovebox by continuously reacting trace O_2 with available H_2 to form H_2O, which was subsequently removed by $CaSO_4$ desiccants. The O_2 and H_2 contents in the

glovebox were continuously monitored by a Coy gas analyser to ensure an atmosphere of <1 ppm O_2 throughout preparation and storage of stock solutions and samples. All experiments were conducted at 25 °C.

All aqueous solutions were prepared within the glovebox using de-ionized (DI) water that was first deoxygenated by purging with O_2-free N_2 gas for at least 1 hour Butler et al. (1994), then stirred for 1 hour in the anoxic atmosphere and left for at least 24 h to allow any residual O_2 to escape and be removed by the catalysts and desiccants. Stock solutions (1 mol kg^{-1}) were prepared by dissolving metal-chloride powders ($FeCl_2{\cdot}4H_2O$, NaCl, and KCl; $\geq$ 99 % Acros Organics, Sigma-Aldrich) in deoxygenated DI water. The Fe^{2+} stock solution was treated with Fe^0 powder ($\geq$ 99 %; Sigma-Aldrich) and HCl to reach a pH <2 and left for 24 h. The goal of this treatment was to chemically reduce any Fe^{3+} that may have existed in stock $FeCl_2{\cdot}4H_2O$ powder prior to the transfer of the reagent to the glovebox. The Fe^0 powder was then removed by running the stock solution through a polymer container with a high-strength Nd magnet inserted in the wall. $NaHCO_3$ stock solutions (0.5 mol kg^{-1}; powder $\geq$ 99.7 %; Sigma-Aldrich) were freshly prepared for each experiment; to ensure the total dissolved carbonate species (calculated for different pCO_2 at different pH) across experiments were not affected by the degassing of the stock solution over time. KCl (2 mmol kg^{-1}) was added to Fe(II)-carbonate system as a reference element to ensure the internal consistency of Fe^{2+} concentration analyses. NaCl powder was added to the experiment to balance the ionic strength for each solution composition. It should be noted that the choice of ionic strength of 0.2 mol kg^{-1} across all experiments is decided by the experiments with the highest amount of dissolved $NaHCO_3$.

For this study, calcium was excluded from all experiments to isolate and study the behaviour of Fe(II)-carbonate precipitation separately from that of other Ca-bearing carbonates. There are a number of practical reasons for this choice. First, consistent with thermodynamic expectations, preliminary experiments show that, in the presence of Fe^{2+} a modern seawater level of Ca^{2+} (10

mmol kg^{-1}) under the pCO_2 levels representative of current estimates for the Precambrian ocean (i.e., Blättler et al. 2017) results in rapid precipitation of $CaCO_3$ results in almost every case; complicated the characterisation of solid material and Fe(II)-carbonate mineralisation pathway. However, in apparent conflict with these results, recent isotopic constraints suggest that steady-state Ca^{2+} concentrations in the Archaean-Palaeoproterozoic oceans may have been even higher than the present ocean Blättler et al. (2017). The apparent incompatibility between the Ca-carbonate and the Fe(II)-carbonate system may have a number of causes, some of which include the kinetics of carbonate nucleation in Ca^{2+} and Fe^{2+}-containing water, or a difference between depositional environments or solution chemistries that tended to preserve $CaCO_3$-dominated versus $FeCO_3$-dominated products in the rock record. For example, Archaean-Palaeoproterozoic shelf carbonates are dominated by thick encrustations of calcite and aragonite on the seafloor (with variable dolomitisation) Sumner and Grotzinger 2004, whereas Fe(II)-carbonate appears to dominate primarily in certain iron formation facies interpreted to reflect transgressive events Beukes and Gutzmer (2008), Beukes et al. (1990), Kaufman et al. (1990) and Rasmussen and Muhling (2018). Regardless, the incompatibility between the two carbonate systems cannot be resolved until the behaviour of the Fe(II)-carbonate system is studied in detail.

The pH of each experiment was held constant by a combination of MOPS (3-(N-morpholino) propanesulfonic acid; 0.05 mol kg^{-1}) pH buffer and a large DIC pool. MOPS features significant steric hindrance of acid-base functional groups and therefore exhibits negligible metal complexation Kandegedara and Rorabacher (1999). The pH adjustment was divided into two separate stages due to the influence on the pH exerted by the addition of $NaHCO_3$ and subsequent pH-dependent carbonate speciation Zeebe and Wolf-Gladrow (2001). The pH was first raised to within 0.5 unit to the desired value, followed by the addition of KCl, and NaCl, and left for 24 h to homogenise. Predetermined amounts of $NaHCO_3$ stock solution were then added to the homogenised solu-

tion, followed by pH adjustments using a Metrohm 902 Titrando autotitrator with NaOH (0.5 mol kg^{-1}). In some cases where the desired pCO_2 was high at high pH (e.g., 8.5), $NaHCO_3$ powder was added directly to the experiments. The pH measurement of each experiment at termination shows that all pH changes were within 0.07-unit. In order to minimise degassing of CO_2 over the course of experiments, the head-space in the reaction vessels was essentially eliminated (i.e., <1 mL of head-space in 1000 mL bottles), and solutions were sealed with gas-tight septum caps to facilitate solution sampling. To avoid instantaneous nucleation on the entry of the concentrated Fe^{2+} stock solution into the matrix, the stock solution was first diluted to 0.1 mol kg^{-1} before being pipetted into the matrix and mixed immediately.

2.2.1 Analytical technique and procedure

Solution samples ($\approx$ 1 mL) were withdrawn through the septum caps of the reaction vessels. The solution samples were syringe-filtered (0.22 µm) and centrifuged for 90 s at 10,000 rpm. The upper 0.5 mL was pipetted into HDPE vials with 10 mL of 4 % HNO_3 solution for elemental analysis. Dilution factors for each sample were calculated by weight. Elemental analysis of solution samples was performed via solution-phase inductively coupled optical emission spectrometry (ICP-OES) at the Scottish University Environmental Research Centre, University of Glasgow. All analyses utilised matrix-matched element standard with the corresponding level of MOPS and ionic strength (after dilution). All stock solutions were analysed alongside the samples in order to recalibrate the thermodynamic calculations of the actual solution chemistry.

Upon experiment termination, the solution was vacuum filtered through a 0.22 µm nylon filter membrane, and the solid materials were left to dry under the low-humidity anoxic atmosphere in the glovebox. Solid materials were analysed by powder X-ray diffraction (XRD) using a PANalytical Empyrean Series 2 X-ray diffractometer with a Co Kα source, operated at 40 kV and 40 mA, and scanned between 5 and 80 degrees 2Θ; step size 0.026

degrees. Powders were loaded on single crystal silicon sample holders and sealed with Kapton film within the glovebox to minimise oxidation during XRD analysis. Final X-ray diffractograms are shown with "background" patterns removed after subtracting several analyses performed on blank sample holders covered with Kapton film. Fourier transform infrared spectroscopy (FT-IR) analyses were performed on powdered products and were acquired in transmission mode using a PerkinElmer Frontier mid-IR spectrometer. FT-IR transmission measurements were collected on optically transparent KBr pellets with a sample:KBr ratio of $\approx$ 1:200. KBr powder and solid materials were ground and compressed into pellets at 7 ton and analysed within 15 min of exposure to air (Fe(III)-O vibrations were closely monitored to ensure minimal oxidation had taken place). Measurements were collected from 400 to 4000 cm^{-1} at 1 cm^{-1} resolution using a deuterated triglycine sulphate (DTGS) detector with a KBr window and beamsplitter. After analysis, pellets were left in an oven at 150 °C for 24 h to remove any adsorbed H2O that gave a broad FT-IR absorption peak between 3200 to 3700 cm^{-1} and analysed again. In-house scanning electron microscopy with energy dispersive X-ray spectroscopy (SEM-EDS) was performed all samples to characterise the morphology and elemental composition of the solid materials precipitated on the seeds. Imaging and spectral analyses were conducted using FEI Quanta 650 FEG SEM in high vacuum mode. To minimise oxidation during sample preparation, a small amount of solid was mounted on an adhesive carbon layer on an Al stub within the glovebox, then transported to a gold-coating unit in a parafilm-sealed container; sample exposure to air was <1 min. Once gold-coated (15 nm Au), samples were immediately transferred into the evacuated SEM-EDS chamber.

2.3 Analytical results

ICP-OES analyses show no detectable Fe^{2+} uptake in solutions with initial compositions below an apparent supersaturation threshold even after a maximum of 25 days of reaction. Experiments employing initial supersaturation above this threshold corresponded to increasing rates of Fe^{2+} consumption as a result of precipitation (Fig. 2.1A). In general, the rate of Fe^{2+} consumption was characterised by two stages: (1) an initial stage of rapid drawdown, corresponding to homogeneous nucleation, (2) a protracted stage of drawdown, corresponding to decreasing nucleation rate and continued growth of solid nuclei at decreasing saturation. The second stage proceeded until solution compositions were relatively invariant, which suggests that a steady state was reached between the solution and the newly precipitated solid.

Figure 2.2 illustrates the supersaturation threshold corresponding to Fe(II)-carbonate precipitation in pH-pCO_2 space. Our results delineate a supersaturation threshold with a steeper slope than predicted by siderite supersaturation, suggesting that the initially precipitated solids exhibit a stronger dependence on pH than siderite (or any pure $FeCO_3$ phase). The significance of these observations is detailed in discussion below.

Powder XRD analyses clearly identified the crystalline Fe(II)-carbonate phases formed during the experiments; these were limited to either siderite or chukanovite (Fig. 2.3). FT-IR spectra provided additional characterisation; some showed clear absorption peaks corresponding to chukanovite at 655, 694, 785, and 838 cm^{-1} (CO_3^{2-} bending), 956 cm^{-1} (OH deformation), 1066 cm^{-1} (symmetric CO_3^{2-} stretching), 1356, 1406, 1536 cm^{-1} (asymmetric CO_3^{2-} stretching); 3324 and 3485 cm^{-1} (as Fe(II)-OH stretching; absorption assignments summarised in Rémazeilles and Refait 2009. Absorption peaks corresponding to siderite occur around 738, 864 (CO_3^{2-} bending), 1429, and 1811 cm^{-1} (CO_3^{2-} stretching; Fig. 2.4). In combination, XRD and FT-IR data reveal that when the initial supersaturation threshold is surpassed, chukanovite

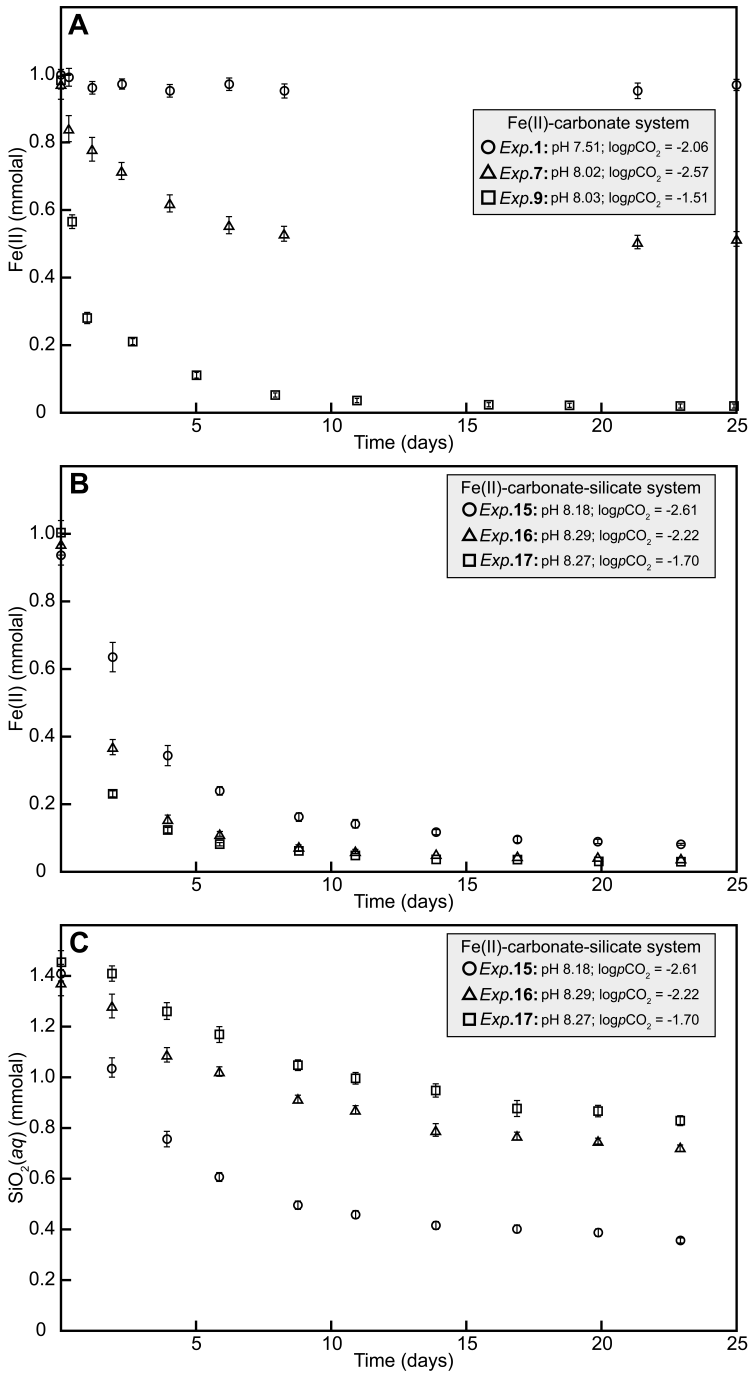


Figure 2.1: (A) The effect of precipitation on solution chemistry in Fe(II)-carbonate system. Fe(II) is removed from solution during precipitation until a steady-state condition is reached. The rate of Fe consumption increases with solution saturation. (B) The effect of precipitation on solution chemistry in Fe(II)-carbonate-silicate system. Fe consumption increases with saturation, meanwhile the corresponding $SiO_2(aq)$ consumption decreases (C) This reflects a switch from Fe(II)-silicate dominated precipitation to Fe(II)-carbonate dominated. Experiment numbers correspond to Fig. 2.2.

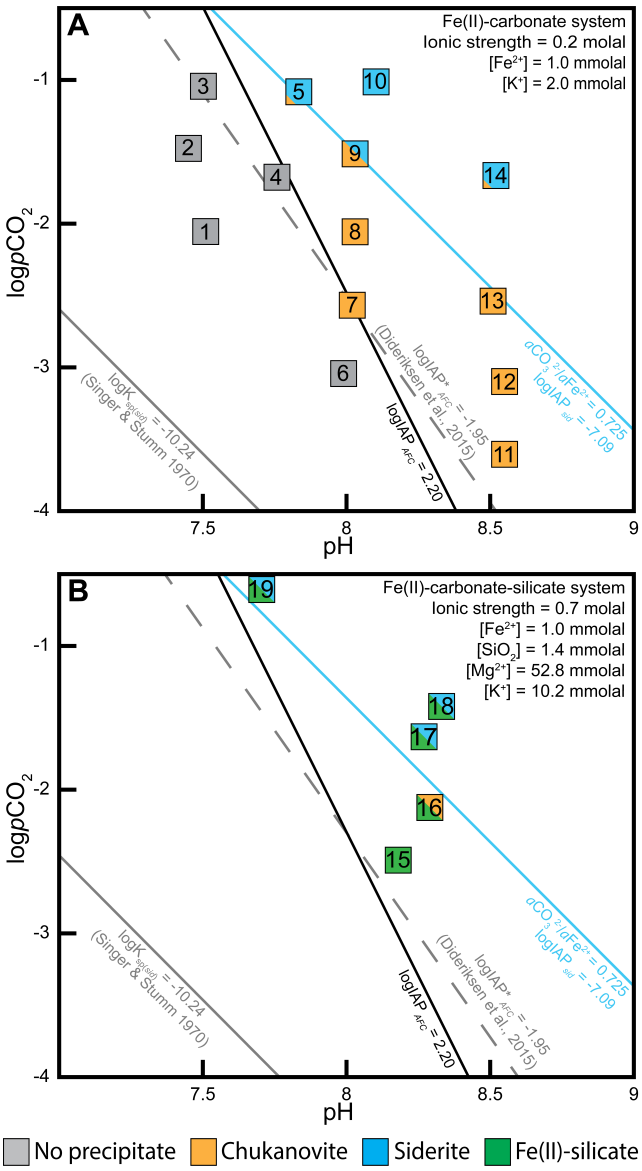


Figure 2.2: log$p$CO$_2$-pH plot of precipitation experiments. (A) Fe(II)-carbonate system and (B) Fe(II)-carbonate-silicate system, with their corresponding chemical compositions. Overall, homogeneous nucleation of different Fe(II)-carbonate phases only occurred at high supersaturation (high log$p$CO$_2$ and pH); critical supersaturation threshold for nucleation are placed where the corresponding mineral was identified from the experiment with the lowest initial saturation index: amorphous Fe carbonate $\log IAP_{AFC} = 2.20$ (black solid line); siderite $\log IAP_{sid} = -7.09$ or $a_{CO_3^{2-}} : a_{Fe^{2+}} = 0.725$ (blue solid line). Siderite solubility $\log K_{sp,sid} = -10.24$ (grey solid line; Singer and Stumm 1970) and AFC composition reported by Dideriksen et al. (2015) ($Fe(OH)_{0.6}(CO_3)_{0.7}$; $\log IAP^*_{AFC} = -1.95$; grey dashed line) are plotted here for reference.

dominated the crystalline products. However, mixtures of siderite and chukanovite are often observed along a threshold $a_{CO_3^{2-}} : a_{Fe^{2+}} \cong 0.725$ (blue solid line; Fig. 2.2), indicating an effective transition in Fe(II)-carbonate mineralogy under the conditions investigated here; siderite becomes the dominant phase in solutions with initial $a_{CO_3^{2-}} : a_{Fe^{2+}} \geq 0.725$, equivalent to $\log IAP_{\text{sid}} \geq -7.09$ in the conditions investigated here (blue solid line; Fig. 2.2). Siderite equilibrium $\log K_{sp,sid} = -10.24$ is plotted as a grey solid line for reference (Singer and Stumm 1970; Fig. 2.2).

SEM-EDS analyses revealed that the precipitated materials dominantly occur as spherical particles with a narrow size distribution (10-15 µm; Fig. 2.5A). XRD, FT-IR, and SEM observations on mono-mineralic precipitates show that siderite occurs as rhombohedral crystals $\leq$ 0.5 µm in size (Fig. 2.5B&C). These rhombs encrust some, but not all, ≈15 µm spheres and appear to increase in size towards the outer edge of the sphere (Fig. 2.5C). These two observations support the formation of rhombs through a crystallisation front that appears to have migrated outwards along the radius of the spherical aggregates. Chukanovite, on the other hand, occurs as hexagonal platy crystals ($\leq$ 0.1 µm in thickness; $\leq$ 1 µm in size) and displays parallel- and radial-columnar arrangement (Fig. 2.5D). Chukanovite also appears to encrust some spherical particles, resulting in larger spherical to sub-spherical polycrystalline aggregates (Fig. 2.5D). Finally, some products include Fe-bearing spheres that display no distinct crystal morphology (Fig. 2.5E) at least down to the effective resolution of the SEM (at 10s of nm). These spheres are often observed in products extracted from short duration experiments, along with the siderite- and chukanovite-encrusted spherical aggregates described above. Precipitates from high $\log pCO_2$ experiments (Exp. 5&10; Fig. 2.2A), however, show no direct evidence of siderite or chukanovite crystallisation from a spherical phase. Instead, the precipitates are dominantly comprised of larger siderite (7-10 µm) with radial-columnar chukanovite growing on the surface (Fig. 2.5F).

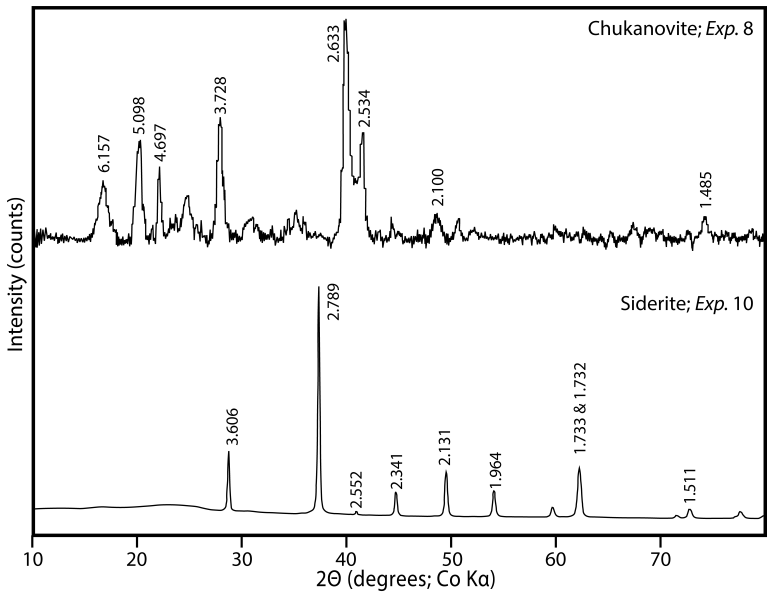


Figure 2.3: XRD diffractograms (Kapton background removed) of precipitated chukanovite (Exp. 8) and siderite (Exp. 10). Major diffraction peaks are denoted by corresponding d-spacing (Å).

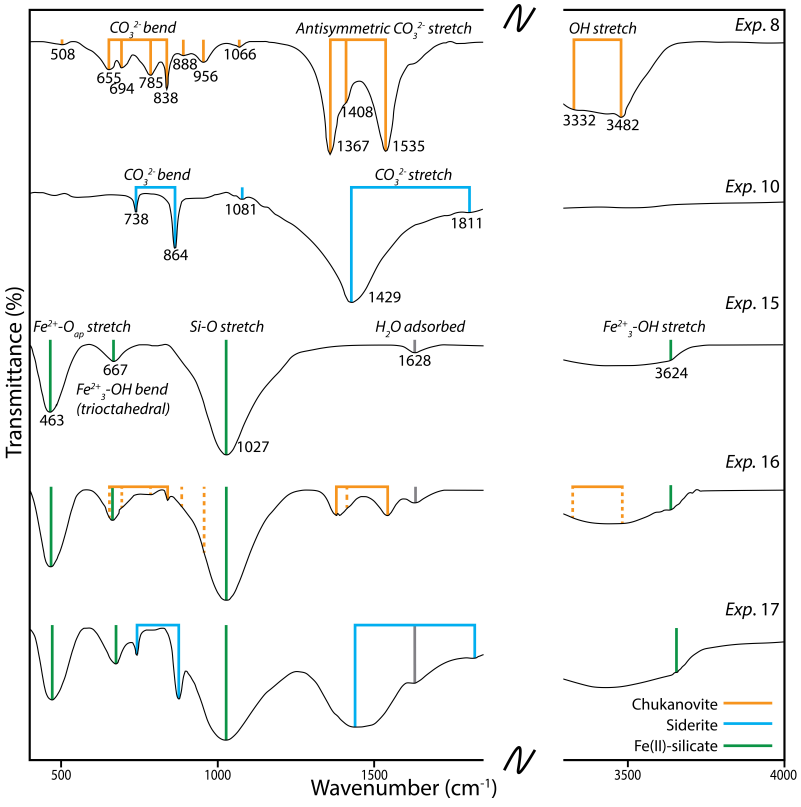


Figure 2.4: FT-IR transmittance spectra of precipitates from Fe(II)-carbonate system and Fe(II)-carbonate-silicate system. Absorptions are orange for chukanovite (Exp. 8), blue for siderite (Exp. 10) and green for the Fe(II)-silicate precursor phase (Exp. 15).

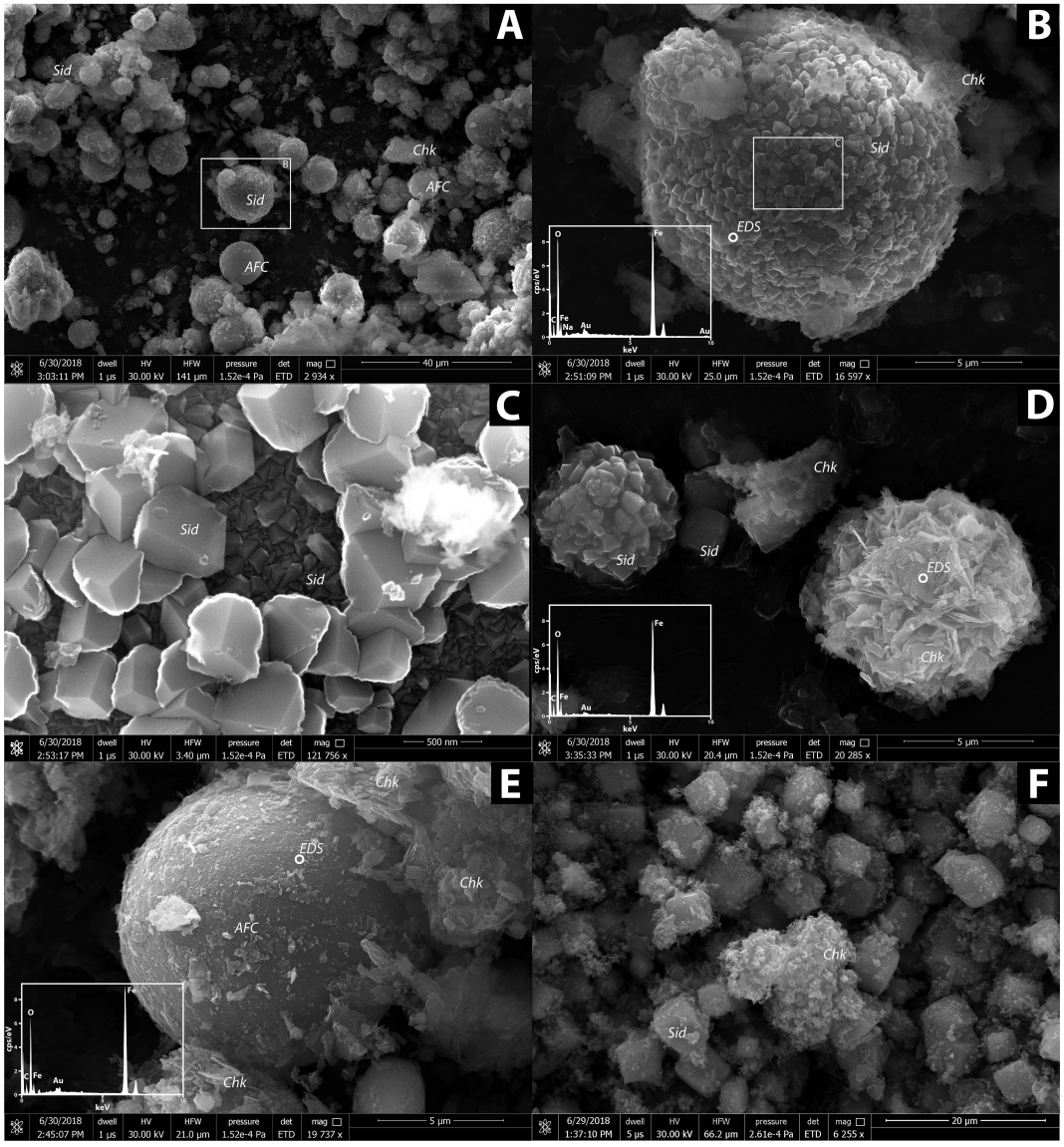


Figure 2.5: SEM images of precipitated materials. (A) Fe-bearing spherical particles that reflect homogeneous precipitation from water column, ranging between 5 and 15 µm in size. Mineralogies labelled as Sid (siderite), Chk (chukanovite), AFC (amorphous Fe carbonate). (B) Spherical aggregate comprised of rhombohedral siderite crystals ($\approx$ 0.5 µm). (C) High magnification view of the surface of aggregate shown in (B), where siderite crystal size increases outwards. (D) Spherical aggregates of siderite and chukanovite. Hexagonal chukanovite crystals are always observed in radial- or parallel-columnar (the fragment in the middle of the image) arrangement. Siderite rhombs ($\approx$ 1.5 µm) are likely broken off from larger spherical aggregates during sample preparation. (E) Fe-bearing spherical phase displays discernible crystal morphology, interpreted to be the amorphous Fe carbonate precursor phase. (F) Precipitate from high $\log pCO_2$ solution (Exp. 10), dominantly comprised of euhedral siderite rhombs (7-10 µm) with radial-columnar chukanovite crystal growing on the surface. EDS elemental analyses and localities are shown on the images.

2.4 Discussion

2.4.1 Mineralisation pathway

Our experiments place a number of constraints on the pathways and supersaturation thresholds associated with homogeneous nucleation of Fe(II)-carbonate from anoxic seawater. First, consistent with previous studies of Fe(II)-carbonate precipitation (Dideriksen et al. 2015; Jimenez-Lopez and Romanek 2004; Montes-Hernandez and Renard 2016; Sel et al. 2012), our data indicate that amorphous iron carbonate (AFC) acts as an important precursor in the ultimate crystallisation of chukanovite and siderite. SEM-EDS data (Fig. 2.5) clearly show that precipitation begins with the formation of spherical particles with no discernible crystalline morphology at the 10s of nm resolution (Fig. 2.5A&E). With time, these particles variably crystallise to microcrystalline siderite (Fig. 2.5B&C) or chukanovite (Fig. 2.5D) but retain their initially spherical morphology. This morphological evolution is characteristic of AFC crystallisation (Dideriksen et al. 2015) and has been observed in a number of previous studies of Fe(II)-carbonate precipitation (Jimenez-Lopez and Romanek 2004; Montes-Hernandez and Renard 2016). Amorphous precursors ultimately provide an energetically favourable pathway for the precipitation of carbonate minerals (e.g., Dideriksen et al. 2015; Gebauer et al. 2008; Sel et al. 2012, and references therein). In fact, recent in-situ TEM data (Nielsen et al. 2014) have shown that once amorphous precursors are formed, the secondary nucleation of carbonate phases occurs at their surface, suggesting that amorphous precursors provide reactive surface area for nucleation, and may be consumed as a secondary nucleation progressively decreases the saturation state of the system (Nielsen et al. 2014; Steefel and Van Cappellen 1990). Together these observations suggest that for solution chemistries relevant to Precambrian seawater, once the critical threshold for AFC nucleation is surpassed, AFC forms, which promotes the crystallisation of either chukanovite or siderite at its highly reactive surface.

The supersaturation threshold corresponding to homogeneous Fe(II)-carbonate nucleation, delineated by our experiments, reflects the compositional dependence of the initially precipitated AFC (black solid line; Fig. 2.2). For the conditions investigated here, the slope of this threshold suggests an apparent chemical composition for AFC that exhibits a higher OH^-:CO_3^{2-} ratio than previously reported (Dideriksen et al. 2015; $\log IAP^*_{AFC}$; grey dashed line; Fig. 2.2). However, the amorphous nature of the precursor permits a degree of freedom in its chemical composition that depends on the aqueous condition from which it forms (e.g., Dideriksen et al. 2015; Gebauer et al. 2008; Nielsen et al. 2014). For example, Dideriksen et al. (2015) using X-ray photoelectron spectroscopy (XPS), showed that AFC exhibited a dehydrated composition of $Fe(CO_3)_{0.85}(OH)_{0.3}$ when precipitated using $NaHCO_3$, and $Fe(CO_3)_{0.7}(OH)_{0.6}$ when precipitated using Na_2CO_3. Hence, we derive an apparent composition for AFC of $Fe(CO_3)_{0.5}OH$ and suggest this threshold $\log IAP_{AFC} = 2.20$ (black solid line; Fig. 2.2) corresponds to the critical supersaturation required for homogeneous AFC nucleation from anoxic ferruginous seawater (see Supplementary material, section 2.6.1 for calculations).

The crystalline products generated in our experiments also provide insight into the factors that favour either chukanovite or siderite crystallisation once AFC nucleates. Fig. 2.2 shows that products dominated by siderite only occur at a $a_{CO_3^{2-}} : a_{Fe^{2+}}$ ratio of 0.725 and higher, which under our conditions equates to a $\log IAP_{sid} \geq -7.09$. Thus, the availability of CO_3^{2-} might play a crucial role, mainly because the CO_3^{2-}:Fe^{2+} ratio is much higher for siderite (1.0) than that for chukanovite (0.5), and therefore, variations in this ratio in solution, will correspond to variations in saturation state and crystallisation rates for both minerals. The readers are reminded that the $a_{CO_3^{2-}} : a_{Fe^{2+}}$ ratio that differentiates chukanovite versus siderite mineralisation is estimated from the starting solution chemistry in closed-system synthesis. In natural systems where Fe(II) is the limiting species (e.g., modern oxidised ocean) or at a high pCO_2 (e.g., Archaean oceans), the effect of cation:anion ratio on

mineralisation pathway deserves further examination. Because chukanovite is metastable thus, leaving only the thermodynamically stable siderite in the geologic record, it is difficult to examine the mineralisation pathway at the time of deposition.

Finally, our proposed pathway for homogeneous AFC precipitation suggests that at very high saturation and therefore higher rates of AFC crystallisation, AFC was in some cases fully consumed, and its original morphology was destroyed (Fig. 2.5F; Exp. 5&10). Under these conditions, after AFC nucleation, the maintenance of a lower but still supersaturated condition may have supported crystal growth via Ostwald ripening whereby larger crystals grow at the expense of smaller ones (Steefel and Van Cappellen 1990). This rapid crystallisation would have lowered the availability of CO_3^{2-} ions below the critical threshold for siderite, finally allowing the precipitation of chukanovite on the surface of siderite (Fig. 2.5F).

2.4.2 Homogeneous precipitation kinetics

An examination of the overall precipitation rate determined in our experiments provides insight as to why a "critical supersaturation" threshold for homogeneous nucleation exists for Fe(II)-carbonate mineralisation. Following the mineralisation pathway proposed above, it is reasonable to assume the solution chemistry during nucleation was stoichiometrically controlled by the chemical composition of AFC. Based on the changes in Fe^{2+} concentration (ICP-OES results), we subtract the stoichiometric equivalents of CO_3^{2-} from the total dissolved inorganic carbon (DIC) pool in the solutions and calculate the residual $a_{CO_3^{2-}}$ at the time of sampling (assuming instantaneous carbonate speciation and negligible degassing; see Supplementary material, section 2.6.2 for calculation). Hence, we were able to estimate the apparent saturation state relative to AFC as precipitation progressed, as well as a precipitation rate ($\mu mol\,kg^{-1}/min$) for each sampling interval.

As we observe that the overall precipitation rate is dominated by nucle-

ation phenomena (pervasive formation of spherical particles of narrow size distribution; Fig. 2.5), we chose to fit our estimated rates of homogeneous AFC precipitation with an exponential function that describes the nucleation rate (r) of a substance from water (Steefel and Van Cappellen 1990):

$$r = \frac{2D}{d^5} \exp(\frac{-N_a \Delta G^*}{RT}) \ [\mathrm{cm^{-3}\,s^{-1}}], \tag{2.1}$$

where D is the aqueous species diffusion constant, d is the molecular diameter of the nuclei, N_a is Avogadro's number, and ΔG^* is a term which incorporates the surface energy and molar properties of spherical nuclei and the saturation state of the solution. By separating the saturation state term and collecting unknown variables, we can simplify this relationship:

$$r = k \exp(b \log IAP_{\mathrm{AFC}}) \ [\mathrm{cm^{-3}\,s^{-1}}], \tag{2.2}$$

where k is an overall rate constant, and b is a factor which incorporates the surface energy and molar properties of AFC nuclei. Although neither k or b are known *a priori*, or from the literature, they can be derived from our experimental data and some additional assumptions about the properties of the AFC nuclei (Fig. 2.6). In other words, our estimated minimum precipitation rates are in good agreement with kinetic behaviour predicted by the nucleation rate theory (Lasaga 1998b; Steefel and Van Cappellen 1990; Van Cappellen 1991). It is worth noting that precipitation rate data are limited at low values of supersaturation by the time scales at which Fe(II)-carbonate precipitation can be observed in the laboratory. Importantly, because the nucleation rate dependence on supersaturation is a strong exponential relationship (Lasaga 1998b; Steefel and Van Cappellen 1990; Van Cappellen 1991), it clarifies the kinetic factors behind the "critical supersaturation" of the Fe(II)-carbonate phases observed in our experiments—the strong exponential dependence of Fe(II)-carbonate precipitation on saturation state means that rates are prohibitively slow at values less than the critical supersaturation for homogeneous

nucleation shown in Fig. 2.2; so slow that observable increments of Fe(II)-carbonate exceed reasonably early diagenetic timescales.

It is important to point out that for a natural system, the critical supersaturation constrained here represents an upper limit for the saturation state of the corresponding mineral. In other words, in a solution with no other surface to precipitate on, a mineral saturation state could be maintained at the critical supersaturation without pervasive precipitation. A multitude of other mechanisms, including heterogeneous nucleation, operate at saturation states lower than the critical supersaturation, and thus, at slower precipitation rates (e.g., Fig. 2.6, $\log IAP_{\mathrm{AFC}} < 2.20$). Nevertheless, for at least some major late Archaean iron formations, stratigraphic and sedimentological evidence indicates that the chemical sediments have been re-worked after their initial precipitation and so sedimentary accumulation rates probably do not directly correspond to precipitation rates unless the chemical source of the sediments can be uniquely identified (i.e., Krapež et al. 2003).

2.4.3 Could Fe(II)-carbonate have precipitated from anoxic ferruginous seawater?

Because the precipitation of both Fe(II)-silicate and Fe(II)-carbonate would compete for Fe^{2+}, the equilibria and kinetic relationships between the two mineralisation processes would have exerted an important control on the Fe^{2+} concentration of the Precambrian oceans (Holland 1984; Raiswell et al. 2011). Many studies have suggested that siderite equilibrium is a reasonable upper limit for Fe^{2+} concentration in steady-state ambient Precambrian oceans (Halevy et al. 2017; Raiswell et al. 2011). However, the distinct banding of Fe(II)-bearing minerals in the late-Archaean banded iron formations reflects dynamic chemical precipitations where the transient maximum Fe^{2+} determines which phase would have nucleated from the water column. Our experimental data show that greenalite (simplest Fe(II)-silicate; $Fe_3Si_2O_5(OH)_4$) persists as the dominant Fe(II)-bearing phase despite significant supersaturation

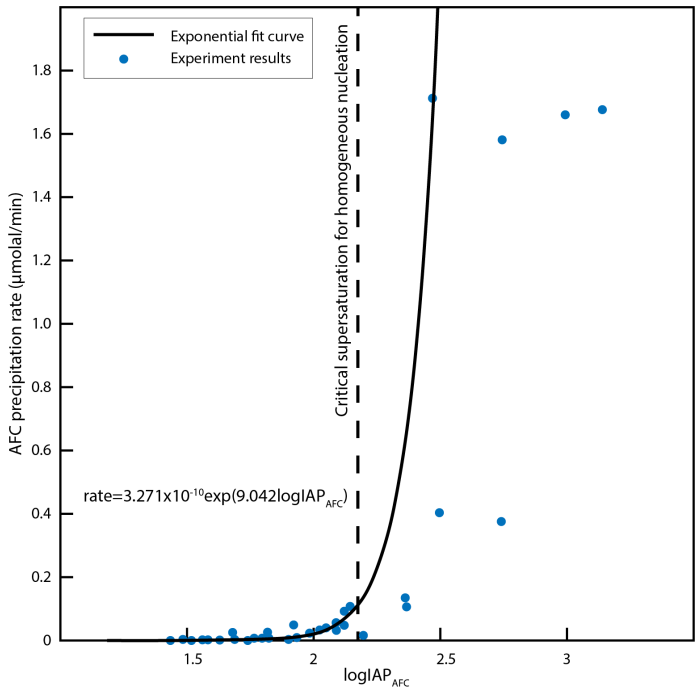


Figure 2.6: Experimentally derived amorphous Fe carbonate (AFC) precipitation rate as a function of solution saturation state ($\log IAP_{AFC}$). These data define a relationship identical in form to nucleation rate predicted by nucleation theory. Critical supersaturation for homogeneous nucleation is set by the precipitated experiment with the lowest saturation state (Exp. 7).

with respect to amorphous Fe(II)-carbonate (AFC; Fig. 2.1B), which raises the possibility that greenalite acted as the solubility-limiting phase controlling the transient maximum Fe^{2+} concentrations in anoxic ferruginous Precambrian seawater.

Our experimental observations allow us to examine the competition between Fe(II)-silicate and Fe(II)-carbonate, and to determine which phase would have capped Fe^{2+} concentrations in ferruginous oceans. In the absence of silicifying organisms, Precambrian oceans were proposed to be poised at amorphous silica saturation (120-140 ppm or $\log a_{SiO_2(aq)} = -2.7$; Maliva et al. 2005; Siever 1992), which would promote authigenic Fe-silicate mineralisation, as observed in the rock record (e.g., Beukes and Gutzmer 2008; Klein 2005; Rasmussen et al. 2016, 2017). If the maximum Fe^{2+} concentration was poised at the apparent solubility of nucleated Fe(II)-silicate precursor (to greenalite; $\log IAP_{grn} = 27.6$; as determined by Tosca et al. 2016; Fig. 2.7A), then we can determine the saturation state with respect to AFC across a finite range in pH and atmospheric pCO_2. These calculations show that in order for AFC to nucleate homogeneously from ferruginous seawater at equilibrium, the requisite equilibrium pCO_2 values are far beyond reasonable reconstructions (i.e., critical supersaturation is not met even at $pCO_2 = 0.5$ bar; Fig. 2.7C), and inconsistent with other proxies on the ocean carbonate system (i.e., DIC from Ca isotopes; Blättler et al. 2017). In other words, greenalite apparent solubility-controlled Fe^{2+} concentrations place the requisite pCO_2 levels for homogeneous AFC precipitation between 0.15 (quartz saturation $\log a_{SiO_2(aq)} = -3.75$; Rimstidt 1997) and 3.64 bar (amorphous silica saturation; Fig. 2.7D; Supplementary material, section 2.6.3, Eq. 2.26). The requisite pCO_2 level could have been even higher considering the competition for CO_3^{2-} between Fe(II)- and Ca-carbonate precipitation, which shall be investigated in future studies.

These simple calculations allow two conclusions; the first is that significant accumulations of siderite in Precambrian sedimentary rocks require an origin from fluids that were distinct from seawater in equilibrium with the ocean-

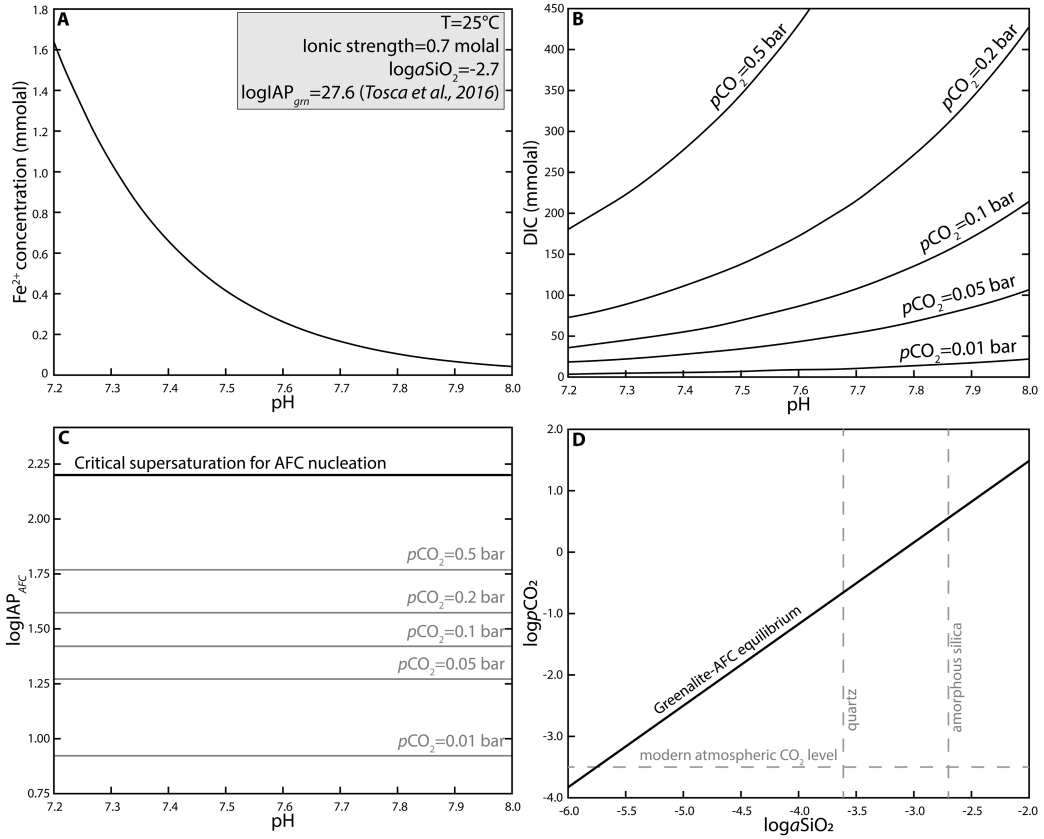


Figure 2.7: (A) Maximum Fe^{2+} concentration limited by greenalite apparent solubility (Tosca et al. 2016) for conditions relevant to Archaean seawater. (B) Total dissolved inorganic carbon (DIC) at equilibria with various levels of pCO_2 in Precambrian seawater. (C) AFC saturation state under various levels of pCO_2 with Fe^{2+} concentration controlled by greenalite apparent solubility. Critical supersaturation for AFC nucleation is plotted as black solid line (Supplementary material, section 2.6.3, Eq. 2.25). (D) Requisite pCO_2 level for homogeneous AFC precipitation at equilibrium with greenalite as a function of silica concentration (Supplementary material, section 2.6.3, Eq. 2.26). Dashed lines indicate quartz (Rimstidt 1997) and amorphous silica solubility.

atmosphere carbon system, at least at Earth surface temperatures. The second conclusion is that our results confirm the maximum transient Fe^{2+} concentrations were controlled by greenalite precipitation, and therefore strongly linked to $SiO_2(aq)$ concentrations. It is important to differentiate the transient maximum from the steady-state Fe^{2+} concentration in the Precambrian oceans, the former is decided by the dominant nucleating phases whereas the latter is determined by continued crystal growth of the existent/nucleated Fe(II)-minerals towards, but not necessarily reaches, their respective equilibria.

2.4.4 Constraints on the origin of siderite in late Archaean/early Palaeoproterozoic iron formations

Because Archaean-Palaeoproterozoic siderite is comparatively well-preserved in many iron formations, there has been much debate surrounding its origin and relationship to seawater chemistry. Petrographic evidence for late diagenetic or burial diagenetic origins of Fe(II)-carbonate includes large euhedral crystals that replace or include other products (Beukes and Gutzmer 2008; Klein and Beukes 1989; Klein 2005). In fact, in the majority of these instances, the Fe(II)-carbonates studied are ankeritic, based on electron microprobe and bulk chemical analyses (e.g., Kaufman et al. 1990; Klein and Beukes 1989). This ankerite is typically expressed as poikilotopic, euhedral crystals that contain siderite inclusions (Klein and Beukes 1989; Klein 2005), further attesting to a late diagenetic origin.

However, some siderite accumulations in iron formation exhibit petrographic evidence for an early diagenetic or perhaps even primary origin. For example, Rasmussen and Muhling (2018), in a high-resolution petrographic study of magnetite in Hamersley Group iron formation, observed that siderite occurs as microcrystalline aggregates precipitated on Fe(II)-silicate-rich laminae, which sometimes pre-dates compaction. These observations imply that siderite may have precipitated heterogeneously on the surface of pre-existing sediments, which would require a lower, currently unconstrained, heterogeneous nucle-

ation threshold. Other examples from the Transvaal Supergroups include finely disseminated micritic textures (<20 µm in diameter) which mineralogically, are composed of siderite rather than ankerite (Beukes et al. 1990; Heimann et al. 2010; Kaufman et al. 1990; Klein and Beukes 1989; Klein 2005). These fabrics may be derived from microcrystalline accumulations of Fe(II)-carbonate that originated from the water column, which, as our results suggest, must have been chemically modified relative to equilibrium seawater.

A number of studies have used the δ^{56}Fe and δ^{13}C signals of iron formation carbonates to place constraints on their paragenetic pathways (Fischer and Knoll 2009; Heimann et al. 2010; Johnson et al. 2008b, 2013; Kaufman 1996; Kaufman et al. 1990; Klein and Beukes 1989). Reported δ^{56}Fe values of micritic siderite from iron formation intervals of the Hamersley Basin (Australia) and Transvaal Craton (South Africa) display a δ^{56}Fe range within -1.7 ‰to $+1$ ‰, and mostly cluster around -1 ‰to 0 ‰(Heimann et al. 2010; Johnson et al. 2008b, 2013). Experimentally determined Fe(II)(aq)-siderite fractionation factors suggest that siderite with moderately negative δ^{56}Fe values (-1.5 ‰to -0.5 ‰) may be interpreted as being influenced, in part, by precipitation from hydrothermally sourced Fe(II)(aq) (assuming a hydrothermal δ^{56}Fe signal of 0 ‰). A similar conclusion was reached for Fe-isotopic studies of fine-grained siliciclastics of Archaean-Palaeoproterozoic age (Yamaguchi et al. 2005). More positive δ^{56}Fe values, however, may indicate distinct formation pathways, diagenetic alteration (Wiesli et al. 2004).

The coupled analysis of iron and carbon isotopes has led previous authors to conclude that dissimilatory iron reduction (DIR) may have been a dominant process in generating iron formation siderite (e.g., Heimann et al. 2010; Johnson et al. 2008b, 2013). However, because this process would require at least some oxidised Fe to iron formation precursor sediments, a pervasive role for DIR appears to be at odds with: (1) high-resolution petrographic evidence revealing the dominantly ferrous Fe mineralogy of phases that precipitated syndepositionally and entered iron formation sediments, and (2) very low

C_{org} abundance, with $\delta^{13}C$ values varying, with increasing metamorphic grade (Klein 2005; Rasmussen and Muhling 2018; Rasmussen et al. 2016). Thus, to what extent dissimilatory iron reduction might be expressed in specific iron formation carbonate remains open to interpretation.

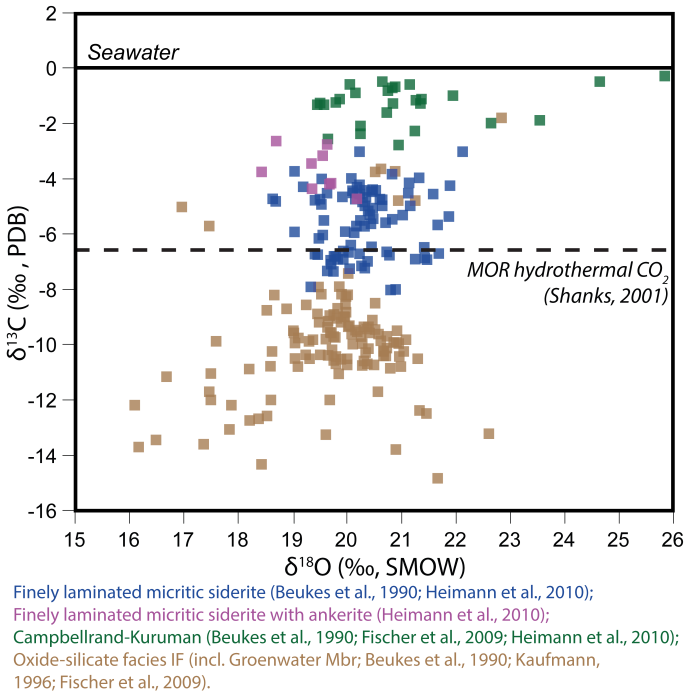


Figure 2.8: Compilation of $\delta^{13}C$–$\delta^{18}O$ from reported siderite facies in banded iron formations. $\delta^{13}C$ of finely laminated micritic siderite cluster between that of the seawater (≈ 0 ‰; Shields and Veizer 2002) and hydrothermal (≈ -6.5 ‰; Shanks 2001) signals. Large euhedral siderite/ankerite crystals in Fe-oxide-silicate iron formation exhibit the largest negative $\delta^{13}C$ signals, consistent with a metamorphic overprint.

In order to clarify the $\delta^{13}C$ values of siderite that display petrographic evidence for early versus late origins, we consider published $\delta^{13}C$ analyses where petrographic data and isotopic data can be closely correlated (a similar compilation was previously reported by Heimann et al. 2010; Fig. 2.8). Although these data are heavily biased toward the Transvaal Supergroup, these data show that there is a strong relationship between the $\delta^{13}C$ of siderite and petrographic facies in many Precambrian iron formations. More specifically, fine-grained micritic siderite displays a $\delta^{13}C$ range that lies between seawater (believed to be near 0 ‰; Shields and Veizer 2002) and the presumed $\delta^{13}C$ of hydrothermal input (≈ -6.5 ‰, assuming the mantle $\delta^{13}C$ has not

changed significantly; Shanks 2001). Measurements that report $\delta^{13}C$ values below this, however, are expressed in large euhedral carbonates that are dominated by ankerite (Beukes et al. 1990; Heimann et al. 2010; Kaufman 1996). These data delineate a $\delta^{13}C$–$\delta^{18}O$ trend that, although scattered, is consistent with burial diagenesis, or, in some specific cases, contact metamorphism (Beukes et al. 1990; Kaufman 1996). Together, although dissimilatory iron reduction may have played a role, these relationships suggest that the simplest interpretation for finely laminated micritic siderite in iron formation would be dominantly abiotic precipitation resulting from mixing between seawater and hydrothermal effluent; this is consistent with other chemical proxies such as REEs and Nd isotopes (see reviews by Derry and Jacobsen 1990; Jacobsen and Pimentel-Klose 1988; Klein 2005 and references therein). Studies of mineral precipitation at modern black smokers (i.e., Janecky and Seyfried 1984) have demonstrated that mixing between hydrothermal effluent and seawater actually occurs inside the vents (i.e., through conductive heating of seawater), and/or immediately at the seafloor. In addition, isotopic studies indicate that much of the DIC in the hydrothermal effluent is derived from water-rock alteration in the hydrothermal reaction zone (i.e., re-processing of magmatic C and release of CO_2 inclusions; Shanks 2001). Thus, isotopic compositions reflecting seawater-hydrothermal vent fluid mixing would be expected to be set upon precipitation at or near the vent interface, before significant dilution of the effluent in the water column might occur (Janecky and Seyfried 1984). This is demonstrated, for example, by the isotopic signatures retained by metalliferous Fe-carbonates found in Red Sea sediments near sites of hydrothermal venting (Zierenberg and Shanks 1988). Indeed, very small crystal size and generally narrow crystal size distributions present in laminated micritic siderite indicate that nucleation may have occurred in the water column (near the vent interface) rather than in confined sediment pore space (Beukes et al. 1990; Klein and Beukes 1989), which would be expected to produce cement displaying, for example, isopachous rims or drusy crystalline fabric typically consistent with

a marine phreatic diagenetic environment.

2.5 Conclusion

Our experimental data reveal multi-step pathways associated with Fe(II)-carbonate mineralisation from anoxic ferruginous seawater. The initial homogeneous nucleation of amorphous Fe carbonate, which itself is highly dependent on pH, acts as a reactive substrate controlling the subsequent crystallisation/nucleation of siderite and/or chukanovite. Our kinetic constraints further highlight the reasons why a high supersaturation threshold must be overcome to initiate spontaneous Fe(II)-carbonate precipitation from seawater, and the rates at which this occurs. That several mineralisation pathways are possible, yet geological products are dominated by thermodynamically stable siderite, suggest that some sedimentary Fe(II)-carbonate may retain an isotopic memory of these processes.

The results presented here also provide quantitative constraints on the chemistry of anoxic ferruginous seawater more broadly, and the inorganic aspects of the biogeochemical Fe cycle through the Precambrian, more specifically. The results of our experimental study identify the dominant Fe(II)-mineralisation processes that control the maximum transient Fe^{2+} concentrations in Precambrian seawater, and, in the process, shed new light on the long-debated origins of chemical sediments hosting abundant Fe(II)-carbonates, such as siderite-rich Archaean-Palaeoproterozoic iron formation.

Nevertheless, an important caveat to the kinetic behaviour of Fe(II)-carbonate is understanding the effect of heterogeneous nucleation, or the nucleation of Fe(II)-carbonate on pre-existing surfaces. Because kinetic theory predicts that some solid surfaces may decrease the energy and threshold to nucleation (Van Cappellen 1991), quantifying this process will be an important step in understanding the chemistry surrounding diagenetic Fe(II)-carbonate formation through the rock record.

Finally, our results carry implications for other sedimentary successions deposited under ferruginous conditions where CO_2 may have been present. For example, based on equilibrium thermodynamic arguments, the absence of siderite in Precambrian palaeosols led to the suggestion that atmospheric pCO_2, through at least part of the Precambrian, may have been insufficient in mitigating a faint young sun on early Earth (Rye et al. 1995); similar arguments have been employed for the lack of siderite in lacustrine mudstones deposited on early Mars (Bristow et al. 2017). However, in the context of precipitation kinetics, our results help reconcile what has been, until now, a puzzling absence of siderite in some geological examples. Indeed, continuing to understand the underlying kinetic mechanisms behind Fe(II)-carbonate precipitation remains an important research goal, and will strengthen the utility of this class of minerals as useful palaeoenvironmental indicators.

Acknowledgements

The authors thank Noah Planavsky and two anonymous reviewers for thoughtful comments, and Derek Vance for editorial handling. The authors acknowledge support from NERC grant NE/M013014/1 to NJT and the Leverhulme Trust (PLP-2015-286). The authors thank Gillian Mackinnon at Scottish Universities Environmental Research Centre for ICP-OES analysis, Jon Wade for assistance with SEM-EDS analysis, Alice Barroll and Katherine Clayton for assistance with XRD analysis, Rosalie Tostevin for assistance in FT-IR analysis. CJ would like to thank Ben Tutolo, Ritwika Sengupta, Rosalie Tostevin, Brooke Johnson, Sascha Holland, and Katherine Clayton for valuable discussions.

2.6 Supplementary material

2.6.1 Thermodynamic calculation

The equilibria between the precipitated mineral phases, siderite (*sid*) and greenalite (*grn*), and the chemical phase amorphous Fe carbonate (*AFC*; composition interpreted from our experiments; see Discussion section 2.4.1) with their corresponding solutions may be written as follows (assuming ideal stoichiometry, pure mineral phases, and water activity of unity):

$$\mathrm{FeCO_3} \overset{K_{sp,sid}}{\rightleftharpoons} \mathrm{Fe^{2+}} + \mathrm{CO_3^{2-}}, \tag{2.3}$$

$$\mathrm{FeOH(CO_3)_{0.5}} + \mathrm{H^+} \overset{K_{sp,AFC}}{\rightleftharpoons} \mathrm{Fe^{2+}} + 0.5\mathrm{CO_3^{2-}} + \mathrm{H_2O}(l), \tag{2.4}$$

$$\mathrm{Fe_3Si_2O_5(OH)_4} + 6\mathrm{H^+} \overset{K_{sp,grn}}{\rightleftharpoons} 3\mathrm{Fe^{2+}} + 2\mathrm{SiO_2}(aq) + 5\mathrm{H_2O}(l), \tag{2.5}$$

and the high (OH)- end-member amorphous Fe carbonate (AFC*) proposed by Dideriksen et al. (2015) can be written as follows:

$$\mathrm{Fe(OH)_{0.6}(CO_3)_{0.7}} + 0.6\mathrm{H^+} \overset{K^*_{sp,AFC}}{\rightleftharpoons} \mathrm{Fe^{2+}} + 0.7\mathrm{CO_3^{2-}} + 0.6\mathrm{H_2O}(l). \tag{2.6}$$

Mineral precipitation is predicted when the ionic activity product (*IAP*) of the corresponding dissolved ions in the solution exceeds the solubility product (K_{sp}) of the mineral. The ratio between *IAP* and K_{sp} is termed the saturation state of a solution, which is often expressed in logarithmic form as the saturation index (*SI*):

$$SI = \log(\frac{IAP}{K_{sp}}) = \log IAP - \log K_{sp}. \tag{2.7}$$

The solubility product K_{sp} of a mineral phase could be derived from the equilibrium constant of a specific mineral dissolution reaction, and it can be

calculated, like equilibrium constant, from the Gibbs free energy of the reaction ΔG_r^o at a given temperature T:

$$K_{sp} = \exp(\frac{-\Delta G_r^o}{RT}), \tag{2.8}$$

where R is gas constant (8.314 $\mathrm{J\,mol^{-1}}$):

K_{sp} for siderite and greenalite could be derived from a thermodynamic database of choice (e.g., Cox et al. 1989). However, due to the lack of thermodynamic data for amorphous Fe carbonate, we express all solution saturation with respect to a mineral/chemical phase in terms of its ionic activity product IAP:

$$IAP_{sid} = a_{\mathrm{Fe^{2+}}} a_{\mathrm{CO_3^{2-}}}, \tag{2.9}$$

$$IAP_{AFC} = \frac{a_{\mathrm{Fe^{2+}}} a_{\mathrm{CO_3^{2-}}}^{0.5}}{a_{\mathrm{H^+}}}, \tag{2.10}$$

$$IAP_{grn} = \frac{a_{\mathrm{Fe^{2+}}}^3 a_{\mathrm{SiO_2}}^2}{a_{\mathrm{H^+}}^6}. \tag{2.11}$$

The activity of the ith dissolved ion is the product of the molality (C_i) and activity coefficient γ_i:

$$a_i = C_i \gamma_i, \tag{2.12}$$

where γ_i is a function of the true ionic strength ($\overline{I}$) of the solution, which could be tabulated using the $\dot{B}$ equation (Helgeson and Kirkham 1974a; Helgeson et al. 1981; Helgeson 1969, 1981):

$$\log \gamma_i = -\frac{A z_i^2 \sqrt{\overline{I}}}{1 + B \mathring{a}_i \sqrt{\overline{I}}} + \dot{B}\overline{I}, \tag{2.13}$$

where the Debye-Hückel constants $A = 0.5092$ and $B = 0.3283{\times}10^8$ in water at 25 °C (Helgeson 1981); the hydrated ion size parameter $\mathring{a}_i$, is experiment-fitted coefficient that represent the distance of closest approach of ions in an electrolyte solution (e.g., Debye and Hückel 1923; Helgeson 1969; Kielland

$T = 298.15$ K and 1 bar

Chemicals	$\mathring{a}$ ($\times 10^{-10}$ mm)	γ ($\overline{I}$=0.2 mol kg^{-1})	γ ($\overline{I}$=0.7 mol kg^{-1})
$CO_2(aq)$	4	1	1
H^+	9	0.81	0.81
HCO_3^-	4.5	0.74	0.69
CO_3^{2-}	4.5	0.29	0.18
Fe^{2+}	6	0.33	0.24

Table 2.1: Thermodynamic properties and constants for activity coefficient calculation. Values of the ion size parameter $\mathring{a}_i$ summarised from Kielland (1937), deviation factor $\dot{B}$ from Helgeson and Kirkham (1974a) and Helgeson (1969), and calculated activity coefficients γ for both matrices using model.

1937). The $\dot{B}$ equation adds a deviation factor $\dot{B}$ (0.041 at 298.15 K) to the extended Debye-Hückel equation to adjust the divergence of the predicted activity coefficients from experiments. The model is parametrised from 0 °C to 300 °C for solutions with ionic strength up to 1 mol kg^{-1}, and is considered reasonably accurate under high $p\mathrm{CO}_2$ conditions (e.g., 1 bar; Marini Luigi 2006); suitable for the current reconstruction of Archaean conditions. Values used in the calculation of solution saturation are listed in Table. 2.1.

2.6.2 Carbonate speciation in Fe(II)-carbonate precipitation.

In a solution, carbon dioxide exists in three different inorganic forms: as free carbon dioxide, $CO_2(aq)$, bicarbonate HCO_3^-, and carbonate ion CO_3^{2-}. The sum of all dissolved forms is referred as total dissolved inorganic carbon (DIC; bracketed in Eq. 2.14), which in turn, could be determined from $CO_2(g)$ partial pressure ($p\mathrm{CO}_2$) using Henry's law (Eq. 2.1.1). In a simplified form, the $CO_2(g)$ dissolution and dissociation may be written as following (assuming water activity of unity):

$$\mathrm{CO_2}(g) \overset{K_0}{\rightleftharpoons} [\mathrm{CO_2}(aq) + \mathrm{H_2O} \overset{K_1}{\rightleftharpoons} \mathrm{HCO_3^-} + \mathrm{H^+} \overset{K_2}{\rightleftharpoons} \mathrm{CO_3^{2-}} + 2\mathrm{H^+}], \qquad (2.14)$$

where the equilibrium constants are equal to:

$$K_0 = \frac{a_{\mathrm{CO_2}(aq)}}{p\mathrm{CO_2}}, \tag{2.15}$$

$$K_1 = \frac{a_{\mathrm{HCO_3^-}} a_{\mathrm{H^+}}}{a_{\mathrm{CO_2}(aq)}}, \tag{2.16}$$

$$K_2 = \frac{a_{\mathrm{CO_3^{2-}}} a_{\mathrm{H^+}}}{a_{\mathrm{HCO_3^-}}}, \tag{2.17}$$

where K_0 is Henry's constant of the solubility of $\mathrm{CO_2}(g)$ (0.033 $\mathrm{mol\,kg^{-1}\,bar^{-1}}$ at 298.15 K; Sander 2015); K_1 and K_2 are referred to as the 1$^{\mathrm{st}}$ and 2$^{\mathrm{nd}}$ dissociation constants of carbonic acid. The effect of ionic strength of the solution on the dissociation constants can be simplified to the corresponding activity coefficients (Eq. 2.13) as follows:

$$\log K_1 = \log K_1^0 - \log \frac{\gamma_{\mathrm{H^+}} \gamma_{\mathrm{HCO_3^-}}}{\gamma_{\mathrm{CO_2}(aq)}}, \tag{2.18}$$

$$\log K_2 = \log K_2^0 - \log \frac{\gamma_{\mathrm{H^+}} \gamma_{\mathrm{CO_3^{2-}}}}{\gamma_{\mathrm{HCO_3^-}}}, \tag{2.19}$$

and $\log K_1^0 = -6.37$, $\log K_2^0 = -10.31$ in solution of $\overline{I} = 0$ $\mathrm{mol\,kg^{-1}}$, calculated from the Gibbs free energy of reactions in Eq. 2.14, with thermodynamic properties taken from CODATA database (Cox et al. 1989).

The $p\mathrm{CO_2}$ and $a_{\mathrm{CO_3^{2-}}}$ of each experiments can thus be calculated from solution pH and DIC via the following equations:

$$p\mathrm{CO_2} = \frac{[\mathrm{H^+}]^2 \mathrm{DIC}}{K_0[\mathrm{H^+}]^2 + K_0 K_1 [\mathrm{H^+}] + K_0 K_1 K_2}, \tag{2.20}$$

$$\log a_{\mathrm{CO_3^{2-}}} = \log p\mathrm{CO_2} + \log(\gamma_{\mathrm{H^+}}^2 \gamma_{\mathrm{CO_3^{2-}}}) + \log(K_0 K_1^0 K_2^0) + 2\mathrm{pH}, \tag{2.21}$$

or:

$$[\mathrm{CO_3^{2-}}] = \frac{K_1 K_2 \mathrm{DIC}}{[\mathrm{H^+}]^2 + K_1[\mathrm{H^+}] + K_1 K_2}. \tag{2.22}$$

As Fe(II)-carbonate precipitation proceed, the change in Fe^{2+} concentration is calculated from ICP-OES measurements between solution sampling, and the stoichiometrically equivalent amount of $[\mathrm{CO_3^{2-}}]$ is subtracted from the total DIC, then the residual $[\mathrm{CO_3^{2-}}]$ is calculated using Eq. 2.22 (assuming spontaneous carbonate speciation and no degassing), which in turn, allows the estimation of a corresponding saturation state of the solution with respect to a mineral/chemical phase.

2.6.3 Fe^{2+} concentration and Fe(II)-carbonate saturation.

In the absence of silicifying organisms, Archaean seawater was likely saturated with respect amorphous silica (120-140 ppm or $\log a_{\mathrm{SiO_2}(aq)} = -2.7$; Maliva et al. 2005; Siever 1992); in favour of authigenic Fe(II)-silicate mineralisation and consistent with the rock record (e.g., Beukes and Gutzmer 2008; Klein 2005; Rasmussen et al. 2016, 2017). If the concentration of Fe^{2+} in Precambrian seawater was limited by greenalite precipitation, Eq. 2.11 could be rearranged to solve for the activity of Fe^{2+}:

$$3 \log a_{\mathrm{Fe^{2+}}} = \log IAP_{grn} - 2 \log a_{\mathrm{SiO_2}(aq)} - 6\mathrm{pH}. \tag{2.23}$$

By applying the greenalite apparent solubility $\log IAP_{grn} = 27.6$ (Tosca et al. 2016), Eq. 2.23 can be simplified into solving the activity of Fe^{2+} as a function of pH and silica concentration:

$$\log a_{\mathrm{Fe^{2+}}} = 9.2 - \frac{2}{3} \log a_{\mathrm{SiO_2}(aq)} - 2\mathrm{pH}. \tag{2.24}$$

And, IAP_{AFC} (Eq. 2.10) can be rearranged as a function of $\log pCO_2$ by inserting the correlations stated in Eq. 2.21 and Eq. 2.24:

$$\log IAP_{AFC} = 9.2 - \frac{2}{3}\log a_{SiO_2(aq)} + \frac{1}{2}(\log pCO_2 + \log(\gamma^2_{H^+}\gamma_{CO_3^{2-}}) + \log(K_0 K_1^0 K_2^0)). \quad (2.25)$$

Through relation stated in Eq. 2.25, the requisite pCO_2 levels for homogenous AFC precipitation ($\log IAP_{AFC} = 2.20$ at Fe^{2+} concentrations controlled by greenalite solubility ($\log IAP_{grn} = 27.6$) could be expressed as a function of silica concentration:

$$\log pCO_2 = \frac{4}{3}\log a_{SiO_2} - \log(\gamma^2_{H^+}\gamma_{CO_3^{2-}}) - \log(K_0 K_1^0 K_2^0) - 14 \quad (2.26)$$

Chapter 3

Growth kinetics of siderite

Reproduced with permission from publication:

Growth kinetics of siderite at 298.15 K and 1 bar

on

Geochimica et Cosmochimica Acta 274(2020) 97-117

10.1016/j.gca.2020.01.047

by

Clancy Zhijian Jiang*, Nicholas J. Tosca

Earth Sciences Department, University of Oxford, OX1 3AN, England, United Kingdom.

Abstract

The widespread occurrence of siderite at the Earth's surface has motivated investigations into the thermodynamic factors controlling its stability for most of the last century. However, despite a new appreciation for multiple Fe(II)-carbonate mineralisation pathways, the rates of siderite growth have not been accurately predicted as a function of solution chemistry. This has impeded a quantitative understanding of myriad geochemical systems, both modern and ancient. To address this issue, we investigated the growth kinetics of synthetic siderite seeds in anoxic closed-system conditions at 298.15 K and 1 bar. On the basis of monitoring the chemical evolution of the bulk solutions over the course of 46 d, our results demonstrate two distinct relationships between kinetic behaviour and solution saturation (Ω) with respect to siderite. These relationships are best explained by chemical affinity-based rate laws that have been extensively applied to the growth kinetics of calcite (a mineral isostructural with siderite). More specifically, the BET-surface area-normalised siderite growth rates display a linear correlation with oversaturation ($\Omega - 1$) when $\Omega \gtrsim 5$, suggesting a growth rate controlled by the transport of ions to the mineral surface (r_{tr}):

$$r_{tr} = 10^{-12.60\pm0.16}(\Omega - 1)^{1.057\pm0.112}\ [\mathrm{mol\,m^{-2}\,s^{-1}}].$$

At low solution saturation, growth rates are consistent with spiral mechanism-dominated surface reactions (r_{sr}), exhibiting a parabolic correlation with ($\Omega - 1$):

$$r_{sr} = 10^{-13.42\pm0.14}(\Omega - 1)^{1.868\pm0.307}\ [\mathrm{mol\,m^{-2}\,s^{-1}}].$$

These data show that at comparable solution saturation at 25 °C, siderite growth is nearly 7-orders of magnitude slower than that of calcite. These kinetic behaviours imply that most examples of natural Fe(II) supply fluxes (e.g., dissimilatory iron reduction, hydrothermal activity, or dissolution of

other Fe(II)-minerals) would only be balanced by siderite precipitation rates at very high supersaturation, or, if the barrier to Fe(II)-carbonate nucleation is surpassed, balanced by episodic fluctuations in precipitation rate in response to Fe(II) accumulation. In combination with kinetic barriers influencing nucleation, this slow growth rate provides a straightforward explanation for the common observation that many anoxic water bodies are persistently supersaturated with respect to siderite, and implies that the precipitation of siderite may be more dynamic than previously appreciated.

3.1 Introduction

Detailed knowledge of Fe(II)-carbonate crystallisation is crucial in understanding and predicting the behaviour of a wide variety of natural and engineered geochemical systems. For example, because it is essentially ubiquitous in ancient sedimentary rocks (in particular of Precambrian age), siderite is thought to have strongly influenced the biogeochemical cycling of Fe and C throughout much of Earth's history (e.g., Bachan and Kump 2015; Beukes and Gutzmer 2008; Heimann et al. 2010; Holland 1984, 2007; Kaufman et al. 1990; Klein 2005; Raiswell et al. 2011; Rasmussen and Muhling 2018; Tosca et al. 2019). Beyond the Earth, siderite is a common component in pre-terrestrial mineral assemblages found in Martian meteorites (Bridges et al. 2019), and appears locally abundant in ancient sedimentary rocks exposed at the Martian surface (Wray et al. 2016). The formation and dissolution of siderite strongly influence corrosion processes (Ogundele and White 1986), as well as nutrient availability and crop production in modern environmental and agricultural systems (Schwab and Lindsay 1983). More recently, Fe-carbonate crystallisation has assumed a central role in efforts to reduce anthropogenic carbon emissions. These include, for example, the application of basaltic rocks rich in Ca, Mg, and Fe(II) at source point (e.g., power plants) to capture CO_2 via carbonate mineralisation (e.g., Callow et al. 2018; Gislason et al. 2010; Oelkers et al. 2008), as well as the injection of CO_2 saturated-fluids into depleted oil and gas reservoirs (e.g., Xu et al. 2004, 2005).

Although the widespread occurrence of siderite has motivated thermodynamic studies for most of the last century (since Smith 1918), the rates and pathways of Fe(II)-carbonate crystallisation remain poorly understood. For example, geochemists have only recently appreciated that Fe(II)-carbonate precipitation commonly involves multiple solid phases and, as a consequence, various precipitation pathways. Recent experimental studies have shown that homogeneous Fe(II)-carbonate precipitation is commonly initiated by the nuc-

leation of amorphous iron carbonate (AFC) at high supersaturation (e.g., Dideriksen et al. 2015; Jiang and Tosca 2019; Montes-Hernandez and Renard 2016; Sel et al. 2012). Once formed, AFC appears to provide a favourable surface promoting the secondary growth of more stable crystalline phases, including chukanovite (which is metastable with respect to siderite) and/or siderite depending on solution chemistry (Dideriksen et al. 2015; Jiang and Tosca 2019; Montes-Hernandez and Renard 2016; Sel et al. 2012).

However, even though recent work has shown that siderite may be produced through multiple pathways, its growth rate has not been accurately predicted as a function of solution saturation. This has impeded a quantitative understanding of myriad geochemical systems, both modern and ancient. While numerous experimental studies have documented the formation of siderite films on corroding steel (i.e., Burkle et al. 2017), few experiments have derived phenomenological rate laws for seeded siderite growth as a function of solution saturation. Of the handful of studies reporting kinetic data, Wajon et al. (1985) reported Fe(II) removal rates through siderite precipitation on to Ca- and Mg-containing carbonate minerals, and Greenberg and Tomson (1992) reported the results of seeded siderite precipitation experiments as a function of temperature, but both studies reported insufficient data to constrain the effect of solution saturation at a given temperature. Jimenez-Lopez and Romanek (2004) examined seeded Fe(II)-carbonate growth at room temperature on uncharacterised solids which were homogeneously precipitated from solution before constant chemical conditions were established. However, data are reported only across a high but narrow range of supersaturation. One recent study, Ma et al. (2018), measured heterogeneous siderite growth on an electrochemical quartz crystal microbalance coated with Fe or Au from 50 to 80 °C, and fitted their data with a temperature- and surface activation energy-dependent kinetic model. The Ma et al. (2018) model, however, if extrapolated to room temperature, yields precipitation rates that diverge from those reported in Jimenez-Lopez and Romanek (2004) by more than 5 orders of

magnitude at the same solution saturation. The scarcity of room temperature kinetic data also leaves the dominant crystal growth mechanisms of siderite, and the ranges in saturation state over which they operate, largely unknown. This, in turn, prevents a detailed understanding of the links between solution chemistry, crystalline morphology, and isotope/trace element incorporation.

To address these issues, we investigated the growth kinetics of siderite at room temperature and pressure across a wide range of saturation state. In what follows, we present the experimental procedure, observations on solution chemistry, characterisations of solids, and development of kinetic expressions correlating siderite growth rate with solution saturation.

3.2 Methodology

3.2.1 Apparatus and reagent preparation

Closed-system siderite syntheses were conducted at 298.15 K within a strictly anoxic Coy polymer glovebox filled with 4 % H_2/96 % N_2 gas and maintained at anoxic conditions by two pairs of palladium catalysts and anhydrous $CaSO_4$ desiccants. The palladium catalysts scrubbed $O_2(g)$ in the glovebox by continuously reacting trace $O_2(g)$ with available $H_2(g)$ to form $H_2O(l)$, which was subsequently removed by $CaSO_4$ desiccants. The O_2 and H_2 contents in the glovebox were continuously monitored by a Coy gas analyser to ensure an atmosphere of < 1 ppm O_2 throughout the preparation and storage of stock solutions and samples.

All solutions were prepared using de-ionised water (resistivity 18.2 MΩ·cm) that was first deoxygenated by purging with O_2-free N_2 gas for at least 2 h (Butler 1964), then placed on a stir plate for 24 h in the glovebox to allow any residual O_2 to escape and be removed by the catalysts and desiccants. Metal-stock solutions (1 mol kg^{-1}) were prepared by dissolving analytical grade metal-chloride powders in the deoxygenated de-ionised water. $FeCl_2$ stock solution was treated with Fe^0 powder ($\geq$ 99 %; Sigma-Aldrich) and HCl (pH

< 2) for 24 h to remove any Fe(III) in the stock $FeCl_2{\cdot}4H_2O$ powder ($\geq$ 99 %; Sigma-Aldrich). The Fe^0 was then removed by running the stock solution through a polymer container with a high-strength Nd magnet inserted in the wall. $NaHCO_3$ stock solutions (0.5 mol kg^{-1}; powder $\geq$ 99.7 %; Sigma-Aldrich) were freshly prepared for each batch of experiments to ensure the total dissolved inorganic carbon (DIC) across experiments was not affected by degassing of the stock solution over time. KCl was added to all growth experiments as a reference element to ensure the internal consistency of elemental analyses. NaCl powder was added to the experiment to balance the stoichiometric ionic strength for each solution composition.

3.2.2 Siderite seed synthesis

Siderite seed was generated in a sealed Teflon reactor constructed outside of the glovebox for the ease of handling and cleaning (Fig. 3.1). $NaHCO_3$ solution (250 mL, 0.2 mol kg^{-1} with 0.01 mol kg^{-1} NaOH, pH $\approx$ 10) and the $FeCl_2$ solution (250 mL, 0.1 mol kg^{-1}, pH $\approx$ 3) were prepared within the glovebox and sealed with three-way stopcocks prior to being taken out of the glovebox. The Teflon reactor and all the tubing were purged with O_2-free N_2 gas for 10 min and 2 min, respectively, before the reagents were connected. A strictly anoxic interior atmosphere was achieved by constantly purging the head-space in the system with N_2 gas throughout the 3-h synthesis. As illustrated in Fig. 3.1, through a combination of stopcocks and unidirectional check valves, $FeCl_2$ solution was first introduced into the Teflon reactor by N_2 gas, and the synthesis was initiated by titrating $NaHCO_3$ solution via a Metrohm 848 Titrino plus autotitrator. The $NaHCO_3$ solution was titrated at 0.025 mL s^{-1}, a rate low enough for the nucleated AFC precursor to start crystallising into siderite, but not too low where the solution $CO_3{}^{2-}/Fe^{2+}$ ratio would favour the crystallisation of chukanovite instead of siderite (Jiang and Tosca 2019). A typical pH profile of seed synthesis increased from pH 3 to near-neutral within 1 h and plateaued at pH $\approx$ 7.5 due to the pH-dependent nucleation of

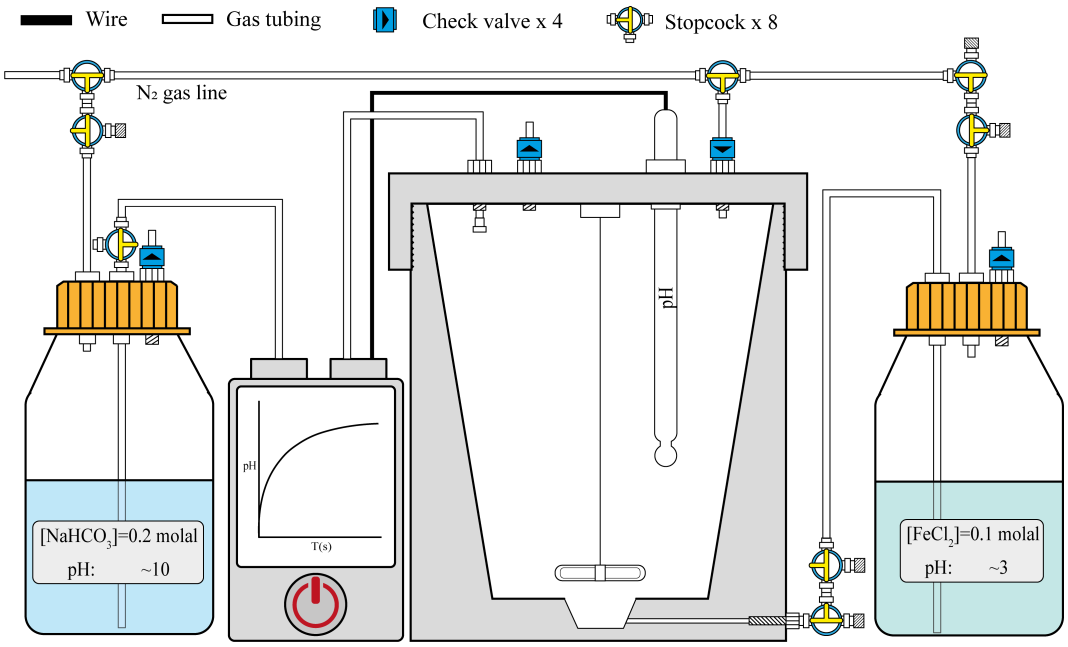


Figure 3.1: Experimental apparatus for siderite seed synthesis. Reagents were prepared and sealed within an anoxic glovebox. All tubing was purged with N_2 gas for 2 min and the Teflon reactor (600 mL) for 10 min before being connected to reagents. $FeCl_2$ solution (250 mL) was pressed into the Teflon reactor by N_2 gas, whereas $NaHCO_3$ solution (250 mL) was titrated at a rate of 0.025 mL·s^{-1}. Upon the termination of synthesis, precipitates and solution were pressed back (by N_2 gas) into the $FeCl_2$ container and transferred into the glovebox for filtration.

AFC. Upon the completion of seed synthesis, solution in the Teflon reactor was pressed back into the $FeCl_2$ container by N_2 gas, sealed and transferred into the glovebox for filtration. A volume of 550 mL of 5 % HNO_3 acid was introduced into the reactor (in the same manner as $FeCl_2$ reagent) prior to any exposure to the atmosphere for effective removal of residual reagents, the reactor was then flushed with de-ionised water three times. This method allows a reliable and consistent production of a large quantity of siderite seed; $\approx$ 1.5 g every 4 h.

3.2.3 Growth and reprecipitation experiments

Two sets of closed-system experiments were conducted using freshly prepared siderite seed (0.5 g each): growth experiments (G-series) and reprecipitation experiments (RP-series). Growth experiments were carried out in

1 L borosilicate glass reaction vessels wrapped in Al-foil to prevent photo-oxidation within the glovebox. After the establishment of initial solution chemistry (Table. 3.1), all solutions were allowed to react over the course of 46 d and gently hand-shaken twice a day. Reprecipitation experiments (RP-series) were designed to replicate growth experiments apart from having no dissolved Fe(II) in the matrices, and allowed to react over the course of 288 d.

The pH of both growth and reprecipitation experiments was held constant by a combination of MOPS (3-(N-morpholino) propanesulfonic acid; 0.05 $\mathrm{mol\,kg^{-1}}$) pH buffer and large DIC pools (up to 0.084 $\mathrm{mol\,kg^{-1}}$). MOPS features significant steric hindrance of acid-base functional groups and therefore exhibits negligible metal complexation (Kandegedara and Rorabacher 1999). MOPS was first added to deoxygenated de-ionised water, and the solution pH was raised to within 0.5 unit of the target value by manual addition of NaOH solution (1 $\mathrm{mol\,kg^{-1}}$), followed by the addition of KCl and NaCl and left for 24 h to homogenise. Predetermined amounts of $NaHCO_3$ stock solution were then added to the homogenised solution, followed by pH adjustments using a Metrohm 902 Titrando autotitrator (within the glovebox) with NaOH solution (0.5 $\mathrm{mol\,kg^{-1}}$). This procedure was to minimise changes to carbonate speciation associated with pH adjustment. For example, a high proportion of $CO_2(aq)$ in low pH solution would lead to $CO_2(g)$ escape during preparation. To avoid instantaneous nucleation on the entry of the concentrated $FeCl_2$ solution, the stock solution was first diluted to 0.05 $\mathrm{mol\,kg^{-1}}$ before being pipetted into the matrices and gently mixed immediately. In order to minimise $CO_2(g)$ degassing over time, the head-space in the reaction vessels were essentially eliminated (i.e., < 1 mL), and sealed with gas-tight septum caps to facilitate solution sampling. Both the growth and reprecipitation experiments were initiated by the addition of 0.5 g of seed.

Complete starting solution compositions of all experiments are provided in Table. 3.1. Solution saturations of growth experiments with respect to siderite equilibrium (Singer and Stumm 1970) and the critical supersaturation

T = 298.15 K and 1 bar

Ex.No	pH	MOPS mol kg^{-1} ×10^3	KCl mol kg^{-1} ×10^3	NaCl mol kg^{-1} ×10^3	$NaHCO_3$ mol kg^{-1} ×10^3	$FeCl_2$ mol kg^{-1} ×10^3	Ionic strength mol kg^{-1}	Initial Ω
G-1	7.515	50.183	2.013	125.617	6.366	0.502	0.176	22
G-2	7.496	50.183	2.009	111.849	20.090	0.502	0.176	66
G-3	7.752	50.009	2.009	120.887	11.071	0.502	0.176	67
G-4	7.378	50.184	2.014	83.491	48.444	0.502	0.176	120
G-5	7.760	50.183	2.024	97.116	35.035	0.502	0.176	217
G-6	7.638	50.184	2.148	48.231	83.739	0.502	0.176	389
RP-1	7.478	50.003	2.000	125.152	6.332	0.000	0.173	—
RP-2	7.496	50.020	2.001	111.499	20.031	0.000	0.174	—
RP-3	7.770	50.009	2.000	120.464	11.036	0.000	0.174	—
RP-4	7.363	50.056	2.002	83.305	48.318	0.000	0.174	—
RP-5	7.742	50.039	2.001	96.658	34.921	0.000	0.174	—
RP-6	7.622	50.100	2.004	48.136	83.604	0.000	0.174	—

Table 3.1: Starting solution compositions of growth (G) and reprecipitation (RP) experiments. Concentrations of all reagents calculated from added powders and analysed (ICP-MS) stock solutions. Ionic strength calculation includes pH buffer MOPS; $I_{\mathrm{MOPS}} = 0.04$ mol kg^{-1} (Buffer Calculator: http://www.liv.ac.uk/buffers). Reagents were added to deoxygenated de-ionised water in the order listed in the table (left→right).

for homogeneous nucleation of precursor amorphous Fe(II)-carbonate (Jiang and Tosca 2019) are illustrated in Fig. 3.2.

3.2.4 Analytical procedures

Solution samples (≈ 1.5 mL) were withdrawn through the septum caps of the reaction vessels. To further assure minimum CO_2 degassing into the vacuum caused by solution-extraction, a O_2-free N_2 gas-filled syringe was inserted alongside the sampling syringe to replace the extracted solution volume. The solution samples were then syringe-filtered (0.22 µm), and an aliquot of 0.5 mL was pipetted into a metal-free polypropylene centrifuge tube with 10 mL of 2 % HNO_3 solution for in-house ICP-MS elemental analysis. All stock solutions were analysed alongside the samples in order to recalibrate the thermodynamic calculations of the actual solution chemistry. The terminal pH measurements indicate < 0.1-unit change over the course of the reaction.

All solids, including the seeds, were filtered out the parent solutions through 0.22 µm nylon filter membranes and left to dry under the low-humidity anoxic atmosphere in the glovebox for 24 h. Solids harvested from growth experiments were analysed by powder X-ray diffraction (XRD) using a PANalytical

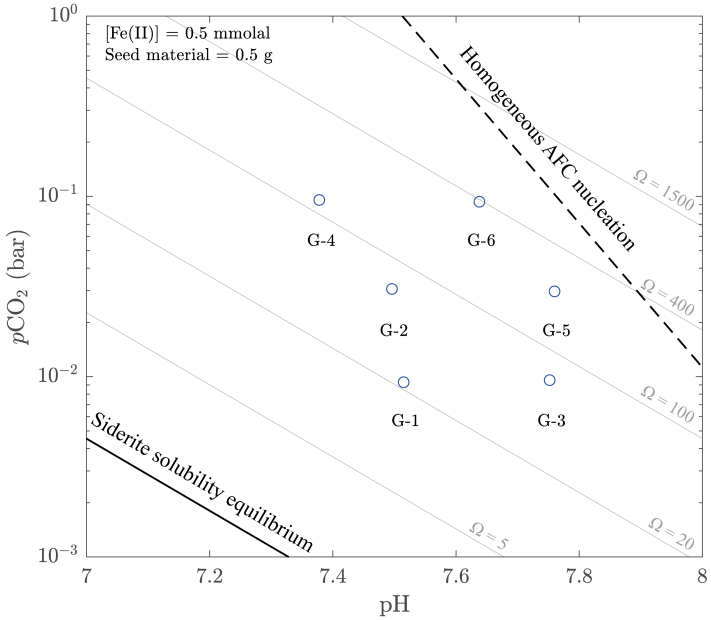


Figure 3.2: $p\mathrm{CO}_2$-pH space illustrates the initial solution saturations (Ω) of growth experiments with respect to siderite solubility equilibrium ($\log K_{sp} = -10.24$; Singer and Stumm 1970; solid line) and the critical supersaturation for homogeneous nucleation of amorphous Fe(II)-carbonate precursor ($\log IAP_{AFC} = 2.20$; Jiang and Tosca 2019; dashed line; IAP: ionic activity product). Complete solution compositions are provided in Table. 3.1. Thermodynamic calculations are provided in Supplementary information.

Empyrean Series 2 X-ray diffractometer with a Co Kα source, operated at 40 kV and 40 mA, and scanned between 5 and 80 deg 2Θ at a step size of 0.026 deg. Powders were loaded on single-crystal silicon sample holders and sealed with Kapton film within the glovebox to minimise oxidation during XRD analysis. Final X-ray diffractograms are shown with background patterns removed (subtracting patterns obtained on Kapton film).

Fourier transform infrared spectroscopy (FT-IR) analyses were performed on powdered products and were acquired in transmission mode using a PerkinElmer Frontier mid-IR spectrometer. FT-IR transmission measurements were collected on optically transparent KBr pellets with a sample : KBr ratio of $\approx$ 1 : 200. KBr powder and sample were ground and compressed into pellets at 7 tons and analysed within 30 min of exposure to air (Fe(III)-O vibrations were closely monitored to ensure minimal oxidation had taken place). Measurements were collected from 400 to 4000 cm^{-1} at 1 cm^{-1} resolution using a deuterated triglycine sulphate (DTGS) detector with a KBr window and beam-splitter.

After identifying oxidation of the solids from growth experiments during sample preparation and analyses (but not during growth experiments), subsequent modifications were made to both XRD and FT-IR procedures for reprecipitation experiments; discussed in Section. 3.3.2.

In-house scanning electron microscopy (SEM) was performed on all samples to characterise the morphology of the seed and harvested solids. Imaging was conducted using an FEI Quanta 650 FEG SEM in high vacuum mode. To minimise oxidation during sample preparation, small amounts of solid were mounted on adhesive carbon layers on aluminium stubs within the glovebox, then transported to a gold-coating unit in a parafilm-sealed container; sample exposure to air was $<$ 1 min. Once gold-coated (9 nm Au), samples were immediately transferred into the evacuated SEM-EDS chamber.

The BET-surface area of seed and three harvested solids were measured using a Micromeritics TriStar II Plus surface area and porosity analyser with N_2

gas at a bath temperature of -195.850 °C. BET-surface area analysis was conducted at the Surface Analysis Facility, Department of Chemistry, University of Oxford.

3.3 Results

3.3.1 Solution chemistry evolution

ICP-MS analyses show monotonic decreases in solution Fe(II) concentrations from all growth experiments (Fig. 3.3A). A higher initial solution saturation (Ω) corresponds to a higher rate of Fe(II) consumption, and the rate decreases as the solution and solid approach siderite equilibrium (Fig. 3.4). Importantly, experiments with similar siderite saturations show similar rates of Fe(II) consumption (e.g., G-2 and G-3; Fig. 3.3A), despite different initial pH-pCO_2 conditions (Fig. 3.2). Cumulative Fe(II) consumption (in moles) as solution saturation evolved is presented in Fig. 3.4

The solution chemistry of reprecipitation experiments (first 46 d; Fig. 3.3B) shows initial increases in Fe(II) concentrations corresponding to rapid dissolution of nanocrystalline siderite seed (see solid characterisation below), followed by gradual decreases that, though at much lower concentrations, imitate the saturation-correlated growth kinetics of siderite (Fig. 3.3A). Although the sampling frequency was too low to constrain the dissolution kinetics of nanocrystalline siderite (completely dissolved in $\leq$ 3 d), the maximum solution saturation with respect to siderite reached via dissolution was confined to $7 < \Omega < 18$ (Table. 3.3); at this point in the experiments, the dissolution of nanocrystalline siderite, once complete, was overtaken by the secondary growth of coarsely crystalline siderite.

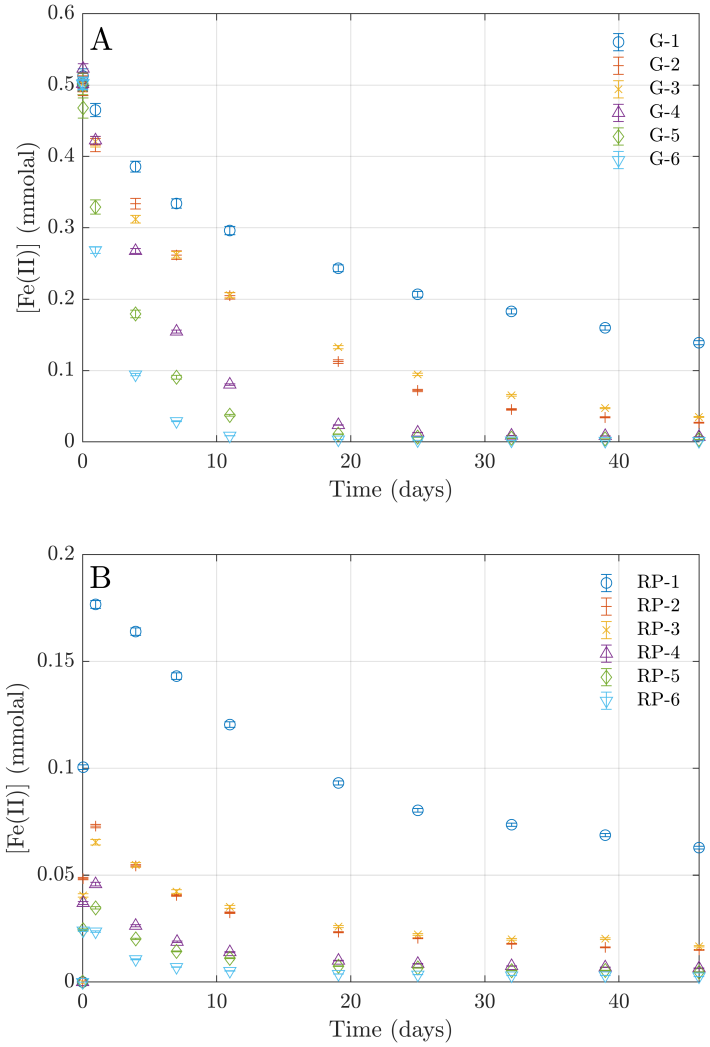


Figure 3.3: Evolution of solution [Fe(II)] (ICP-MS analysis) in (A) the growth experiments (G series) and (B) the reprecipitation experiments (RP series; first 46 d). The reprecipitation experiments are exact replica of the growth experiments except that their initial [Fe(II)] = 0 mmol kg^{-1}. Analytical errors (3σ) are < 3 % of measurements.

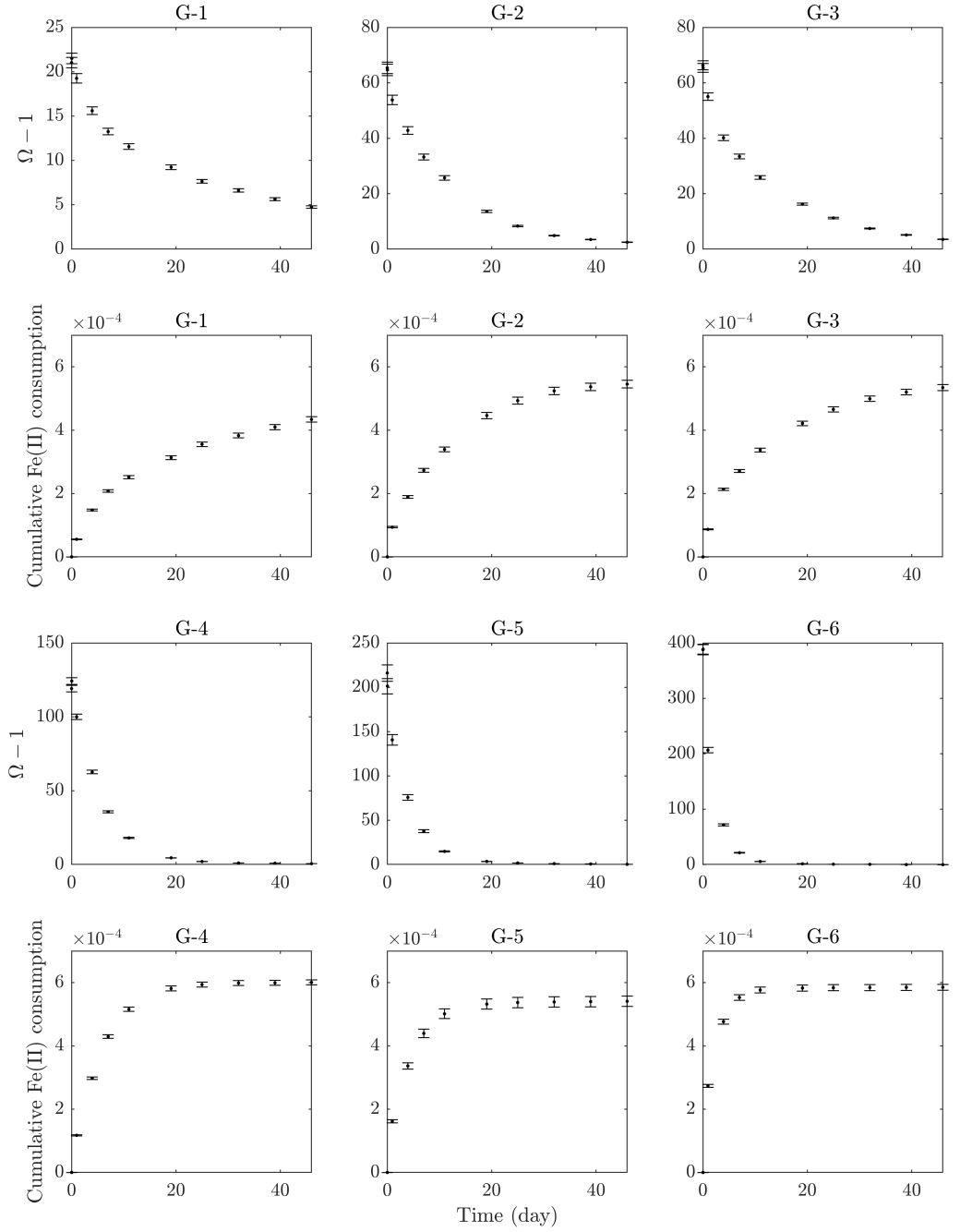


Figure 3.4: The evolution of solution saturation (Ω) and the cumulative Fe(II) consumption (in moles) of growth experiments. Error bars are 3σ, σ_Ω is calculated by assuming $\sigma_{[CO_3^{2-}]}$=$\sigma_{[Fe^{2+}]}$; calculations shown in Supplementary information.

3.3.2 Solid characterisations

XRD and FT-IR characterisation

The siderite seed yields a monomineralic X-ray diffractogram and an FT-IR spectrum corresponding to siderite (Fig. 3.5 & 3.6). This indicates the initially nucleated AFC rapidly crystallised to siderite during seed synthesis; XRD and FT-IR characterisations of the precursor AFC are provided in Jiang and Tosca (2019). In addition to XRD and FT-IR patterns corresponding to siderite, solids harvested from growth experiments show weak diffraction and absorption peaks that correspond to minor amounts of goethite (FeO(OH)); its peak intensities appear to increase in the order that the samples were analysed (G-1 to G-6).

As described in the analytical procedure (Section. 3.2.4), harvested solids from growth experiments were sealed with Kapton film within the glovebox to minimise oxidation. However, due to the scattering of X-rays by Kapton film, the scanning time of each sample was extended to 50 min to obtain a clear diffractogram. This procedure resulted in up to 4 h and 10 min exposure to the atmosphere when G-6 was analysed. Pervasive oxidation of solids under Kapton film is observed by the colour change from grey-green to orange-red of the solids at the end of XRD analysis. Kapton film's inability to prevent oxidation has also been reported in the characterisation of synthetic amorphous Fe(II)-carbonate by Dideriksen et al. (2015). Similarly, after mixing with KBr powder in the glovebox, grinding and preparing KBr pellet, and FT-IR analysis accounted for $\approx$ 30 min exposure to the atmosphere for each sample, cumulatively 2 h and 30 min when G-6 was analysed.

To test the hypothesis that siderite oxidation occurred during sample analysis and not in the glovebox during crystal growth experiments, solids from reprecipitation experiments (RP series) were treated with extra precaution. For both XRD and FT-IR analyses, only one sample was taken out of the glovebox each time. Individual XRD analysis was conducted without Kapton

film, which allowed a significantly reduced scanning time (19 min). KBr-sample mixture was ground within the glovebox before individually taken out for pellet preparation and analysis. All reprecipitation experiments show X-ray diffractograms and FT-IR spectra corresponding to pure siderite (Fig. 3.5 & 3.6).

The absence of goethite in the reprecipitation experiments rules out the possibility of goethite formation by (1) residual $O_2(aq)$ in the matrix solution, and (2) trace $O_2(g)$ in the glovebox atmosphere that diffused through the septum cap over the course of experiments, because (1) growth and reprecipitation were prepared with same deoxygenated matrix solutions and reagents and (2) reprecipitation experiments resided in the glovebox over a period of 288 d, compared to 46 d of growth experiments. Importantly, the cumulative Fe(II) consumption in all growth experiments was governed by solution saturation with respect to siderite (Fig. 3.4). Therefore, we reason that the kinetic constraints obtained from the evolution of solution chemistry can be solely attributed to the precipitation of siderite, and the formation of goethite likely occurred during solid sample drying, preparation, and analyses.

SEM imaging

The unreacted siderite seed is dominated by spherical particles of ≈ 2 µm in diameter, with a minor occurrence (< 5 %) of $\approx$ 10–15 µm larger population (Fig. 3.7A&B). Neither of the two populations displays discernible crystal morphology, suggesting the seed particles are aggregates of nanocrystalline siderite nuclei. The surface of some ≈ 10 µm spheres shows partially formed globules (≈ 2 µm; Fig. 3.7A), indicating an early stage of rhomb formation.

After 46 d, solids from growth experiments show two types of crystalline siderite. (1) Interlocking siderite rhombs that are ≤ 50 nm in edge length; these are observed on all harvested solids (e.g., Fig. 3.7F&H). The formation of the interlocking small siderite rhombs can be attributed to the crystallisation of seed particles themselves. (2) Overgrown siderite rhombs of edge length

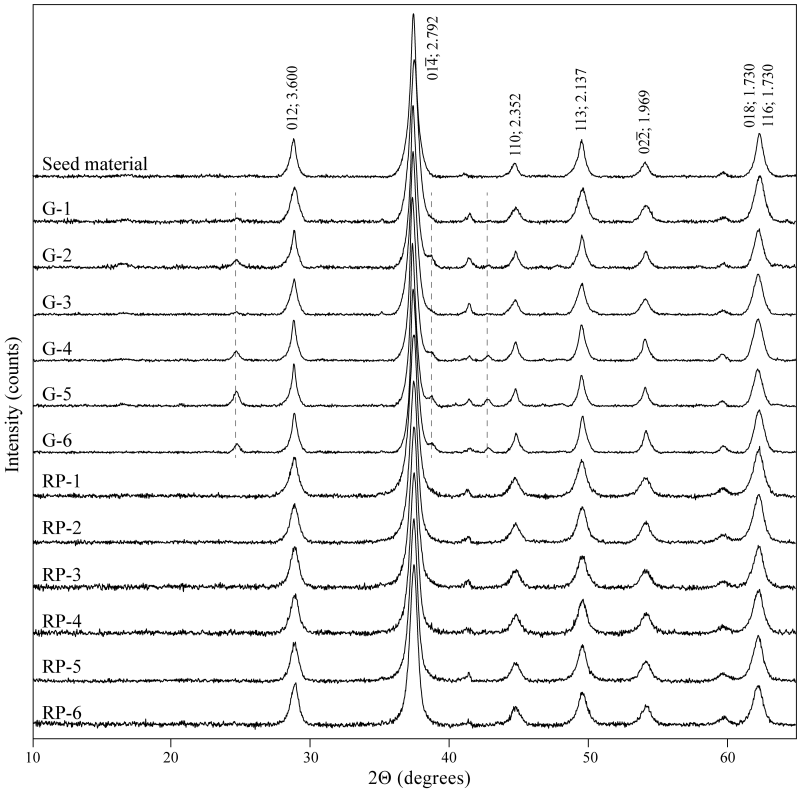


Figure 3.5: Powder X-ray diffractograms (Co Kα source) of siderite seed and the growth experiments (G-series) harvested after 46 d (Kapton film background removed; 50 min scanning time) and reprecipitation experiments (RP-series) harvested after 288 d (no Kapton film, 19 min scanning time). All solids show diffraction peaks corresponding to siderite, labelled with Miller indices and *d*-spacing (Å). Dashed lines indicate the minor occurrence of goethite (FeO(OH)) in the harvested solids from growth experiments but absent in reprecipitation experiments. The origin of goethite is discussed in Section. 3.3.2.

$\leq$ 200 nm on the surface of seed particles. This population is interpreted to result from localised growth from the oversaturated solutions. The degree of siderite overgrowth is qualitatively consistent with the initial solution saturation. At the lowest initial saturation, G-1 is dominated by interlocking small siderite rhombs (Fig. 3.7C&D). With increasing initial saturations, G-2 (Fig. 3.7E&F), G-3 (Fig. 3.7G&H), G-4 (Fig. 3.7I&J), and G-5 (Fig. 3.7K&L) show the overgrown siderite crystals increase both in size and abundance, as well as a better-developed rhombohedral morphology. Finally, G-6 (Fig. 3.7M&N) shows complete encrustation of overgrown siderite rhombs of $\approx$ 200 nm in edge length.

Similar observations can be made from the reprecipitation experiments

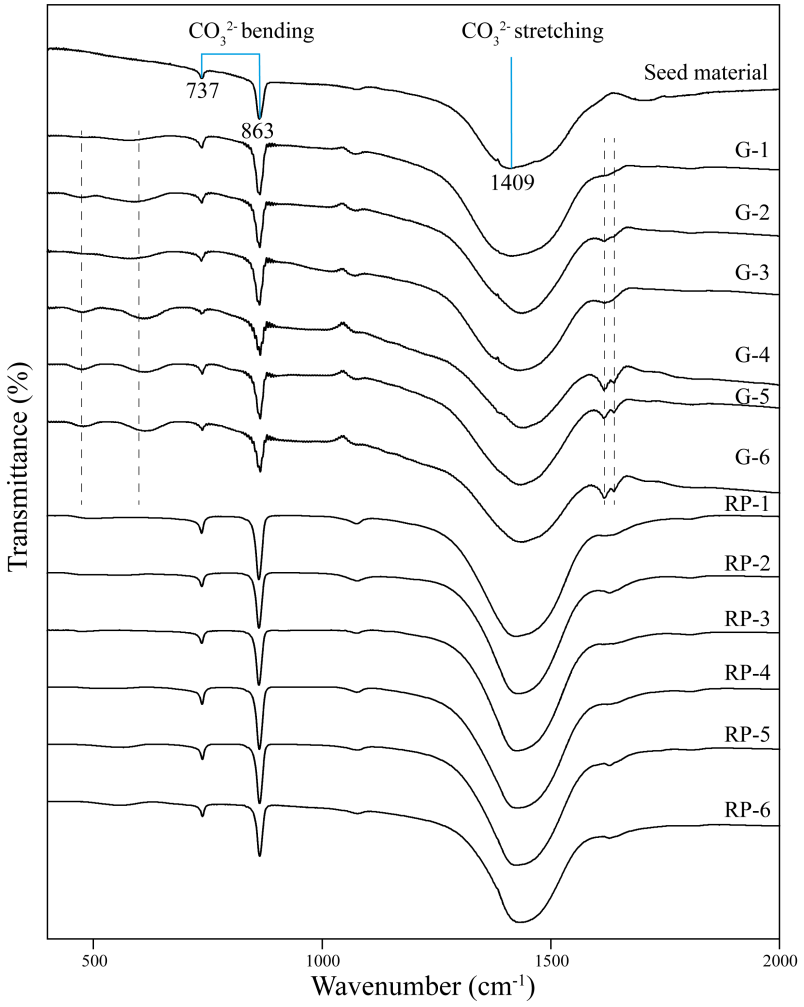


Figure 3.6: FT-IR transmittance spectra of seed and harvested solids. Solids from growth experiments (G) show the absorption peaks corresponding minor occurrences of goethite (dashed lines) that is absent in the reprecipitation experiments (RP). The origin of goethite is discussed in Section. 3.3.2

(288 d), that the seed particles crystallised into interlocking small siderite rhombs ($\leq$ 10 nm) with various degrees of siderite overgrowth ($\leq$ 200 nm) from oversaturated solutions (Fig. 3.8). However, as indicated by solution chemistry (Fig. 3.3B), reprecipitation experiments first underwent dissolution of nanocrystalline siderite seeds and followed by secondary growth. Therefore, the degree of siderite overgrowth on the seed particles was not only tied to the supersaturation but also the amount of Fe(II) released via dissolution. For example, because of the high solution pH and DIC, RP-6 reached the highest solution saturation (Ω = 18) with the least amount of seed dissolu-

tion (d[Fe(II)] = 0.0241 × 10^{-3} mol kg^{-1}; Table. 3.3); SEM imaging of RP-6 show interlocking small siderite but an insignificant amount of overgrowth (Fig. 3.8F).

It is important to note that the diameters of both size-populations (≈ 2 µm and ≈ 10–15 µm) of seed particles were retained after growth and reprecipitation experiments, and the acicular needle morphology that is typical of water-column goethite precipitation was not observed in all harvested solids (a total of 50 SEM images).

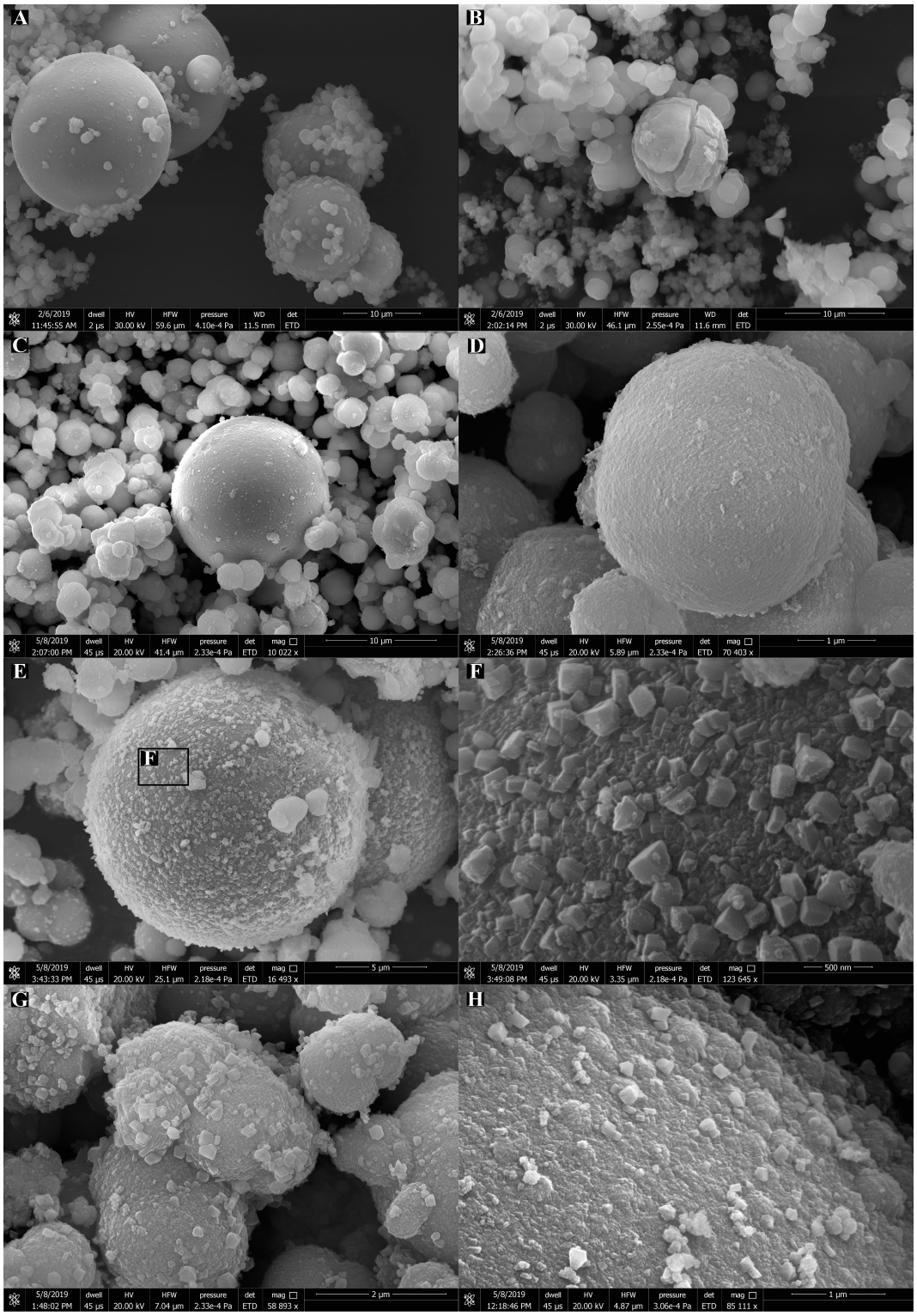
BET-surface area

Surface analyses show the unreacted siderite seed has a BET surface area (A_{BET}) of 109.75 m^2 g^{-1} and a micropore volume (v_{pore}; t-Plot) of 1.788 mm^3 g^{-1}. Three solids harvested from growth experiments show reductions in both surface area and micropore volume; G-2: A_{BET} = 82.48 m^2 g^{-1}, v_{pore} = 0.036 mm^3 g^{-1}, G-4: A_{BET} = 81.12 m^2 g^{-1}, v_{pore} = 0.074 mm^3 g^{-1}, and G-6: A_{BET} = 81.39 m^2 g^{-1}, v_{pore} = 0.076 mm^3 g^{-1}. Though lacking measurements on the evolution of the surface area during growth experiments, the changes in the surface area can be correlated with the amounts of siderite growth, which themselves were stoichiometrically equivalent to the changes in solution Fe(II) concentrations: $\Delta A_{BET} \propto \Delta$[Fe(II)]. By fitting the BET-surface area of siderite seed and the end values of three harvested solids, scaling to the ratio of the mass of precipitated siderite (m_{ppt}) over the mass of siderite seed (m_{seed}), the following relation can be established:

$$A_{BET} = -211.39(\frac{m_{ppt}}{m_{seed}}) + 109.41, \tag{3.1}$$

with R^2 = 0.97 (n = 3). Eq. 3.1 is used to estimate the BET-surface area of all the solids at each sampling time, against which the growth rates are normalised (Table. 3.2).

The same approximation, however, cannot be applied to the reprecipitation


A
2/6/2019 11:45:55 AM | dwell 2 µs | HV 30.00 kV | HFW 59.6 µm | pressure 4.10e-4 Pa | WD 11.5 mm | det ETD | 10 µm
B
2/6/2019 2:02:14 PM | dwell 2 µs | HV 30.00 kV | HFW 46.1 µm | pressure 2.55e-4 Pa | WD 11.6 mm | det ETD | 10 µm
C
5/8/2019 2:07:00 PM | dwell 45 µs | HV 20.00 kV | HFW 41.4 µm | pressure 2.33e-4 Pa | det ETD | mag 10 022 x | 10 µm
D
5/8/2019 2:26:36 PM | dwell 45 µs | HV 20.00 kV | HFW 5.89 µm | pressure 2.33e-4 Pa | det ETD | mag 70 403 x | 1 µm
E
F
5/8/2019 3:43:33 PM | dwell 45 µs | HV 20.00 kV | HFW 25.1 µm | pressure 2.18e-4 Pa | det ETD | mag 16 493 x | 5 µm
F
5/8/2019 3:49:08 PM | dwell 45 µs | HV 20.00 kV | HFW 3.35 µm | pressure 2.18e-4 Pa | det ETD | mag 123 645 x | 500 nm
G
5/8/2019 1:48:02 PM | dwell 45 µs | HV 20.00 kV | HFW 7.04 µm | pressure 2.33e-4 Pa | det ETD | mag 58 893 x | 2 µm
H
5/8/2019 12:18:46 PM | dwell 45 µs | HV 20.00 kV | HFW 4.87 µm | pressure 3.06e-4 Pa | det ETD | mag 85 111 x | 1 µm

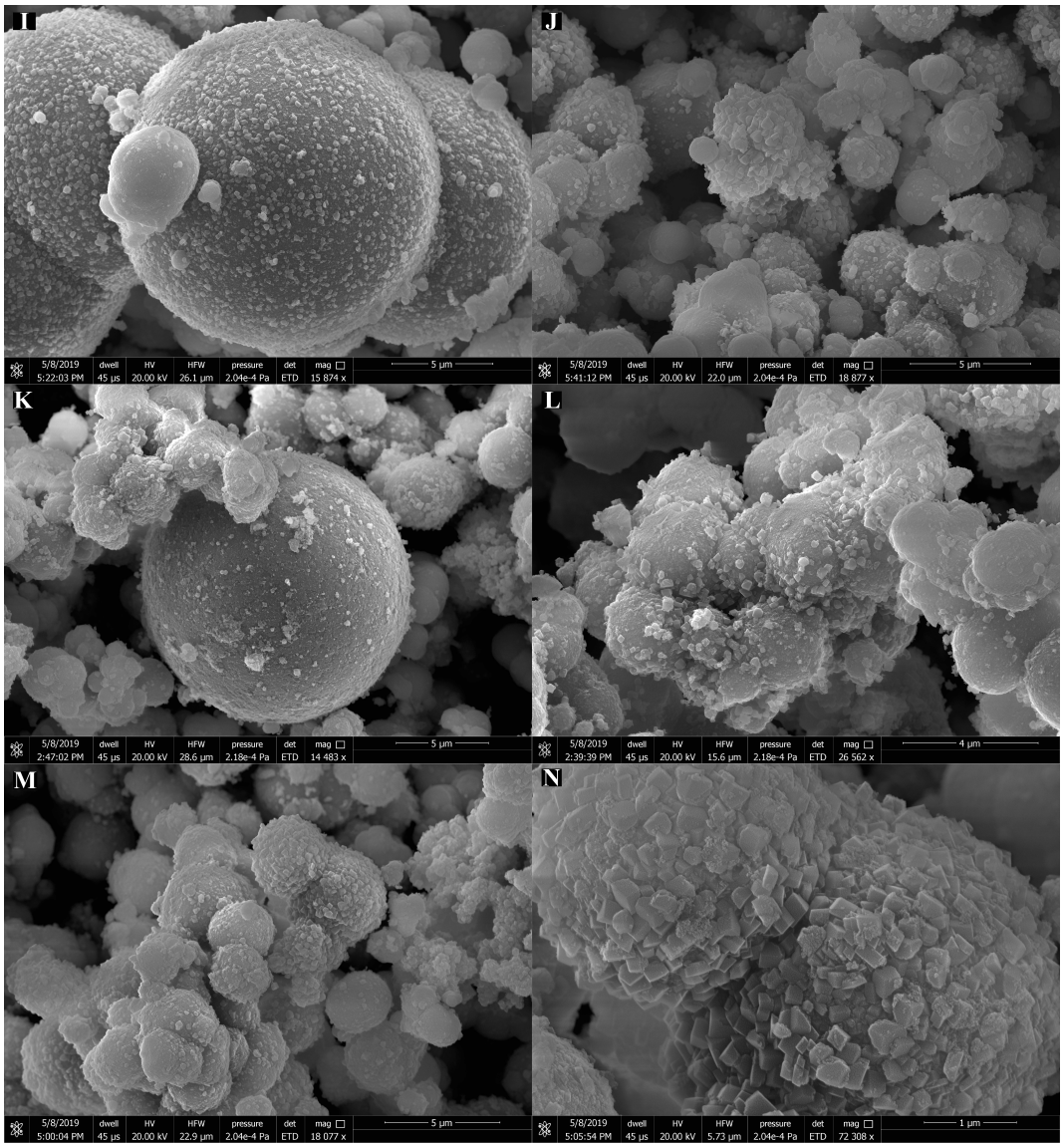


Figure 3.7: SEM images of siderite seed and harvested solids from growth experiments (46 d). (A&B) Siderite seeds, predominantly composed of spherical particles of ≈ 2 µm in diameter with a minor occurrence (≤ 5 %) of larger particles of ≈ 10–15 µm in diameter. (C&D) G-1 shows minor siderite encrustation (≤ 20 nm in edge length). With increasing initial solution saturation, G-2 (E&F), G-3 (G&H), G-4 (I&J), and G-5 (K&L) show siderite encrustation increases both in size and abundance, as well as a better-developed rhombohedral morphology. (M&N) G-6 shows complete encrustation of siderite rhombs of ≈ 200 nm in edge length.

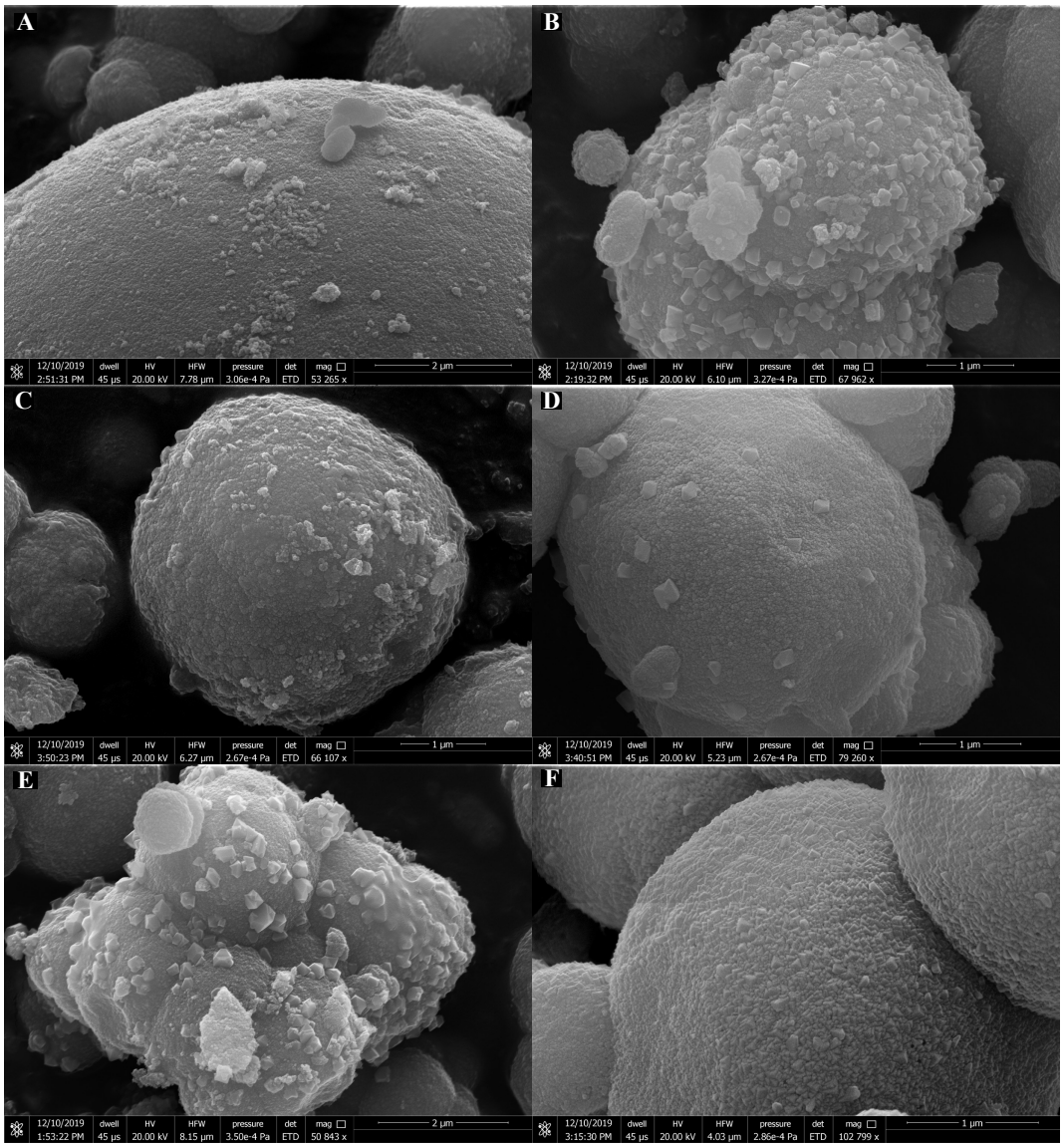


Figure 3.8: SEM images of harvested solids from reprecipitation experiments (288 d). RP-1 (A) and RP-6 (F) show crystallised seed particles of interlocking small siderite rhombs that are $\leq$ 10 nm in edge length. RP-2 (B), RP-3 (C), RP-4 (D), and RP-5 (E) show various degrees of localised growth of rhombohedral siderite crystals of edge length $\leq$ 200 nm, in addition to the crystallised surface of the seed particles.

experiments as they underwent both dissolution and growth. These processes complicate the evolution of the surface area and its correlation with solution chemistry. Therefore, the secondary growth rates from reprecipitation experiments are only normalised against the initial surface area of the siderite seed $A_{BET} = 109.75\ \mathrm{m^2\,g^{-1}}$ (Table. 3.3).

3.4 Discussion

3.4.1 Chemical affinity-based rate laws

Since the publication of the influential Burton, Cabrera, and Frank crystal growth theory (Burton et al. 1951), numerous mechanistic models have been further developed to correlate the kinetic behaviour of mineral-water interactions with solution chemistry. The most widely applied are the chemical affinity-based rate laws (e.g., Aagaard and Helgeson 1982; House 1981; Lasaga 1984; Nancollas and Reddy 1971; Nielsen 1984), which generalise growth and dissolution kinetics as a function of energetics (free energy of reaction ΔG_r, or as $\Omega = \exp \frac{\Delta G_r}{RT}$), and can be cast in the following general formalism (e.g., Nielsen 1984):

$$\text{rate} = k(\Omega - 1)^n/(1 - \Omega)^n, \tag{3.2}$$

where k is the rate constant, and n indicates the reaction order of growth rate on supersaturation $(\Omega - 1)$, or dissolution rate on undersaturation $(1 - \Omega)$. The following discussion focuses on crystal growth.

Experimentally derived reaction orders (n) from macroscopic precipitation (i.e., solution chemistry) have been ascribed to the following rate-determining microscopic processes associated with the transfer of the constituent ions (summarised from Lasaga 1998c; Nielsen 1981; Nielsen and Toft 1984; Van Cappellen 1991):

1. From the bulk solution to the mineral-water interface.

2. From the solution into an adsorption layer.

3. From the solution or an adsorption layer to surface defects and subsequent integration into the crystal lattice.

4. From the solution or an adsorption layer to or to form surface nuclei.

These processes are thought to contribute to overall reaction rates in the following ways:

1. Transport-controlled growth rates are linearly dependent on diffusion: rate $\propto (\Omega - 1)$ (Mullin 1972; Nielsen 1964)

2. Surface-controlled growth by adsorption, with rates linearly dependent on diffusion: rate $\propto (\Omega - 1)$ (Nancollas and Reddy 1971; Nielsen 1983, 1984; Nielsen and Christoffersen 1982; Shiraki and Brantley 1995)

3. Surface-controlled growth at crystal defects dominated by spiral growth, which follows a parabolic rate law: rate $\propto (\Omega - 1)^2$ (Nancollas 1979; Nielsen 1981; Shiraki and Brantley 1995)

4. Surface nucleation that follows an exponential dependence on saturation: rate $\propto \exp(-\frac{U}{\ln \Omega})$, where U incorporates the molar properties and the geometry of nuclei (Christoffersen and Christoffersen 1992; Hillig 1966; Nielsen 1984; Shiraki and Brantley 1995; Van Cappellen 1991).

Process (1) is a transport process, and (2–4) can be grouped as surface reaction mechanisms. Typically, the kinetic behaviour of crystal growth is simultaneously influenced by two or more of these processes. An important distinction is that those surface reactions are parallel mechanisms—their individual rates are added, and the faster is the rate-determining mechanism. In contrast, transport and surface reactions are consecutive processes—the slower one is the rate-determining process (e.g., Nielsen 1984).

At low supersaturation, surface reactions proceed at defect sites including step edges, kink, ledge, and hillock/adatom, where the adsorbed ions are preferentially integrated into crystal lattice (e.g., Burton et al. 1951; Lasaga

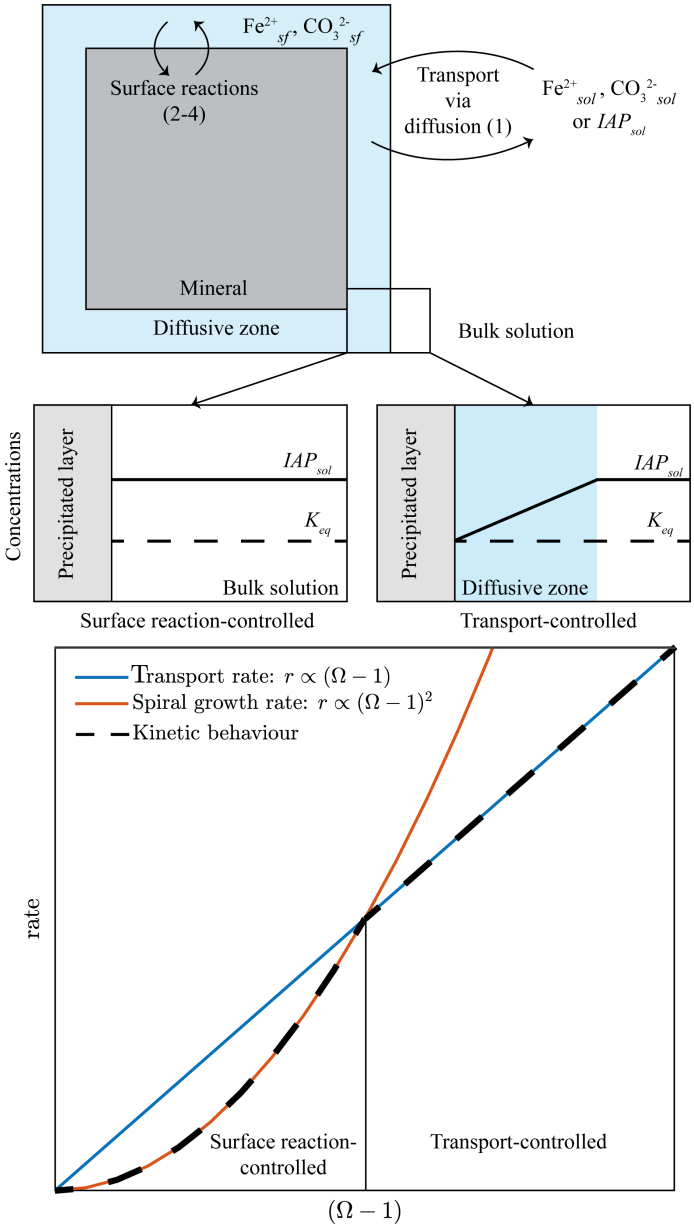


Figure 3.9: An illustration of microscopic processes at the mineral-water interface (above) and a schematic of the overall kinetic behaviour of the system (below). Water-mineral interactions (exemplified here is crystal growth) follows the surface reaction kinetic model summarised by DePaolo (2011). At low supersaturation, the kinetic behaviour is determined by surface reactions rate, while the solution is sufficiently homogenised (left column). At high supersaturation, a fast surface reaction rate drives the surface fluid (*sf*; in blue) in proximity to the mineral surface to equilibrium, creates a diffusive zone where the transport of dissolved species from the bulk solution (*sol*) becoming the slowest process (right column). The overall kinetic behaviour (dashed line) is dictated by the slowest process, thus, can be cast as surface reaction-controlled versus transport-controlled as a function of supersaturation.

1998c; Nielsen 1984; Van Cappellen 1991; Watkins et al. 2017). Because step and kink sites are the most abundant defect sites on crystal surface (Burton et al. 1951; Zhang and Nancollas 1990; Zhang and Nancollas 1998), growth at defects is commonly observed to be dominated by a spiral growth spiral mechanism ($n \approxeq 2$) (Nancollas 1979; Nielsen 1981; Saldi et al. 2009; Shiraki and Brantley 1995; Teng et al. 2000; van Enckevort et al. 1981). In the absence of favourable surface structure, or if the energetics of the system do not favour growth at defects, growth by adsorption ($n = 1$) may become the dominant mechanism (Nielsen 1983, 1984). Growth by adsorption has been used to successfully model quartz dissolution and precipitation across a wide range of solution saturation and temperature (Rimstidt and Barnes 1980), but has only been documented for calcite precipitation near-equilibrium (Nancollas and Reddy 1971; Shiraki and Brantley 1995). As supersaturation increases, surface nucleation will, from a certain point on, become the more efficient growth mechanism (e.g., calcite growth; Shiraki and Brantley 1995; Teng et al. 2000).

Because surface reaction rates (apart from adsorption) are high-power functions of supersaturation, deviation from equilibrium increases reaction rates drastically; this consumes ions in the surface fluid faster than they can be homogenised with the bulk solution. This process establishes a diffusive zone where the surface fluid is maintained at equilibrium by fast surface reactions, and the saturation state in the diffusive zone increases towards the bulk solution (Fig. 3.9). In this scenario, the rate of surface reactions is capped by the transport of the ions through the diffusive zone, and the overall kinetic behaviour of the system becomes transport-controlled (e.g., DePaolo 2011; Mullin 1972; Nielsen 1984; Shiraki and Brantley 1995; Van Cappellen 1991; Watkins et al. 2017). This phenomenon can be illustrated by plotting rate $\propto (\Omega - 1)$ and rate $\propto (\Omega - 1)^2$ in Fig. 3.9, indicating that transport-controlled kinetic behaviour is expected in conditions far from equilibrium.

3.4.2 Siderite growth kinetics

The growth rate (r; $\mathrm{mol\,m^{-2}\,s^{-1}}$) of siderite is calculated here as the difference in [Fe(II)] divided by the time lapse between sampling and normalised against the BET-surface area. To calculate the evolving solution saturation during siderite precipitation, a stoichiometrically equivalent amount (to Δ[Fe(II)]) of carbon is subtracted from the total DIC, followed by calculation of the remaining [CO_3^{2-}] and supersaturation (Supplementary information, 3.6.2); assuming relatively rapid re-equilibration of carbonate species and no $CO_2(g)$ exchange. These calculations permit us to assign an average growth rate over the sampling interval to the solution saturation at the time of sampling. All measured and calculated values for growth and reprecipitation experiments are listed in Tables 3.2 and 3.3, respectively.

Taking the logarithmic form of the general chemical affinity-based rate law (Eq. 3.2):

$$\log \mathrm{rate} = \log k + n \log (\Omega - 1),$$

kinetic data from growth experiments (53 data; Table. 3.2) can be fitted to obtain n as the gradient, and k as the intercept:

$$r = 10^{-12.92 \pm 0.10} (\Omega - 1)^{1.223 \pm 0.10} \ [\mathrm{mol\,m^{-2}\,s^{-1}}], \tag{3.3}$$

with 95 % confidence bound, $R^2 = 0.94$, and the sum of squared errors of prediction (SSE) of 2.386. The fitted equation indicates an overall mixed transport- and surface reaction-controlled kinetic behaviour, with the former being the dominant.

It is, however, noticeable that the growth rate deviates from the Eq. 3.3 at low supersaturation (e.g., $\Omega \lesssim 5$; Fig. 3.10A). Such deviation may reflect a transition from transport-controlled growth to surface reaction-controlled as the system approaches equilibrium. However, due to the sparsity of low-supersaturation kinetic data from the growth experiments, a rate law in this

$I = 0.175$ mol kg^{-1}; $T = 298.15$ K and 1 bar

Ex.No	Time h	[Fe(II)] mol kg^{-1} $\times 10^3$	[DIC] mol kg^{-1} $\times 10^3$	[CO_3^{2-}] mol kg^{-1} $\times 10^6$	BET surface area m^2 g^{-1}	Ω	Growth rate mol m^{-2} s^{-1} $\times 10^{12}$
G-1	0.77	0.5127	6.366	23.595	109.75	22.5	—
pH=7.515	22.95	0.4650	6.318	23.419	109.41	20.3	12.984
	94.70	0.3858	6.239	23.125	107.24	16.6	6.952
	167.98	0.3340	6.188	22.933	102.69	14.3	4.577
	263.38	0.2962	6.150	22.793	99.71	12.6	2.621
	457.72	0.2433	6.097	22.597	97.53	10.2	1.854
	599.68	0.2069	6.060	22.462	94.51	8.6	1.789
	767.48	0.1829	6.036	22.373	92.42	7.6	1.009
	935.25	0.1599	6.013	22.288	91.05	6.6	0.980
	1103.07	0.1390	5.992	22.210	89.73	5.7	0.902
G-2	0.83	0.4964	20.084	71.107	109.75	65.6	—
pH=7.496	23.02	0.4160	20.004	70.822	109.06	54.8	22.489
	94.73	0.3338	19.922	70.531	104.43	43.9	7.429
	168.05	0.2617	19.850	70.276	99.72	34.2	6.648
	263.42	0.2049	19.793	70.075	95.58	26.7	4.169
	457.75	0.1126	19.701	69.748	92.33	14.6	3.515
	599.72	0.0721	19.660	69.605	87.07	9.3	2.166
	767.55	0.0454	19.633	69.510	84.76	5.9	1.225
	935.32	0.0345	19.623	69.472	83.25	4.5	0.507
	1103.13	0.0269	19.615	69.445	82.63	3.5	0.351
G-3	0.73	0.4951	11.064	72.088	109.75	66.4	—
pH=7.752	22.92	0.4206	10.990	71.602	109.00	56.0	20.776
	94.68	0.3120	10.881	70.895	104.70	41.1	9.938
	167.95	0.2622	10.831	70.570	98.48	34.4	4.596
	263.37	0.2054	10.774	70.200	95.62	26.8	4.161
	457.70	0.1328	10.702	69.727	92.36	17.2	2.729
	599.67	0.0946	10.664	69.478	88.22	12.2	2.010
	767.45	0.0654	10.634	69.288	86.05	8.4	1.324
	935.22	0.0474	10.616	69.171	84.39	6.1	0.827
	1103.03	0.0350	10.604	69.090	83.36	4.5	0.574
G-4	0.90	0.5231	48.444	128.728	109.75	125.3	—
pH=7.378	23.08	0.4226	48.343	128.461	109.41	100.9	28.032
	94.77	0.2676	48.188	128.049	104.81	63.7	14.591
	168.12	0.1547	48.075	127.749	95.93	36.7	11.127
	263.45	0.0804	48.001	127.551	89.47	19.1	5.903
	457.78	0.0237	47.944	127.401	85.23	5.6	2.296
	599.75	0.0131	47.934	127.373	82.00	3.1	0.587
	767.62	0.0089	47.930	127.361	81.40	2.1	0.201
	935.38	0.0084	47.929	127.360	81.16	2.0	0.022
	1103.20	0.0071	47.928	127.357	81.13	1.7	0.061
G-5	0.80	0.4679	35.001	232.382	109.75	202.3	—
pH=7.760	22.98	0.3291	34.862	231.461	107.44	141.6	40.771
	94.72	0.1792	34.712	230.466	99.47	76.9	14.876
	168.02	0.0906	34.624	229.877	90.89	38.7	9.103
	263.40	0.0374	34.570	229.524	85.83	16.0	4.354
	457.73	0.0109	34.544	229.348	82.79	4.6	1.081
	599.70	0.0067	34.540	229.320	81.28	2.9	0.232
	767.52	0.0051	34.538	229.309	81.05	2.2	0.079
	935.28	0.0042	34.537	229.303	80.95	1.8	0.042
	1103.10	0.0033	34.536	229.298	80.90	1.4	0.042
G-6	0.87	0.5028	83.739	416.588	109.75	389.9	—
pH=7.638	23.05	0.2687	83.505	415.423	109.41	207.5	71.350
	94.75	0.0944	83.330	414.556	96.00	72.8	18.312
	168.08	0.0290	83.265	414.231	86.02	22.4	7.007
	263.43	0.0087	83.245	414.130	82.29	6.7	1.702
	457.77	0.0033	83.239	414.103	81.12	2.5	0.220
	599.73	0.0022	83.238	414.098	80.82	1.7	0.059
	767.58	0.0019	83.238	414.096	80.76	1.5	0.017
	935.35	0.0014	83.237	414.094	80.74	1.1	0.021
	1103.17	0.0012	83.237	414.093	80.71	—	—

Table 3.2: Evolution of solution chemistry of growth experiments. [Fe(II)] measured via ICP-MS, the initial DIC determined from added $NaHCO_3$ powder, whereas the subsequent evolutions of DIC, [CO_3^{2-}], BET-surface area, and solution saturation are calculated via methods detailed in Supplementary information and Section. 3.3.2. Change in ionic strength due to siderite growth is $\lessapprox 1\%$. Growth rates between the designed [Fe(II)] and the first measurement are discarded.

$I = 0.175$ mol kg^{-1}; $T = 298.15$ K and 1 bar

Ex.No	Time h	[Fe(II)] mol kg^{-1} $\times 10^3$	[DIC] mol kg^{-1} $\times 10^3$	[CO_3^{2-}] mol kg^{-1} $\times 10^6$	Ω	Secondary growth rate mol m^{-2} s^{-1} $\times 10^{12}$
RP-1	1.03	0.1005	6.433	21.807	4.1	—
pH=7.478	23.27	0.1767	6.510	22.066	7.3	—
	95.00	0.1640	6.497	22.023	6.7	0.948
	168.18	0.1432	6.476	21.952	5.8	1.523
	263.63	0.1205	6.453	21.875	4.9	1.269
	457.97	0.0932	6.426	21.783	3.8	0.750
	600.03	0.0803	6.413	21.739	3.3	0.481
	767.87	0.0736	6.407	21.716	3.0	0.213
	935.47	0.0687	6.402	21.700	2.8	0.155
	1103.28	0.0629	6.396	21.680	2.5	0.185
RP-2	1.03	0.0484	20.075	71.073	6.4	—
pH=7.496	23.27	0.0729	20.099	71.160	9.7	—
	95.00	0.0543	20.081	71.094	7.2	1.391
	168.15	0.0405	20.067	71.045	5.4	1.005
	263.60	0.0324	20.059	71.016	4.3	0.454
	457.97	0.0233	20.050	70.984	3.1	0.249
	600.00	0.0205	20.047	70.974	2.7	0.107
	767.83	0.0179	20.044	70.965	2.4	0.081
	935.43	0.0162	20.043	70.959	2.1	0.055
	1103.25	0.0150	20.041	70.955	2.0	0.037
RP-3	1.03	0.0405	11.077	75.294	5.7	—
pH=7.770	23.27	0.0654	11.102	75.464	8.2	—
	95.00	0.0549	11.091	75.392	7.7	0.789
	168.20	0.0423	11.079	75.307	5.9	0.914
	263.65	0.0351	11.072	75.258	4.9	0.402
	457.97	0.0260	11.062	75.195	3.6	0.252
	600.05	0.0223	11.059	75.170	3.1	0.138
	767.88	0.0200	11.056	75.155	2.8	0.073
	935.48	0.0203	11.057	75.157	2.8	—
	1103.30	0.0167	11.053	75.133	2.3	0.114
RP-4	1.03	0.0370	48.310	123.733	8.5	—
pH=7.363	23.27	0.0458	48.319	123.755	10.5	—
	95.00	0.0263	48.299	123.705	6.1	1.453
	169.10	0.0188	48.292	123.686	4.3	0.542
	263.57	0.0140	48.287	123.674	3.2	0.273
	457.97	0.0100	48.283	123.664	2.3	0.109
	599.97	0.0085	48.281	123.660	2.0	0.056
	767.80	0.0075	48.280	123.657	1.7	0.033
	935.40	0.0069	48.280	123.656	1.6	0.020
	1103.22	0.0065	48.279	123.655	1.5	0.013
RP-5	1.03	0.0245	34.925	222.251	10.1	—
pH=7.742	23.27	0.0347	34.935	222.317	14.4	—
	95.00	0.0202	34.920	222.224	8.3	1.084
	168.17	0.0143	34.915	222.187	5.9	0.429
	263.62	0.0112	34.911	222.167	4.6	0.176
	457.97	0.0074	34.908	222.143	3.1	0.103
	600.02	0.0066	34.907	222.138	2.7	0.032
	767.85	0.0054	34.906	222.130	2.2	0.039
	935.45	0.0054	34.906	222.130	2.2	—
	1103.27	0.0046	34.905	222.125	1.9	0.026
RP-6	1.03	0.0241	83.476	399.761	17.9	—
pH=7.622	23.27	0.0236	83.475	399.759	17.6	0.108
	95.00	0.0107	83.462	399.697	7.9	0.966
	168.13	0.0070	83.459	399.679	5.2	0.269
	263.58	0.0052	83.457	399.671	3.9	0.101
	457.97	0.0038	83.455	399.664	2.8	0.039
	599.98	0.0035	83.455	399.662	2.6	0.012
	767.82	0.0031	83.455	399.660	2.3	0.013
	935.42	0.0031	83.455	399.661	2.3	—
	1103.23	0.0026	83.454	399.658	1.9	0.015

Table 3.3: Evolution of solution chemistry (first 46 d) of reprecipitation experiments. Secondary growth rates are normalised against BET-surface area of the seed material (109.75 m^2 g^{-1}). DIC and [CO_3^{2-}] are calculated as a function of siderite dissolution and precipitation (Supplementary information). Note that siderite dissolution kinetics are excluded from this table.

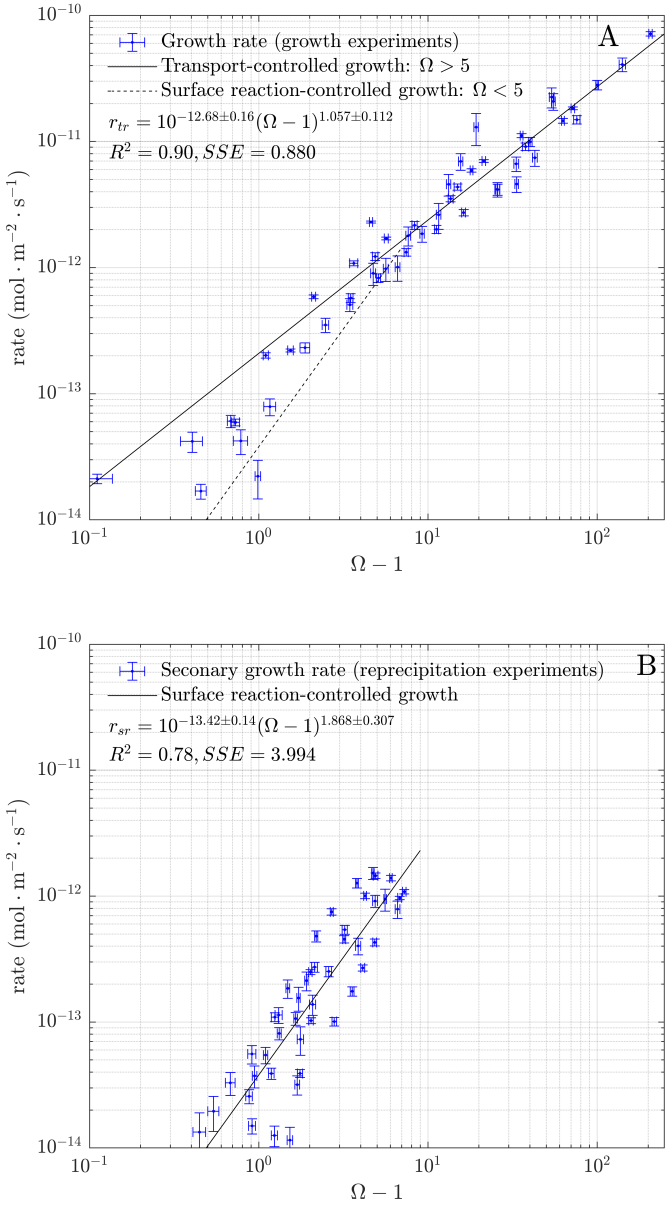


Figure 3.10: Kinetic data of (A) growth experiments and (B) secondary growth of reprecipitation experiments plotted against supersaturation with respect to siderite. The secondary growth rate (B) is in a good agreement with surface reaction-controlled kinetic behaviour: $r_{sr} \propto (\Omega - 1)^2$. By excluding the deviation at lower supersaturation ($\Omega < 5$; 16 data), the growth experiments (A) are consistent with a transport-controlled kinetic behaviour: $r_{tr} \propto (\Omega - 1)$. Error ($3\sigma$) propagation for growth and reprecipitation rate are calculated from $\sigma_{d[Fe^{2+}]}$, σ_Ω is based on $\sigma_{[Fe^{2+}]}$, assuming $\sigma_{[CO_3^{2-}]} = \sigma_{[Fe^{2+}]}$, and only considers the uncertainty in calculating Ω at the time of sampling.

growth region can not be established with confidence (i.e., 16 data at $\Omega \leq 5$ yield a $R^2 = 0.76$).

Given the theoretical derivation summarised above and the observations that the reprecipitation experiments were capped to a confined range of low supersaturation ($7 < \Omega < 18$; Table. 3.3), we reason that the secondary growth in reprecipitation experiments was controlled by surface reactions (r_{sr}; $n \approx 2$) instead of transport. This interpretation is supported by the fitted equation (Fig. 3.10B; 48 data):

$$r_{sr} = 10^{-13.42 \pm 0.14}(\Omega - 1)^{1.868 \pm 0.307} \ [\mathrm{mol\,m^{-2}\,s^{-1}}], \tag{3.4}$$

with 95 % confidence bounds, $R^2 = 0.78$, and $SSE = 3.994$. This kinetic-saturation correlation ($n = 1.868$) indicates that siderite growth at low supersaturation is likely dominated by spiral mechanism. A further differentiation among growth by adsorption, at defect sites, and by surface nucleation will require direct microscopic observation employing, for example, atomic force microscopy (Duckworth and Martin 2004; Saldi et al. 2009; Teng et al. 2000). The effect on DIC and Ω during nanocrystalline siderite dissolution is taken into account in the calculations; DIC increase due to dissolution was ≤ 1.2 % (Table. 3.3).

If the kinetic behaviour from the growth experiments at low supersaturation was surface reaction-controlled, by excluding them from fitting (e.g., $\Omega \lesssim 5$; Fig. 3.10A), a correlation can be obtained that is consistent with a transport-controlled growth rate (r_{tr}; 37 data):

$$r_{tr} = 10^{-12.68 \pm 0.16}(\Omega - 1)^{1.057 \pm 0.112} \ [\mathrm{mol\,m^{-2}\,s^{-1}}], \tag{3.5}$$

with 95 % confidence bounds, $R^2 = 0.90$, and $SSE = 0.880$. It is important to note that the choice of the cut-off saturation level $\Omega = 5$ is specific to the conditions (temperature, pressure, and ionic strength) and the nature of the siderite seed used in this study.

Transport-controlled kinetic behaviour is subject to the thickness of the diffusive layer, which itself can be a function of fluid dynamics (e.g., stirring speed). Effect of fluid dynamics on transport-controlled kinetic behaviour has been discussed in detail by Mullin (1972), Nielsen (1964, 1984), PLUMMER et al. (1979) and Watkins et al. (2017). Nielsen (1964, 1984) and Nielsen and Toft (1984) argued that for crystals smaller than $\approx$ 5 µm (siderite seeds in this study are predominantly $\approx$ 2 µm spherical particles; Section. 3.3.2), the thickness of the diffusive layer is apparently independent of stirring speed; such small particles are carried with the solution and they sediment so slowly that the liquid flow over their surface is too weak to influence diffusion rate. The stirring speed was not examined as a variable here, but experiments were gently agitated twice a day. We, therefore, predict the observed growth rates have little to no dependence on stirring speed.

3.4.3 Comparison with previous siderite kinetic studies

A number of studies have conducted siderite precipitation experiments at surface temperature, with the purpose of deriving siderite solubility (Greenberg and Tomson 1992; Jensen et al. 2002; Singer and Stumm 1970), constraining isotopic fractionation (Dijk et al. 2018; Jimenez-Lopez and Romanek 2004; Wiesli et al. 2004), understanding trace metal incorporation (Romanek et al. 2009), and the recent efforts in characterising the amorphous Fe(II)-carbonate precursor (AFC) and its subsequent mineralisation pathways (Azoulay et al. 2012; Dideriksen et al. 2015; Jiang and Tosca 2019; Montes-Hernandez and Renard 2016; Sel et al. 2012). To our knowledge, only Jimenez-Lopez and Romanek (2004) provided the necessary constraints on experimental conditions for a direct comparison of growth kinetics at 25 °C. Jimenez-Lopez and Romanek (2004) conducted two sets of experiments, (1) closed-system/free-drifting syntheses and (2) controlled-chemistry experiments where a constant chemical condition was maintained by an autotitrator. They reported multiple metastable precursor phases in their harvested solids, and as the import-

ant roles of AFC and chukanovite were not known at the time, they chose to report only the precipitation rate of samples that contained > 50 % siderite (determined by XRD). The mixture of multiple phases may have led to the scattering of kinetic data when plotted against supersaturation with respect to pure siderite. This can be demonstrated by refitting their results with the speciation scheme used in this study (Fig. 3.11). Importantly, our kinetic data are 2 orders of magnitude lower than those reported by Jimenez-Lopez and Romanek (2004) at a comparable supersaturation.

There are a number of factors behind this discrepancy. First, the reported mixtures of multiple phases indicate that the high supersaturation in Jimenez-Lopez and Romanek (2004) experiments might have surpassed and perhaps maintained above the critical supersaturation threshold for homogeneous AFC nucleation (Fig. 3.2; Jiang and Tosca 2019). If so, two or more mineralisation processes may have withdrawn solution [Fe(II)], from which the precipitation rate was calculated by Jimenez-Lopez and Romanek (2004). Secondly, the siderite seed used in their study were crystalline siderite with a BET-surface area of ≤ 1.86 $m^2\,g^{-1}$ (where rates were calculated), compared to the 109.75 $m^2\,g^{-1}$ of the synthetic seeds used in this study. Aside from the difference in the surface area, the surface activation energy between crystalline and nanocrystalline siderite seeds are no doubt different. Unfortunately, there is insufficient information to conduct a numerical comparison between the surface activation energy of the siderite seed between this investigation and theirs.

Siderite precipitation kinetics has been a core interest of corrosion sciences, particularly concerning the corrosion of mild steel in carbonated media (e.g., Barker et al. 2018; Burkle et al. 2017; Johnson and Tomson 1991; Ma et al. 2018; Saheb et al. 2008, 2010; Sk et al. 2017; Sun and Nešić 2008). Though focused on elevated temperature, multiple studies reported transport-controlled kinetic behaviour across a wide range of physico-chemical conditions (Ma et al. 2018; Sk et al. 2017; Sun and Nešić 2008). For example, Ma et al. (2018) carefully conducted a series of siderite precipitation experiments at a temperature

range of 50–80 °C, in which the growth of siderite was measured as weight-gain on an electrochemical quartz crystal micro-balance coated with either ≈ 1 µm of iron or ≈ 0.5 µm of gold. The *in-situ* micro-balance allowed real-time recording of solid mass on the coated quartz plate, enabled Ma et al. (2018) to differentiate between the initial surface nucleation of Fe(II)-carbonate on the coated plate and the continued growth of the nuclei. They fitted the growth rate to a temperature- and surface activation energy-dependent kinetic model originally proposed by Johnson and Tomson (1991) and modified by Sun and Nešić (2008):

$$r = k_r e^{-\frac{\Delta G_a}{RT}} K_{sp,T,I}(\Omega - 1)\ [\mathrm{mol\,m^{-2}\,s^{-1}}], \tag{3.6}$$

where k_r is kinetic constant: 3.32×10^7 $\mathrm{m^4\ mol^{-1}\,s^{-1}}$, ΔG_a is surface activation energy for growth on siderite nuclei: 73739 $\mathrm{J\,mol^{-1}}$, R is the gas constant 8.314 $\mathrm{J\,mol^{-1}\,K^{-1}}$. In the Ma et al. (2018) model, solution saturation (Ω) with respect to siderite is calculated as the product of concentrations instead of activities, and the effects of temperature (T; in K) and stoichiometric ionic strength (I) are taken into account in the solubility product $K_{sp,T,I}$ in the following empirical equation summarised by Sun et al. (2009):

$$\log K_{sp,T,I} = -59.3498 - 0.041377T - \frac{2.196.}{T} + 24.5724 \log T + 2.518\sqrt{I} - 0.657I. \tag{3.7}$$

It should be noted that the temperature-dependent terms in Eq. 3.7 are based on the relationship proposed by Greenberg and Tomson (1992, and Eq. 2 therein), and the stoichiometric ionic strength-dependent terms are taken from Silva et al. (2002), with the constant in Eq. 3.7 modified to fit with the average of selected siderite solubility values. The average solubility value concluded by Sun et al. (2009) is identical to the crystalline siderite solubil-

ity proposed by Nordstrom et al. (1990): $\log K_{sp,T,I}$=-10.89 at 298.15 K and I=0 mol kg^{-1}. This value, in fact, was based on the dissolution experiments conducted by Smith (1918), refitted with a speciation scheme that included $FeHCO^{3+}$, $FeCO_3(aq)$, and $FeOH^+$ (Nordstrom et al. 1990). The apparent concordance reached between Greenberg and Tomson (1992) and Nordstrom et al. (1990) can be partially attributed to the adaptation of speciation scheme and equilibrium constants from the latter by the former. In fact, Nordstrom et al. (1990) also proposed $\log K_{sp}$=-10.45 for precipitated siderite solubility, refitted from the work by Singer and Stumm (1970); a more suitable value for siderite precipitation experiments but nevertheless not used. We, therefore, reason that the difference between siderite solubility calculated from Eq. 3.7 and the value adopted in this study is largely an artefact between calculation schemes instead of a matter of accuracy.

Because this study considers the effect of stoichiometric ionic strength in the calculation of solution saturation and adopts a basic speciation scheme (no Fe(II)-compound; Supplementary information. 3.6.1), we may implement the temperature dependence proposed by Greenberg and Tomson (1992), and modify the constant to yield a $\log K_{sp}$=-10.24 at 298.15 K:

$$\log K_{sp,T} = -58.6989 - 0.041377T - \frac{2.196.}{T} + 24.5724 \log T.$$

In so doing, the kinetic model by Ma et al. (2018) (Eq. 3.6) and Sun and Nešić (2008) can be extrapolated to 298.15 K for comparison (Fig. 3.11). Note that a different temperature dependence has been proposed by Bénézeth et al. (2009) for temperature range of 25–250 °C, but the difference in the temperature range of 25–80 °C from that of Greenberg and Tomson (1992) is minor.

The similarity between our kinetic data and that extrapolated from Ma et al. (2018) and Sun and Nešić (2008) does not extend beyond the transport-controlled growth kinetic behaviour (linear correlation with supersaturation); our results are more than 2 orders of magnitude higher than the extrapolated

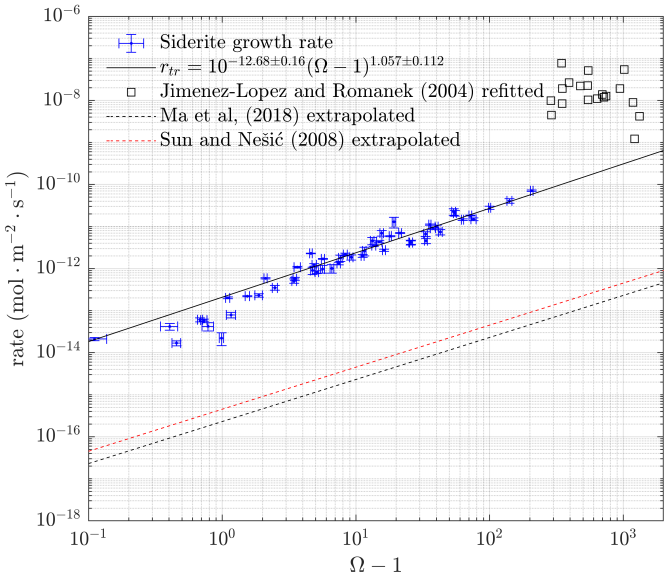


Figure 3.11: Comparison of siderite growth rates with previous kinetic studies. Jimenez-Lopez and Romanek (2004) experimental results at 25 °C are refitted with the speciation scheme used in this study (squares), ionic strength correction is calculated based on their measured [Fe^{2+}], pH, and alkalinity. Ma et al. (2018) and Sun and Nešić (2008) used same kinetic model based on high-temperature experiments, and are both extrapolated to 25 °C using the temperature corrections provided in their models (dashed lines).

constraints (Fig. 3.11). This exercise underscores the need for more thermodynamic and kinetic data between 25 °C and 80 °C. For example, Stefánsson et al. (2013) demonstrated the importance of $NaCO_3^-(aq)$ and $NaHCO_3(aq)$ complexes in carbonate speciation at elevated temperature. Not including these carbonate species in high-temperature experiments might have led to overestimations of solution saturation with respect to siderite, thus, potentially contributing to underestimations of kinetic behaviour when extrapolated to 25 °C.

3.4.4 Comparison with Ca- and Mg-carbonate growth

To compare siderite growth kinetics with the well-documented process of calcite precipitation, calcite growth kinetics are refitted from a comprehensive investigation by Busenberg and Plummer (1986, and Table. 10 therein) at 25

°C in solutions stirred at 260 revolutions per minute (RPM). Busenberg and Plummer (1986) recognised two distinct precipitation regions of calcite (*cal*): (1) near-equilibrium, where growth rate is very low and (2) from Ω_{cal}=1.45 and higher, where growth rate is proportional to the activity product of dissolved species (Fig. 3.12A; a similar conclusion was reached in a review by Shiraki and Brantley 1995).

In inhibitor-free aqueous conditions at surface temperature and pressure, the growth rate of siderite is nearly 7-orders of magnitude slower than that of calcite at their respective supersaturation (Fig. 3.12B). If extrapolated from the observed transport-controlled kinetic behaviour (Eq. 3.5), for siderite to achieve a comparable growth rate with that of calcite near-equilibrium, Ω_{sid} needs to exceed 10^5 (Fig. 3.12B). Such a supersaturated condition is unrealistic in a natural system, as it is far above the critical supersaturation for homogeneous nucleation of precursor AFC phase ($\Omega_{sid} \approx 600$; Jiang and Tosca 2019); pervasive and rapid nucleation of AFC acts as a ceiling for the maximum solution saturation in a natural system.

The significant difference in calcite and siderite growth kinetics has been attributed to the difference in the average surface charge density of Fe^{2+} versus Ca^{2+} (Jimenez-Lopez and Romanek 2004). Due to the smaller ionic radius of Fe^{2+} (0.078 nm) than that of Ca^{2+} (0.1 nm; ionic radii taken from Marcus 1988), a higher activation energy is required to dehydrate the more densely charged Fe^{2+} ion on the crystal surface to form siderite—which can also be conceptualised as a lower dehydration frequency (e.g., Nielsen 1984) or a lower exchange rate of the solvation shell (e.g., Pokrovsky and Schott 2002) associated with smaller cations.

If cation charge density is the main contributor behind the slower growth rate of siderite compared to calcite, one may speculate an even slower growth rate of magnesite ($MgCO_3$) due to the even lower dehydration frequency of Mg^{2+} (0.072 nm) (Nielsen 1984; Pokrovsky and Schott 2002). Indeed, it has long been hypothesised that high dehydration energy for Mg^{2+} prohib-

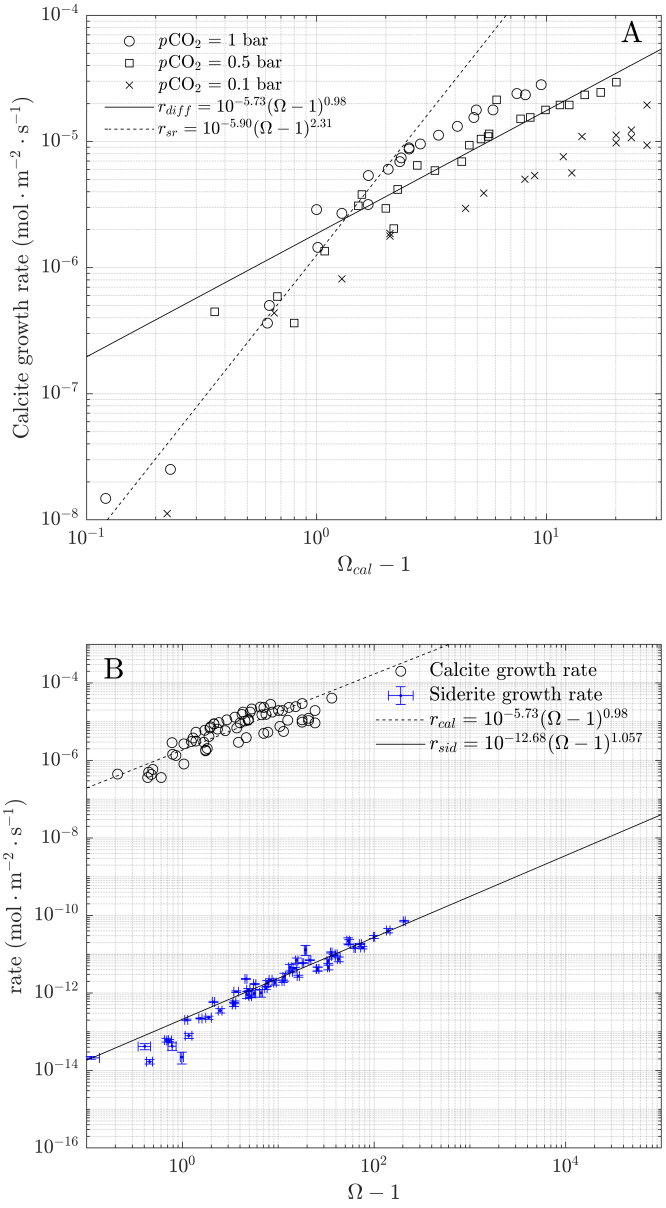


Figure 3.12: Comparison of growth kinetics between siderite and calcite. (A) Calcite growth kinetics under different pCO_2 levels at 25 °C, recalculated from measurements by Busenberg and Plummer (1986). Though the absolute kinetic behaviours of calcite growth are different under different pCO_2 conditions, two precipitation regions can be identified: a linear correlation with supersaturation at $\Omega_{cal} \gtrsim 2$, but a higher-order correlation near-equilibrium. Exemplary fitted-lines of two separate precipitation regions are plotted for kinetic behaviour under $pCO_2 = 0.5$ bar. Calcite solubility $\log K_{sp,cal}$=-8.48 (Mucci 1983). (B) Siderite growth rate compared to that of calcite (r_{cal}) (Busenberg and Plummer 1986) at their respective supersaturations.

its the formation of magnesite at surface conditions (e.g., Christ and Hostetler 1970; Kowacz et al. 2007; Sayles and Fyfe 1973). Instead, low-temperature Mg-carbonate precipitation involves the formation of metastable nesquehonite ($MgCO_3{\cdot}3H_2O$) and hydromagnesite ($Mg_5(CO_3)_4(OH)_2{\cdot}4H_2O$).

Abiotic magnesite growth kinetics have only been documented from high-temperature experiments, and the most complete data set to date (e.g., Saldi 2009; Saldi et al. 2009) indicates the growth behaviour of magnesite is controlled by extremely slow surface reactions that involve the desolvation of Mg^{2+} for Ω_{mag} up to 100 in a temperature range of 80–200 °C. Saldi et al. (2009) presented an experimental investigation employing a self-constructed hydrothermal atomic force microscope, which allowed direct measurements of the microscopic propagation velocity of the 2.7 Å-high monomolecular steps on magnesite crystal surface, as well as the frequencies of new steps generation, both as functions of supersaturation. Their diligent examination demonstrated that at elevated temperature (1) step propagation velocity is linearly proportional to supersaturation ($n = 1$) and (2) step generation show a parabolic correlation with supersaturation that is consistent with spiral growth at screw dislocation ($n = 2$). Based on their estimation of activation energies as a function of temperature, Saldi et al. (2009) concluded that spiral growth mechanism for magnesite is prohibited by the much slower step propagation velocity at 25 °C. As such, despite the importance of magnesite growth kinetics, a comparison with siderite growth can not be achieved through temperature extrapolation alone.

3.5 Conclusion

Experimentation on siderite crystal growth at 25 °C yields important constraints on growth kinetics as a function of solution saturation; analogous to calcite growth mechanisms but orders of magnitude slower at comparable saturation. The observed kinetic behaviour of siderite growth is best explained

by a chemical affinity-based kinetic model, which predicts a linear correlation with supersaturation ($\Omega - 1$) for growth controlled by transport of dissolved species from the parent solution to the surface fluid (Eq. 3.5), and a parabolic for growth controlled by spiral mechanism-dominated surface reactions (Eq. 3.4). Though the differentiation between these two kinetic behaviours with respect to supersaturation is likely sample- and condition-specific, it lays the foundation for further theoretical and experimental exploration on the kinetic isotope fractionation and trace element incorporation during the precipitation of Fe(II)-carbonate; especially in light of the growing understanding of the thermodynamic properties and mineralisation pathways of this group of carbonates.

The slow kinetics of siderite growth explains the commonly reported siderite supersaturation in anoxic water bodies that are either (1) lacking a suitable surface for heterogeneous siderite precipitation, or (2) open-systems with influxes of Fe(II). In the absence of a suitable surface, siderite precipitates via homogeneous nucleation of the precursor phase amorphous Fe(II)-carbonate, where solution saturation has to surpass a critical threshold that is significantly higher than siderite equilibrium solubility (Fig. 3.2; Jiang and Tosca 2019). Because the near-equilibrium growth rate of siderite is extremely slow, any Fe(II) influxes (e.g., microbial Fe(III) reduction, hydrothermal activity, or dissolution of other Fe(II)-minerals) would outpace the slow growth of siderite and lead to the accumulation of Fe^{2+} in the solution, which in turn, increases the solution saturation. This is expected to continue until solution saturation builds to support an appreciable growth/nucleation rate (at high Ω) that balances the Fe(II) influx. In this light, siderite precipitation may be more dynamic and episodic than previously understood, potentially involving multiple mineralisation pathways if nucleation barriers are crossed. This knowledge has important implications for engineering efforts in wetland management, steel corrosion, carbon capture and storage, and long-term nuclear waste storage plan.

Further experimentation is, of course, pivotal in filling the knowledge gap between low- and high-temperature precipitation kinetics and differentiating different surface reaction mechanisms. A complete kinetic framework for Fe(II)-carbonate precipitation holds the key to the genesis of the siderite-rich sedimentary rocks that are fundamental to our understanding of the biogeochemical evolution in the distant past (e.g., Beukes and Gutzmer 2008; Jiang and Tosca 2019; Raiswell et al. 2011; Rasmussen and Muhling 2018; Tosca et al. 2019). More importantly, such knowledge will make a crucial contribution to the Mars 2020 Mission, where the rover will land at Jezero Crater—the only regionally expansive Fe(II)-Mg-carbonate deposit on Mars (Bridges et al. 2019; Wray et al. 2016)—and study these sedimentary formations *in-situ*. Our interpretations of the mineralogical observations from more than 54 million kilometres away, however, will be hindered by the lack of kinetic constraints.

Acknowledgement

The authors thank Chris Romanek and two anonymous reviewers for their thoughtful and constructive comments, and Chen Zhu and Jeffrey G. Catalano for editorial handling. The authors acknowledge funding support from NERC (NE/M013014/1) and the Leverhulme Trust (PLP-2015-286) to NJT. The authors thank Phil Holdship (Earth Sciences, University of Oxford) for conducting ICP-MS analysis, Robert Jacobs (Chemistry, University of Oxford) for performing BET-surface area analysis, Katherine Clayton (Earth Sciences) for directing XRD analysis, and Jon Wade (Earth Sciences) for assistance with SEM characterisation. CZJ would like to extend appreciation towards Ben Tutolo (Earth Sciences, University of Calgary), Ritwika Sengupta, Sascha Holland, and Raphael Pietzsch for in-depth discussions, and to express gratitude towards Sam B. Cornish, Tomas Jonathan, and Helene Asbjørnsen for substantial assistance in Matlab coding and data processing.

3.6 Supplementary information

3.6.1 Thermodynamic calculations

Solution saturation is conventionally expressed as saturation state (Ω) with respect to a mineral phase in the following form:

$$\Omega = \frac{IAP}{K_{sp}},$$

where K_{sp} is the solubility product of the mineral phase and IAP is the ionic activity product of the corresponding dissolved ions in the solution. If $\Omega > 1$, mineral precipitation is predicted, otherwise, dissolution.

Siderite dissolution reaction may be written as follows:

$$\mathrm{FeCO_3} \overset{K_{sp}}{\rightleftharpoons} \mathrm{Fe^{2+}} + \mathrm{CO_3^{2-}},$$

and the IAP of this reaction takes the following form (assuming water activity of unity and pure mineral phase):

$$IAP = a_{\mathrm{Fe^{2+}}} a_{\mathrm{CO_3^{2-}}},$$

where a_i is the thermodynamic activity of the ith dissolved species, and can be estimated as a product of its molar concentration (C_i) and its activity coefficient (γ_i) in a given solution chemistry:

$$a_i = \gamma_i C_i.$$

Approximation of single-ion activity coefficients in a complex, multi-electrolyte solution is still intensely debated. The most widely adopted approximation is often one derivative or another of the Debye-Hückel equation (Debye and Hückel 1923). This study adopts the $\dot{B}$ equation, formulated within the framework of the Helgeson-Kirkham-Flowers model (Helgeson and Kirkham 1974b; Helgeson et al. 1981; Helgeson 1969; Shock et al. 1992; Tanger and Helgeson

$I = 0.175$ mol kg^{-1}; $T = 298.15$ K and 1 bar		
Species	$\mathring{a}$ ($\times 10^{-10}$ m)	γ
H^+	9	0.818
Fe^{2+}	6	0.350
CO_3^{2-}	4.5	0.306
HCO_3^-	4.5	0.753
OH^-	3.5	0.732
$CO_2(aq)$	4	1.017
Constants	Values	Sources
A (kg$^{1/2}$·mol$^{-1/2}$)	0.5039	
B (kg$^{1/2}$·mol$^{-1/2}$·m^{-1})	3.2716×10^{9}	Helgeson and Kirkham (1974b)
$\dot{B}$	0.041	
K_0 (mol kg^{-1}·bar^{-1})	3.3×10^{-2}	Sander (2015)
$\log K_1$	−6.1486	Eq. 3.10
$\log K_2$	−9.8349	Eq. 3.11
$\log K_{sp}$	−10.24	Singer and Stumm (1970)

Table 3.4: Thermodynamic properties and constants for activity coefficient calculation. Ion size parameter $\mathring{a}$ of dissolved species taken from Kielland (1937). Single-ion activity coefficients calculated through $\dot{B}$ equation (Eq. 3.8).

1944 1988):

$$\log \gamma_i = -\frac{Az_i^2\sqrt{\overline{I}}}{1 + B\mathring{a}_i\sqrt{\overline{I}}} + \dot{B}\overline{I}, \tag{3.8}$$

1945 where A and B are the mol kg^{-1} Debye-Hückel coefficients, z_i is the valency
1946 of the ith ion, $\mathring{a}_i$ is the ion size parameter describing the mean distance of
1947 the closest approach of the ith ion, $\dot{B}$ is a temperature-dependent fitting para-
1948 meter, and $\overline{I}$ is the true ionic strength that describes the electrostatic force an
1949 ion experiences from surrounding charged species (all parameters are listed in
1950 Table. 3.4). The true ionic strength ($\overline{I}$) differs from the more widely used stoi-
1951 chiometric ionic strength (I) by taking into account the formation of aqueous
1952 compounds/complexes. In other words, at conditions where ion association
1953 is significant, the true ionic strength of a solution may be significantly lower
1954 than the stoichiometric ionic strength. The stoichiometric ionic strength of
1955 all experiments are fixed at 0.175 mol kg^{-1} (including $I_{\mathrm{MOPS}} = 0.04$ mol kg^{-1};
1956 Buffer Calculator: http://www.liv.ac.uk/buffers).

1957 At the conditions and solution concentrations investigated here, the num-
1958 ber of Fe(II)-bearing complexes and their abundance are intensely debated
1959 and often poorly constrained. For example, many studies include soluble
1960 $FeCO_3(aq)$ and $FeHCO_3^+(aq)$ species in their calculations of siderite solubil-
1961 ity (e.g., Greenberg and Tomson 1992; Jensen et al. 2002; Ptacek 1992; Silva
1962 et al. 2002). Some studies included a number of additional complexes (e.g.,

$FeOH^+$, $Fe(OH)_2(aq)$, $Fe(OH)_3^-$, $Fe(CO_3)_2^{2-}(aq)$, etc.), but others questioned whether any of these complexes exist at all (e.g., see review by Fosbøl et al. 2010 and experimental examination by Singer and Stumm 1970). The differences in the employed speciation schemes contribute to a wide range of reported values of siderite solubility, from $\log K_{sp}$=-10.24 (Singer and Stumm 1970) to -11.06 (Ptacek 1992) (Table. 3.5). It is, therefore, important to specify the use of speciation schemes in any discussion and comparison regarding solution saturation and reaction kinetics.

It is worth noting that $NaCO_3^-(aq)$ and $NaHCO_3(aq)$ complexes may become important when extrapolating the kinetic-saturation relationship presented here to elevated temperatures. For example, Stefánsson et al. (2013) experimentally investigated carbonic acid ionisation/dissociation in dilute hydrothermal solutions up to 200 °C. By fitting their measurements on the dissociation constants of carbonic acid to an extended van't Hoff expression (Stefánsson et al. 2013, and Table. 2 & 3 therein), Stefánsson et al. (2013) concluded $NaCO_3^-(aq)$ is important at temperature $\geq$ 80 °and $NaHCO_3(aq)$ when $\geq$ 100 °C.

For maintaining the internal consistency of calculations, and ensuring the kinetic-saturation relations presented here are not dependent on assumptions regarding Fe(II)-speciation, this study adopts a basic speciation scheme with no soluble complex (complete dissociation) and the corresponding siderite solubility $\log K_{sp}$=-10.24 (Singer and Stumm 1970). By assuming complete dissociation, the true ionic strength equates to the stoichiometric ionic strength of the solution, which can be easily calculated as half the sum of the concentrations (C) times the square of valencies (z) of all dissolved species (Lewis and Randall 1921):

$$\overline{I} \approx I = \frac{1}{2} \sum C_i z_i^2.$$

$I = 0$ mol kg^{-1}, $T = 298.15$ K, and 1 bar, unless noted

$\log K_{sp}$	Method	Speciation scheme	Sources
-10.24	Precipitation		Singer and Stumm (1970)
-10.32[3]	Dissolution (wet)	$FeHCO^{3+}$, $FeCO_3(aq)$	Jensen et al. (2002)
-10.43[4]	Dissolution (wet)	$FeHCO^{3+}$, $FeCO_3(aq)$	Jensen et al. (2002)
-10.45[3]	Refitting Singer and Stumm (1970)	$FeHCO^{3+}$, $FeCO_3(aq)$, $FeOH^+$	Nordstrom et al. (1990)
-10.46[1,2]	Dissolution	$Fe(HCO_3)_2(aq)$	Smith (1918)
-10.50[1]	Refitting Smith (1918)	$Fe(HCO_3)_2(aq)$	Kelley and Anderson (1935)
-10.59[5]	Refitting Greenberg and Tomson (1992)	$FeCO_3(aq)$, $Fe(CO_3)_2^{2-}$	Preis and Gamsjäger (2002)
-10.68[3]	Dissolution (dry)	$FeHCO^{3+}$, $FeCO_3(aq)$	Jensen et al. (2002)
-10.68	Refitting Smith (1918)	$Fe(HCO_3)_2(aq)$	Kelley and Anderson (1935)
-10.77[3]	Precipitation	$FeHCO^{3+}$, $FeCO_3(aq)$, $FeOH^+$	Greenberg and Tomson (1992)
-10.80[5]	Dissolution	$FeCO_3(aq)$, $Fe(CO_3)_2^{2-}$	Bruno et al. (1992)
-10.89[3]	"Refitting Smith (1918)	$FeHCO^{3+}$, $FeCO_3(aq)$, $FeOH^+$	Nordstrom et al. (1990)
-11.03[4]	Dissolution (dry)	$FeHCO^{3+}$, $FeCO_3(aq)$	Jensen et al. (2002)
-11.06[3]	Dissolution	$FeHCO^{3+}$, $FeCO_3(aq)$, $FeOH^+$	Ptacek and Blowes (1993)

Table 3.5: A shortlist of reported values of siderite solubility product. Speciation scheme section indicates soluble Fe(II)-complex(s) in addition to the basic speciation scheme used in the calculation of solubility product. Note the equilibrium constants can vary significantly for the same Fe(II)-complex, the reader is referred to references provided in the source. (wet) and (dry) differentiate solubility experimentation using freshly precipitated (wet) versus matured crystalline (dry) siderite. [1]: calculated for temperature at 30 °C. [2]: no ionic strength control was applied to experiments. [3]: equilibrium constants for soluble Fe(II)-complexes from Nordstrom et al. (1990). [4]: equilibrium constants for soluble Fe(II)-complexes from Fouillac and Criaud (1984). [5]: equilibrium constants for soluble Fe(II)-complexes from Bruno et al. (1992). It is demonstrated here the disparity in $\log K_{sp}$ can be caused by the differences in the methods of achieving equilibrium, the natures (e.g., wet vs. dry) of materials used, the applied speciation schemes, and the equilibrium constants of Fe(II)-complexes for the same speciation scheme.

3.6.2 Carbonate speciation calculation

Carbonate speciation in the solution is estimated based on the initial dissolved inorganic carbon (DIC; the total amount of $NaHCO_3$ added; bracketed in Eq. 3.9), pH, and activity coefficients of all carbonate species (Table. 3.4). In a simplified form, the $CO_2(g)$ dissolution and dissociation reactions may be written as follows:

$$CO_2(g) \overset{K_0}{\rightleftharpoons} [CO_2(aq) + H_2O \overset{K_1}{\rightleftharpoons} HCO_3^- + H^+ \overset{K_2}{\rightleftharpoons} CO_3^{2-} + 2H^+], \tag{3.9}$$

where the equilibrium constants are equal to:

$$K_0 = \frac{a_{CO_2(aq)}}{pCO_2},$$

$$K_1 = \frac{a_{HCO_3^-} a_{H^+}}{a_{CO_2(aq)}},$$

$$K_2 = \frac{a_{CO_3^{2-}} a_{H^+}}{a_{HCO_3^-}},$$

and K_0 is the Henry's law constant of the solubility of $CO_2(g)$ ($0.033\,\mathrm{mol\,kg^{-1}{\cdot}bar^{-1}}$ at 298.15 K; Sander 2015); K_1 and K_2 are referred to as the 1st and 2nd dissociation constants of carbonic acid. The deviation of the dissociation constants from their values at $I = 0\,\mathrm{mol\,kg^{-1}}$ (K_1^0 and K_2^0) with increasing solution ionic strength can be estimated from the deviation in the activity coefficients of the carbonate species:

$$\log K_1 = \log K_1^0 - \log \frac{\gamma_{H^+}\gamma_{HCO_3^-}}{\gamma_{CO_2(aq)}}, \tag{3.10}$$

$$\log K_2 = \log K_2^0 - \log \frac{\gamma_{H^+}\gamma_{CO_3^{2-}}}{\gamma_{HCO_3^-}}, \tag{3.11}$$

and $\log K_1^0 = -6.3663$, $\log K_2^0 = -10.3135$, calculated from the Gibbs free energy of reactions in Eq. 3.9, with thermodynamic properties taken from CODATA database (Cox et al. 1989).

The $p\mathrm{CO}_2$ and $[\mathrm{CO}_3^{2-}]$ of each experiment can be subsequently calculated from solution pH and DIC via the following equations:

$$p\mathrm{CO}_2 = \frac{[\mathrm{H}^+]^2\mathrm{DIC}}{K_0[\mathrm{H}^+]^2 + K_0K_1[\mathrm{H}^+] + K_0K_1K_2},$$

$$[\mathrm{CO}_3^{2-}] = \frac{K_1K_2\mathrm{DIC}}{[\mathrm{H}^+]^2 + K_1[\mathrm{H}^+] + K_1K_2}, \tag{3.12}$$

or:

$$[\mathrm{CO}_3^{2-}] = \frac{p\mathrm{CO}_2K_0K_1K_2}{[\mathrm{H}^+]^2}.$$

Chapter 4

Kinetic isotope effect of carbon in siderite growth at 25 °C and 1 bar

4.1 Introduction

Iron formation represents a unique sedimentary expression of Earth system processes through Earth's early history. The role of microbial activity in influencing chemical sedimentation has become a central question in recent years. For example, isotopic studies on siderite associated with late Archaean banded iron formation ($\approx$ 2.5 Ga, Hamersley Basin, Australia, and Transvaal Craton, South Africa) mostly show δ^{56}Fe values of $\cong -0.5‰$ that indicate equilibrium with Late Archaean seawater (e.g., Heimann et al. 2010; Johnson et al. 2008b, 2013). However, some very negative δ^{56}Fe values in siderite, coupled with C isotope data, have been regarded as a support for an important role of dissimilatory iron reduction (DIR) in the genesis of iron formations (e.g., Heimann et al. 2010; Johnson et al. 2008b, 2013). As discussed in Jiang and Tosca (2019), δ^{13}C signals in these iron formation-siderite are facies-specific, and the texturally and petrographically syndepositional and/or early diagenetic siderite exhibits δ^{13}C fractionation range between 0 and -8 ‰ (Beukes

et al. 1990; Fischer et al. 2009; Heimann et al. 2010; Kaufman 1996). This δ^{13}C range of siderite can be interpreted in three ways: (1) precipitation from hydrothermal-seawater mixing fluid with a mixed isotopic composition between the mantle and seawater, (2) vital isotope effect including dissimilatory iron reduction, and (3) kinetic isotope fractionation associated with abiotic precipitation. However, available experimental data are too sparse to evaluate or differentiate among these processes.

To the authors' knowledge, only one experimental study conducted by Jimenez-Lopez and Romanek (2004) provide some information on C isotope fractionation and siderite precipitation rate; they reported permil fractionation for siderite precipitation from DIC solution $10^3 \ln \alpha_{sid-\mathrm{DIC}} = +1.5$ ‰. This permil fractionation value deserves a closer examination. As discussed in Jiang and Tosca (2020), precipitation processes examined by Jimenez-Lopez and Romanek (2004) likely reflected multiple metastable phases that potentially resulted from homogeneous nucleation of a precursor phase in the sustained high solution saturation in their experiments. Mineral precipitation encompasses both nucleation and crystal growth, but they are mechanistically different in the microscopic processes and associated isotopic discrimination. Therefore, the applicability of the C fractionation constraints reported by Jimenez-Lopez and Romanek (2004) is unclear without a more detailed understanding.

The difference between C isotope fractionation by nucleation versus crystal growth can be examined from a theoretical point of view. Chemical reactions during crystal growth prefer the incorporation of the lighter isotope (DePaolo 2011; Nielsen et al. 2012; Watkins et al. 2017). In the classical theoretical treatment of nucleation, especially in the homogenous nucleation of a precursor phase, the assembly of small aggregates (nuclei) is triggered by thermal fluctuations in the bulk solution (Lasaga 1998b; Van Cappellen 1991, and references therein). C isotope fractionation in the assembly of nuclei is uncertain, though one may argue that the heavier isotope has the advantage of being less

reactive (due to its higher fractional mass), thus, aids the nucleus in reaching a stable critical size (positive fractionation). More importantly, during the crystallisation of the precursor amorphous Fe(II)-carbonate phase into siderite seeds (as observed in Jiang and Tosca 2020), ^{13}C is likely to be retained in the seed material, leading to a positive fractionation in the nucleated stable phase; differ from the negative fractionation often associated with growth mechanisms.

Delineation of the kinetics and mechanisms behind siderite growth (Jiang and Tosca 2020) lays the foundation for a theoretical exploration on isotope fractionation as a function of growth rate. This chapter derives a kinetic fractionation model of C isotopes that explains observed δ^{13}C values in the precipitated siderite from the growth experiments (Jiang and Tosca 2020).

4.2 Theoretical treatment

4.2.1 Microscopic processes at mineral-water interface

Isotope fractionation is a physical phenomenon caused by the difference in the masses among the different isotopes. Such a phenomenon is specific to the microscopic physical processes at the mineral-water interface, which has been discussed in Jiang and Tosca (2020). Here we focus on isotope fractionation associated with transport-controlled versus surface reaction-controlled crystal growth (Fig. 4.1).

In surface reaction-controlled growth (left column), the fractionation factor of grown siderite from DIC solution ($\alpha_{sid-\mathrm{DIC}}$) is controlled principally by surface reaction (α_{sr}), which can be calculated from the isotopic ratio of the precipitated solid (in this case, siderite; $^{13}R_{sid}$) and that of the bulk solution ($^{13}R_{\mathrm{DIC}}$):

$$\alpha_{sid-\mathrm{DIC}} = \alpha_{sr} = \frac{^{13}R_{sid}}{^{13}R_{\mathrm{DIC}}}.$$

In transport-controlled growth (right column), the growth fractionation factor

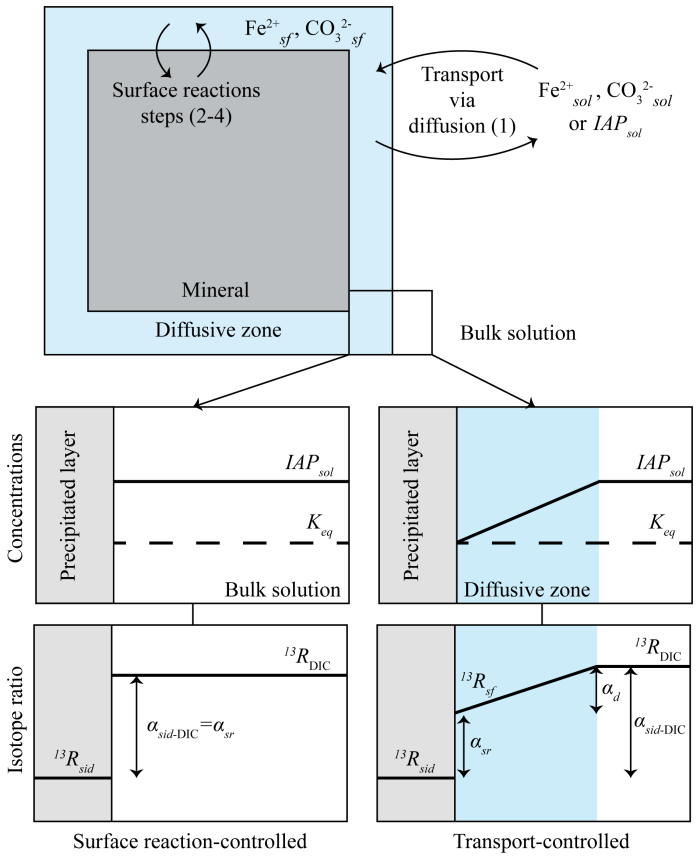


Figure 4.1: Illustration of microscopic processes at mineral-water interface with associated fractionation. Kinetic behaviour of crystal growth is categorised into surface reaction-controlled versus transport-controlled (Jiang and Tosca 2020). In surface reaction-controlled growth (left column), the growth fractionation factor from DIC solution ($\alpha_{sid-\mathrm{DIC}}$) is the ratio between the grown siderite ($^{13}R_{sid}$) and that of the bulk solution ($^{13}R_{\mathrm{DIC}}$). In transport-controlled growth (right column), $\alpha_{sid-\mathrm{DIC}}$ encompasses fractionation by diffusion (α_d) through the diffusive zone and fractionation by surface reaction (α_{sr}). $_{sf}$ denotes to surface fluid, $_{sol}$ denotes to bulk solution, the effects of fractionation processes are marked with arrowed line.

encompasses two isotope effects (Fig. 4.1): (1) fractionation by diffusion (α_d) between the bulk solution and the surface fluid ($_{sf}$):

$$\alpha_d = \frac{^{13}R_{sf}}{^{13}R_{\mathrm{DIC}}},$$

and (2) fractionation by surface reaction from the surface fluid:

$$\alpha_{sr} = \frac{^{13}R_{sid}}{^{13}R_{sf}}.$$

Thus, the growth fractionation factor is written as:

$$\alpha_{sid-\mathrm{DIC}} = \frac{\alpha_{sr}}{\alpha_d}.$$

Kinetic constraints from siderite growth experiments indicate the growth rate was dominantly transport-controlled (Jiang and Tosca 2020). Therefore, both α_d and α_{sr} need to be addressed in order to correlate the measured product fractionation with growth kinetics. Furthermore, the isotopic composition of the bulk solution each experienced independent Rayleigh distillation in closed-system siderite growth, which will be taken into account in a kinetic fractionation model present below.

4.2.2 Fractionation by diffusion: α_d

From a theoretical point of view, following the ideal gas law, the diffusion coefficient (D; $\mathrm{m^2\,s^{-1}}$) of molecule A through a medium composed of molecule B obeys the following relationship (e.g., Lasaga 1998a, p.318-329):

$$D_A = \frac{RT}{3\sqrt{2}\pi P N_A d^2}\sqrt{\frac{8RT}{\pi M_{A-B}}},$$

where R, T, P, N_A, and d stand for gas constant, temperature (K), pressure (bar), Avogadro number, and the molecular diameter, and M_{A-B} is the reduced

mass of A in medium B, expressed as (e.g., Mook 1986):

$$M_{A-B} = \frac{M_A M_B}{M_A + M_B}.$$

Therefore, the ratio of diffusion coefficients of the molecule A and its isotope A' in media B can be simplified into a function of the difference of their respective reduced masses (assuming the same molecular diameter):

$$\frac{D_A}{D_{A'}} = (\frac{M_A + M_B}{M_A M_B} \times \frac{M_{A'} M_B}{M_{A'} + M_B})^{\frac{1}{2}}. \tag{4.1}$$

This expression is the basis for the square-root-of-mass law, or as Graham's law of diffusion, which is only valid for systems in which the assumptions of kinetic theory (point masses and low pressure such that collisions are infrequent and intermolecular forces are negligible) are approximately valid (Lasaga 1998a; Watkins et al. 2017).

To illustrate a normal kinetic isotope effect under an ideal condition, we may take the diffusion of $CO_2(aq)$ in water as an example. The diffusion rate between $^{12}CO_2(aq)$ and $^{13}CO_2(aq)$ can be calculated as (assuming all ^{16}O in CO_2 and water):

$$\frac{D_{^{12}CO_2(aq)}}{D_{^{13}CO_2(aq)}} = (\frac{44.00 + 18.00}{44.00 \times 18.00} \times \frac{44.99 \times 18.00}{44.99 + 18.00})^{\frac{1}{2}} = 1.0032,$$

which indicates, in theory, the diffusion of $^{12}CO_2(aq)$ in water is about 3.2 ‰ faster than that of $^{13}CO_2(aq)$. However, it has been demonstrated that the measured isotopic diffusion coefficient ratio of a neutral molecule in condensed media (like water) is significantly lower the value calculated from Eq. 4.1; measured values are: e.g., 1.0007 (O'Leary 1984) and 1.00087 (Jähne et al. 1987). The primary reason behind such deviation is the network of non-negligible potential interactions between the diffusing $CO_2(aq)$ and the condensed water molecules; the complex interaction potential attenuates the normal kinetic isotope effect. Such attenuation is further pronounced among

charged molecules, that the formation of hydration shell around the charged molecule significantly increases the size of the diffusing package (e.g., CO_3^{2-} with 6 H_2O molecules), and reduces the fractional mass difference between the isotopically different packages. For example, through Eq. 4.1:

$$\frac{D_{^{12}CO_3^{2-}(H_2O)_6}}{D_{^{13}CO_3^{2-}(H_2O)_6}} = 1.0003,$$

which is considerably smaller than:

$$\frac{D_{^{12}CO_3^{2-}}}{D_{^{13}CO_3^{2-}}} = 1.0019.$$

For these considerations, Eq. 4.1 is customarily expressed as an inverse power-law (β) function of the ratio of their masses:

$$\frac{D_A}{D_{A'}} = (\frac{M_A + M_B}{M_A M_B} \times \frac{M_{A'} M_B}{M_{A'} + M_B})^{\beta}, \tag{4.2}$$

where β is best derived from experimentation or predicted from computer simulation. By employing molecular dynamic simulations (Mol-dy, version 3.6), Zeebe (2011) concluded β for CO_3^{2-} diffusion to be -0.04 to 0.17 at 25 °C among all variants of O isotopic compositions. Through Eq. 4.2, the isotopic diffusion coefficient ratio of $^{12}CO_3^{2-}$ to $^{13}CO_3^{2-}$ (without a hydration shell, thus, the most pronounced fractional mass difference) is between 0.9998 and 1.0006; $^{13}CO_3^{2-}$ diffuses only 0.2 ‰ faster or 0.6 ‰ slower with respect to $^{12}CO_3^{2-}$ (among all variants of O isotopic compositions).

Fractionation by diffusion (α_d) is also a function of the distance through which the dissolved species need to be transported (i.e., the thickness of the diffusive zone; Fig. 4.1). A comprehensive theoretical treatment on fractionation by diffusion during crystal growth has been provided by Watkins et al. (2017, Eq. 13–20 therein). In brief, Watkins et al. (2017) treated surface reaction-controlled growth rate (r_{sr}) as linearly dependent on the difference in the concentrations (C) of the dissolved species between the surface fluid ($_{sf}$)

and equilibrium ($_{eq}$) with a rate constant k:

$$r_{sr} = k(C_{sf} - C_{eq}),$$

In situation where growth rate is limited by the transport of dissolved species through a diffusive layer of thickness h (in m), r_{sr} must be equal to the flux from the bulk solution ($_{sol}$) to the surface fluid which follows the law of mass action:

$$k(C_{sf} - C_{eq}) = \frac{D}{h}(C_{sol} - C_{sf}),$$

where D is the diffusive coefficient ($m^2\,s^{-1}$)of the species or isotope of interest. Solving for C_{sf} and rearrange, an expression for growth rate (r) as a function h and D is as follows:

$$r = \frac{kD(C_{sol} - C_{eq})}{D + hk},$$

which can also be written in terms of an effective rate constant k_{eff}:

$$r = \frac{kD}{D + hk}(C_{sol} - C_{eq}) = k_{eff}(C_{sol} - C_{eq}) = k_{eff}K_{sp}(\Omega - 1).$$

At this stage, we may fit the effective rate constant with the transport-controlled rate constant from Eq. 3.5 (Chapter. 3):

$$k_{eff}K_{sp} = \frac{kDK_{sp}}{D + hk} = 10^{-12.68\pm0.16}. \tag{4.3}$$

Now, the key question is, which dissolved species was responsible for the diffusive zone observed in transport-controlled growth? Though lacking direct observations, the starting solution chemistry of [Fe(II)] $\approxeq$ 0.5 mmol kg^{-1} and DIC $\approxeq$ 6.4–83.8 mmol kg^{-1} in a pH range of 7.38–7.76 (Table. 3.1) suggest that Fe^{2+} was the primary cause of the transport-controlled growth kinetics; this is also supported by the small error range in the fitted $k_{eff}K_{sp}$ value from a wide range of DIC pools and/or solution saturation. Therefore, the thickness of Fe^{2+} diffusive zone calculated from Eq. 4.3 does not apply directly to C isotopes.

Though can not be quantified with available information, it is reasonable to expect that the diffusive zone concerning C isotopes in the growth experiments, if indeed existed at high solution saturation, was thin and probably negligible compared to that concerning Fe^{2+}. Otherwise, significant scattering would be expected in the $k_{eff}K_{sp}$ value due to the wide range of DIC pool.

Another consideration in the theoretical treatment presented above is that surface reaction-controlled siderite growth expresses a parabolic rate law (Eq. 3.4). It is uncertain how the theoretical treatment summarised by Watkins et al. (2017) shall be modified to appreciate the growth mechanism of siderite, as it has not been done so for the better-understood calcite growth mechanism.

The diffusion coefficient ratio calculation show sub-‰ difference between $^{13}CO_3^{2-}$ and $^{12}CO_3^{2-}$ and the thickness of the diffusive zone for DIC is unconstrained but expected to be small, for the purpose of this study, α_d is assumed to be 1 until better experimental results become available.

It is worth noting that, in addition to the fractional mass difference, an ion with a higher charge density (thus a higher dehydration energy) maintains a more rigid first hydration shell and potentially a secondary hydration shell, leading to further attenuated mass discrimination among its isotopes. For the interest of this study, Fe^{2+} and Mg^{2+} have smaller ionic radii (0.078 and 0.072 nm respectively) than that of Ca^{2+} (0.1 nm; Marcus 1988), and experimentally determined β for Mg isotope system is 0.0000 ± 0.0015 (Richter et al. 2006), for Fe isotope system is 0.0025 ± 0.0003 (Rodushkin et al. 2004), smaller than that of Ca isotope system 0.0045 ± 0.0005 (Richter et al. 2006). It is, therefore, expected that smaller kinetic isotope effects in the diffusion of Fe and Mg isotopes system than that of Ca, though an exact derivation is beyond the scope of this study.

4.2.3 Fractionation by surface reaction: α_{sr}

Kinetic behaviours of different isotopes in a chemical reaction can be expressed in a similar manner as the corresponding chemical reaction, but with

different forward (k_f) and backward (k_b) rate constants associated with different isotopes as a result of mass discrimination. The isotope-specific rates of forward reactions can be written as:

$$^{13}r_f = {}^{13}k_f a_{\mathrm{Fe}^{2+}{}_{sf}} a_{^{13}\mathrm{CO}_3^{2-}{}_{sf}},$$

$$^{12}r_f = {}^{12}k_f a_{\mathrm{Fe}^{2+}{}_{sf}} a_{^{12}\mathrm{CO}_3^{2-}{}_{sf}},$$

where $_{sf}$ denotes surface fluid, and the rates of backward reactions:

$$^{13}r_b = {}^{13}k_b a_{\mathrm{Fe}^{13}\mathrm{CO}_3},$$

$$^{12}r_b = {}^{12}k_b a_{\mathrm{Fe}^{12}\mathrm{CO}_3}.$$

It is generally observed that the rate of reaction involving the light isotope is greater than that involving the heavy isotope ($k_f^{12} > k_f^{13}$ and $k_b^{12} > k_b^{13}$).

Implicit in these expressions are the two kinetic fractionation factors associated with the forward and backward reactions:

$$^{13}\alpha_f = \frac{^{13}k_f}{^{12}k_f},$$

$$^{13}\alpha_b = \frac{^{13}k_b}{^{12}k_b},$$

and the fractionation factor at chemical equilibrium (eq) can be written as:

$$\alpha_{eq} = \frac{\alpha_f}{\alpha_b} = \frac{^{13}k_f}{^{12}k_f} / \frac{^{13}k_b}{^{12}k_b} = \frac{^{13}k_f}{^{13}k_b} / \frac{^{12}k_f}{^{12}k_b} = \frac{^{13}K_{eq}}{^{12}K_{eq}} = (\frac{^{13}R_{sid}}{^{13}R_{sf}})_{eq},$$

where $^{13/12}K_{eq}$ is the isotope-specific equilibrium constant, $^{13}R_{sid}$ is the isotopic ratio in the precipitated siderite, and $^{13}R_{sf}$ is the isotopic composition of the surface fluid.

In the diffusive zone, the transport of the heavier versus the lighter C isotopes is expected to result in a $^{13}R_{sf}$ that is slightly smaller than the bulk solution $^{13}R_{\mathrm{DIC}}$, but such effect is considered negligible in this study (see dis-

cussion in Section. 4.2.2). For simplicity, we allow:

$$^{13}R_{sf} \approxeq {}^{13}R_{\mathrm{DIC}}.$$

The isotope-specific forward and backward rates can now be related to fractionation factors:

$$^{13}r_f = \alpha_f {}^{13}R_{\mathrm{DIC}} {}^{12}k_f a_{\mathrm{Fe}^{2+}{}_{sol}} a_{{}^{12}\mathrm{CO}_3^{2-}{}_{sol}} = \alpha_f {}^{13}R_{\mathrm{DIC}} {}^{12}r_f, \tag{4.4}$$

and:

$$^{13}r_b = \alpha_b {}^{13}R_{sid} {}^{12}k_b a_{\mathrm{Fe}^{12}\mathrm{CO}_3} = \alpha_b {}^{13}R_{sid} {}^{12}r_b = \frac{\alpha_f}{\alpha_{eq}} {}^{13}R_{sid} {}^{12}r_b. \tag{4.5}$$

These equations are in the same forms as proposed by DePaolo (2011) for Ca isotope system during calcite precipitation.

To formulate a mathematical expression for the instantaneous fractionation by surface reaction (α_{sr}), a steady state equation (ss) can be imposed that at a given constant growth rate (r; $r = r_f - r_b$), α_{sr} remains constant, thus, the isotopic ratios in the growing solid remains constant:

$$\frac{d^{13}R_{sid}}{dt} = 0.$$

Because:

$$^{13}R_{sid} = \frac{^{13}\mathrm{C}_{sid}}{^{12}\mathrm{C}_{sid}},$$

the steady state condition can be expanded following the quotient rule:

$$\frac{d^{13}R_{sid}}{dt} = 0 = \frac{d(^{13}\mathrm{C}_{sid}/^{12}\mathrm{C}_{sid})}{dt} = \frac{1}{^{12}\mathrm{C}_{sid}}(\frac{d^{13}\mathrm{C}_{sid}}{dt} - {}^{13}R_{sid}\frac{d^{12}\mathrm{C}_{sid}}{dt}).$$

And because:

$$^{13}r = \frac{d^{13}\mathrm{C}_{sid}}{dt},$$

and:

$$^{12}r = \frac{d^{12}\mathrm{C}_{sid}}{dt},$$

we arrive at an isotope-specific, reaction rate-dependent steady state relation:

$$\frac{d^{13}R_{sid}}{dt} = 0 = \frac{1}{^{12}\mathrm{C}_{sid}}(^{13}r - {}^{13}R_{sid}{}^{12}r). \tag{4.6}$$

By substituting Eq. 4.4 and 4.5 into Eq. 4.6, and assuming no fractionation by diffusion ($\alpha_{sid-\mathrm{DIC}} \cong \alpha_{sr}$), the instantaneous fractionation of C isotopes in siderite growth can be cast as a function of growth rate (r), backward reaction rate (r_b), forward and equilibrium fractionation factors (α_f and α_{eq}):

$$\alpha_{sid-\mathrm{DIC}} \cong \alpha_{sr} = (\frac{^{13}R_{sid}}{^{13}R_{\mathrm{DIC}}})_{ss} = \frac{\alpha_f}{1 + \frac{r_b}{r+r_b}(\frac{\alpha_f}{\alpha_{eq}} - 1)}. \tag{4.7}$$

This equation is in the same form as the model proposed for Ca isotope in calcite growth by DePaolo (2011), and that $\alpha_{sid-\mathrm{DIC}}$ depends only on the reaction rates, regardless of the the form of kinetic expression, when $r \to 0$ (approaching chemical equilibrium), $\alpha_{sid-\mathrm{DIC}} \to \alpha_{eq}$ and isotopic equilibrium condition is recovered; transition from α_f to α_{eq} occurs where $r \approx r_b$ (DePaolo 2011). Implementation of this model is detailed in Section. 4.4.2.

4.3 Experimental and analytical method

Experimental method of siderite growth at 25 °C and 1 bar has been described in details in the previous contribution dedicated to delineate the growth kinetics as a function of solution saturation (Jiang and Tosca 2020). In brief, 6 closed-system seeded siderite growth experiments were carried out in $FeCl_2$–$NaHCO_3$ solutions under an strictly anoxic atmosphere over the course of 46 days, with the borosilicate reaction vessels wrapped in Al-film to prevent photo-oxidation. 10 solution samples (1 mL each) were extracted through an air-tight septum cap of each experiment over the duration 46 days, filtered through a 0.22 µm membrane and diluted in 4 % HNO_3 for elemental analyses (ICP-MS). Growth rate is calculated from the changes in solution Fe(II) concentrations between sampling intervals, which is assigned to the solution sat-

uration (Ω) at the time of sampling. After confirming the mineralogy (XRD), chemical composition (FT-IR), and morphology of the precipitate to be pure siderite, the BET-surface area normalised siderite growth rate (r) is delineated as a function of Ω:

$$r = 10^{-12.68}(\Omega - 1)^{1.057}\ [\mathrm{mol\,m^{-2}\,s^{-1}}], \tag{4.8}$$

with $R^2 = 0.90$ and sum of squared errors $SSE = 0.880$.

C isotope analyses were performed via a head-space equilibration method (modified from Assayag et al. 2006) on a Thermo Gasbench 2 device coupled to a Delta V Advantage isotope ratio mass spectrometry (IRMS) alongside Ivigtut BGS standard, NBS-18, and NBS-19. For solid sample analysis, 140–190 µg of seeds, solids harvested from growth experiments, as well as the $NaHCO_3$ stock powder were loaded in borosilicate exetainers and sealed with septum caps to be flushed with ultra-pure He gas. 0.05 mL of 100 % H_3PO_4 were syringe-injected into the exetainers to dissolve the solid samples into aqueous and gaseous CO_2. After a 24-hour $CO_2(aq)$–$CO_2(g)$ equilibration time, a portion of the head-space gas (He + $CO_2(g)$) was introduced into the IRMS to measure the C isotope ratio of the released $CO_2(g)$, from which the δ^{13}C was determined via a calibration procedure that includes the carbonate isotope fractionation associated with $CO_2(aq)$–$CO_2(g)$ partition (Assayag et al. 2006). Isotopic ratio of the head-space gas was calculated from 6 consecutive mass 45/44 and 46/44 voltage readings, and the standard deviations (1 σ) of samples were calculated from the deviation in the measurements of NOCZ in-house marble standard.

4.4 Results and discussion

4.4.1 Product isotopic composition of precipitated siderite

The measured C isotopic ratios of solid materials ($^{13}R_{solid}$) are treated with a mass-balance equation that considers the seed material ($^{13}R_{seed}$) and

the precipitated siderite ($^{13}R_{sid,exp}$) on the seeds:

$$^{13}R_{solid}M_{solid} = {}^{13}R_{seed}M_{seed} + {}^{13}R_{sid,exp}M_{sid,exp},$$

which can be rearranged to solve for $^{13}R_{sid,exp}$:

$$^{13}R_{sid,exp} = \frac{^{13}R_{solid}M_{solid} - {}^{13}R_{seed}M_{seed}}{M_{sid,exp}},$$

where $M_{sid,exp}$ is the mole of grown siderite that can be stoichiometrically calculated from the cumulative Fe(II) consumption, M_{solid} is the mole of the total solid material ($M_{solid} = M_{seed} + M_{sid}$; $M_{seed} = 4.316 \times 10^{-3}$ mol or $m_{seed} =$ 0.500 g). Thus, the product isotopic composition ($\delta^{13}\mathrm{C}_{sid,exp}$) of precipitated siderite can be calculated:

$$\delta^{13}\mathrm{C}_{sid,exp} = (\frac{^{13}R_{sid,exp}}{^{13}R_{\mathrm{VPDB}}} - 1) \times 1000\ [‰],$$

where $^{13}R_{\mathrm{VPDB}} = 0.0112372$ is the standard isotopic ratio of Vienna Pee Dee Belemnite. It is worth noting that the seed material prepared via homogeneous nucleation of AFC and recrystallised into siderite show a positive fractionation of $\delta^{13}\mathrm{C}_{sid,exp} = -0.760 \pm 0.077$ ‰ from a DIC solution with an initial composition of $\delta^{13}\mathrm{C}_{\mathrm{DIC}}(0) = -2.895 \pm 0.013$ ‰; in contrast the all the growth experiments show negative $\delta^{13}\mathrm{C}_{sid,exp}$ ranging from -4.359 ± 0.103 to -12.674 ± 0.264 ‰ (Table. 4.1).

An apparent correlation can be identified between the initial solution saturation ($\Omega(0)$) and the product isotopic composition in the precipitated siderite: a higher initial solution saturation—thus a higher initial growth rate ($r(0)$)—corresponds to a more negative product $\delta^{13}\mathrm{C}_{sid,exp}$ value (Fig. 4.2). This apparent correlation is limited in its application, as the observed fractionation is derived from specific closed-systems, where the solution in each experiment underwent Rayleigh distillation to different extent. The following sections elaborate on the implementation of the kinetic fractionation model

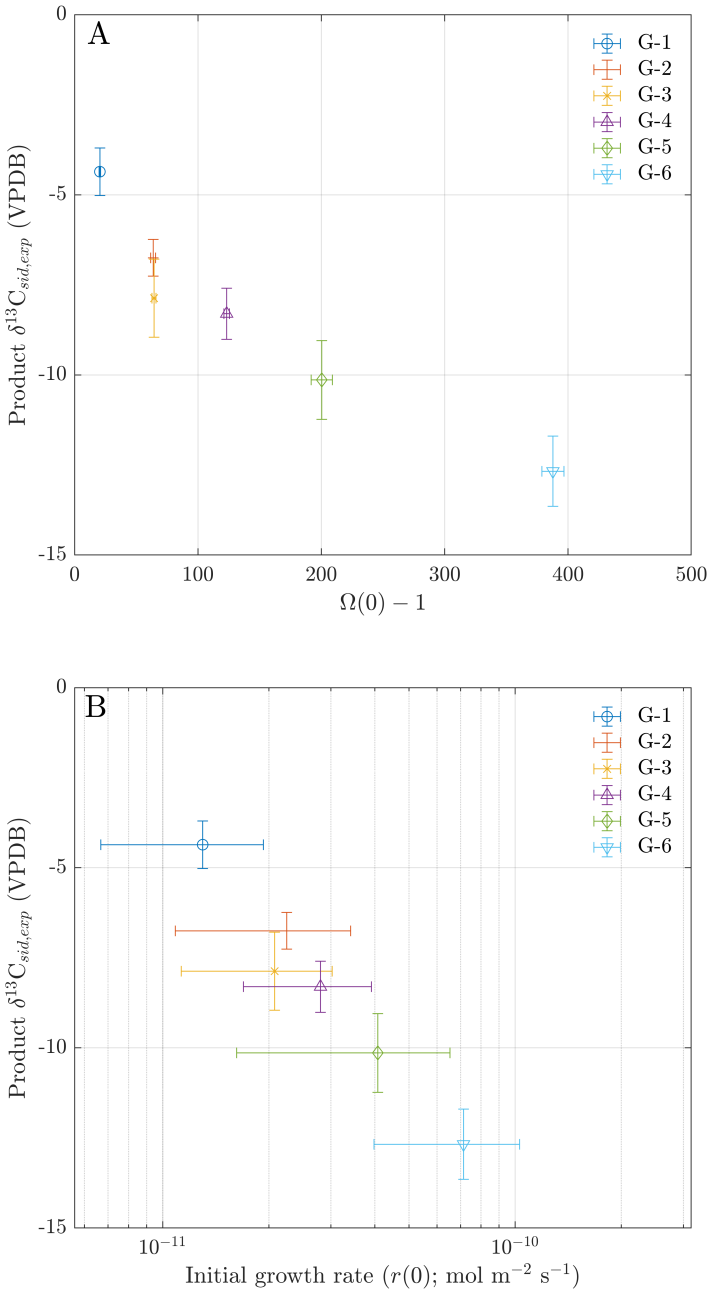


Figure 4.2: Measured isotopic composition $\delta^{13}C$ (‰; VPDB) of siderite from growth experiments plotted against (A) initial solution saturation ($\Omega(0)$) and (B) initial growth rate ($r(0)$). Values listed in Table. 4.1, error bars are 3σ.

Ionic strength = 0.175 mol kg^{-1}, T = 298.15 K, and 1 bar

Ex.No	pH	$[Fe^{2+}](0)$ mol kg^{-1} $\times 10^3$	DIC(0) mol kg^{-1} $\times 10^3$	$\delta^{13}C_{DIC}(0)$ ‰ 1σ	$\delta^{13}C_{sid,exp}$ ‰ 1σ	$\delta^{13}C_{sid,mod}$ ‰
Seed				-2.895±0.013	-0.760±0.077	
G-1	7.515	0.5127	6.366	-2.342±0.015	-4.359±0.103	-3.951
G-2	7.496	0.4961	20.084	-2.754±0.043	-6.749±0.118	-7.108
G-3	7.752	0.4951	11.064	-2.808±0.032	-7.873±0.240	-7.055
G-4	7.378	0.5231	48.444	-2.765±0.029	-8.302±0.169	-9.160
G-5	7.760	0.4679	35.001	-2.909±0.032	-10.139±0.273	-10.510
G-6	7.638	0.5028	83.739	-2.926±0.025	-12.674±0.264	-12.071
Constants:	unit					
m_{seed}	g					0.500
m_{sol}	kg					1.17
SA	m^2 g^{-1}					109.75
K_1						$10^{-6.1486}$
K_2						$10^{-9.8349}$
K_{sp}						$10^{-10.24}$
γ_{H^+}						0.8180
$\gamma_{Fe^{2+}}$						0.3501
$\gamma_{CO_3^{2-}}$						0.3058

Table 4.1: Initial (t = 0 s) solution chemistry and measured $\delta^{13}C_{sid,exp}$ of each growth experiment. Modelled isotopic composition values ($\delta^{13}C_{sid,mod}$; model detailed in Section. 4.4.2) are listed with measured values. Condition specific variables, K_1, K_2, γ_{H^+}, $\gamma_{Fe^{2+}}$,$\gamma_{CO_3^{2-}}$ are calculated using B-dot equation (Helgeson et al. 1981) (Supplementary Information; Chapter. 3), and K_{sp} taken from (Singer and Stumm 1970) assuming no Fe(II) speciation in solution.

(discussed above) to explained the observed $\delta^{13}C_{sid,exp}$ values.

4.4.2 Kinetic fractionation model of C isotopes during siderite growth

In delineating a kinetic-saturation relation, Jiang and Tosca (2020) concluded that the growth kinetics were transport-controlled, with a designated growth rate r_{tr} to be distinguished from surface reaction-controlled growth rate r_{sr}. These designations, however, are solely for the purpose of differentiating the limiting process in the kinetic behaviours of the system. To clarify, surface reactions are the underlying mechanisms of crystal growth, with their rates limited by the transport of dissolved species through a diffusive zone at high supersaturation. The kinetic fractionation model (Eq. 4.7) depends only on the reaction rates regardless of the form. Therefore, to set aside the differentiation of kinetic behaviours, the kinetic-saturation correlation (Eq. 4.8) is adapted and r equals to r_{tr} in the use of the kinetic fractionation model.

The essentials to the kinetic fractionation model include: (1) the initial solution chemistry (i.e., $[Fe^{2+}](0)$, DIC(0), and pH), (2) the initial isotopic

composition of the parent DIC solution, and (3) the product isotopic composition of precipitated siderite (all values are presented in Table. 4.1).

The master variable in the model is the amount of precipitated siderite (dM_{sid}; mol; d denotes for *difference* in all following equations) as a function of time (t in s):

$$dM_{sid}(t) = r(t) m_{seed} SA \text{ [mol]},$$

where m_{seed} are the mass of siderite seed (g) of a surface area (SA) in $\mathrm{m^2\,g^{-1}}$. As the changes in solution [Fe^{2+}] (assuming all Fe(II) as Fe^{2+}; no Fe(II) complexation) and DIC stoichiometrically equate to precipitated siderite, their evolutions from the initial concentrations ($t = 0s$) are as follows:

$$[\mathrm{Fe^{2+}}](t) = [\mathrm{Fe^{2+}}](0) - \frac{dM_{sid}(t)}{m_{sol}} \text{ [mol kg}^{-1}\text{]},$$

$$\mathrm{DIC}(t) = \mathrm{DIC}(0) - \frac{dM_{sid}(t)}{m_{sol}} \text{ [mol kg}^{-1}\text{]},$$

where m_{sol} is the mass (kg) of the parent solution (all values presented in Table. 4.1).

By assuming instantaneous carbonate speciation, the concentration of CO_3^{2-} ion in the parent solution can be calculated by the following relation:

$$[\mathrm{CO_3^{2-}}](t) = \frac{K_1 K_2 \mathrm{DIC}(t)}{[\mathrm{H^+}]^2 + K_1[\mathrm{H^+}] + K_1 K_2} \text{ [mol kg}^{-1}\text{]},$$

where K_1 and K_2 are the first and second dissociation constants of carbonic acid. Because the pH conditions of growth experiments were fixed with pH buffer MOPS, and changed $\leq$0.1 unit at the termination of experiments (Jiang and Tosca 2020), $[\mathrm{H^+}] = \frac{10^{-pH}}{\gamma_{\mathrm{H^+}}}$ is regarded as constant throughout siderite growth.

The evolution of solution saturation can thus be calculated as a function

of time (Fig. 4.3):

$$\Omega(t) = \frac{IAP(t)}{K_{sp}} = \frac{a_{Fe^{2+}}(t)a_{CO_3^{2-}}(t)}{K_{sp}} = \frac{\gamma_{Fe^{2+}}[Fe^{2+}](t)\gamma_{CO_3^{2-}}[CO_3^{2-}](t)}{K_{sp}}, \quad (4.9)$$

where IAP stand for solution ionic activity product, K_{sp} is the solubility product of siderite, and a and γ denote the activity and activity coefficient of the corresponding dissolved species (Table. 4.1).

Based on this kinetic model, the instantaneous isotopic ratios in outermost-layer of precipitated siderite ($^{13}R_{sid}$) and the parent solution ($^{13}R_{\mathrm{DIC}}$) can be formulated through a mass-balance relation where the precipitated siderite is molar equivalent to the sum of C removed from the DIC solution:

$$dM_{sid}(t) = r_{sr}(t)m_{seed}SA = {}^{13}\mathrm{C}_{sid}(t) + {}^{12}\mathrm{C}_{sid}(t) \text{ [mol]}.$$

Given that $^{13}R_{sid} = 0$ at $t = 0$ s, and once precipitation commences, the subsequent instantaneous $^{13}R_{sid}(t)$ can be approximated from $\alpha_{sid-\mathrm{DIC}}$ and $^{13}R_{\mathrm{DIC}}$ from the previous instance $(t-1)$:

$$^{13}R_{sid}(t) = \frac{^{13}\mathrm{C}_{sid}(t)}{^{12}\mathrm{C}_{sid}(t)} \approxeq \alpha_{sid-\mathrm{DIC}}(t-1)^{13}R_{\mathrm{DIC}}(t-1),$$

where $\alpha_{sid-\mathrm{DIC}}$ is calculated through Eq. 4.7, and $^{13}R_{\mathrm{DIC}}(0)$ is converted from the measured initial solution isotopic composition (Table. 4.1).

As siderite growth continued, a mass-balance relation can be placed on the amount of carbon in the system, assuming siderite precipitation being the only sink:

$$\begin{aligned} {}^{13}\mathrm{C}_{\mathrm{DIC}}(t) &= {}^{13}\mathrm{C}_{\mathrm{DIC}}(0) - {}^{13}\mathrm{C}_{sid}(t) \\ &= \frac{\mathrm{DIC}(0)m_{sol}{}^{13}R_{\mathrm{DIC}}(0)}{^{13}R_{\mathrm{DIC}}(0)+1} - dM_{sid}(t)\frac{^{13}R_{sid}(t)}{^{13}R_{sid}(t)+1} \text{ [mol]}, \end{aligned}$$

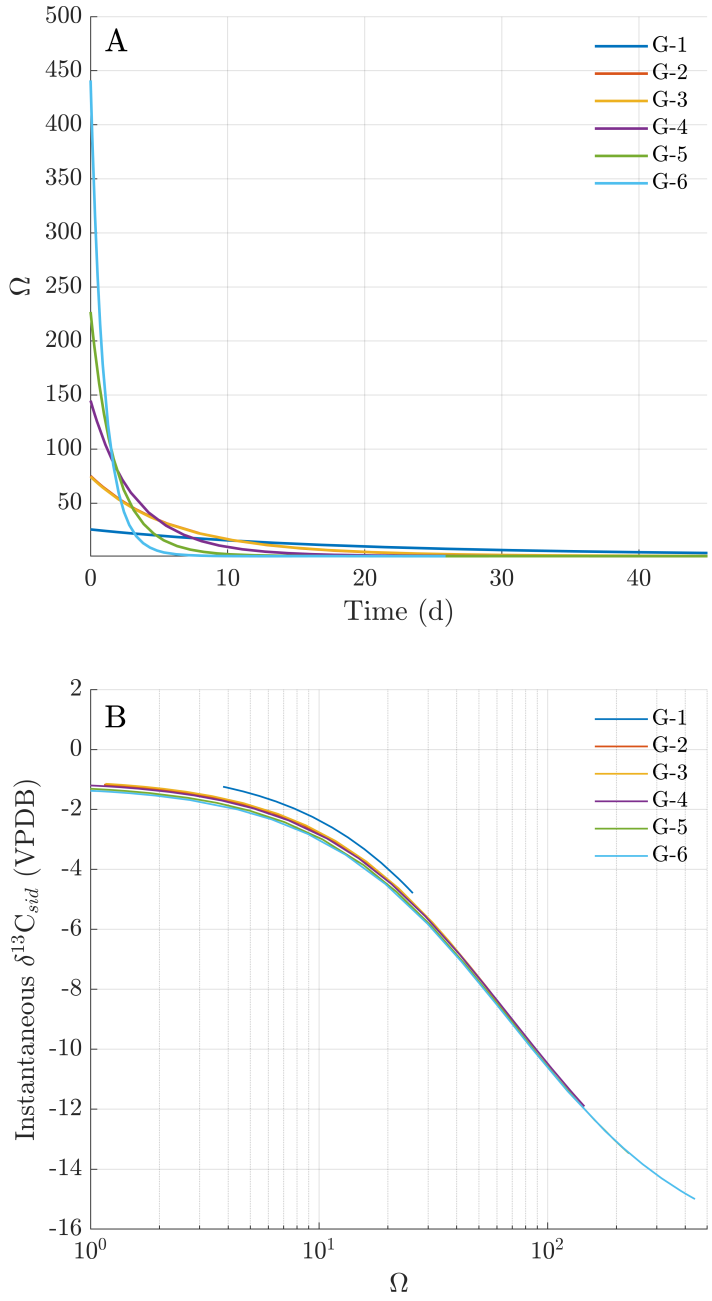


Figure 4.3: (A) Modelled evolution of solution saturation of all growth experiments over time (Eq. 4.9) and (B) the instantaneous $\delta^{13}C_{sid}$ in freshly precipitated siderite (i.e., the outermost layer) as Ω decreases overtime. Because each closed-system growth experiment evolved from their corresponding starting conditions independently (Rayleigh distillation), instantaneous $\delta^{13}C_{sid}$ evolved independently. To better differentiate each experiment, Ω in (B) is plotted on a logarithmic scale. Note that G-2 and G-3 had similar starting Ω and their evolution overlapped; G-1 stands out from the rest due to its smallest DIC pool experienced the most Rayleigh distillation.

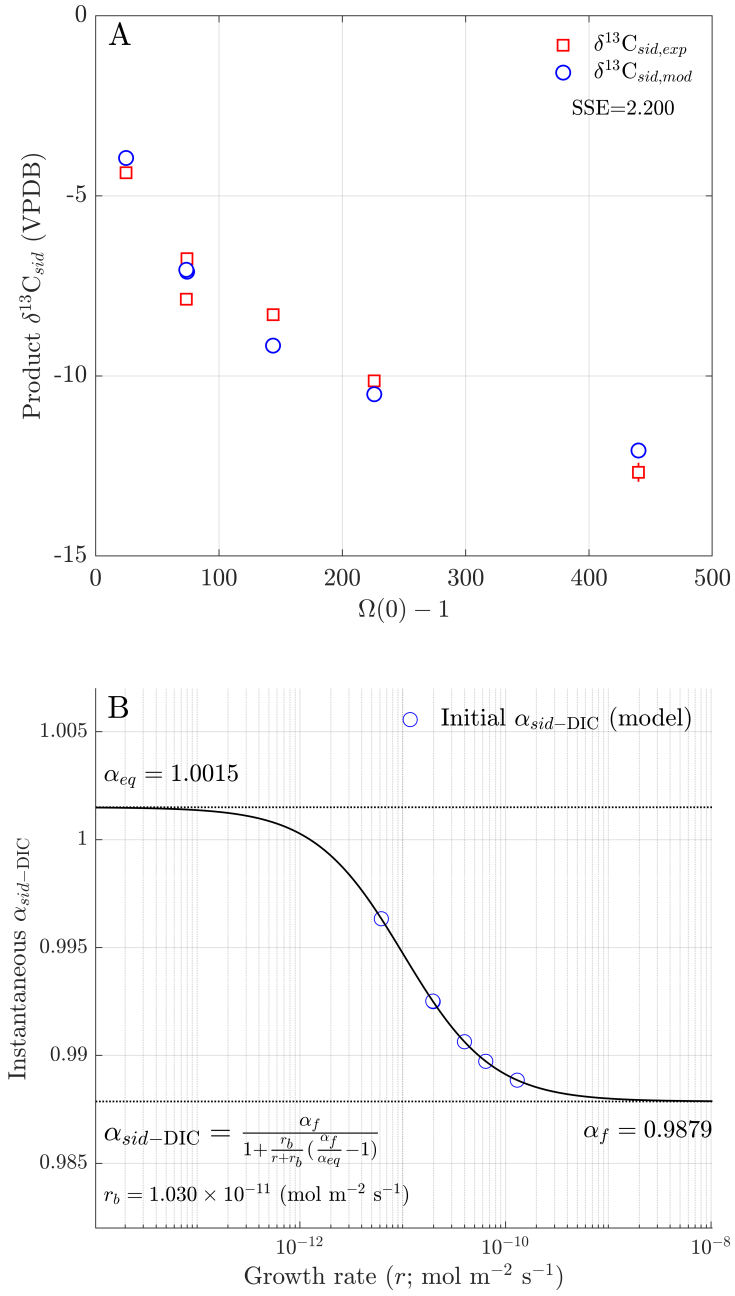


Figure 4.4: (A) Modelled isotopic composition ($\delta^{13}C_{sid,mod}$; ‰) after 46 days according to the kinetic fractionation model compared to the measured isotopic composition ($\delta^{13}C_{sid,exp}$) from growth experiments (all values listed in Table. 4.1). (B) Modelled initial fractionation factor plotted at the initial siderite growth rate.

$$
\begin{aligned}
{}^{12}\mathrm{C}_{\mathrm{DIC}}(t) &= {}^{12}\mathrm{C}_{\mathrm{DIC}}(0) - {}^{12}\mathrm{C}_{sid}(t) \\
&= \frac{\mathrm{DIC}(0) m_{sol}}{{}^{13}R_{\mathrm{DIC}}(0) + 1} - dM_{sid}(t) \frac{1}{{}^{13}R_{sid}(t) + 1} \text{ [mol]}.
\end{aligned}
$$

Therefore, the instantaneous ${}^{13}R_{sid}(t)$ and ${}^{13}R_{\mathrm{DIC}}(t)$ are tabulated iteratively for every second over the course of 46 days; the results are best presented as the evolution of the instantaneous $\delta^{13}\mathrm{C}_{sid}$ as a function of Ω (Fig. 4.3B).

The kinetic fractionation relations stated above provide a set of ordinary differential equations that can be forward integrated to simulate the product isotopic composition of each growth experiment. In the use of Eq. 4.7, little information is known regarding α_{eq}, α_f, and r_b during siderite growth. Jimenez-Lopez and Romanek (2004) reported fractionation factor for siderite precipitation from DIC solution: $10^3 \ln \alpha_{sid-\mathrm{DIC}} = 1.5$ ‰ (Table. 3 therein). Their value, however, reflects neither α_f nor α_{eq}, and probably resulted from mixed precipitation mechanisms that involved both nucleation and crystal growth (see review by Jiang and Tosca 2020). Lacking any other references, $10^3 \ln \alpha_{eq} = 1.5$ ‰ is adapted in this treatment and stands to be corrected with ongoing investigation.

Each growth experiment is simulated with a starting $\alpha_f = 0.950$ and $r_b = 10^{-10}$ mol m^{-2} s^{-1}, and proceeds to minimises the difference between the modelled ($\delta^{13}C_{sid,mol}$) and the measured product isotopic composition ($\delta^{13}C_{sid,exp}$), as well as minimises the difference of α_f and r_b among all simulations. Calculations return $\alpha_f = 0.9879$ and $r_b = 1.0302 \times 10^{-11}$ mol m^{-2} s^{-1} with sum of squared error (SSE) of 2.200. The measured ($\delta^{13}\mathrm{C}_{sid,exp}$) and modelled product isotopic composition values ($\delta^{13}\mathrm{C}_{sid,mod}$) are listed in Table. 4.1 and compared in Fig. 4.4A, modelled starting instantaneous $\alpha_{sid-\mathrm{DIC}}$ is plotted against the starting growth rate of each growth experiment in Fig. 4.4B.

The modelled $\alpha_f = 0.9879$ indicates the maximum kinetic fractionation of C in siderite growth is $10^3 \ln \alpha_{sid-\mathrm{DIC}} = -12.13$ ‰, if (1) the nucleation threshold for AFC precursor is not surpassed and (2) the parent solution does

not undergo Rayleigh distillation; both processes will reduce the product fractionation in the precipitated siderite.

The modelled $r_b = 1.0302 \times 10^{-11}$ mol m^{-2} s^{-1} is internally consistent in explaining the observed $\delta^{13}C_{sid,exp}$, however, appears to differ significantly from reported values.

4.4.3 Backward reaction rate r_b

The macroscopic precipitation of the mineral phase is the surplus of the forward reaction rate over the backward reaction rate ($r = r_f - r_b$). On this basis, when a mineral dissolves in a solution far from equilibrium, thus $r_f \approxeq 0$, the backward reaction rate can be approximated as the dissolution rate: $r_b \approxeq -r$.

A relatively complete data set on siderite dissolution rate at 25 °C is provided by Duckworth and Martin (2004), they employed a flow-through reactor in which a fluid was pumped at 0.01–1.5 mL min^{-1} over the $(10\bar{1}4)$ crystal face of a natural siderite sample, and the Fe(II) concentrations in the effluents were measured to calculate siderite dissolution rate. The authors concluded a dissolution rate of 2.24×10^{-9} mol m^{-2} s^{-1}, normalised against the surface area of the crystal plane, for $5.5 <$ pH < 12. The dissolution rate reported by Duckworth and Martin (2004), if taken as the backward reaction rate, is two orders of magnitude larger than our BET-surface area normalised model output: $r_b = 1.0302 \times 10^{-11}$ mol m^{-2} s^{-1}.

More recently, Golubev et al. (2009) conducted a comprehensive study (77 experiments) on siderite dissolution over a temperature range of 25–100 °C and a pH range of 1–4.6. Importantly, in their discussion, Golubev et al. (2009) compared measured dissolution rate normalised against (1) a crystal plane, (2) geometric surface area of a particulate, and (3) BET-surface area of a particulate. They concluded that the geometric-surface area normalised dissolution rate of a particulate is about an order of magnitude lower than measured crystal plane-surface area normalised rate, and BET-surface area

normalised rate of particulate is about two orders of magnitude lower than crystal plane (Fig. 9 therein). Golubev et al. (2009) further demonstrated that within comparable pH range, their measured dissolution rate from crystal plane is comparable to the values reported by Duckworth and Martin (2004)—two orders of magnitude higher than BET-surface area normalised dissolution rate of particulate.

Although a detailed comparison of surface properties between this study and that of Duckworth and Martin (2004) is not available, it is reasonable to expect the surface area-induced two orders of magnitude difference would persist at the pH range investigated here. Our BET-surface area normalised model output $r_b = 1.0302 \times 10^{-11}\ \mathrm{mol\,m^{-2}\,s^{-1}}$ of siderite particulate is therefore agreeable with crystal plane normalised dissolution rate reported by Duckworth and Martin (2004).

4.5 Conclusion

Isotopic analysis of siderite growth from a wide range of solution saturation indicates a significant C isotope fractionation associated with growth rate. This study present a kinetic fractionation model that delineate the forward fractionation factor $\alpha_f = 0.9879$, indicating a maximum kinetic isotope effect of C in siderite growth of $10^3 \ln \alpha_{sid-\mathrm{DIC}} = -12.13$ ‰. This value, however, depends on a better constraint of the equilibrium fractionation factor (α_{eq}) in siderite growth. In studying natural systems that operate near equilibrium, α_{eq} becomes the dominant factor in the product isotope composition. Experimental studies to fill the knowledge gap is crucial in correctly interpreting Fe(II)-$CO_2(aq)$-H_2O systems, both ancient and modern. That been said, experimental investigation on near-equilibrium kinetic isotope effect is hindered by the extremely slow siderite growth rate.

The slow siderite growth rate constrained by Jiang and Tosca (2020) implies a requisite moderate to high supersaturation for significant accumulations

of siderite in the sediments within an early diagenetic timescale. Coupled with the observed C fractionation as a function of growth rate, the episodic and dynamic precipitation of siderite in many natural settings is likely to cause kinetic fractionation among C isotopes, resulting in negative δ^{13}C signals. These experimental observations bear significant implication for interpreting the genesis of late Archaean iron formation-siderite, and other examples from the geological record.

Negative δ^{13}C signals have led a number of authors to conclude that dissimilatory iron reduction (DIR) may have been the dominant process in generating sideritic iron formations (e.g., Heimann et al. 2010; Johnson et al. 2008b, 2013. This process would require at least some oxidised Fe fluxes to iron formation precursor sediments, necessitating a network of Fe(II)-oxidising or photosynthetic microbes. A facies-specific examination on the iron formations in the Transvaal Supergroup reveals that texturally primary micritic siderite displays a δ^{13}C range between seawater ($\approx$ 0 ‰; Shields and Veizer 2002) and hydrothermal input (assuming hydrothermal input samples a mantle value that is largely invariant over Earth history; ≈ -6.5 ‰; Shanks 2001), whereas more negative values are expressed in large euhedral carbonates (including ankerite) that are often associated with burial diagenesis or metamorphism. These isotopic signatures in the micritic primary siderite can be explained by enhanced hydrothermal activities where the critical supersaturation for precursor AFC nucleation was surpassed in the mixing with ambient seawater, and the subsequent growth of siderite nuclei in the sediment pile resulted in further C isotope fractionation until chemical equilibria were reached. Such an abiotic genesis of iron formations-siderite is also consistent with other chemical proxies such as REEs and Nd isotopes associated with hydrothermal effluent (Derry and Jacobsen 1990; Jacobsen and Pimentel-Klose 1988; Klein 2005), as well as a very low organic carbon content (Klein 2005; Rasmussen and Muhling 2018; Rasmussen et al. 2016) in Precambrian iron formations, prompting a re-evaluation of isotopic bio-signatures in ancient rocks.

Chapter 5

The Iron cycle on early Earth

This thesis presents the results of two sets of experimental investigations on the kinetics of homogeneous nucleation, crystal growth, and the associated kinetic C isotope effect in Fe(II)-carbonate precipitation. The objective of this study is to obtain a mechanistic understanding of the kinetic controls on authigenic Fe(II)-carbonate precipitation (25 °C) and to expand the utility of Fe(II)-carbonate in palaeoenvironmental reconstruction as well as chemical engineering.

5.1 Summary of Fe(II)-mineralisations

5.1.1 Fe(II)-carbonate system

Nucleation experiments (Chapter. 2) reveal multi-step pathways associated with Fe(II)-carbonate mineralisation from anoxic ferruginous seawater. The initial homogeneous nucleation of a precursor amorphous Fe(II)-carbonate (AFC) acts as a reactive substrate controlling the subsequent crystallisation/nucleation of siderite and/or chukanovite. Kinetic constraints on AFC homogeneous nucleation rate show a strong exponential dependence on solution saturation, which clarifies the kinetic factors behind the "critical supersaturation" of the Fe(II)-carbonate phases observed in our experiments—the strong exponential dependence of Fe(II)-carbonate homogeneous nucle-

ation on solution chemistry means that rates are prohibitively slow at values lower than the critical supersaturation; so slow that observable increments of Fe(II)-carbonate via homogeneous nucleation exceed reasonably early diagenetic timescales. Instead, Fe(II)-carbonate precipitation at lower saturation is dominated by (1) heterogeneous nucleation on favourable substrates and/or (2) crystal growth on existing nuclei. Though several mineralisation pathways of the precursor phase are possible, geological products are dominated by the thermodynamically stable siderite.

In addition, Homogeneous nucleation of Fe(II)-carbonate was examined in the presence of $SiO_2(aq)$ concentrations relevant to the Precambrian oceans (Chapter. 2, Section. 2.4.3). Experimental observations indicate that, an Fe(II)-silicate precursor to greenalite (identical to that reported in Tosca et al. 2016) persists to be the dominant precipitate despite relatively high pCO_2 and pH (high supersaturation with respect to Fe(II)-carbonate). Concluding from these observations, homogeneous nucleation of Fe(II)-minerals in ferruginous and low-SO_4 water bodies was likely dominated by Fe(II)-silicate instead of Fe(II)-carbonate, consequently, the maximum transient Fe^{2+} concentrations in these water bodies likely resides between the homogeneous nucleation critical supersaturation and the solubility of the Fe(II)-silicate precursor (a detailed review is provided below), instead of AFC. To surpass the homogeneous nucleation threshold of AFC, the water bodies must experience either (1) a surge in Fe^{2+} influxes that outpaces the pervasive nucleation of the Fe(II)-silicate precursor, or (2) pCO_2-pH conditions that are far beyond any reasonable reconstructions of the steady-state Precambrian seawater carbonate chemistry allow (e.g., Blättler et al. 2017; Halevy and Bachan 2017; Holland 2007; Krissansen-Totton et al. 2018).

Siderite growth experiments (Chapter. 3) yielded a complete data set of the kinetic behaviour from near-nucleation (of AFC) to near-equilibrium solution saturation. These results delineate a chemical affinity-based kinetic model that predicts growth rate limited by the transport of dissolved species to the

mineral surface at high solution saturation, but limited by the rate of surface reactions when the system approaches equilibrium. These observations are analogous to calcite precipitation studies, with the exception that, at 25 °C siderite grows nearly 7 orders of magnitude slower than that of calcite. The presumed similarity in the growth mechanisms but the stark contrast in the growth rates between calcite and siderite, lend support to the physico-chemical difference between hydrated Ca^{2+} and Fe^{2+} ions—Fe^{2+} reflects a higher charge density due its smaller size, thus a higher dehydration energy or a lower exchange frequency of the solvation shell than Ca^{2+}. Therefore, siderite precipitates significantly slower than calcite and often involve the formation of hydrous/hydroxylated metastable phases (i.e., AFC and chukanovite); similar to that of Mg-carbonate system.

The slow kinetics of siderite growth explains the commonly reported siderite supersaturation in anoxic water bodies that are either (1) lacking a suitable surface for heterogeneous siderite precipitation, or (2) open-systems with influxes of Fe(II). In the absence of a suitable surface, siderite precipitates via homogeneous nucleation of the precursor AFC where the critical supersaturation needs to be surpassed. Even in the presence of suitable surface, because the growth rate of siderite is extremely slow near equilibrium, any Fe(II) influxes (e.g., microbial Fe(III) reduction, hydrothermal activity, or dissolution of other Fe(II)-minerals) would outpace the slow growth of siderite and lead to the accumulation of Fe^{2+} in the solution, which in turn, increase the solution saturation. This is expected to continue until solution saturation builds to support an appreciable growth/nucleation rate that balances the Fe(II) influx. In this light, siderite precipitation may be more dynamic and episodic than previously understood, potentially involving multiple mineralisation pathways if nucleation barriers (heterogeneous and homogeneous) are crossed. This knowledge bears important implications for engineering efforts in wetland management, steel corrosion, carbon capture and storage, and long-term nuclear waste storage plan.

The dynamic and episodic origin of siderite is consistent with petrographic observations, notably, from the Archaean iron formations. While the building block of iron formations appears to be Fe(II)-silicate-rich siliceous mud (e.g., Muhling and Rasmussen 2020; Rasmussen et al. 2014, 2013, 2015b, 2016, 2017), siderite is often observed to be precipitating on the surfaces of, and within, Fe(II)-silicate-rich laminae (Muhling and Rasmussen 2020; Rasmussen and Muhling 2018; Fig. 1.5C). Muhling and Rasmussen (2020) systematically examined drill cores of ferruginous cherts and iron formations range in age from 3.46 to 2.45 Ga in the Pilbara and Yilgarn cratons (Western Australia), and throughout the best-preserved iron formations in the Hamersley (Western Australia) and Transvaal (South Africa) basins. The high-resolution petrographic investigation conducted by Muhling and Rasmussen (2020, and Fig. 1–3 therein) revealed multiple populations of siderite associated with cherts, jaspilites and iron formations: (1) siderite nanoparticles (200-500 nm) occur with primary nanoparticle greenalite in some dusty chert, (2) laminae of fine-grained (2–50 µm) siderite parallel to or intergrown with greenalite-bearing dusty chert, and (3) scattered coarser (50 µm–0.5 mm) rhombic crystals of late diagenetic and/or metamorphic products. Though the exact origins of these fine-grained and nanoparticle siderite—whether they were products of homogeneous or heterogeneous nucleation—are still speculative, based on their textural relationship with chert shrinkage polygons, Muhling and Rasmussen (2020) concludes these siderite populations were early diagenetic phases formed contemporarily or soon after dehydration of the greenalite-rich dusty chert.

Isotopic analyses (Chapter. 4) of both the solution and the precipitate indicate that siderite precipitated from supersaturated solution exhibits significant discrimination against ^{13}C. Though many parameters are poorly constrained, the observed isotopic compositions in precipitated siderite are satisfactorily explained with a kinetic fractionation model, which indicates the maximum kinetic isotope effect of C in abiotic siderite growth can be as much as $10^3 \ln \alpha_{sid-\mathrm{DIC}} = -12.13$ ‰. Because a high supersaturation is required to

support an appreciable siderite precipitation rate in an early diagenetic time frame, a noticeable kinetic isotope effect is inevitable. These experimental constraints provide a straightforward explanation for the systematically slightly negative δ^{13}C values (≤ -8 ‰) in the micritic iron formation-siderite (< 4 µm) (Chapter. 2, Section. 2.4.4). These micritic siderite are textually and isotopically consistent with a primary-early diagenetic origin from the mixing hydrothermal effluent (≈ -6.5 ‰, assuming the mantle δ^{13}C has not changed significantly; Shanks 2001) and ambient seawater (believed to be near 0 ‰; Shields and Veizer 2002).

Combining the geochemical constraints from this investigation with recent high-resolution petrographical observations, an emerging view on the iron cycle in the Archaean oceans and the genesis of iron formations is discussed below.

5.1.2 Fe(II)-$SiO_2(aq)$ system

In anoxic, low-SO_4^{2+}, and high-$SiO_2(aq)$ Archaean oceans, Fe-mineralisation was limited to the formation of Fe(II)-carbonate and Fe(II)-silicate, in turn reflecting a distinct network of biogeochemical cycles established long before the appearance of atmospheric oxygen (Beukes et al. 1990; Holland 2007; Klein 2005; Krapež et al. 2003; Rasmussen et al. 2016, 2017). An obvious question arises: which mineral phase would have acted as a sink for Fe^{2+} in the hydrothermal effluents, mixing hydrothermal-seawater bodies, and the ambient seawater? A brief review is provided in the following sections on the parallel Fe-mineralisation pathways in the Archaean ocean (reproduced with permission from Tosca et al. 2019), in addition to Fe(II)-carbonate.

The Archaean marine sedimentary record abounds with evidence indicating that seawater was enriched in $SiO_2(aq)$, persistently anoxic, and at times, ferruginous. Under what conditions might Fe^{2+} and $SiO_2(aq)$ interact with one another? In conducting a series of closed-system anoxic precipitation experiments, Tosca et al. (2016) observed that, over a wide range of conditions, Fe^{2+} and $SiO_2(aq)$ concentrations in synthetic seawater were limited by the

nucleation of a poorly-crystalline Fe(II)-silicate phase. These results suggest that Fe(II)-silicate precipitation may have been an important sink for Fe^{2+} in the early oceans.

Utilising powder X-ray diffraction, FT-IR spectroscopy, thermo-gravimetric analysis, and TEM, Tosca et al. (2016) showed that the synthetic material exhibited close structural similarities with the mineral greenalite ($Fe_3Si_2O_5(OH)_4$), commonly observed in Archaean iron formation (i.e. Rasmussen et al. 2014, 2013, 2015b, 2017). For example, absorption features present in FT-IR spectra corresponded closely to those observed for natural greenalite, indicating that although the material was poorly crystalline, it featured nearly identical structural characteristics (i.e., a trioctahedral layer occupied by Fe(II) and the attachment of that layer, at least at the local scale, to silica tetrahedra; Tosca et al. 2016). TEM data also identified the presence of nano-crystalline domains within the hydrous Fe(II)-silicate precursor, which implied that incipient dehydration and rearrangement of the structure (thermodynamically favoured but kinetically slow) had begun during the experiments.

Given the close correspondence between the experimentally produced solids and natural greenalite, Tosca et al. (2016) suggested that greenalite could be readily precipitated from Archaean seawater. They suggested that such a process would be initiated by the nucleation of a poorly crystalline Fe(II)-silicate precursor directly from solution (homogeneous nucleation) and structural rearrangement to greenalite. By extension, they concluded that the solubility of the Fe(II)-silicate precursor itself may have exerted an important control on the maximum transient Fe^{2+} concentrations in the Archaean water column (Fig. 5.1).

Experiments conducted by Tosca et al. (2016) revealed that a supersaturation threshold must be crossed in order for the Fe(II)-silicate precursor to form directly from seawater (Fig. 5.2). At or above this level of supersaturation, nucleation from solution was observed; below this, Fe^{2+} and $SiO_2(aq)$-bearing seawater solutions apparently persisted in a metastable state with no

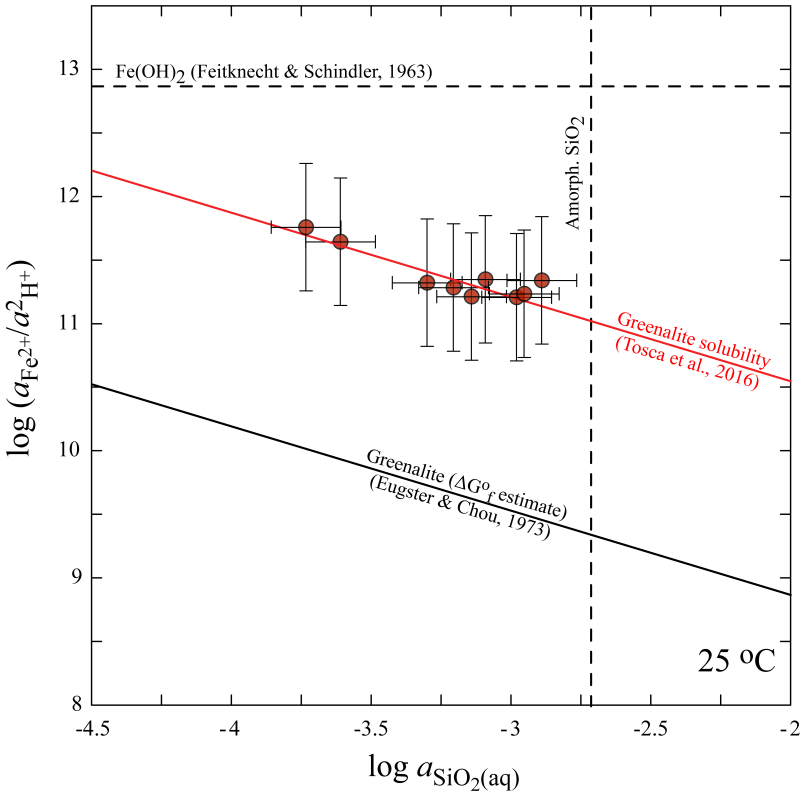


Figure 5.1: Solubility diagram for the Fe^{2+}-SiO_2-H_2O system at 25 °C. Increases in pH and/or Fe^{2+} result in higher y-axis values, and increases in $SiO_2(aq)$ result in higher x-axis values. Dashed lines include solubility limiting phases: amorphous silica (Siever 1962) and freshly precipitated $Fe(OH)_2$ (Feitknecht and Schindler 1963). Solid line corresponds to previously estimated greenalite solubility (Eugster and Chou 1973). Final solution compositions are plotted as filled circles, corresponding to the apparent solubility of greenalite derived from experimental data. From Tosca et al. (2016).

detectable nucleation. Analogous to the homogeneous nucleation of amorphous Fe(II) carbonate, the strong exponential dependence of Fe(II)-silicate nucleation rate on supersaturation implies that nucleation rates are prohibitively slow at values lower than the apparent threshold (Fig. 5.2).

On the basis of their experimental measurements, Tosca et al. (2016) proposed that the formation and stability of the Fe(II)-silicate precursor should be dictated by specific combinations of pH, $SiO_2(aq)$, and Fe^{2+} concentrations. For example, by expressing the apparent solubility of the Fe(II)-silicate precursor in terms of pH, Tosca et al. (2016) showed that for previous estimates of Fe^{2+} concentrations in the Archaean ocean (∼10–120 µmol kg^{-1},

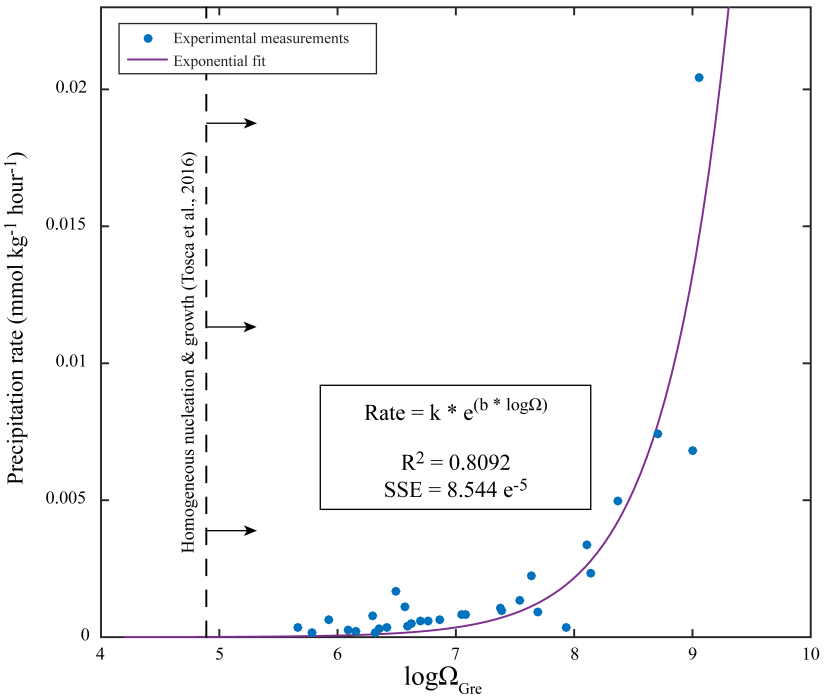


Figure 5.2: Experimentally determined nucleation-dominated greenalite precipitation rate as a function of solution saturation ($\log\Omega_{\mathrm{Gre}}$). Data points represent experimental measurements of greenalite precipitation rate by Tosca et al. (2016). These data define a relationship identical in form to nucleation rates predicted by kinetic theory.

based on the assumption of siderite equilibrium solubility), and the assumption that $SiO_2(aq)$ values were poised at amorphous silica saturation, nucleation of Fe(II)-silicate from Archaean seawater would have required a pH of $\sim$ 7.7–8.3. These values are higher than recent model estimates of the pH of late Archaean/early Palaeoproterozoic seawater, which place the expected pH between 6.3 and 7.7 (Blättler et al. 2017; Halevy and Bachan 2017; Krissansen-Totton et al. 2018).

Alternatively, if Fe(II)-silicate was the solubility-limiting phase precipitating directly from Archaean seawater, and pH levels were instead between 6.3 and 7.7, to explain the voluminous accumulation of greenalite in the iron formations, Fe^{2+} concentrations in the parent solution must need to be about an order of magnitude higher than siderite equilibrium solubility. These geochemical constraints resonate with the experimental observation from Fe(II)-carbonate system, that neither Fe(II)-silicate nor Fe(II)-carbonate could have nucleated homogeneously from the currently accepted reconstruction of the steady-state Archaean ocean. If the concentration of Fe^{2+} increases rapidly, Fe(II)-silicate precursor nucleates before Fe(II)-carbonate precursor under the currently understood Archaean ocean chemistry. These key understandings lend support to a dynamic and abiotic genesis for Archaean iron formations that will be detailed below.

5.1.3 Green rusts

Aside from Fe(II)-carbonate and Fe(II)-silicate, green rusts, a class of mixed valence Fe-rich double layer hydroxides, represent a third potentially important sink for Fe^{2+} in ferruginous non-sulphidic systems. On the basis of thermodynamic evidence, Halevy et al. (2017) suggested that green rust may represent an important sink for Fe in Precambrian depositional systems and may have acted as a reactive intermediate responsible for generating multiple minerals observed in iron formation deposits. To examine this hypothesis, the authors conducted an experimental investigation based on a two-stage approach: (1)

synthesis of green rust, and (2) ageing of green rust in aqueous media in the presence of $SiO_2(aq)$ and dissolved inorganic carbon. In their investigation of the first process, Halevy et al. (2017) observed that the exposure of anoxic Fe^{2+}-bearing seawater-type solutions to a slow diffusive flux of $O_2(g)$ resulted in the relatively rapid precipitation of green rust. Ageing the precipitates in various solutions (simulating the settling of green rust particles from the surface ocean to deeper anoxic waters) resulted in the recrystallisation of green rust into a variety of mineral phases depending on the chemistry of the ageing solution (for example, pH, $SiO_2(aq)$ and DIC concentration). The resultant precipitates included mixtures of siderite, magnetite, and various Fe-bearing silicates. To further examine the importance of green rust precipitation to the global geochemical cycles, Halevy et al. (2017) constructed a time-resolved model for the early Fe cycle to explore the potential role of green rust as a major sink for Fe^{2+} in the Archaean ocean. The modelling results show that green rust may have been important at a global scale, dependent on the chemistry of seawater and the relative stability of other Fe-bearing phases.

In addition to the oxidative pathway envisaged by Halevy et al. (2017) for green rust formation, strictly anoxic pathways for precipitating green rust are possible, and these may in fact be applicable to Archaean systems. For example, Tosca et al. (2018) examined the evolution of pore water chemistry during the deposition and anoxic diagenesis of the Murray Formation, part of an ancient fluvio-lacustrine deposit examined by the Mars Science Laboratory mission. Experimental results showed that the deposition of fine-grained basaltic sediment leads to pore water chemistries that may trigger the precipitation of $Fe(OH)_2$ if pH increased to values of ~ 8.0 and above.

Interestingly, $Fe(OH)_2$, once precipitated from water, is highly unstable in anoxic solutions at these pH levels; Tosca et al. (2018) documented that $Fe(OH)_2$ decomposes to green rust in a matter of minutes. $Fe(OH)_2$ is, in fact, a sufficiently strong electron donor that it reduces $H_2O(l)$, generating $H_2(aq)$ in the process. Some of the structural Fe within $Fe(OH)_2$ itself oxidises dur-

ing this process, generating octahedral layers composed of Fe(II) and Fe(III); the intercalation of anions from solution into interlayers satisfies the resulting charge imbalance and results in green rust formation. Given the structural similarity between $Fe(OH)_2$ and green rust, this mechanism offers a straightforward pathway to form Fe(II)-Fe(III)-bearing double layer hydroxides under strictly anoxic conditions. Because, under the conditions investigated, green rust is metastable with respect to magnetite, the latter mineral was generated via dissolution/reprecipitation in a matter of days (Tosca et al. 2018). Although this pathway may be applicable to magnetite observed in Precambrian iron formation, petrographic constraints on the relative timing of magnetite precipitation will be critical. Because experimental data suggest that the rates of $Fe(OH)_2$ decomposition appear to be rapid, the sedimentological expression of this pathway are likely to generate syndepositional or very early diagenetic magnetite rather than fabric destructive magnetite (i.e., more likely a product of siderite decomposition).

For both oxic (Halevy et al. 2017) and anoxic (Tosca et al. 2018) pathways, anion concentration is key to the formation and stability of green rust (Hansen 2001). For example, because Halevy et al. (2017) conducted green rust syntheses at maximum $SiO_2(aq)$ concentrations of 0.25 $\mathrm{mmol\,kg^{-1}}$ (compared to amorphous silica saturation at ~ 2.2 $\mathrm{mmol\,kg^{-1}}$), it is unclear whether elevated $SiO_2(aq)$ concentrations might influence the kinetics of green rust precipitation and/or the ageing process. Similarly, experimental results obtained for the anoxic pathway (Tosca et al. 2018) involved only slightly higher concentrations of $SiO_2(aq)$ (~ 0.5 $\mathrm{mmol\,kg^{-1}}$), but still relatively low compared to amorphous silica saturation that likely have persisted in the Precambrian ocean.

These two studies offer additional intriguing pathways for the formation of minerals observed in iron formations and other Precambrian sediments through reactive intermediates. However, their contributions to the accumulation of iron formations are unclear. This is mainly because observational data collected on Archaean iron formation cannot uniquely identify green rust trans-

formation products, and iron formation mineralogy and paragenesis appears, at present, consistent with dominantly anoxic processes (detailed in Chapter. 1).

5.2 The Archaean iron cycle: merging sedimentological and geochemical constraints

New results from high-resolution petrography and experimental geochemistry place a number of constraints on the nature of the ancient Fe cycle and the major mineral sinks that balanced the supply of soluble Fe^{2+} to Archaean marine basins. Recent petrographic studies indicate that (Chapter. 1): (1) abundant Fe(II)-silicate was delivered to deep water environments and formed the principal building blocks of iron formations, and (2) Fe(II)-carbonate was a common early diagenetic—potentially primary—constituent of iron formations often in the form of intermittent laminae. At the same time, experimental studies indicate that: (3) the maximum transient concentrations of dissolved Fe^{2+} in the water column of Archaean ocean were likely controlled by the solubility of amorphous Fe(II)-silicate precursor (to greenalite) instead of amorphous Fe(II)-carbonate precursor.

Here, we discuss an emerging view of the Archaean iron cycle that focuses on Fe(II)-silicate and Fe(II)-carbonate mineralisation and consistent with the three conclusions above. Central to this view is understanding the dynamic physico-chemical interactions among different water bodies where different mechanisms of mineral precipitation operate (e.g., nucleation versus growth). In the following discussion, distinctions are made among (1) hydrothermal effluents, (2) mixing of ambient deepwater and hydrothermal effluents, and (3) the ambient seawater. Such differentiation of the Archaean hydrosphere permits a closer examination on the iron cycle, from the source (hydrothermal effluents) to the sink (ferruginous sediments) and the implications for the reservoir (ambient seawater).

5.2.1 Hydrothermal effluent-seawater mixing and the origin of iron formation

Although experimental work provides insight into homogeneous nucleation of Fe(II)-silicates (Tosca et al. 2016) and Fe(II)-carbonate at 25 °C, it is unclear whether low temperature precipitation from the ambient seawater column is capable of accounting for the emplacement of extensive Fe(II)-silicate-rich chemical muds. This consideration is supported by stratigraphic and sedimentological relationships of iron formation intervals within the Hamersley Group, which are most consistent with deposition via density currents and subsequent re-working of chemical muds along the seafloor by bottom water currents or gravity-driven turbidity currents (Krapež et al. 2003; Pickard et al. 2004). These observations suggest that the original sediments were deposited on the flanks of submarine volcanoes and the accumulation of iron formation precursor sediment was linked to periods of high relative sea level and/or vigorous hydrothermal activity, perhaps driven by pulses of seafloor spreading (Krapež et al. 2003; Pickard et al. 2004). Because the major iron formation deposits of the Hamersley Group are inconsistent with pelagites derived by particle settling out of the water column (Krapež et al. 2003; Pickard et al. 2004), another process must have generated and re-deposited Fe(II)-silicates and Fe(II)-carbonate specifically in deep water basinal environments.

Much of the uncertainty relating to the origins of voluminous Fe(II)-silicate production in basinal settings relates to how exactly ambient seawater was modified by hydrothermal input. In a detailed petrographic analysis of iron formation in the Transvaal Supergroup, South Africa, Rasmussen et al. (2017) suggested that hydrothermal effluent and ambient deepwater chemically interacted to produce a plume of Fe(II)-silicate particles ultimately deposited on the seafloor. They envisioned that precipitation was triggered upon mixing acidic hydrothermal fluids rich in Fe^{2+} and $SiO_2(aq)$ with the relatively alkaline ambient seawater to generate greenalite. This hypothesis can, in fact,

be examined and tested in light of available constraints on Precambrian hydrothermal effluent chemistry and ambient seawater.

In their consideration of the effluent chemistry of Precambrian hydrothermal systems, Kump and Seyfried (2005) noted that the interaction between low-SO_4^{2-} seawater and basalt in on-axis hydrothermal reaction zones would have driven the production of hydrothermal effluent enriched in $Fe^{2+}(aq)$. This is because SO_4^{2-} is a major oxidant that helps buffer the Fe-S-O subsystem in reaction zones at mid-ocean ridges today, and so low concentrations of SO_4^{2-} in Precambrian seawater would have buffered the fluid interacting with basalt at a more reduced chemical state (Kump and Seyfried 2005; Seyfried and Ding 1993). This influence, in combination with the strong complexation of Fe^{2+} by Cl species at elevated temperatures and pressures (Ding and Seyfried 1992), would have generated hydrothermal effluent fluids associated with high Fe^{2+}/H_2S ratios. This effect would be particularly magnified at relatively low reaction zone pressures (i.e., 400 bar and lower, owing to P-T effects on Fe complexation; Ding and Seyfried 1992). Such low pressures are thought to have been more common in mid-ocean ridge systems developed during the Archaean when higher heat flow led to shallower depths to the magma chamber (Ding and Seyfried 1992; Isley 1995; Kump and Seyfried 2005).

Although they examined mixing and cooling of modelled hydrothermal effluent in the presence of oxygenated seawater, Kump and Seyfried (2005) did not examine mixing with anoxic seawater, which is of particular interest given recent constraints on iron formation precursor mineralogy. In modern black smoker systems, mineral precipitation is triggered upon mixing between hot effluent fluids (on the order of 250 °C upon expulsion at the seafloor; Seyfried et al. 1997) with cold ambient seawater, both within and near the vent itself (Janecky and Seyfried 1984). Because modern hydrothermal effluent is characterised by high H_2S/Fe ratios, most Fe is titrated out as pyrite, which is only a minor component of many black smoker mineral assemblages today (Janecky and Seyfried 1984; Tivey and McDuff 1990; Tivey 1995). But what

precipitates might have characterised mid-ocean ridge systems in the Precambrian when seawater was anoxic and hydrothermal effluent characterised by a high Fe/H_2S ratio?

To examine this process, we can investigate the simple mixing between generalised hydrothermal effluent (following Kump and Seyfried (2005)) and Precambrian seawater (i.e., anoxic, low SO_4^{2-}, and $SiO_2(aq)$ concentrations at or near amorphous silica solubility) (Fig. 5.3). These simple calculations show that, depending on the amount of magmatic $H_2S(aq)$ delivered to seafloor vents (ultimately derived from pyrrhotite equilibria in the subseafloor reaction zone; Kump and Seyfried 2005), mineral assemblages are likely to be dominated by greenalite and siderite with minor pyrite (Fig. 5.3). Although this calculation greatly simplifies a rather complicated physical process, similar approaches have successfully explained the origin of mineral species produced at modern black smokers (Janecky and Seyfried 1984).

The amounts of greenalite and siderite precipitated at Precambrian hydrothermal vents are, of course, dependent on the Fe and $SiO_2(aq)$ concentrations of the effluent fluid. These concentrations could have been modified during cooling and decompression as the reaction fluid was separated from the rock buffer and ascended through the oceanic crust (Alt 1995; Seyfried et al. 1997). Interestingly, these calculations show that much of the $SiO_2(aq)$ delivered to seafloor vent systems is determined by quartz solubility at elevated temperature and pressure, rather than ambient $SiO_2(aq)$ in seawater (Von Damm et al. 1991). Iron, on the other hand, may be influenced by Fe-chlorite precipitation during cooling and decompression as fluids ascend through the oceanic crust. Fe-chlorite is a common product of subseafloor alteration assemblages; this may have attenuated Fe^{2+} in reaction fluids, in turn modifying minerals precipitated upon venting at the seafloor (Alt 1995; Seyfried et al. 1997; Zierenberg et al. 1988). Nevertheless, if even broadly correct, such a hypothesis would provide one way to reconcile the stratigraphy, sedimentology, and geochemistry of major Archaean iron formation deposits. In addition, a hydrothermal

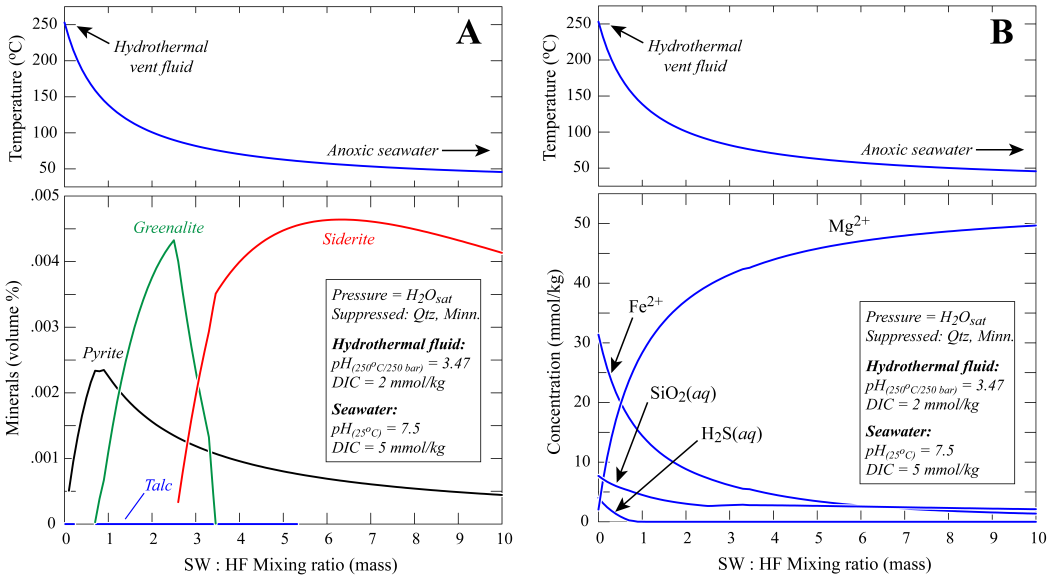


Figure 5.3: Reaction path modelling of the mixing between hydrothermal effluent and anoxic seawater. Hydrothermal effluent composition is modelled after Kump and Seyfried (2005) (pH 5 at 400 °C and 400 bar; Fe-S-O subsystem buffered by pyrrhotite-fayalite-magnetite-quartz equilibrium), and subsequently cooled and decompressed to 250 °C and 250 bar (allowing for pyrite and chlorite precipitation with decreasing temperature and pressure; Seyfried et al. 1997) to more closely represent conditions upon seafloor venting (Janecky and Seyfried 1984; Seyfried et al. 1997). Seawater is based on modern composition but anoxic, SO_4^{2-}-free, with a dissolved inorganic carbon (DIC) pool of 5 mmol kg^{-1}, and pH 7.5. (A) Minerals precipitated from fluid (back reaction is permitted) as a function of temperature and mixing ratio (by mass). Mineral assemblages are dominated by greenalite, siderite and lesser amounts of pyrite; these precipitate at low mixing ratios and elevated temperatures, indicating precipitation is likely to occur relatively close to seafloor vents. (B) Evolution of fluid chemistry upon mixing between hydrothermal effluent and seawater. Fe^{2+} is rapidly depleted as minerals precipitate. Because Fe $\gg$ $H_2S(aq)$ (i.e., Kump and Seyfried 2005), $H_2S(aq)$ is quantitatively removed upon pyrite precipitation. Thermodynamic data were generated using SUPCRT92 via DBCreate (Johnson et al. 1992; Kong et al. 2013), except for quartz solubility from Von Damm et al. (1991) and Fe–Cl complexation constants from Ding and Seyfried (1992). Quartz and minnesotaite were suppressed from forming because, although quartz controls $SiO_2(aq)$ concentrations at reaction zone conditions, amorphous silica is likely to dominate silica polymorphs upon venting at the seafloor (Janecky and Seyfried 1984) and minnesotaite is widely recognised as a metamorphic product of greenalite (Klein 1974; Rasmussen et al. 1998). From Tosca et al. (2019).

origin for at least some siderite produced at hydrothermal vent systems offers an additional interpretation for the systematically slightly depleted $\delta^{13}C$ values associated with some iron formation-associated micritic siderite, originally thought to reflect primary sedimentation, as observed in iron formation of the Transvaal Supergroup (Beukes et al. 1990). Given that recent data suggest the fluxes of oxidised Fe to iron formation precursor sediments appears to have been limited, the $\delta^{13}C$ composition of iron formation carbonates may in fact be consistent with simple mixing between a mantle CO_2 source (assuming its isotopic composition, currently $\delta^{13}C$ of $\cong$ -6 ‰, has not changed through time) and ambient seawater ($\cong$ 0 ‰; Chapter. 2), followed by crystal growth that further induced kinetic isotope effect (Chapter. 4). Because the precipitation of hydrothermally derived iron may also, under some circumstances, give rise to depleted Fe isotope compositions (Rouxel et al. 2004, 2003), this offers an additional interpretation for some instances where iron formation carbonates retain isotopic compositions depleted in both $\delta^{56}Fe$ and $\delta^{13}C$ (Yamaguchi et al. 2005).

Finally, mixing calculations (Fig. 5.3) show that mineral precipitation upon fluid venting would have significantly decreased Fe^{2+} concentrations relative to current estimates; our calculations commonly estimate dissolved Fe^{2+} concentrations on the order of 1–3 $mmol\,kg^{-1}$ following mineral precipitation upon venting and mixing with seawater. In fact, these concentrations can be considered upper estimates given that Fe^{2+} may be further attenuated as Fe-chlorite precipitates upon the ascension of hydrothermal fluids through the oceanic crust (Seyfried et al. 1997) and through mineral precipitation triggered by conductive heating and subsequent mixing of seawater within vent structures prior to venting at the seafloor (Janecky and Seyfried 1984).

If mineral precipitation would have strongly attenuated Fe^{2+} fluxes to Archaean hydrothermal fluids, then how could this process have impacted globally averaged Fe^{2+} fluxes to Archaean oceans? One approach to estimate the impact on Fe^{2+} fluxes is to estimate the average post-precipitation Fe^{2+} con-

centrations of hydrothermal fluids and multiply this value by the amount of water thought to circulate through axial ridge systems. If precipitation commonly left 1–3 mmol kg^{-1} Fe^{2+} released to seawater after fluid mixing, then using modern estimates of water fluxes out of near axis hydrothermal vents (3×10^{13} L yr^{-1}; Elderfield and Schultz 1996) leads to globally averaged hydrothermal fluxes of $\sim$ 0.1–0.2 $\times$ 10^{12} mol yr^{-1} of Fe^{2+}. Hydrothermal water fluxes, however, may have been higher than present for the Archaean (Des Marais 2000), but some have argued that they may have been lower (Korenaga 2006). In addition, shallower ridge systems might have favoured higher Fe concentrations through low pressure Fe-Cl complexation effects and two-phase separation (Ding and Seyfried 1992; Kump and Seyfried 2005). Despite this uncertainty, even if hydrothermal fluids contained much higher Fe^{2+} concentrations, mineral precipitation upon fluid venting would have remained a key process attenuating Fe^{2+} fluxes to the Archaean ocean. This is because increases in Fe^{2+} concentrations, in most cases, simply lead to larger quantities of minerals precipitating upon venting and mixing.

Combining this estimate of hydrothermal Fe^{2+} fluxes with globally averaged riverine Fe^{2+} fluxes in turn allows us to estimate the total supply of Fe^{2+} to Archaean oceans. Applying a generous estimate of averaged riverine Fe^{2+} fluxes (assuming $\sim$ 65 % of the continental crust was formed by 2.4 Ga; Taylor and McLennan 1985), modern riverine water fluxes of 4 $\times$ 10^{16} L yr^{-1} (Elderfield and Schultz 1996), and an average river water Fe^{2+} concentration of 0.112 mmol L^{-1}), yields total Fe^{2+} fluxes to the oceans that fall in the range of $\sim$3 $\times$ 10^{12} mol yr^{-1} of Fe^{2+}. What processes might have balanced these Fe^{2+} sources?

5.2.2 Early diagenetic Fe(II)-carbonate precipitation as a deep water sink for Fe^{2+}

A variety of evidence supports the notion that early diagenetic siderite precipitation may have acted as a significant sink for hydrothermal Fe^{2+}, which

would have further attenuated the soluble Fe^{2+} flux to the surface ocean. In addition to evidence for early diagenetic siderite precipitation in Hamersley Group iron formation (Rasmussen and Muhling 2018), siderite is also an important early diagenetic constituent in clastic intervals of the Hamersley Group (Krapež et al. 2003; Pickard et al. 2004). For example, Krapež et al. (2003) and Pickard et al. (2004) show that siderite is the earliest-forming and most common Fe-rich phase in clastic rocks throughout the Brockman Supersequence, sometimes forming siderite-rich partings punctuating detrital dolomitic sediments re-worked into continental shelf environments. In fact, similar lithofacies descriptions have been reported for iron formation deposited in the Krivoy Rog basin of the Ukraine (Kulik and Korzhnev 1997) and for iron formation intervals of the Kaapvaal Craton (Beukes et al. 1990; Kaufman et al. 1990; Klein and Beukes 1989). For example, Beukes et al. (1990), Kaufman et al. (1990), and Klein and Beukes (1989) cite petrographic evidence for "primary" siderite, occurring as finely disseminated crystals comprising siderite-rich micro and mesobands. These studies refer to siderite as "microspar" which leaves open the possibility that siderite-rich sediments were deposited and then recrystallised during early diagenesis or were formed *de novo* as a pore-filling cement during early diagenetic reactions in pore waters.

Fe isotope studies also indicate that the isotopic signature of siderite-rich siliciclastic sedimentary rocks is consistent with a hydrothermal source for Fe. For example, Yamaguchi et al. (2005) noted that the average δ^{56}Fe value of -0.5 ‰ for siderite-enriched shales ranging from 3.3 to 2.2 Ga in age is best interpreted as a hydrothermal signature. Indeed, although typically assumed to be characterised by a δ^{56}Fe value of close to zero in a dominantly anoxic ocean (Johnson et al. 2008a; Yamaguchi et al. 2005), studies of modern hydrothermal systems have shown significant variability in the δ^{56}Fe values of fluids and sulphides from modern systems (Rouxel et al. 2003), as well as for altered segments of Mesozoic oceanic crust (Rouxel et al. 2003). The processes responsible for isotopic variation in Precambrian systems and their range in

composition is nevertheless deserving of continued study.

Early diagenetic siderite precipitation clearly represented an important process in distal slope to basinal settings (Krapež et al. 2003; Pickard et al. 2004; Sumner 1997; Yamaguchi et al. 2005) and, in the case of the Kuruman and Griquatown iron formations, across the full spectrum of depositional environments shortly after the drowning of the Campbellrand platform (Beukes 1984). What conditions would have promoted early diagenetic siderite precipitation if nucleation of Fe(II)-carbonate from the ambient seawater was kinetically inhibited?

The experimental results of this study indicate that the homogeneous precipitation of siderite from the ambient Archaean seawater was probably not a common process given that the supersaturation threshold was unlikely to have been reached in the ambient seawater (Chapter. 2). However, two possibilities pertaining to the origin of Fe(II)-carbonate: (1) heterogeneous precipitation of Fe(II)-carbonate on pre-existing mineral surfaces, and (2) continued crystal growth of Fe(II)-carbonate nuclei that formed alongside Fe(II)-silicate at the mixing of hydrothermal effluents and seawater.

It is well understood from kinetic theory that certain particulate surfaces may catalyse the nucleation of a mineral if the solution is adequately supersaturated and the substrate possesses favourable characteristics (Lasaga 1998b,c; Steefel and Van Cappellen 1990; Stumm 1992; Van Cappellen 1991). Importantly, that a certain type of surface can initiate heterogeneous nucleation means that the threshold for supersaturation will be lower than the that for homogeneous nucleation. In order for a substrate to be suitable, however, the energetics of the interface between the precipitating cluster and the substrate (σ_{CS}) must be more favourable than the interface between the precipitating cluster and the aqueous solution (σ_{CW}) (Lasaga 1998b,c; Steefel and Van Cappellen 1990; Stumm 1992; Van Cappellen 1991). Such a surface should minimise the work involved in creating a precipitate cluster on a substrate and must have a substrate-solution interfacial energy (σ_{SW}) similar to that of the

precipitated clusters ($\sigma_{SW} \approx \sigma_{CW}$). In addition, the surface must strongly adsorb the ions of the precipitate (Fe^{2+} and/or CO_3^{2-} in the case of siderite) and it must be present in sufficient amounts such that surface area is large (Lasaga 1998b,c; Steefel and Van Cappellen 1990; Stumm 1992; Van Cappellen 1991). In other words, a few grains will not be sufficient to trigger significant heterogeneous nucleation.

That early diagenetic siderite is commonly associated with greenalite-rich muds in iron formation intervals deposited on the Pilbara and Kaapvaal cratons (e.g., Beukes 1984; Rasmussen and Muhling 2018) suggests that greenalite may have satisfied the above criteria and acted as a favourable surface to trigger Fe(II)-carbonate nucleation. Although not yet understood quantitatively, it is likely that greenalite would adsorb Fe^{2+}, possess a high specific surface area, and, may also possess similar interfacial energy to initially-formed Fe(II)-carbonate nuclei (if AFC acted as a precursor phase) (Nielsen and Söhnel 1971; Stumm 1992; Van Cappellen 1991). This logic may apply to amorphous silica as well, which is expected to possess similar energetic properties on the basis of surface energy-solubility correlations (Nielsen and Söhnel 1971). Finally, it is worth noting that both homogeneous and heterogeneous nucleation will occur simultaneously but that low degrees of supersaturation will always permit rates of heterogeneous nucleation to dominate over homogeneous nucleation (Fig. 5.4) (Stumm 1992; Van Cappellen 1991).

These constraints suggest that the heterogeneous precipitation of siderite on greenalite surfaces should be favoured at supersaturation levels less than the threshold for homogeneous nucleation, but greater than siderite equilibrium. Although this threshold has not yet been determined, simple calculations show that, in light of current estimates of pH and pCO_2 for the Archaean ocean-atmosphere system (Blättler et al. 2017; Halevy and Bachan 2017; Krissansen-Totton et al. 2018), the ambient seawater may have commonly exceeded the threshold required for heterogeneous Fe(II)-carbonate nucleation. It is important to note that this may only require relatively low bottom water Fe^{2+}

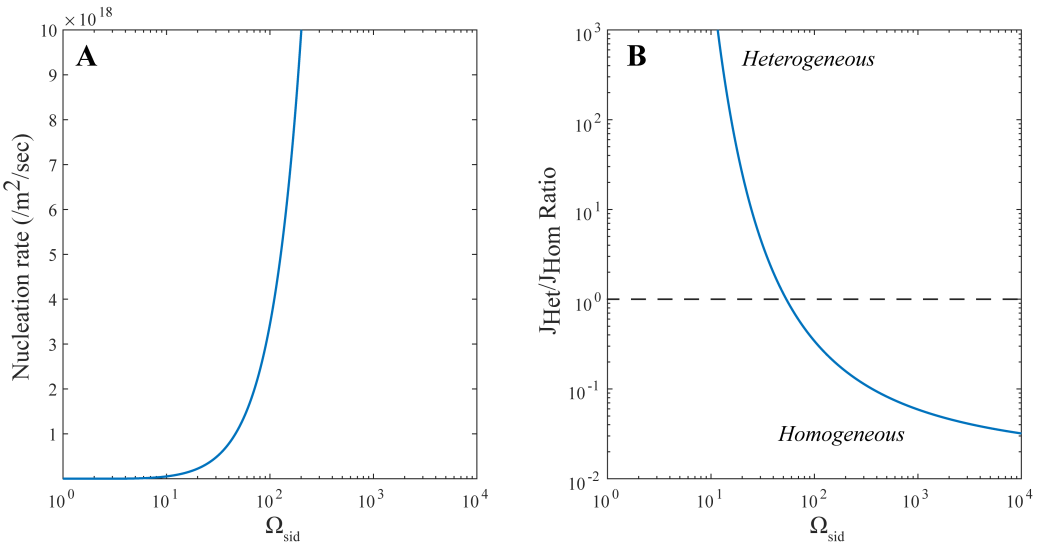


Figure 5.4: (A). Heterogeneous nucleation rate of siderite as a function of supersaturation ($\Omega = \frac{IAP}{K_{sp}}$). Similar to homogeneous nucleation, kinetic theory predicts a strong exponential relationship between heterogeneous nucleation rates and supersaturation such that an effective threshold can be identified. Above this threshold, heterogeneous nucleation will dominate, and below this threshold, only crystal growth on pre-existing siderite crystals will occur. (B). The ratio of heterogeneous nucleation rate (J_{Het}) to the homogeneous nucleation rate (J_{Hom}) of siderite as a function of supersaturation. At high supersaturation, homogeneous nucleation dominates. Calculations follow Steefel and Van Cappellen (1990) where: $\sigma = 50$ mJ m^{-2}, molar volume of siderite (v_m) $= 2.938 \times 10^{-5}$ m^3 mol^{-1}, K_{ad}, or the linear sorption coefficient $= 1000$, $K^o_{ad} = 100$, saturation concentration is based on Jiang and Tosca (2019), and $\Delta G_{in} = 50$ kJ mol^{-1}.

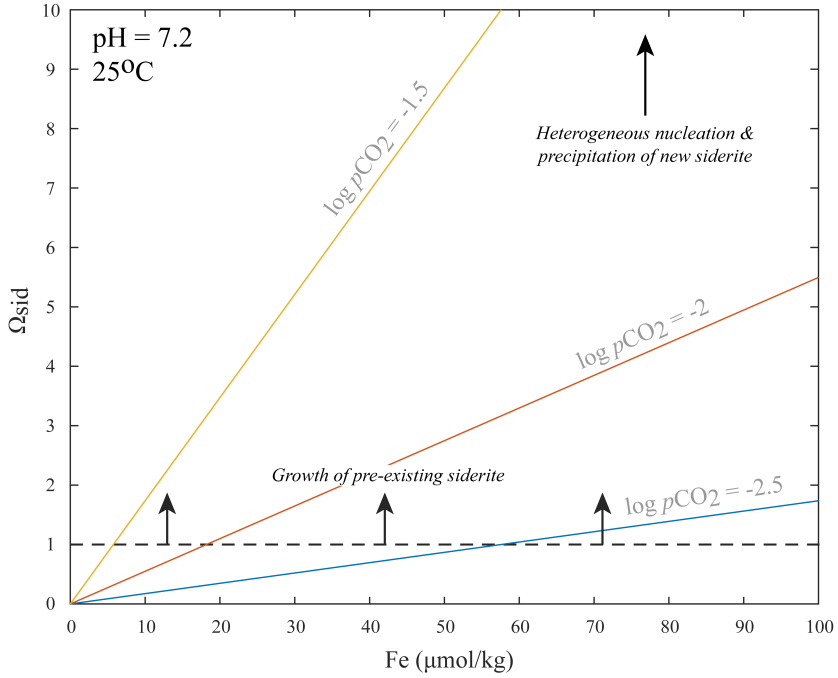


Figure 5.5: Relationship between siderite supersaturation and Fe concentration as a function of pCO_2 levels estimated for the late Archaean (Blättler et al. 2017). Although the threshold for heterogeneous nucleation (i.e., Fig. 5.4A) is unconstrained, it is likely to lie in a range lower than estimated for the homogeneous case in Chapter. 2. Thus, at pCO_2 levels relevant to the late Archaean, transient Fe^{2+} concentrations less than 1 mmol kg^{-1} are likely to have triggered heterogeneous nucleation and the development of new Fe(II)-carbonate in sediments. However, growth of pre-existing siderite will occur at any Ω value greater than 1.

concentrations, which are in turn dependent on ambient pH (Fig. 5.5). Another possibility is that Fe concentrations in sediment pore waters may have been buffered by Fe(II)-silicate dissolution. This result leaves open the possibility that early diagenetic siderite may have precipitated inorganically without the assistance of Fe-reducing bacteria, if the Fe concentration in pore waters was influenced by greenalite solubility.

Regardless of the origins of the initial siderite nuclei (i.e., homogeneous versus heterogeneous) in the iron formation precursor sediments, diagenetic crystal growth of these nuclei would have acted as a sink for Fe^{2+} as long as a diffusional contact with the overlying water column was maintained, with the growth rates followed the saturation-kinetic correlation investigated in Chapter. 3. As discussed above, petrographic evidence for early diagenetic

siderite in chemical and clastic deep water sediments of the Brockman Supersequence suggest that this process continued as sediments were re-worked along the basin floor. How significant of a sink for Fe^{2+} would diagenetic siderite growth have been to the Archaean Fe cycle?

As an instructive calculation, we can consider the global impact of the growth of siderite nuclei in the Hamersley Group alone. First, we assume that deepwater chemical and clastic sediments occupied an area equivalent to the estimated area of the Hamersley Group ($\sim$ 100,000 km^2; Trendall and Blockley 1970), that the upper 50 cm of sediment was active during early diagenesis, characterised by 75 % pre-compaction porosity (Morse and Mackenzie 1990), and contained initially 1 % siderite nuclei by volume. Assuming the siderite nuclei to be spherical particle of $\approx$ 5 µm in diameter—small enough to be suspended and dispersed in water (e.g., Nielsen 1964, 1984; Nielsen and Toft 1984)—thus, a specific surface area of 7.85 $\times 10^{-11}$ m^2 and a volume of 6.54 $\times 10^{-17}$ m^3 per particle. Considering the high volume of direct silica precipitation during the deposition of iron formations, we may conservatively estimate only 1 % of the siderite nuclei were not locked-up in silica gel like the "dusty" greenalite. In addition, further assuming only 1 % of the surface area of the free siderite nuclei is available for crystal growth (e.g., restricted pore space and surface complexation that limits growth sites). This translates into a total effective surface area of 4.5 $\times 10^{10}$ m^2 in the top 50 cm of sediments with 75 % porosity in the Hamersley Basin. Taking the modelling constraints on late-Archaean ocean pH = 7 and atmosphere pCO_2 level of $10^{-1.5}$ (Halevy and Bachan 2017), assuming the same ionic strength of the modern ocean (I = 0.7 mol kg^{-1}), with an Fe^{2+} flux of 1–3 mmol kg^{-1} after mineral precipitation upon hydrothermal venting and mixing with seawater, the peculating fluid in the precursor sediments is thus Ω = 10–30 oversaturated with respect to siderite equilibrium. According to the rate-saturation correlation for seeded siderite growth (Eq. 3.5; Chapter. 3), the growth rate is therefore 1.88–6.06 $\times 10^{-12}$ mol m^{-2} s^{-1}, that is, 1.0–3.2 $\times 10^{15}$ mol yr^{-1} of Fe in the Hamersley

basin alone, if, the solution saturation was sustained.

These simple calculations demonstrate that a conservative estimate on diagenetic siderite growth as a sink of Fe in a single basin is more than capable of accounting for a generous estimate on the global Fe flux to the Archaean ocean ($\sim$ 3 $\times 10^{12}$ moL yr^{-1}). Upscaling siderite growth as a sink of Fe on a global scale is riddled with uncertainties, however, an important conclusion can be drawn from this mathematical exercise: the precipitation of Fe(II)-minerals was a directly response to episodically enhanced Fe influxes (e.g., intense hydrothermal activity), where the ambient seawater likely remained at steady-state composition (Fig. 5.6). This conclusion resonates with petrographic observations from Archaean iron formations that: (1) Fe(II)-silicate nanoparticles locked-up in chert were product of nucleation upon venting and mixing, (2) nano–micrometer siderite accumulations sometimes makes up 10-20 vol.% of ferruginous cherts (Muhling, *personal comment*) are observed in the form of intermittent laminae, and (3) the facies-specific isotopic observation that micritic siderite exhibits only slightly negative δ^{13}C resulted from hydrothermal effluent-seawater mixing and kinetic isotope effect during crystal growth.

5.3 Summary

Geochemical constraints arising from this thesis prompt a re-evaluation on the palaeoenvironmental reconstruction based on ferruginous sediments, notably, late Archaean iron formation. Incorporating recent advances in high-resolution petrography, experimental geochemistry, and modelling studies of Fe-minerals, this study presents an updated understanding of the Fe cycle on early Earth, in which the deposition of ferruginous sediments was a direct response to enhanced Fe(II) influxes (e.g., hydrothermal venting), where Fe(II)-silicate nucleation was the dominant mechanism that attenuated hydrothermal Fe(II) fluxes to seawater, and Fe(II)-carbonate precipitation served

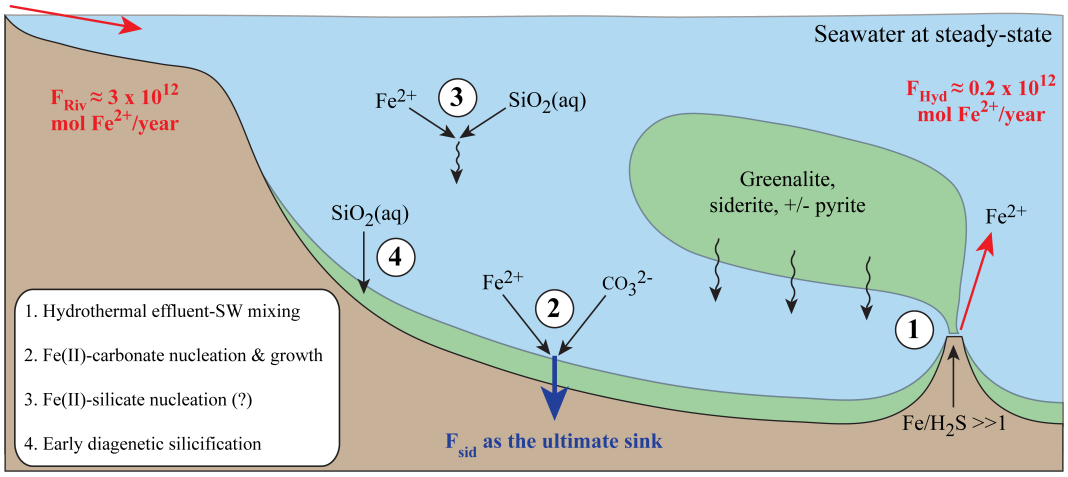


Figure 5.6: Schematic of the Fe cycle before the oxygenation of the oceans and atmosphere (i.e., before the GOE). Because of mineral precipitation upon mixing, soluble hydrothermal Fe^{2+} fluxes into the oceans are likely to lie within the range of modern hydrothermal Fe^{2+} fluxes, based in simple mixing calculations. If, as the rock record suggests, clastic and/or chemical deep water sediments initially contained 1 vol.% siderite nuclei (either through hydrothermal particulate input or through transient heterogeneous nucleation), of which only 1 % of siderite nuclei were in contact with overlying fluid, and only 1 % of that were contain active sites for crystal growth, siderite growth within the upper 50 cm of the sediment across an area equivalent to the Hamersley Basin could have balanced or even exceeded global Fe inputs into the Archaean ocean. Hence, in this model, Fe(II)-carbonate precipitation is considered as the ultimate sink of seawater Fe(II), whereas Fe(II)-silicate nucleation is considered the major mechanism in attenuating Fe(II) concentration from hydrothermal effluent.

as the ultimate sink of a comparatively small seawater Fe(II) reservoir. More specifically:

1. The maximum transient Fe^{2+} concentration in Archaean ocean was controlled by the solubility of amorphous Fe(II)-silicate precursor (to greenalite) instead of amorphous Fe(II)-carbonate precursor (to siderite). This conclusion is consistent with the ubiquitous distribution of greenalite in many Precambrian iron formation, whereas the micritic siderite is concentrated in intermittent laminae.

2. Micritic siderite facies in many Precambrian iron formations bear morphological and textural evidence for direct precipitation (homogeneous nucleation) from water bodies that were chemically modified from steady-state seawater chemistry. The simplest explanation of water column precipitation of siderite was caused by hydrothermal-seawater mixing, where the requisite critical supersaturation for precursor amorphous Fe carbonate nucleation was surpassed.

3. Rapid nucleation of Fe(II)-carbonate and -silicate at the hydrothermal-seawater mixing zone supplied nanoparticles of nuclei/seeds to the sediment and drew down the concentration of Fe^{2+} in the bottom water via crystal growth until equilibria are reached. This dynamic process disentangles the deposition of ferruginous sediments from the steady-state composition of the seawater, in the sense that the abundance of ferruginous sediments in the late Archaean does not imply a prolonged oversaturation of the seawater with respect to these minerals.

4. Because siderite is nearly 2 orders of magnitude less soluble than calcite and precipitates 7 orders of magnitude slower, at a given pH-pCO_2 condition, siderite supersaturation varies considerably more significantly in response to cation fluxes than Ca^{2+}–DIC system, implying a more dynamic and episodic precipitation process. In this light, the enhanced Fe

flux caused by hydrothermal input in the late Archaean oceans might have allowed siderite growth to temporarily surpass calcite growth as the major sink of DIC. This possibility deserves more investigation from a theoretical and experimental point of view.

5. Microbial activity, namely the dissimilatory Fe(III) reduction, has been suggested to generate the negative $\delta^{13}C$ signature in iron formation-associated siderite facies, which in turn, necessitated Fe(III) fluxes that were provided by microbial Fe(II)-oxidation or photosynthetic oxidation. In the light that the steady-state seawater composition was disentangled from enhanced Fe influxes by proportionally enhanced Fe(II)-mineralisation, microbial Fe(II)-oxidation and/or photosynthetic oxidation from the surface water (at steady-state Fe(II) concentration) were likely negligible compared to the total Fe that entered Archaean iron formations (e.g., $\approxeq 9.4 \times 10^{13}$ tonne of Fe in the Hamersley Group alone; Trendall and Blockley 1970, page 275).

6. Aside from Fe(II)-bearing carbonate facies (including ankerite) that clearly show metamorphic overprints, texturally primary siderite exhibits $\delta^{13}C$ signatures that are consistent with abiotic precipitation fractionation from a hydrothermal-seawater mixing fluid and/or crystal growth at elevated solution saturation (kinetic isotope effect). This prompts a re-evaluation of how biological processes might have controlled the formation of siderite in the geologic record.

The end.

Supplementary chapters

S.1 Siderite solubility determination

S.1.1 Thermodynamic properties of Fe(II) carbonate.

Thermodynamic properties of minerals and their dissolved species are essential in understanding water-mineral interaction and as well as constructing kinetic models during precipitation and dissolution, with associated isotopic fractionation. The dissolution reactions of siderite with its corresponding dissolved species may be written as follows (assuming ideal stoichiometry, pure mineral phases, and water activity of unity):

$$\mathrm{FeCO_3} \overset{K_{sp,sid}}{\rightleftharpoons} \mathrm{Fe^{2+}} + \mathrm{CO_3^{2-}}, \tag{S.1}$$

where the solubility product K_{sp} of a mineral phase is the equilibrium constant K_{eq} of a specific dissolution reaction, and it can be obtained from careful experimentation. In the dissolution reactions stated above, K_{sp} is conventionally determined by measuring the concentrations of dissolved species in the form of thermodynamic activity (a) in a solution at equilibrium state, known as the ionic activity product (IAP) of a solution. Take siderite dissolution (Eq. S.1) as an example:

$$K_{sp,sid} = K_{eq,sid} = IAP_{eq,sid} = a_{\mathrm{Fe^{2+}}} a_{\mathrm{CO_3^{2-}}}, \tag{S.2}$$

where eq denotes equilibrium condition. Mineral precipitation is predicted when solution IAP is greater than the K_{sp} of a mineral phase, otherwise, dissolution is predicted. The ratio between IAP and K_{sp} is termed the saturation state (Ω) of a solution, which is often expressed in logarithmic form as the saturation index (SI):

$$SI = \log(\frac{IAP}{K_{sp}}) = \log IAP - \log K_{sp}. \tag{S.3}$$

K_{sp} can also be estimated from the standard state Gibbs free energy of

reaction (ΔG_r^o; 298.15 K; 1 bar) in the following:

$$K_{sp} = \exp(\frac{-\Delta G_r^o}{RT}), \tag{S.4}$$

where T is temperatures in K; R is the ideal gas constant 8.3144598 J K^{-1} mol^{-1}. ΔG_r^o (J mol^{-1}) of dissolution reactions listed above can be tabulated from the standard state Gibbs free energy of formation (ΔG_f^o) of their corresponding reactants and species, from a thermodynamic database of choice, in the following formalisms:

$$\Delta G_r^o(\mathrm{FeCO_3}) = \Delta G_f^o(\mathrm{Fe^{2+}}) + \Delta G_f^o(\mathrm{CO_3^{2-}}) - \Delta G_f^o(\mathrm{FeCO_3}). \tag{S.5}$$

Estimation of K_{eq} and K_{sp} from the thermodynamic properties of dissolved species (calorimetric determination) only provide guidance where experimental results (solubility determination) are lacking. When discrepancy arises between these two methods of determination, direct solubility measurements are always referred to as reliable and accurate values. Since Smith (1918) first experimentally determined siderite solubility, voluminous experimental evaluations have been provided by numerous authors (Bénézeth et al. 2009; Bruno et al. 1992; Greenberg and Tomson 1992; Jensen et al. 2002; Ptacek 1992; Singer and Stumm 1970). Similarly, after Richards and Behr (1906) first documented the standard state properties of Fe^{2+}, the determination method and results have been updated with continuous effort (e.g., Parker and Khodakovskii 1995; Patrick and Thompson 1953; Randall and Frandsen 1932; Robie and Hemingway 1995; Robie et al. 1978; Tremaine and Leblanc 1980; Tremaine et al. 1977; Wagman et al. 1982). However, as Nordstrom et al. (1990) eloquently stated "Unfortunately, an internally consistent thermodynamic database that is accurate for all modelling objectives, has not been achieved. Nor is it likely to be achieved in the near future, the best that can be hoped for is a tolerable level of inconsistency, with continuing progress toward the utopian goal through national and international consensus... The use of

free energies both for the database and to calculate equilibrium constants has been avoided as much as possible because such an approach can introduce much larger errors than the use of equilibrium constants... hence, the best data for use in chemical modelling will be those values based on reaction equilibria and not those based on free energies of individual reactants and products."

Under such notion, this chapter is set out to revisit key experimentations from which their solubility products have been widely used in the literature, to state the sources of discrepancies where known, and to clarify the values employed in the calculation of mineral solubility and solution saturation. Table. S.1 presents a list of reported siderite solubility products that will be discussed herein, for a more complete compilation of available thermodynamic properties of Fe(II)-carbonate minerals, the readers are referred to the public technical report from the U.S. Department of Energy Office of Scientific and Technical Information (Apps and Wilkin 2015). Recent critical reviews and recommendations on the compatibility and consistency among the reported properties and auxiliary thermodynamic databases regarding siderite solubility have also been provided by Preis and Gamsjäger (2002) and Fosbøl et al. (2010).

S.1.2 Speciation schemes.

The experimental determination of equilibrium constant or solubility product can be broadly categorised into two methods, either by approaching the solid-solution equilibrium from undersaturated solution via a mineral dissolution reaction, or by approaching equilibrium from supersaturated solution via a mineral precipitation reaction. In both methods, the concentrations of dissolved species in the solution are measured using various techniques until no change is observed, that is, an equilibrium state between the solid and solution is reached. The solution chemistry at equilibrium is then used to calculate the solubility product of a mineral phase. However, the measured concentration of a dissolved species should not be directly translated back to its activity (thermodynamic availability) without placing a careful consideration on the

I = 0 molal, T = 298.15 K, and 1 bar, unless noted

$\log K_{sp}$	Method	Speciation scheme	Sources
-10.24	Precipitation		Singer and Stumm (1970)
-10.32[3]	Dissolution (wet)	$FeHCO^{3+}$, $FeCO_3(aq)$	Jensen et al. (2002)
-10.43[4]	Dissolution (wet)	$FeHCO^{3+}$, $FeCO_3(aq)$	Jensen et al. (2002)
-10.45[3]	Refitting Singer and Stumm (1970)	$FeHCO^{3+}$, $FeCO_3(aq)$, $FeOH^+$	Nordstrom et al. (1990)
-10.46[1,2]	Dissolution	$Fe(HCO_3)_2(aq)$	Smith (1918)
-10.50[1]	Refitting Smith (1918)	$Fe(HCO_3)_2(aq)$	Kelley and Anderson (1935)
-10.59[5]	Refitting Greenberg and Tomson (1992)	$FeCO_3(aq)$, $Fe(CO_3)_2^{2-}$	Preis and Gamsjäger (2002)
-10.68[3]	Dissolution (dry)	$FeHCO^{3+}$, $FeCO_3(aq)$	Jensen et al. (2002)
-10.68	Refitting Smith (1918)	$Fe(HCO_3)_2(aq)$	Kelley and Anderson (1935)
-10.77[3]	Precipitation	$FeHCO^{3+}$, $FeCO_3(aq)$, $FeOH^+$	Greenberg and Tomson (1992)
-10.80[5]	Dissolution	$FeCO_3(aq)$, $Fe(CO_3)_2^{2-}$	Bruno et al. (1992)
-10.89[3]	"Refitting Smith (1918)	$FeHCO^{3+}$, $FeCO_3(aq)$, $FeOH^+$	Nordstrom et al. (1990)
-11.03[4]	Dissolution (dry)	$FeHCO^{3+}$, $FeCO_3(aq)$	Jensen et al. (2002)
-11.06[3]	Dissolution	$FeHCO^{3+}$, $FeCO_3(aq)$, $FeOH^+$	Ptacek and Blowes (1993)

Table S.1: A shortlist of reported siderite solubility product. Speciation scheme section indicates additional soluble Fe(II)-compound(s) to the basic speciation scheme used in the calculation of solubility product. (wet) and (dry) differentiate solubility experimentation using freshly precipitated (wet) versus matured crystalline (dry) siderite [1]: calculated for temperature at 30 °C. [2]: no ionic strength control was applied to experiments. [3]: equilibrium constants for soluble Fe(II)-compounds from Nordstrom et al. (1990). [4]: equilibrium constants for soluble Fe(II)-compounds from Fouillac and Criaud (1984). [5]: equilibrium constants for soluble Fe(II)-compounds from Bruno et al. (1992). It is demonstrated here the disparity in $\log K_{sp}$ can be caused by the differences in the methods of achieving equilibrium, the natures (e.g., wet vs. dry) of materials used, the applied speciation schemes, and the equilibrium constants of Fe(II)-compounds for the same speciation scheme.

possible existence of multiple soluble compounds/complexes at the time of sampling. For instance, in this study, ICP-OES and ICP-MS elemental analyses are carried out on diluted and acidified (pH < 2) solution sample, which provide the total iron content (Fe(II)) in the sample regardless of the properties or proportions of possible soluble Fe(II)-compounds (Fe_{cmd}) in the original solution. Other methods that directly measure the concentration of free ferrous iron (Fe^{2+}) in the solution (e.g., divalent cation electrode) are subject to sample preparation and treatment which may or may not release all Fe_{cmd}, thus, may lead to a conclusion of a lower K_{sp} value.

To account for such potential deviation between measured and estimated mineral solubility, a number of soluble compounds have been proposed to be present in a system saturated with respect to $FeCO_3$. The combinations of different compounds and dissolved species are referred to as speciation schemes in the following discussion. It is usually assumed that $H_2O(l)$, H^+, OH^-, Fe^{2+}, $CO_2(aq)$, HCO_3^-, and CO_3^{2-} are present in a solution, where $[Fe(II)] = [Fe^{2+}]$; these dissolved species constitute a basic speciation scheme. Extended speciation schemes have been proposed and used in many studies, where Fe(II) is partitioned among Fe^{2+} and soluble Fe(II)-compounds: $[Fe(II)] = [Fe^{2+}] + \sum[Fe_{cmd}]$. The choice of additional compounds, their combinations, and properties vary significantly in the literature (Table. S.1), therefore, it is important to specify the speciation scheme from which the solubility product is calculated. For a detailed evaluation of the speciation schemes used in solubility calculation, the readers are referred to Fosbøl et al. (2010, and references therein).

S.1.3 Siderite solubility product.

Smith (1918) conducted a series of closed-system anoxic dissolution experiments in which 50 to 100 g of synthetic siderite were placed in 1 L of water saturated at different pCO_2 levels and rotated in a sealed steel bottle at 30 °C for a week to reach an equilibrium state. Noting that siderite ($FeCO_3$) is more

soluble in carbonated water (e.g., Wagner 1867), Smith (1918) included a more soluble Fe(II)-bicarbonate ($Fe(HCO_3)_2(aq)$) phase in his speciation scheme, where Fe^{2+} was calculated as an ionisation product of $Fe(HCO_3)_2(aq)$ with degrees of ionisations (α'; to be differentiated from thermodynamic activity a): $[Fe^{2+}]=\alpha' \times [Fe(HCO_3)_2(aq)]$. The degrees of ionisations for $Fe(HCO_3)_2(aq)$ were assumed to be the same as for barium nitrate solutions of equivalent concentrations; $\alpha' \approx 0.9$. In this extended speciation scheme, the total iron is expected to be: $[Fe(II)] = [Fe^{2+}] + [Fe(HCO_3)_2(aq)] = (1+\alpha')\ [Fe(HCO_3)_2(aq)]$. Solution $[CO_3^{2-}]$ was calculated by subtracting the stoichiometric amount of $Fe(HCO_3)_2(aq)$ from the measured total CO_2 content, followed by carbonate speciation calculation with 1st dissociation constant of carbonic acid (K_1) provided by Kendall (1916) and 2nd dissociation constant (K_2) from Seyler and Lloyd (1917). In so doing Smith (1918) upscaled K_1 (25 °C) to 30 °C by assuming a same linear increase as from 0 °C to 25 °C, and used K_2 (25 °C) as the value at 30 °C due to the lack of experimental data regarding the temperature dependence of K_2 at the time of publication. By determining the Fe(II) via redox extraction and titration with potassium permanganate, and the total $CO_2(aq)$ via acidified purging and absorption with soda-lime + phosphorus pentoxide, Smith (1918) obtained $K_{sp} = [Fe^{2+}] \times [CO_3^{2-}] = 3.453 \times 10^{-11}$ at 30 °C, or $\log K_{sp}$ (30 °C) $= -10.46$.

Many subsequent studies employed similar dissolution method, and the experimental data by Smith (1918) have been revaluated and reinterpreted for numerous times. It should be noted that Smith (1918) did not apply ionic strength control to his experiments, nor ionic strength correction in the calculation of solubility (as the concept of ionic strength was only formally introduced later by Lewis and Randall 1921). Fosbøl et al. (2010) noted that the extended speciation scheme used by Smith (1918) is uncommon compared to the more recent advance in the field. By setting $\alpha' = 1$ and $[Fe(II)] = [Fe(HCO_3)_2(aq)]$, Fosbøl et al. (2010) derived $\log K_{sp}$ (30 °C)$= -10.32$ in CO_2-free solution; no review has been provided on the refitting by Fosbøl et al.

(2010).

Kelley and Anderson (1935) provided a summary on existent thermodynamic data for metal carbonate and dissociation constants of carbonic acid at the time. They refitted Smith (1918) measurements with a different set of dissociation constants of carbonic acid (K_1 and K_2) and computed $\log K_{sp}$ (30 °C)= −10.50. This value has been adopted by a number of databases as the value at 25 °C, notably the National Institute of Standards and Technology (NIST) database compiled by Wagman et al., (1982), and the previous version of the United States Geological Survey (USGS) database compiled by Robie et al. (1978). Kelley and Anderson (1935) also provided $\log K_{sp}$ (25 °C)= −10.68 with a temperature correction; though the conversion method was not specified. Fosbøl et al. (2010) criticised such conversion by pointing out that $\log K_{sp}$ (25 °C)= −10.68 can only be reached by incorrectly assuming the Gibbs free energy of reaction are the same at the two temperatures; ΔG_r^o (30 °C) = ΔG_r^o (25 °C). Nevertheless, $\log K_{sp}$ (25 °C) = −10.68 has been incorporated in many data collections, notably by Latimer (1952) and Helgeson (1969), which were extensively used in water treatment and corrosion sciences among many others (Martell and Smith 1976; Stumm and Lee 1960). Consequently, $\log K_{sp} = -10.68$ became the most commonly used value in the literature.

Noting the observed supersaturation in natural water with respect to reported siderite solubility (e.g., Ghosh et al. 1966; Hem 1960), Singer and Stumm (1970) conducted a series of siderite precipitation experiments using iron perchlorate ($Fe(ClO_4)_2$) and sodium bicarbonate ($NaHCO_3$) at four different temperatures between 17 and 30 °C for one to five months to reach equilibria. All experiments were set to solution ionic strength of 0.1 mol L^{-1} to ensure the constancy of the activity coefficients. A basic speciation scheme was used in their study, where [Fe(II)]=[Fe^{2+}]. [Fe(II)] was determined by filtering an aliquot of solution (100 µm pore diameter) into diluted acid under a CO_2 atmosphere and treating with bathophenanthroline (Ghosh et al. 1967). Alkalinity (≈

$[HCO_3^-] + 2[CO_3^{2-}]$) was determined by acidimetric titration. Using an ionic strength correction based on Davies equation (Davies 1962) and a temperature correction based on van't Hoff law, Singer and Stumm (1970) concluded $\log K_{sp} = -10.24 \pm 0.17$ at 25 °C; three times higher than $\log K_{sp} = -10.68$ from Kelley and Anderson (1935). In addition, by using a divalent cation electrode sensitive to Fe^{2+} in a different set of experiments, Singer and Stumm (1970) demonstrated there was no measurable deviation of $[Fe^{2+}]$ from a given [Fe(II)] in solution with alkalinity up to 1.1×10^{-2} eq L^{-1}, indicating a negligible presence of soluble Fe(II)-compounds at least in solution pH between 4.82 to 5.85.

It should be noted that, with a basic speciation scheme, the K_{sp} value by Singer and Stumm (1970) is one of the highest among reported values. When fitted with an extended speciation scheme that includes soluble compounds $FeHCO_3^+$, $FeCO_3(aq)$, and $FeOH^+$, Nordstrom et al. (1990) derived $\log K_{sp} = -10.45$ and recommended for the solubility of precipitated siderite. Moreover, Singer and Stumm (1970) were the first to obtain K_{sp} by approaching equilibria via precipitation from a supersaturated solution, in contrast to a dissolution reaction employed in most experimentations before and after (Braun 1991; Bruno et al. 1992; Jensen et al. 2002; Ptacek and Blowes 1993; Smith 1918). Another potential contributor to the high solubility value was the pore size used in filtration by Singer and Stumm (1970); 100 µm in diameter. The present study observed that nucleated Fe(II)-carbonate spherical particles are typically of $\sim 5 - 15$ µm in diameter (Chapter 2, Fig. 2.5; Jiang and Tosca 2019). Though the diameter of nuclei is subject to the physical (e.g., stirring) and chemical conditions (e.g., nucleation and growth rate), the possibility of unfiltered siderite particulate re-dissolved in the analytical aliquots should still be noted.

Jensen et al. (2002) conducted a series of precipitation and dissolution experiments in Fe^{2+}-Ca^{2+}-Mn^{2+} systems and reported that equilibrium via dissolution of siderite was reached after 10 days. In contrast, equilibrium via

precipitation of siderite was not reached after 474 days. It was possible that in Singer and Stumm (1970) experiments equilibria were not reached after 30 to 150 days, as the evolution of solution chemistries was not reported. However, the supersaturation reported by Jensen et al. (2002, and Fig. 1 therein) at day 474 should only be taken as a grain of salt, due to the scarcity of measurements and apparent deviation in the later stage of their experiments. In addition, Jensen et al. (2002) precipitated siderite heterogeneously on the surface of bentonite in the presence of Ca^{2+} and Mn^{2+}, in contrast to the homogeneous precipitation from $NaClO_4$ matrix by Singer and Stumm (1970).

Based on their dissolution experiments, Jensen et al. (2002) concluded two K_{sp} values depending on the condition of siderite crystals used; $\log K_{sp} = -10.43$ for freshly prepared wet crystals, and $\log K_{sp} = -11.03$ for dry and matured crystals (105 °C for 24 h), using a speciation scheme proposed by Fouillac and Criaud (1984), and ionic strength correction based on Davies equation (Davies 1962). To further demonstrate the influence of speciation schemes on solubility calculation, Jensen et al. (2002) applied the equilibrium constants for soluble Fe(II)-compounds from Nordstrom et al. (1990) and calculated $\log K_{sp}$ (wet)$= -10.32$ and $\log K_{sp}$ (dry)$= -10.68$, for comparison.

Preis and Gamsjäger (2002) made a critical review on the thermodynamic properties of siderite and revaluated experimental data from dissolution studies (Bruno et al. 1992; Greenberg and Tomson 1992; Reiterer et al. 1981; Silva et al. 2002; Smith 1918) by using a Gibbs energy minimisation program ChemSage to attain the best internal consistency. Preis and Gamsjäger (2002) recommended ΔG^o_f (Fe^{2+})$= -90.5 \pm 1.0$ kJ mol^{-1} from Parker and Khodakovskii (1995), concluded ΔG^o_f ($FeCO_3$)$= -678.9 \pm 1.2$ kJ mol^{-1}, and presented a siderite solubility translates into $\log K_{sp} = -10.59$ (they used a dissolution reaction differ from Eq. S.1) by adopting the speciation scheme proposed by Bruno et al. (1992) and experimental measurements from Greenberg and Tomson (1992).

S.1.4 Conclusion.

In summary, the significant discrepancies among the experimentally determined siderite solubility values can be attributed to:

1. Methods in achieving solid-solution equilibrium: precipitation versus dissolution.
2. Properties of siderite used in dissolution: freshly prepared versus mature crystalline.
3. Reagents used in precipitation: e.g., $FeCl_2$ versus $Fe(ClO_4)_2$, and Na_2CO_3 versus $NaHCO_3$.
4. Activity coefficient approximation: Davies equation (Davies 1962), $\dot{B}$ equation (Helgeson and Kirkham 1974a), or Pitzer equation (Pitzer and Brewer 1961).
5. Temperature correction.
6. Speciation schemes of soluble Fe(II)- and CO_3^{2-}-compounds.
7. Equilibrium constants for soluble Fe(II)- and CO_3^{2-}-compounds.

Overall, the use of different speciation scheme places the greatest difference among the reported solubility values. The existence of many soluble Fe(II)-compounds is still an ongoing debate, their properties and proportions in different aqueous conditions are uncertain, and their combinations vary significantly in the literature (see review by Fosbøl et al. 2010, and references therein). A detailed discussion on the existent speciation scheme is, unfortunately, beyond the scope of this study.

In order to employ the most direct measurements from experimental conditions most relevant to this study, the choice of solubility product of siderite from the reported values (Table. S.1) follows the differentiation listed above. Siderite solubility $\log K_{sp} = -10.24$ by Singer and Stumm (1970) is chosen for

this study, for reasons that the value was measured from homogeneous precipitation using similar reagents and calculated with a basic speciation scheme. In addition, Singer and Stumm (1970) value has been reviewed and recommended by Fosbøl et al. (2010) for both NIST and CODATA thermodynamic database, and it is in good agreements with recommended thermodynamic properties of $FeCO_3$ and Fe^{2+} by Preis and Gamsjäger (2002).

S.2 Thermodynamics of aqueous electrolyte systems

S.2.1 Introduction

In the realm of thermodynamic modelling, numerous elaborate mathematical equations that stem from established physical laws have often been employed in predicting the behaviour of an aqueous electrolyte system. As the complexity of such a system increases, these thermodynamic models have been extended to adjust predictions to be concordant to the ever-advancing experimentation with inexhaustible and diligent effort. The key thermodynamic formalisms concerned in this study is the mathematical expressions against which the chemical properties of aqueous electrolyte systems can be scaled, thus, the kinetics of chemical reactions in such systems can be accurately predicted.

The current standard physical chemistry approach is one derivative or another of the Debye-Hückel equation, formulated on the concepts like thermodynamic activity and activity coefficient, which is itself a function of another concept, solution ionic strength. Such approach was instigated and developed by Gilbert Lewis (1875-1946), Merle Randall (1888-1950), Peter Debye (1884-1966), Erich Hückel (1895-1980), Kenneth Pitzer (1914-1997), and Harold Helgeson (1931-2007), among many other remarkable.

By the late twentieth century, increasingly complicated mathematical equations containing a growing number of empirical correction factors were being used for describing complex and, notably, concentrated electrolyte solutions ranging from the intracellular fluids to the oceans. However, criticisms arose regarding the extensive use of empirical parameters that lack physical significance, the expedient generalisation of ionic strength, and the arbitrary nature of the concepts of activity and activity coefficient. Overall, the extension of a limited physical model into a curve-fitting exercise without necessarily improving the understanding of the underlying quantum mechanics (e.g., Berg 2015; Darvell and Leung 1991; Franks 1991; Monk 1993).

This chapter briefly revisits the developmental history of the now widely-used Debye-Hückel model, states the key parameters in its conceptualisation, assumptions in its generalisation, and additions of empirical parameters in its adaptation. A brief summary is provided on the limitation of adapting such formalisms in this study.

S.2.2 Activity, activity coefficient, and ionic strength

In the earlier studies of electrolyte solution, van't Hoff observed that the osmotic pressure (π_{os}) of a dilute non-electrolyte solution followed the relation $\pi_{os}V = RT$ (V is the volume of solution per mole of solute dissolved, R is the gas constant, T is temperature in K), whereas the osmotic pressure of a dilute electrolyte solution like NaCl followed roughly $\pi_{os}V = 2RT$; consistent with the notion that NaCl was completely dissociated into two parts in the solution that resulted in doubling the osmotic pressure. Therefore, van't Hoff (1886, in French) proposed the equation $\pi_{os}V = jRT$ where j was an empirical factor used to interpret dissociation of electrolyte in dilute solution, for example, $j = 1$ for non-electrolyte, $j = 2$ for 1:1 electrolyte, $j = 3$ for 2:1 electrolyte.

van't Hoff equation formed the key concept of electrolytic dissociation theory led by Arrhenius (1884, 1887, 1912, 1914), in which it was proposed that one molecule of a stable salt like NaCl dissociates in solution into one molecule of positively charge Na^+ ion and one molecule of negatively charged Cl^- ion. The dissociation theory is so fundamental in modern chemistry, the controversies of its admittance can be easily overlooked; it was not known at the time, that the parts of a crystalline salt were already charged and held together in a solid form via the later-defined ionic bonding, and many notable empirical chemists objected the dissociation theory by questioning the source of electricity that charged the salts in the process of dissolution and dissociation (Armstrong 1887, 1889; Fitzgerald 1896; Kahlenberg 1900, 1905)

Nevertheless, the similarity between van't Hoff equation $\pi_{os}V = jRT$ and the ideal gas law $PV = RT$ led some chemists of the era to suppose the solute

molecules in an ideal solution must behave like ideal gas molecules (i.e., ideal solution law stems from Raoult's law; Raoult 1886, in French). In practice, van't Hoff factor j is often calculated to be different, sometimes substantially, from the expected integers, which led to the conceptualisation of thermodynamic degree of dissociation in the dissociation theory (e.g., Arrhenius 1884, 1887), stated that dissociation of electrolytes can be partial in complex and concentrated solutions, thus, deviate from their ideal behaviours. An important implication of thermodynamic degree of dissociation is that, in an infinitely dilute solution close to ideality electrolytes completely dissociate and the chemical potential of the electrolyte solution is directly dependent on the concentrations of their dissociated ions; the degree of dissociation equals to unity. The deviations from ideality in complex and concentrated solutions had been regarded as the "effective concentration" or the "active mass" of a species. The "active mass" was coined as thermodynamic activity (a) by Gilbert N. Lewis (Lewis 1907), in the sense that the species' chemical potential depends on the activity of a real solution in the same way that it would depend on the concentration for an ideal solution.

In their subsequent contributions, Lewis (1912) and Lewis and Randall (1921) redefined the term activity coefficient (γ), first introduced by Bronsted (1920), to be used in modifying the molality (C) of a fully dissociable electrolyte into its geometric/stoichiometric mean activity ($a_{\pm}$) of the two particles resulting from dissolution. In general, if an electrolyte of composition X_nY_m fully dissociates as $X_nY_m = nX + mY$, then the mean molality ($C_{\pm}$) of the dissociated electrolyte is: $C_{\pm} = C(CX_nCY_m)^{\frac{1}{n+m}}$, and the stoichiometric mean activity is: $a_{\pm} = (a_X^n a_Y^m)^{\frac{1}{n+m}}$, thus, the geometric/stoichiometric mean activity coefficient ($\gamma_{\pm}$) takes the following form:

$$\gamma_{\pm} = \frac{a_{\pm}}{C_{\pm}} = (\gamma_X^n \gamma_Y^m)^{\frac{1}{n+m}}. \tag{S.6}$$

From Eq. S.6, single-ion activity coefficients may be estimated from meas-

ured mean activity coefficient of an electrolyte in a simple solution where the stoichiometry is known (Debye and Hückel 1923; Lewis and Randall 1921). However, single-ion activity coefficients are regarded as either experimentally unmeasurable or physically meaningless (Guggenheim 1928; Lewis and Randall 1921; Moore 1999; Nic et al. 2009; Rockwood 2015). Because for an electrolyte solution to retain its electroneutrality, the charges of individual ions must be neutralised by oppositely charged ions. That is, the measurable properties of an electrolyte solution are always affected by both, if not more, dissolved species. Single-ions activity coefficients are nonetheless desirable in modelling an electrolyte solution of multiple components. With careful considerations, Lewis and Randall (1921) provided estimated single-ion activity coefficients in Table XXIV (pp. 1147; therein). Yet, caution is urged in universally applying single-ion activity coefficients to mixed electrolyte solutions, in which the activity coefficients all electrolytes have not been experimentally validated

Noting that with an increasing solution salt concentration, the mean activity of a species deviates from the proportionality to its molality, that is, a non-linear inverse correlation of the mean activity coefficient with an increasing salt concentration (Lewis 1912), Lewis and Randall (1921) established the concept of stoichiometric ionic strength as a measure of the bulk solution chemistry with which the mean activity coefficient could be correlated. Such concept is formulated on the proposition that the mean activity coefficient of a given electrolyte depends simply upon the total equivalent molal concentration of electrolytes (by assuming that one molecule of a bivalent ion has the effect of two molecules of a univalent ion). The stoichiometric ionic strength (I; molal) of a solution is calculated as half of the sum of the product of the molality (C) of each dissolved species and the square of its charge (z) when fully dissociated, the subscript i denotes to the ith species in a solution:

$$I = \frac{1}{2} \sum_i C_i z_i^2. \tag{S.7}$$

By fitting available experimentally measured mean activity coefficients with stoichiometric ionic strength, Lewis and Randall (1921) proposed a generalisation that states the activity coefficient of every strong electrolyte, and the individual activity coefficient of ion, is the same in all dilute solutions of the same stoichiometric ionic strength; $\gamma_{\pm} \propto \sqrt{I}$ and $\gamma_i \propto \sqrt{I}$. Such generalisation has been and still is, widely popular and influential, despite scepticisms and objections throughout the century (e.g., Darvell and Leung 1991; Franks 1991; Heyrovska 1991, and references therein). In addition, Lewis and Randall (1921, and Table XIV therein, pp. 1132) observed that the activity coefficients of typical electrolytes first decreases with increasing ionic strength, only to increase at ionic strength around 0.5 molal or higher (see later discussion).

S.2.3 Debye-Hückel equation

Shortly after the introduction of the concepts of activity, activity coefficient, and their correlation with stoichiometric ionic strength, a quantum-mechanic explanation for the ionic behaviours in an electrolyte solution was first formulated in the prominent Debye-Hückel theory (Debye and Hückel 1923, in German). In the Debye-Hückel theory, a solvent is treated as an ideal structureless dielectric fluid, with ions as spherically uniform particles with charges located at their centres. The primary interactions among ions are considered to be the long-range electrostatic interactions (i.e., Coulombic forces) that cause each ion to be surrounded by an ionic atmosphere of the oppositely charged ions (causing order), competing against the effects of thermal motions (causing disorder). Two physical parameters were specified in the original theory that contributes to the electrostatic interactions, they are: (1) the electrostatic potential for an ion expressed by Poisson's equation, and (2) the local charge density of the surrounding ionic cloud at a given distance calculated by Boltzmann distribution.

In the calculation of the local charge density, an equation that is similar to Lewis and Randall (1921) stoichiometric ionic strength generalisation

was included in Debye and Hückel (1923) Poisson-Boltzmann equations; in a simplified form, the local charge density equation is the same as Eq. S.7. However, the local charge density in the Debye-Hückel theory is an integral part of the calculation that specifically describes the electrostatic force one ion experiences from surrounding charged species, in contrast to the empirical generalisation of stoichiometric ionic strength based on the bulk solution molality. One could expect the local charge density surrounding a charged ion to decrease in a concentrated multi-electrolyte solution due to the formation of neutral compounds; the local charge density may be considerably smaller than the stoichiometric ionic strength. In fact, a number of authors regard Debye-Hückel's local charge density to be the exact definition that shall be assigned to ionic strength, and choose not to refer to Lewis-Randal generalisation when dealing with Debye-Hückel treatment (e.g., Harned and Owen 1958; Monk 1993; Sastre de Vicente 2004, and references therein). For example, Helgeson and Kirkham (1974a) and Helgeson (1969, 1981) re-emphasised on the local charge density in the Debye-Hückel theory and termed it "true ionic strength" ($\overline{I}$), whereas Monk (1993) considered such an integral part of the theory need not be given a name as it was not a stand-alone concept. The difference between stoichiometric ionic strength and local charge density in dilute solution at 25 °C and 1 bar is often considered negligible, hence, the use of Eq. S.7 interchangeably for both definitions has been a common practice. In the following theoretical discussion, the Debye-Hückel local charge density is referred to as the true ionic strength ($\overline{I}$), whereas solution concentrations are expressed in the terms of stoichiometric ionic strength (I) as reported in most of the literature.

A complete derivation of the physical parameters and assumptions in the Debye-Hückel theory is necessary for understanding its limitations and applications, the reader is referred to available standard references such as Bockris and Reddy (1970), Harned and Owen (1958), Monk (1961) and Robinson and Stokes (2002). Presented below is the extended Debye-Hückel equation that

has been widely used for dilute natural solutions like freshwater or groundwater ($I < 0.1$ molal; e.g., Anderson 2017; Stumm and Morgan 1996):

$$\log \gamma_{\pm} = -\frac{A z_i^2 \sqrt{I}}{1 + B \mathring{a}_i \sqrt{I}}, \tag{S.8}$$

where A and B are the Debye-Hückel coefficients; $\mathring{a}_i$ is the ion size parameter describing the mean distance of the closest approach of ions.

The Debye-Hückel coefficients are derived from the physical properties of the solvent. Although the original units were given in molarity (Debye and Hückel 1923), the use of coefficients A and B often converted into molality. Below are the revised versions adapted from Helgeson and Kirkham (1974b), for Eq. S.8 with $\mathring{a}_i$ expressed in metre:

$$A = \frac{e^3 (2\pi N_A \rho_{\mathrm{H_2O}})^{\frac{1}{2}}}{72.8141 (\varepsilon_{\mathrm{H_2O}} k_B T)^{\frac{3}{2}}}, \tag{S.9}$$

$$B = \left(\frac{80\pi e^2 N_A \rho_{\mathrm{H_2O}}}{\varepsilon_{\mathrm{H_2O}} k_B T}\right)^{\frac{1}{2}}, \tag{S.10}$$

where e is the elementary charge (4.8033×10^{-10} esu), N_A is Avogadro's number (6.0221×10^{23} mol^{-1}), k_B is Boltzmann constant (1.3806×10^{-16} erg K^{-1}), $\rho_{\mathrm{H_2O}}$ is the density of pure water (g cm^{-3}), $\varepsilon_{\mathrm{H_2O}}$ is the relative permittivity of pure water (dimensionless), and numerical values in the equations convert CGS-Gaussian units into SI units. All the fundamental physical parameters are either taken or converted from CODATA 2014 (Mohr et al. 2016). The determining factors for the Debye-Hückel coefficients are simplified to the temperature (T; K) and pressure (bar) (both are taken into account in $\rho_{\mathrm{H_2O}}$ and $\varepsilon_{\mathrm{H_2O}}$) of the system. At 298.15 K and 1 bar, $\rho_{\mathrm{H_2O}} = 0.9971$ g cm^{-3} (Gildseth et al. 1972) and $\varepsilon_{\mathrm{H_2O}} = 78.4526$ (Uematsu and Frank 1980), thus, $A = 0.5039$ kg$^{\frac{1}{2}}$ mol$^{-\frac{1}{2}}$ and $B = 3.2716 \times 10^9$ kg$^{\frac{1}{2}}$ mol$^{-\frac{1}{2}}$ m^{-1}.

The ion size parameter $\mathring{a}_i$ was loosely defined throughout the development and extension of the Debye-Hückel theory. It has been commonly referred to

as a parameter describing the mean distance of the closest approach of ions; some times it has been taken as the effective diameter of a hydrated ion; to a lesser extent, it has been interpreted as the sum of the radii of the ions of opposite charges. Without an exact definition or a standardised method of determination, considerable discrepancies exist among estimated $\mathring{a}$ values for individual ions. For example, as ions are generally found in solid crystalline ionic compounds (i.e., salt), the radius of an unhydrated ion is often taken as a half of the measured inter-ionic distance in the crystal lattices, or with theoretical considerations of how this distance is apportioned among the ions (Bonino and Centola 1933; Brüll 1934; Goldschmidt 1926; Pauling 1927). The diameter of a hydrated ion is then tabulated by adding the thickness of a hydration shell, with an assumed coordination number (often 6, octahedral), to the radius of the unhydrated ion. Other methods of estimating $\mathring{a}$ include calculation from ionic mobility (Brüll 1934) and chemical hydration determination by entropy deficiency method (Ulich 1930), the values of various early approximations have been compiled and compared by Kielland (1937, and Table.1 therein).

Recent determinations of aqueous ionic size have utilised monochromatic diffraction on aqueous solution, including X-ray, neutron, and electron diffraction, NMR structure analysis, in combination with a variety of computer simulation methods (e.g., Jenkins and Thakur 1979; Kruh 1962; Mallouk et al. 1984; Marcus 1988; Ohtaki and Radnai 1993; Roobottom et al. 1999; Simoes et al. 2017). In calculating the size of a hydrated ion, only the first hydration shell is conventionally considered, known as the first-neighbour model. In the case of monatomic ions, the effective hydrated diameter can be approximated from the internuclear distance from the unhydrated ion to the oxygen atom in the nearest water molecule (d_{ion-w}) plus the radius of a water molecule (r_w); $\mathring{a}_i \approx 2 \times (d_{ion-w} + r_w)$; note that r_w is an appropriate distance that characterises the "radius" of a water molecule. One approximation of r_w is a half of the mean intermolecular distance d_{w-w} in liquid water, which has been

reported with great consistency: $r_w = 0.142 \pm 0.0005$ nm (Marcus 1988, and references therein). Ionic radii of most monatomic ions and even many polyatomic ions have been estimated through a combined diffraction and computer simulation methods to a satisfactory precision and with continuous improvement (e.g., Marcus 1988; Ohtaki and Radnai 1993; Roobottom et al. 1999; Simoes et al. 2017). For example, taking values compiled by Marcus (1988), $\mathring{a}_{\mathrm{Fe}^{2+}} \approx 2 \times (d_{\mathrm{Fe}^{2+}-w} + r_w) \approx 2 \times (0.21 + 0.142) \approx 0.704$ nm, compared to widely used $\mathring{a}_{\mathrm{Fe}^{2+}} = 0.6$ nm summarised by Kielland (1937).

However, it is conceded that in many cases fixed values of $\mathring{a}$ determined by various methods fit poorly into Debye-Hückel formula, for them to yield activity coefficients that are consistent with experimental data from concentrated solutions. This is partially attributed to the limiting physical model that restricts the extended Debye-Hückel equation (Eq. S.8) to sufficiently dilute solutions; where the term "sufficiently dilute" was never explicitly defined. Importantly, two assumptions underlie the term ion size parameter: (1) the ion (and associated water molecules) exert spherically symmetrical force fields that constitute an overall spherical size; (2) an arbitrary boundary could be placed to define the sphere of influence of a hydrated ion. In practice, polyatomic species, including water molecule, are in general non-spherical. And the sphere of influence of a given hydrated ion is subject to short-range electrostatic interactions (e.g., ion association); in itself a function of concentration. Therefore, $\mathring{a}$ has been commonly treated as an adjustable parameter and to be derived by regression-fitting the Debye-Hückel equation (or derivatives) to experimentally determined activity coefficients (Butler 1964; Helgeson and Kirkham 1974b; Helgeson 1969, 1981; Kielland 1937; Pitzer and Brewer 1961; Truesdell and Jones 1974). Nonetheless, the most widely cited $\mathring{a}$ values in the use of the extended Debye-Hückel equation (Eq. S.8) were summarised by Kielland (1937), determined or estimated from various methods (Bjerrum and Unmack 1929; Born and Heisenberg 1924; Landolt et al. 1936) to be used for solution ionic strength up to 0.2 molal. The compilation by Kielland (1937) was later exten-

ded by Butler (1964) and has been incorporated in many popular geochemical modelling tools/software.

The deviation in the $\mathring{a}$ as a function of solution chemistry can be, in part, explained by the change in the sphere of electrostatic influence in the mean-field Poisson-Boltzmann theory. In sufficiently dilute solutions, the electric potential (V_E) of a given ion decays exponentially with distance (d), and the decay constant (κ_D) is defined by the distance from the ion to where V_E is $\frac{1}{e_u}$ (Euler's constant) of its central value ($V_{E,0}$): $V_E = V_{E,0} \times \frac{1}{e_u} = V_{E,0} \times e^{-\kappa_D d}$. From this definition, a specific length can be derived that is the inverse of the decay constant, $d = \kappa_D^{-1}$, and it is referred to as Debye length. κ_D^{-1} in itself is inversely correlated to the square root of true ionic strength and takes the following form (simplified by Russel et al. 1989 for monovalent ions; the validity of Deybe-length formula for multivalent electrolyte has received scepticisms, e.g., Kohonen et al. 2000, and references therein):

$$\kappa_D^{-1} = \left(\frac{\varepsilon_0 \varepsilon_{\mathrm{H_2O}} k_B T}{2 \times 10^3 N_A e^2 \overline{I}}\right)^{\frac{1}{2}}, \tag{S.11}$$

where e is the elementary charge (1.6022×10^{-19} C), N_A is Avogadro's number (6.0221×10^{23} mol^{-1}), ε_0 is the vacuum permittivity (8.8542×10^{-12} C^2 s^2 m^{-2} kg^{-1}), $\varepsilon_{\mathrm{H_2O}}$ is the relative permittivity of water, k_B is Boltzmann constant (1.3806×10^{-23} kg m^2 s^{-2} K^{-1}), T is temperature (K); again, all physical constants taken from CODATA 2014 (Mohr et al. 2016). Following this definition, Debye length for monovalent ions decreases monotonically with increasing true ionic strength. To illustrate, we may take a completely dissociated electrolyte solution ($\overline{I} = I$), and calculate $\kappa_D^{-1} \approx 9.603$ nm in NaCl solution at $I = 0.001$ molal, corresponding to roughly 34 water diameters, whereas $\kappa_D^{-1} \approx 0.947$ nm at $I = 0.1$ molal, equivalent to just over 3 water diameters (Fig. S.7). A shorter Debye length translates into a smaller å, which in turn, a higher activity coefficient; such an effect can be demonstrated by fitting different å values into the extended Debye-Hückel equation (Eq. S.8; Fig.S.8).

At higher concentrations, κ_D^{-1} becomes comparable to molecular dimensions, the Debye-Hückel theory is thus no longer expected to be applicable; ion size effects and ion association come into play (Bockris and Reddy 1998; Smith et al. 2016).

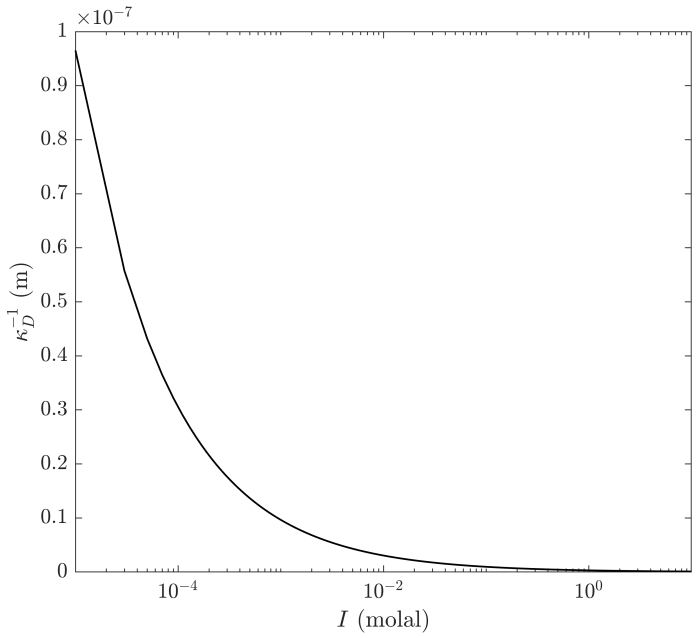


Figure S.7: Debye length (κ_D) of monovalent ion as a function of stoichiometric ionic strength, calculated through Eq. S.7, assuming completely dissociated NaCl solution.

In fact, it is well-known that the Debye length of an ion varies non-monotonically with increasing salt concentration: κ_D^{-1} typically decreases in the dilute regime only to increases at higher concentration (e.g., Bockris and Reddy 1970, 1998; Kjellander and Mitchell 1992; Kjellander and Ulander 1998; Leote de Carvalho and Evans 1994; Onsager 1933; Smith et al. 2016; Stillinger and Lovett 1968); which may explain the non-monotonic variation in activity coefficients initially reported in Lewis (1912) and Lewis and Randall (1921). There have been many theoretical attempts to model additional interactions that occur at higher ionic strength, detailed summaries have been provided by Friedman (1962) and Helgeson (1981). Many derivatives have been proposed to the extended Debye-Hückel equation (Eq. S.8) to be used at higher solution ionic strength, and they are rather similar in effect, in that they add a more or

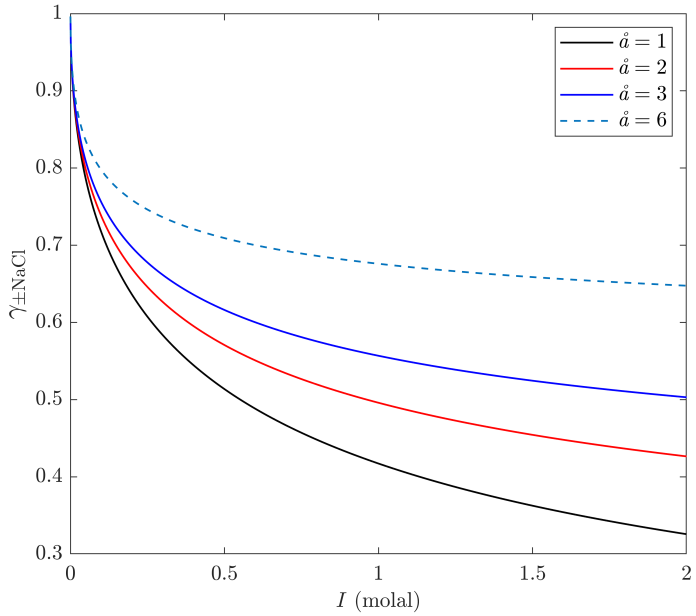


Figure S.8: Mean activity coefficient of NaCl solution as a function of hypothetical $\mathring{a}$, calculated through Eq. S.8

less linear positive term to the right side of the extended Debye-Hückel equation, with more or less empirical approaches. Widely used derivatives include Davies equation (Davies 1938; Davies 1962), ion hydration approach (Stokes and Robinson 1948), and $\dot{B}$ equation (Helgeson and Kirkham 1974a; Helgeson et al. 1981; Helgeson 1969).

S.2.4 Conclusion

Conclusion is yet to be reached in this review. Currently widely used approximations of thermodynamic activity are often one derivative or another of the Debye-Hückel equation (Eq. S.8) with additional fitting parameters to adjust the approximation to a wider or a more specific range of aqueous chemistry. For example, Davies equation (Davies 1938; Davies 1962):

$$\log \gamma_{\pm} = -\frac{A z_i^2 \sqrt{I}}{1 + B \mathring{a}_i \sqrt{I}} + 0.3I,$$

empirically extends the applicability of the Debye-Hückel equation to ionic strength up to 0.2 molal (Davies 1962) by a simple fitting function of the

stoichiometric ionic strength. On the other hand, the widely used $\dot{B}$ equation:

$$\log \gamma_{\pm} = -\frac{A z_i^2 \sqrt{\overline{I}}}{1 + B \mathring{a}_i \sqrt{\overline{I}}} + \dot{B} \overline{I},$$

places emphasis on the speciation scheme in a given solution that determine the true ionic strength ($\overline{I}$), and a fitting $\dot{B}$ function of temperature.

Each method has its own advantage of either being simple or thorough, this study adopt $\dot{B}$ equation proposed by Helgeson and Kirkham (1974a), Helgeson et al. (1981) and Helgeson (1969).

Bibliography

Aagaard, P. and H. C. Helgeson (Mar. 1982). 'Thermodynamic and kinetic constraints on reaction rates among minerals and aqueous solutions; I, Theoretical considerations'. In: *American Journal of Science* 282.3, pp. 237–285. ISSN: 0002-9599. DOI: 10.2475/ajs.282.3.237.

Ahrens, T. J., J. D. O'Keefe and M. A. Lange (1989). 'Formation of atmospheres during accretion of the terrestrial planets'. In: *Origin and Evolution of Planetary and Satellite Atmospheres*. Ed. by S.K. Atreya, J.B. Pollack and M.S. Matthews. Vol. -1. Tucson: University of Arizona Press, pp. 328–385. DOI: hdl:10013/epic.10625.

Alt, Jeffrey C. (Mar. 1995). 'Subseafloor Processes in Mid-Ocean Ridge Hydrothennal Systems'. In: *Geophysical Monograph Series*. Ed. by Susan E. Humphris et al., pp. 85–114. DOI: 10.1029/GM091p0085.

Anderson, G. M. (Gregor Munro) (2017). *Thermodynamics of Natural Systems: Theory and Applications in Geochemistry and Environmental Science*. Third Edit, p. 413. ISBN: 9781107175211.

Apps, John A and Richard T Wilkin (Sept. 2015). *Thermodynamic Properties of Aqueous Carbonate Species and Solid Carbonate Phases of Selected Trace Elements pertinent to Drinking Water Standards of the U.S. Environmental Protection Agency*. Tech. rep. Berkeley, CA (United States): Lawrence Berkeley National Laboratory (LBNL). DOI: 10.2172/1333576.

Armstrong, Henry Edward (1887). 'Comparison between the Views of Dr. Arrhenius and Professor Armstrong on Electrolysis. Reply to Professor Lodge's Criticisms'.

In: *Report of the 57th meeting of the British Association for the Advancement of Science*. Ed. by John Murray. London: Spottiswoode and Co., pp. 354–358.

Armstrong, Henry Edward (1889). 'Note on the foregoing Replay'. In: *Report of the 58th meeting of the British Association for the Advancement of Science*. Ed. by John Murray. London: Spottiswoode and Co., pp. 355–360.

Arrhenius, Svante (1884). *Recherches sur la conductibilité galvanique des électrolytes*. PA Norstedt & Söner.

— (1887). 'Über die Dissociation der in Wasser gelösten Stoffe'. In: *Zeitschrift für physikalische Chemie* 1.1, pp. 631–648.

— (Apr. 1912). 'ELECTROLYTIC DISSOCIATION.' In: *Journal of the American Chemical Society* 34.4, pp. 353–364. ISSN: 0002-7863. DOI: 10.1021/ja02205a001.

— (1914). 'The Theory of Elctrolytic Dissociation'. In: *Journal of Chemical Society, Transactions* 105, pp. 1414–1426.

Assayag, Nelly et al. (Aug. 2006). 'Improved method for isotopic and quantitative analysis of dissolved inorganic carbon in natural water samples'. In: *Rapid Communications in Mass Spectrometry* 20.15, pp. 2243–2251. ISSN: 0951-4198. DOI: 10.1002/rcm.2585.

Ayres, D. E. (Dec. 1972). 'Genesis of Iron-bearing Minerals in Banded Iron Formation Mesobands in The Dales Gorge Member, Hamersley Group, Western Australia'. In: *Economic Geology* 67.8, pp. 1214–1233. ISSN: 1554-0774. DOI: 10.2113/gsecongeo.67.8.1214.

Azoulay, I., C. Rémazeilles and Ph Refait (2012). 'Determination of standard Gibbs free energy of formation of chukanovite and Pourbaix diagrams of iron in carbonated media'. In: *Corrosion Science* 58, pp. 229–236. ISSN: 0010938X. DOI: 10.1016/j.corsci.2012.01.033.

Bachan, Aviv and Lee R. Kump (May 2015). 'The rise of oxygen and siderite oxidation during the Lomagundi Event'. In: *Proceedings of the National Academy of Sciences* 112.21, pp. 6562–6567. ISSN: 0027-8424. DOI: 10.1073/pnas.1422319112.

Barker, Richard et al. (Sept. 2018). 'A review of iron carbonate (FeCO3) formation in the oil and gas industry'. In: *Corrosion Science* 142.July, pp. 312–341. ISSN: 0010938X. DOI: 10.1016/j.corsci.2018.07.021.

Bekker, A. et al. (2013). *Iron Formations: Their Origins and Implications for Ancient Seawater Chemistry*. 2nd ed. Vol. 9. Elsevier Ltd., pp. 561–628. ISBN: 9780080983004. DOI: 10.1016/B978-0-08-095975-7.00719-1.

Bekker, Andrey et al. (2010). 'Iron formation: The sedimentary product of a complex interplay among mantle, tectonic, oceanic, and biospheric processes'. In: *Economic Geology* 105.3, pp. 467–508. ISSN: 03610128. DOI: 10.2113/gsecongeo.105.3.467.

Bénézeth, P., J.L. Dandurand and J.C. Harrichoury (July 2009). 'Solubility product of siderite (FeCO3) as a function of temperature (25–250 °C)'. In: *Chemical Geology* 265.1-2, pp. 3–12. ISSN: 00092541. DOI: 10.1016/j.chemgeo.2009.03.015.

Berg, Kevin Charles de (Apr. 2015). 'Foundations of and challenges to electrolyte chemistry'. In: *Foundations of Chemistry* 17.1, pp. 33–48. ISSN: 1386-4238. DOI: 10.1007/s10698-015-9219-y.

Beukes, N. J. (Feb. 1984). 'Sedimentology of the Kuruman and Griquatown Iron-formations, Transvaal Supergroup, Griqualand West, South Africa'. In: *Precambrian Research* 24.1, pp. 47–84. ISSN: 03019268. DOI: 10.1016/0301-9268(84)90069-X.

Beukes, Nicolas J. and Jens Gutzmer (2008). 'Origin and Paleoenvironmental Significance of Major Iron Formations at the Archean-Paleoproterozoic Boundary'. In: *Banded Iron Formation-Related High-Grade Iron Ore*. Vol. 15. August 2016. Society of Economic Geologists, pp. 5–47. ISBN: 0741-0123\r978-1-934969-07-6. DOI: 10.5382/Rev.15.01.

Beukes, Nicolas J. et al. (July 1990). 'Carbonate petrography, kerogen distribution, and carbon and oxygen isotope variations in an early Proterozoic transition from limestone to iron-formation deposition, Transvaal Supergroup, South Africa'. In: *Economic Geology* 85.4, pp. 663–690. ISSN: 03610128. DOI: 10.2113/gsecongeo.85.4.663.

Bjerrum, Niels Janniksen and Augusta Unmack (1929). *Elektrometrische Messungen mit Wasserstoffelektroden in Mischungen von Säuren und Basen mit salzen; die*

Dissoziationskonstanten von Wasser, Phosphorsäure, Citronensäure und Glycin. 9th ed. København: A.F. Høst and Søn.

Blättler, C. L. et al. (Jan. 2017). 'Constraints on ocean carbonate chemistry and pCO2 in the Archaean and Palaeoproterozoic'. In: *Nature Geoscience* 10.1, pp. 41–45. ISSN: 1752-0894. DOI: 10.1038/ngeo2844.

Bockris, John O'M. and Amulya K. N. Reddy (1970). *Modern Electrochemistry.* Boston, MA: Springer US. ISBN: 978-1-4615-7469-9. DOI: 10.1007/978-1-4615-7467-5.

— (1998). *Volume 1: Modern Electrochemistry.* Ed. by John O'M. Bockris. 2nd ed. Boston: Kluwer Academic Publishers, p. 770. ISBN: 978-0-306-46909-1. DOI: 10.1007/b114546.

Bonino, G. B. and G. Centola (1933). 'Researches on the theory of concentrated solutions of strong electrolytes–the possibility of extension to calculate the osmotic coefficient'. In: *Atti della R. Accademia nazionale dei Lincei* 18, pp. 145–149.

Born, M. and W Heisenberg (1924). 'The influence of the deformability of ions on optical and chemical constants.' In: *Zeitschrift für Physik* 23, pp. 388–410.

Braterman, Paul S., A. Graham Cairns-Smith and Robert W. Sloper (May 1983). 'Photo-oxidation of hydrated Fe2+–significance for banded iron formations'. In: *Nature* 303.5913, pp. 163–164. ISSN: 0028-0836. DOI: 10.1038/303163a0.

Braun, Robert D. (1991). 'Solubility of iron(II) carbonate at temperatures between 30 and 80°'. In: *Talanta* 38.2, pp. 205–211. ISSN: 00399140. DOI: 10.1016/0039-9140(91)80131-I.

Bridges, John C., Leon J. Hicks and Allan H. Treiman (2019). 'Carbonates on Mars'. In: *Volatiles in the Martian Crust.* Vol. 5. Elsevier, pp. 89–118. ISBN: 9780128041918. DOI: 10.1016/B978-0-12-804191-8.00005-2.

Bristow, Thomas F. et al. (Feb. 2017). 'Low Hesperian P CO2 constrained from in situ mineralogical analysis at Gale Crater, Mars'. In: *Proceedings of the National Academy of Sciences* 114.9, pp. 2166–2170. ISSN: 0027-8424. DOI: 10.1073/pnas.1616649114.

Bronsted, J. N. (Apr. 1920). 'STUDIES ON SOLUBILITY. I. THE SOLUBILITY OF SALTS IN SALT SOLUTIONS.' In: *Journal of the American Chemical Society* 42.4, pp. 761–786. ISSN: 0002-7863. DOI: 10.1021/ja01449a014.

Brüll, L. A. (1934). 'Consideration of the ionic radius in aqueous solutions of electrolytes.' In: *Gazz. chim. ital* 64, pp. 624–634.

Bruno, Jordi, Paul Wersin and Werner Stumm (1992). 'On the influence of carbonate in mineral dissolution: II. The solubility of FeCO3(s) at 25°C and 1 atm total pressure'. In: *Geochimica et Cosmochimica Acta* 56.3, pp. 1149–1155. ISSN: 00167037. DOI: 10.1016/0016-7037(92)90052-K.

Burkle, D. et al. (Nov. 2017). 'In situ SR-XRD study of FeCO3 precipitation kinetics onto carbon steel in CO2-containing environments: The influence of brine pH'. In: *Electrochimica Acta* 255, pp. 127–144. ISSN: 00134686. DOI: 10.1016/j.electacta.2017.09.138.

Burton, W. K., N. Cabrera and F. C. Frank (June 1951). 'The growth of crystals and the equilibrium structure of their surfaces'. In: *Philosophical Transactions of the Royal Society of London. Series A, Mathematical and Physical Sciences* 243.866, pp. 299–358. ISSN: 0080-4614. DOI: 10.1098/rsta.1951.0006.

Busenberg, E. and L. N. Plummer (1986). 'A comparative study of the dissolution and crystal growth kinetics of calcite and aragonite'. In: *Studies in Diagenesis, U.S. Geological Survey Bulletin 1578* January 1986, pp. 139–168. ISSN: 00831093.

Butler, Ian B., Martin A A Schoonen and David T. Rickard (Feb. 1994). 'Removal of dissolved oxygen from water: A comparison of four common techniques'. In: *Talanta* 41.2, pp. 211–215. ISSN: 00399140. DOI: 10.1016/0039-9140(94)80110-X.

Butler, James Newton (1964). *Ionic Equilibrium: A Mathematical Approach*. Reading MA: Addision-Wesley Pub. Co., p. 547.

Callow, Ben et al. (Mar. 2018). 'Assessing the carbon sequestration potential of basalt using X-ray micro-CT and rock mechanics'. In: *International Journal of Greenhouse Gas Control* 70.December 2017, pp. 146–156. ISSN: 17505836. DOI: 10.1016/j.ijggc.2017.12.008.

Canfield, D.E. (May 2005). 'The Early History of Atmospheric oxygen: Homage to Robert M. Garrels'. In: *Annual Review of Earth and Planetary Sciences* 33.1, pp. 1–36. ISSN: 0084-6597. DOI: 10.1146/annurev.earth.33.092203.122711.

Cawood, P. A., C. J. Hawkesworth and B. Dhuime (2013). 'The continental record and the generation of continental crust'. In: *Bulletin of the Geological Society of America* 125.1-2, pp. 14–32. ISSN: 00167606. DOI: 10.1130/B30722.1.

Cawood, Peter A. and Chris J. Hawkesworth (2014). 'Earth's middle age'. In: *Geology* 42.6, pp. 503–506. ISSN: 19432682. DOI: 10.1130/G35402.1.

Christ, C. L. and P. B. Hostetler (May 1970). 'Studies in the system MgO-SiO 2 -CO 2 -H 2 O (II); the activity-product constant of magnesite'. In: *American Journal of Science* 268.5, pp. 439–453. ISSN: 0002-9599. DOI: 10.2475/ajs.268.5.439.

Christoffersen, Jørgen and Margaret R. Christoffersen (Aug. 1992). 'A revised theory for the growth of crystals by surface nucleation'. In: *Journal of Crystal Growth* 121.4, pp. 608–616. ISSN: 00220248. DOI: 10.1016/0022-0248(92)90568-4.

Cloud, Preston (1973). 'Paleoecological significance of the banded iron-formation'. In: *Economic Geology* 68.7, pp. 1135–1143. ISSN: 03610128. DOI: 10.2113/gsecongeo.68.7.1135.

Cox, J. D., Donald D. Wagman and V. A. Medvedev (1989). *CODATA Key Values for Thermodynamics*. Final Repo. Hemisphere Publishing Corporation. ISBN: 0-89116-758-7.

Darvell, B. W and V. W. H Leung (1991). 'R.I.P. ionic strength 1921-1991'. In: *Chemistry in Britain* 27.1, pp. 23–30.

Davies, Cecil W. (1938). '397. The extent of dissociation of salts in water. Part VIII. An equation for the mean ionic activity coefficient of an electrolyte in water, and a revision of the dissociation constants of some sulphates'. In: *Journal of the Chemical Society (Resumed)* 28, p. 2093. ISSN: 0368-1769. DOI: 10.1039/jr9380002093.

Davies, Cecil Whitfield (1962). *Ion Association*. London: Butterworth, p. 190.

Debye, P. and E. Hückel (1923). 'The theory of electrolytes I. The lowering of the freezing point and related occurrences'. In: *Physikalische Zeitschrift* 24, pp. 185–206.

DePaolo, Donald J. (Feb. 2011). 'Surface kinetic model for isotopic and trace element fractionation during precipitation of calcite from aqueous solutions'. In: *Geochimica et Cosmochimica Acta* 75.4, pp. 1039–1056. ISSN: 00167037. DOI: 10.1016/j.gca.2010.11.020.

Derry, Louis A. and Stein B. Jacobsen (1990). 'The chemical evolution of Precambrian seawater: Evidence from REEs in banded iron formations'. In: *Geochimica et Cosmochimica Acta* 54.11, pp. 2965–2977. ISSN: 00167037. DOI: 10.1016/0016-7037(90)90114-Z.

Des Marais, David J. (2000). 'When Did Photosynthesis Emerge on Earth?' In: *Science* 289.5485, pp. 1703–1705. DOI: 10.1126/science.289.5485.1703.

Dideriksen, Knud et al. (2015). 'Formation and transformation of a short range ordered iron carbonate precursor'. In: *Geochimica et Cosmochimica Acta* 164, pp. 53–70. ISSN: 00167037. DOI: 10.1016/j.gca.2015.05.005.

Dijk, Joep van et al. (Jan. 2018). 'Oxygen isotope fractionation in the siderite-water system between 8.5 and 62 °C'. In: *Geochimica et Cosmochimica Acta* 220, pp. 535–551. ISSN: 00167037. DOI: 10.1016/j.gca.2017.10.009.

Dimroth, Erich and Jean-Jacques Chauvel (1973). 'Petrography of the Sokoman Iron Formation in Part of the Central Labrador Trough, Quebec, Canada'. In: *Geological Society of America Bulletin* 84.1, p. 111. ISSN: 0016-7606. DOI: 10.1130/0016-7606(1973)84<111:POTSIF>2.0.CO;2.

Ding, K and W.E Seyfried (Oct. 1992). 'Determination of Fe-Cl complexing in the low pressure supercritical region (NaCl fluid): Iron solubility constraints on pH of subseafloor hydrothermal fluids'. In: *Geochimica et Cosmochimica Acta* 56.10, pp. 3681–3692. ISSN: 00167037. DOI: 10.1016/0016-7037(92)90161-B.

Drever, James I. (1974). 'Geochemical Model for the Origin of Precambrian Banded Iron Formations'. In: *Geological Society of America Bulletin* 85.7, p. 1099. ISSN: 0016-7606. DOI: 10.1130/0016-7606(1974)85<1099:GMFTOO>2.0.CO;2.

Duckworth, Owen W. and Scot T. Martin (2004). 'Role of molecular oxygen in the dissolution of siderite and rhodochrosite'. In: *Geochimica et Cosmochimica Acta* 68.3, pp. 607–621. ISSN: 00167037. DOI: 10.1016/S0016-7037(00)00464-2.

Elderfield, H. and A. Schultz (May 1996). 'Mid-Ocean Ridge Hydrothermal Fluxes and the Chemical Composition of the Ocean'. In: *Annual Review of Earth and Planetary Sciences* 24.1, pp. 191–224. ISSN: 0084-6597. DOI: 10.1146/annurev.earth.24.1.191.

Eugster, Hans P. and I-Ming Ming Chou (Nov. 1973). 'The Depositional Environments of Precambrian Banded Iron-Formations'. In: *Economic Geology* 68.7, pp. 1144–1168. ISSN: 1554-0774. DOI: 10.2113/gsecongeo.68.7.1144.

Feitknecht, W. and P. Schindler (Jan. 1963). 'Solubility constants of metal oxides, metal hydroxides and metal hydroxide salts in aqueous solution'. In: *Pure and Applied Chemistry* 6.2, pp. 125–206. ISSN: 1365-3075. DOI: 10.1351/pac196306020125.

Fischer, W. W. et al. (2009). 'Isotopic constraints on the Late Archean carbon cycle from the Transvaal Supergroup along the western margin of the Kaapvaal Craton, South Africa'. In: *Precambrian Research* 169.1-4, pp. 15–27. ISSN: 03019268. DOI: 10.1016/j.precamres.2008.10.010.

Fischer, Woodward W. and Andrew H. Knoll (2009). 'An iron shuttle for deepwater silica in late Archean and early Paleoproterozoic iron formation'. In: *Bulletin of the Geological Society of America* 121.1-2, pp. 222–235. ISSN: 00167606. DOI: 10.1130/B26328.1.

Fitzgerald, George Francis (1896). 'Helmholtz Memorial Lecture'. In: *Journal of the Chemical Society, Transactions* 69, p. 885. ISSN: 0368-1645. DOI: 10.1039/ct8966900885.

Fosbøl, P. L., K. Thomsen and E. H. Stenby (Apr. 2010). 'Review and recommended thermodynamic properties of FeCO3'. In: *Corrosion Engineering, Science and Technology* 45.2, pp. 115–135. ISSN: 1478-422X. DOI: 10.1179/174327808X286437.

Fouillac, C. and A. Criaud (1984). 'Carbonate and bicarbonate trace metal complexes: Critical reevaluation of stability constants.' In: *GEOCHEMICAL JOURNAL* 18.6, pp. 297–303. ISSN: 0016-7002. DOI: 10.2343/geochemj.18.297.

Franks, Felix (1991). 'Old habits die hard'. In: *Chemistry in Britain* 27.4, p. 315.

Friedman, Harold (1962). *Ionic Solution Theory*. Interscience Publisher, p. 265.

Garrels, Robert M. and Fred T. Mackenzie (1971). *Evolution of Sedimentary Rocks*. New York: W.W.Norton and Company, INC., p. 397.

Gebauer, Denis, Antje Völkel and Helmut Cölfen (Dec. 2008). 'Stable Prenucleation Calcium Carbonate Clusters'. In: *Science* 322.5909, pp. 1819–1822. ISSN: 0036-8075. DOI: 10.1126/science.1164271.

Ghosh, M.M, J.T O'Connor and R.S. Engelbrecht (1966). 'Precipitation of iron in aerated ground waters'. In: *J. Sanit. Eng. Div., Am. Soc. Civ. Eng.* 92:SA1.

— (1967). 'Bathophenanthroline Method for the Determination of Ferrous Iron'. In: *American Water Work Association* 59.7, pp. 897–905.

Gildseth, Wayne, Anton Habenschuss and Frank H. Spedding (Oct. 1972). 'Precision measurements of densities and thermal dilation of water between 5.deg. and 80.deg.' In: *Journal of Chemical & Engineering Data* 17.4, pp. 402–409. ISSN: 0021-9568. DOI: 10.1021/je60055a005.

Gislason, Sigurdur Reynir et al. (May 2010). 'Mineral sequestration of carbon dioxide in basalt: A pre-injection overview of the CarbFix project'. In: *International Journal of Greenhouse Gas Control* 4.3, pp. 537–545. ISSN: 17505836. DOI: 10.1016/j.ijggc.2009.11.013.

Goldschmidt, V. M. (May 1926). 'Die Gesetze der Krystallochemie'. In: *Die Naturwissenschaften* 14.21, pp. 477–485. ISSN: 0028-1042. DOI: 10.1007/BF01507527.

Golubev, S. V. et al. (2009). 'Siderite dissolution kinetics in acidic aqueous solutions from 25 to 100°C and 0 to 50 atm pCO2'. In: *Chemical Geology* 260.3-4, pp. 295–301. ISSN: 00092541. DOI: 10.1016/j.chemgeo.2008.12.031.

Gough, D. O. (1981). 'Solar interior structure and luminosity variations'. In: *Solar Physics* 74.1, pp. 21–34. ISSN: 00380938. DOI: 10.1007/BF00151270. arXiv: arXiv:1011.1669v3.

Greenberg, Janet and Mason Tomson (Mar. 1992). 'Precipitation and dissolution kinetics and equilibria of aqueous ferrous carbonate vs temperature'. In: *Applied Geochemistry* 7.2, pp. 185–190. ISSN: 08832927. DOI: 10.1016/0883-2927(92)90036-3.

Guggenheim, E. A. (Jan. 1928). 'The Conceptions of Electrical Potential Difference between Two Phases and the Individual Activities of Ions'. In: *The Journal of Physical Chemistry* 33.6, pp. 842–849. ISSN: 0092-7325. DOI: 10.1021/j150300a003.

Guzmán-Marmolejo, Andrés, Antígona Segura and Elva Escobar-Briones (2013). 'Abiotic Production of Methane in Terrestrial Planets'. In: *Astrobiology* 13.6, pp. 550–559. ISSN: 1531-1074. DOI: 10.1089/ast.2012.0817.

Halevy, I. and A. Bachan (Mar. 2017). 'The geologic history of seawater pH'. In: *Science* 355.6329, pp. 1069–1071. ISSN: 10959203. DOI: 10.1126/science.aal4151.

Halevy, I. et al. (Feb. 2017). 'A key role for green rust in the Precambrian oceans and the genesis of iron formations'. In: *Nature Geoscience* 10.2, pp. 135–139. ISSN: 17520908. DOI: 10.1038/ngeo2878.

Hansen, H.C.B.H (2001). 'Environmental chemistry of iron(II)-iron(III) LDHs (green rusts)'. In: *Layered Double Hydroxides: Present and Future*. Ed. by V. Rives. Nova Science Publishers, pp. 413–434.

Harned, Herbert S. and Benton B. Owen (1958). *The Physical Chemistry of electrolytic solutions*. 3rd. New York: Reinhold Pub. Corp., p. 354.

Heimann, Adriana et al. (May 2010). 'Fe, C, and O isotope compositions of banded iron formation carbonates demonstrate a major role for dissimilatory iron reduction in

2.5Ga marine environments'. In: *Earth and Planetary Science Letters* 294.1-2, pp. 8–18. ISSN: 0012821X. DOI: 10.1016/j.epsl.2010.02.015.

Helgeson, H. C. and D. H. Kirkham (Dec. 1974a). 'Theoretical prediction of the thermodynamic behavior of aqueous electrolytes at high pressures and temperatures; I, Summary of the thermodynamic/electrostatic properties of the solvent'. In: *American Journal of Science* 274.10, pp. 1089–1198. ISSN: 0002-9599. DOI: 10.2475/ajs.274.10.1089.

— (Dec. 1974b). 'Theoretical prediction of the thermodynamic behavior of aqueous electrolytes at high pressures and temperatures; II, Debye-Huckel parameters for activity coefficients and relative partial molal properties'. In: *American Journal of Science* 274.10, pp. 1199–1261. ISSN: 0002-9599. DOI: 10.2475/ajs.274.10.1199. arXiv: 6875208.

Helgeson, H. C., D. H. Kirkham and G. C. Flowers (Dec. 1981). 'Theoretical prediction of the thermodynamic behavior of aqueous electrolytes by high pressures and temperatures; IV, Calculation of activity coefficients, osmotic coefficients,

and apparent molal and standard and relative partial molal properties to 600 d'. In: *American Journal of Science* 281.10, pp. 1249–1516. ISSN: 0002-9599. DOI: 10.2475/ajs.281.10.1249.

Helgeson, Harold C (Sept. 1969). 'Thermodynamics of hydrothermal systems at elevated temperatures and pressures'. In: *American Journal of Science* 267.7, pp. 729–804. ISSN: 0002-9599. DOI: 10.2475/ajs.267.7.729.

— (Jan. 1981). 'Prediction of the thermodynamic properties of electrolytes at high pressures and temperatures'. In: *Physics and Chemistry of the Earth* 13-14.C, pp. 133–177. ISSN: 00791946. DOI: 10.1016/0079-1946(81)90009-4.

Hem, J D (1960). *Restraints on dissolved ferrous iron imposed by bicarbonate redox potential, and pH*. Tech. rep. Washington, D.C.: United States Department of the Interior. DOI: 10.3133/wsp1459B.

Herzberg, Claude, Kent Condie and Jun Korenaga (2010). 'Thermal history of the Earth and its petrological expression'. In: *Earth and Planetary Science Letters* 292.1-2, pp. 79–88. ISSN: 0012821X. DOI: 10.1016/j.epsl.2010.01.022.

Hessler, Angela M et al. (2004). 'A lower limit for atmospheric carbon dioxide levels 3.2 billion years ago'. In: *Nature* 428.6984, pp. 736–738. ISSN: 0028-0836. DOI: 10.1038/nature02471.

Heyrovska, Raji (1991). 'Ionic concentration outlives ionic strength'. In: *Chemistry in Britain*, p. 1114.

Hillig, W.B. (Dec. 1966). 'A derivation of classical two-dimensional nucleation kinetics and the associated crystal growth laws'. In: *Acta Metallurgica* 14.12, pp. 1868–1869. ISSN: 00016160. DOI: 10.1016/0001-6160(66)90046-0.

Holland, H. D. (2006). 'The Oxygenation of the aAtmosphere and Oceans'. In: *Philosophical transactions of the Royal Society of London. Series B, Biological sciences* 361.1470, pp. 903–915. ISSN: 0962-8436. DOI: 10.1098/rstb.2006.1838.

Holland, Heinrich D. (Nov. 1973). 'The Oceans; A Possible Source of Iron in Iron-Formations'. In: *Economic Geology* 68.7, pp. 1169–1172. ISSN: 1554-0774. DOI: 10.2113/gsecongeo.68.7.1169.

— (1984). *The Chemical Evolution of the Atmosphere and Oceans*. Princeton: Princeton University Press, p. 598.

Holland, Heinrich D. (2007). 'The Geologic History of Seawater'. In: *Treatise on Geochemistry*. Vol. 6. Elsevier, pp. 1–46. ISBN: 0-08-043751-6. DOI: 10.1016/B0-08-043751-6/06122-3.

House, William A. (1981). 'Kinetics of crystallisation of calcite from calcium bicarbonate solutions'. In: *Journal of the Chemical Society, Faraday Transactions 1: Physical Chemistry in Condensed Phases* 77.2, p. 341. ISSN: 0300-9599. DOI: 10.1039/f19817700341.

Isley, Ann E. (1995). 'Hydrothermal plumes and the delivery of iron to banded iron formation'. In: *The Journal of Geology* 103.2, pp. 169–185.

Isley, Ann E. and Dallas H. Abbott (July 1999). 'Plume-related mafic volcanism and the deposition of banded iron formation'. In: *Journal of Geophysical Research: Solid Earth* 104.B7, pp. 15461–15477. ISSN: 01480227. DOI: 10.1029/1999JB900066.

Jacobsen, Stein B. and Mario R. Pimentel-Klose (1988). 'A Nd isotopic study of the Hamersley and Michipicoten banded iron formations: the source of REE and Fe in Archean oceans'. In: *Earth and Planetary Science Letters* 87.1-2, pp. 29–44. ISSN: 0012821X. DOI: 10.1016/0012-821X(88)90062-3.

Jähne, Bernd, Gerhard Heinz and Wolfgang Dietrich (1987). 'Measurement of the diffusion coefficients of sparingly soluble gases in water'. In: *Journal of Geophysical Research* 92.C10, p. 10767. ISSN: 0148-0227. DOI: 10.1029/JC092iC10p10767.

James, Harold Lloyd (May 1954). 'Sedimentary facies of iron-formation'. In: *Economic Geology* 49.3, pp. 235–293. ISSN: 1554-0774. DOI: 10.2113/gsecongeo.49.3.235.

Janecky, D. R. and W. E. Seyfried (1984). 'Formation of massive sulfide deposits on oceanic ridge crests: Incremental reaction models for mixing between hydrothermal solutions and seawater'. In: *Geochimica et Cosmochimica Acta* 48.12, pp. 2723–2738. ISSN: 00167037. DOI: 10.1016/0016-7037(84)90319-3.

Jenkins, H. D. B. and K P Thakur (Sept. 1979). 'Reappraisal of thermochemical radii for complex ions'. In: *Journal of Chemical Education* 56.9, p. 576. ISSN: 0021-9584. DOI: 10.1021/ed056p576.

Jensen, Dorthe L et al. (Apr. 2002). 'The solubility of rhodochrosite (MnCO3) and siderite (FeCO3) in anaerobic aquatic environments'. In: *Applied Geochemistry* 17.4, pp. 503–511. ISSN: 08832927. DOI: 10.1016/S0883-2927(01)00118-4.

Jiang, Clancy Zhijian and Nicholas J Tosca (Apr. 2020). 'Growth kinetics of siderite at 298.15 K and 1 bar'. In: *Geochimica et Cosmochimica Acta* 274, pp. 97–117. ISSN: 00167037. DOI: 10.1016/j.gca.2020.01.047.

— (Jan. 2019). 'Fe(II)-carbonate precipitation kinetics and the chemistry of anoxic ferruginous seawater'. In: *Earth and Planetary Science Letters* 506, pp. 231–242. ISSN: 0012821X. DOI: 10.1016/j.epsl.2018.11.010.

Jimenez-Lopez, Concepción and Christopher S. Romanek (2004). 'Precipitation kinetics and carbon isotope partitioning of inorganic siderite at 25??C and 1 atm'. In: *Geochimica et Cosmochimica Acta* 68.3, pp. 557–571. ISSN: 00167037. DOI: 10.1016/S0016-7037(03)00460-5.

Johnson, Clark M., Brian L. Beard and Eric E. Roden (May 2008a). 'The Iron Isotope Fingerprints of Redox and Biogeochemical Cycling in Modern and Ancient Earth'. In: *Annual Review of Earth and Planetary Sciences* 36.1, pp. 457–493. ISSN: 0084-6597. DOI: 10.1146/annurev.earth.36.031207.124139.

Johnson, Clark M. et al. (Feb. 2005). 'Experimental constraints on Fe isotope fractionation during magnetite and Fe carbonate formation coupled to dissimilatory hydrous ferric oxide reduction'. In: *Geochimica et Cosmochimica Acta* 69.4, pp. 963–993. ISSN: 00167037. DOI: 10.1016/j.gca.2004.06.043.

Johnson, Clark M. et al. (Jan. 2008b). 'Iron isotopes constrain biologic and abiologic processes in banded iron formation genesis'. In: *Geochimica et Cosmochimica Acta* 72.1, pp. 151–169. ISSN: 00167037. DOI: 10.1016/j.gca.2007.10.013.

Johnson, Clark M. et al. (Nov. 2013). 'Iron formation carbonates: Paleoceanographic proxy or recorder of microbial diagenesis?' In: *Geology* 41.11, pp. 1147–1150. ISSN: 1943-2682. DOI: 10.1130/G34698.1.

Johnson, James W., Eric H. Oelkers and Harold C. Helgeson (1992). *SUPCRT92: A software package for calculating the standard molal thermodynamic properties of minerals, gases, aqueous species, and reactions from 1 to 5000 bar and 0*

to 1000°C. Vol. 18. 7, pp. 899–947. ISBN: 2729401652. DOI: 10.1016/0098-3004(92)90029-Q.

Johnson, Jena E. et al. (Apr. 2018). 'Low-Fe(III) Greenalite Was a Primary Mineral From Neoarchean Oceans'. In: *Geophysical Research Letters* 45.7, pp. 3182–3192. ISSN: 0094-8276. DOI: 10.1002/2017GL076311.

Johnson, M.L. and M.B. Tomson (1991). 'Ferrous Carbonate Precipitation Kinetics and its Impact CO2 Corrosion'. In: *CORROSION* Houston, T, p. 268.

Kahlenberg, Louis (Jan. 1900). 'The Theory of Electrolytic Dissociation as Viewed in the Light of Facts Recently Ascertained'. In: *The Journal of Physical Chemistry* 5.6, pp. 339–392. ISSN: 0092-7325. DOI: 10.1021/j150033a001.

— (1905). 'On the nature of the process of osmosis and osmotic pressure with observations concerning dialysis'. In: *Journal of Physical Chemistry* 10.3, pp. 141–209. ISSN: 00223654. DOI: 10.1021/j150075a001.

Kandegedara, Ashoka and David B. Rorabacher (Aug. 1999). 'Noncomplexing Tertiary Amines as "Better" Buffers Covering the Range of pH 3-11. Temperature Dependence of Their Acid Dissociation Constants'. In: *Analytical Chemistry* 71.15, pp. 3140–3144. ISSN: 0003-2700. DOI: 10.1021/ac9902594.

Kasting, James F (2013). 'How Was Early Earth Kept Warm?' In: *Science* 339.6115, pp. 44–45. ISSN: 0036-8075, 1095-9203. DOI: 10.1126/science.1232662.

— (2014). 'Atmospheric composition of Hadean – early Archean Earth : The importance of CO'. In: 2504.04, pp. 1–10. DOI: 10.1130/2014.2504(04)..

— (1993). *Earth's Early Atmosphere*. DOI: 10.1063/1.2915978.

— (2004). 'Palaeoclimatology: Archaean atmosphere and climate'. In: *Nature* 432.7016, 1 p following 460. ISSN: 0028-0836. DOI: 10.1038/nature03166.

— (2005). 'Methane and climate during the Precambrian era'. In: *Precambrian Research* 137.3-4, pp. 119–129. ISSN: 03019268. DOI: 10.1016/j.precamres.2005.03.002.

Kasting, James F., Alexander A. Pavlov and Janet L. Siefert (2001). 'A coupled ecosystem-climate model for predicting the methane concentration in the archean atmosphere'. In: *Origins of Life and Evolution of the Biosphere* 31.3, pp. 271–285. ISSN: 01696149. DOI: 10.1023/A:1010600401718.

Kaufman, Alan J. (1996). 'Geochemical and mineralogic effects of contact metamorphism on banded iron-formation: an example from the Transvaal Basin, South Africa'. In: *Precambrian Research* 79.1-2, pp. 171–194. ISSN: 03019268. DOI: 10.1016/0301-9268(95)00093-3.

Kaufman, Alan J., J.M. Hayes and C. Klein (Dec. 1990). 'Primary and diagenetic controls of isotopic compositions of iron-formation carbonates'. In: *Geochimica et Cosmochimica Acta* 54.12, pp. 3461–3473. ISSN: 00167037. DOI: 10.1016/0016-7037(90)90298-Y.

Kelley, K. K. and C. T. Anderson (1935). 'Contributions to the data on theoretical metallurgy IV: Metal carbonates: correlations and applications of thermodynamic properties'. In: *US Department of the Interior, Bureau of Mines* 1-73.

Kendall, James (Aug. 1916). 'THE SPECIFIC CONDUCTIVITY OF PURE WATER IN EQUILIBRIUM WITH ATMOSPHERIC CARBON DIOXIDE.' In: *Journal of the American Chemical Society* 38.8, pp. 1480–1497. ISSN: 0002-7863. DOI: 10.1021/ja02265a004.

Kielland, Jacob (Sept. 1937). 'Individual Activity Coefficients of Ions in Aqueous Solutions'. In: *Journal of the American Chemical Society* 59.9, pp. 1675–1678. ISSN: 15205126. DOI: 10.1021/ja01288a032.

Kjellander, Roland and D. John Mitchell (1992). 'An exact but linear and Poisson-Boltzmann-like theory for electrolytes and colloid dispersions in the primitive model'. In: *Chemical Physics Letters* 200.1-2, pp. 76–82. ISSN: 00092614. DOI: 10.1016/0009-2614(92)87048-T.

Kjellander, Roland and JohanOHAN Ulander (Oct. 1998). 'Effective ionic charges, permittivity and screening length: dressed ion theory applied to 1:2 electrolyte solutions'. In: *Molecular Physics* 95.3, pp. 495–505. ISSN: 0026-8976. DOI: 10.1080/00268979809483184.

Klein, C and N J Beukes (1989). 'Geochemistry and Sedimentology of a Facies Transition from Limestone to Iron-Formation Deposition in the Early Proterozoic Transvaal Supergroup, South-Africa'. In: *Economic Geology* 84.7, pp. 1733–1774.

Klein, Cornelis (1974). 'Greenalite, stilpnomelane, minnesotaite, crocidolite and carbonates in a very low-grade metamorphic Precambrian Iron-formation'. In: *Canadian Mineralogist* 12, pp. 475–498.

— (Oct. 2005). 'Some Precambrian banded iron-formations (BIFs) from around the world: Their age, geologic setting, mineralogy, metamorphism, geochemistry, and origins'. In: *American Mineralogist* 90.10, pp. 1473–1499. ISSN: 0003-004X. DOI: 10.2138/am.2005.1871.

Kohonen, Mika M., Marilyn E. Karaman and Richard M. Pashley (June 2000). 'Debye Length in Multivalent Electrolyte Solutions'. In: *Langmuir* 16.13, pp. 5749–5753. ISSN: 0743-7463. DOI: 10.1021/la991621c.

Kong, Xiang-Zhao, Benjamin M. Tutolo and Martin O. Saar (Feb. 2013). 'DBCreate: A SUPCRT92-based program for producing EQ3/6, TOUGHREACT, and GWB thermodynamic databases at user-defined T and P'. In: *Computers & Geosciences* 51, pp. 415–417. ISSN: 00983004. DOI: 10.1016/j.cageo.2012.08.004.

Konhauser, K. O., D. K. Newman and A. Kappler (2005). 'The potential significance of microbial Fe(III) reduction during deposition of Precambrian banded iron formations'. In: *Geobiology* 3.3, pp. 167–177. ISSN: 14724677. DOI: 10.1111/j.1472-4669.2005.00055.x.

Konhauser, K. O. et al. (Sept. 2017). 'Iron formations: A global record of Neoarchaean to Palaeoproterozoic environmental history'. In: *Earth-Science Reviews* 172.April, pp. 140–177. ISSN: 00128252. DOI: 10.1016/j.earscirev.2017.06.012.

Konhauser, Kurt O. et al. (2007). 'Decoupling photochemical Fe(II) oxidation from shallow-water BIF deposition'. In: *Earth and Planetary Science Letters* 258.1-2, pp. 87–100. ISSN: 0012821X. DOI: 10.1016/j.epsl.2007.03.026.

Korenaga, Jun (2006). 'Archean geodynamics and the thermal evolution of Earth'. In: *Geophysical Monograph Series*, pp. 7–32. DOI: 10.1029/164GM03.

Kowacz, M., C.V. Putnis and A. Putnis (Nov. 2007). 'The effect of cation:anion ratio in solution on the mechanism of barite growth at constant supersaturation: Role of the desolvation process on the growth kinetics'. In: *Geochimica et Cosmochim-*

ica Acta 71.21, pp. 5168–5179. ISSN: 00167037. DOI: 10.1016/j.gca.2007.09.008.

Krapež, Bryan, Mark E. Barley and April L. Pickard (Oct. 2003). 'Hydrothermal and resedimented origins of the precursor sediments to banded iron formation: sedimentological evidence from the Early Palaeoproterozoic Brockman Supersequence of Western Australia'. In: *Sedimentology* 50.5, pp. 979–1011. ISSN: 00370746. DOI: 10.1046/j.1365-3091.2003.00594.x.

Krissansen-Totton, Joshua, Giada N. Arney and David C. Catling (Apr. 2018). 'Constraining the climate and ocean pH of the early Earth with a geological carbon cycle model'. In: *Proceedings of the National Academy of Sciences*, p. 201721296. ISSN: 0027-8424. DOI: 10.1073/pnas.1721296115. arXiv: 1804.00763.

Kruh, R. F. (1962). 'Diffraction studies of the structure of liquids'. In: *Chemical Reviews* 62.4, pp. 319–346. ISSN: 15206890. DOI: 10.1021/cr60218a003.

Krumbein, W. C. and R. M. Garrels (Jan. 1952). 'Origin and Classification of Chemical Sediments in Terms of pH and Oxidation-Reduction Potentials'. In: *The Journal of Geology* 60.1, pp. 1–33. ISSN: 0022-1376. DOI: 10.1086/625929.

Kulik, Dmitri A. and Michael N. Korzhnev (1997). 'Lithological and geochemical evidence of Fe and Mn pathways during deposition of Lower Proterozoic banded iron formation in the Krivoy Rog Basin (Ukraine)'. In: *Geological Society, London, Special Publications* 119.1, pp. 43–80. ISSN: 0305-8719. DOI: 10.1144/GSL.SP.1997.119.01.04.

Kump, Lee R. and Heinrich D. Holland (1992). 'Iron in Precambrian rocks: Implications for the global oxygen budget of the ancient Earth'. In: *Geochimica et Cosmochimica Acta* 56.8, pp. 3217–3223. ISSN: 00167037. DOI: 10.1016/0016-7037(92)90299-X.

Kump, Lee R. and William E. Seyfried (2005). 'Hydrothermal Fe fluxes during the Precambrian: Effect of low oceanic sulfate concentrations and low hydrostatic pressure on the composition of black smokers'. In: *Earth and Planetary Science Letters* 235.3-4, pp. 654–662. ISSN: 0012821X. DOI: 10.1016/j.epsl.2005.04.040.

LaBerge, Gene L. (Nov. 1964). 'Development of magnetite in iron formations of the Lake Superior region'. In: *Economic Geology* 59.7, pp. 1313–1342. ISSN: 1554-0774. DOI: 10.2113/gsecongeo.59.7.1313.

Landolt, Hans, Richard Bornstein and Karl Scheel (1936). *Landolt-Börnstein physikalisch-chemische Tabellen*. Ed. by Ergänzungsband. 3rd ed. Berlin: Verlag von Springer.

Lasaga, Antonio C. (June 1984). 'Chemical kinetics of water-rock interactions'. In: *Journal of Geophysical Research: Solid Earth* 89.B6, pp. 4009–4025. ISSN: 01480227. DOI: 10.1029/JB089iB06p04009.

— (1998a). '4. Diffusion'. In: *Kinetic Theory in the Earth Sciences*. Ed. by H. Holland. Princeton: Princeton University Press, pp. 308–440. ISBN: 0-691-03748-5.

— (1998b). '6.4 Nucleation Rate Theory'. In: *Kinetic Theory in the Earth Sciences*. Ed. by Heinrich D. Holland. Princeton: Princeton University Press, pp. 520–580. ISBN: 0-691-03748-5.

— (1998c). '7. Theory of Crystal Growth and Dissolution'. In: *Kinetic Theory in the Earth Sciences*. Ed. by H.D. Holland. Princeton: Princeton University Press, pp. 581–618. ISBN: 0-691-03748-5.

Latimer, W. E. (1952). *The Oxidation States of the Elements and Their Potentials in Aqueous Solutions*. 2nd. Englewood Cliffes, N. J.: Prentice Hall, p. 392.

Leote de Carvalho, R.J.F. and R. Evans (Nov. 1994). 'The decay of correlations in ionic fluids'. In: *Molecular Physics* 83.4, pp. 619–654. ISSN: 0026-8976. DOI: 10.1080/00268979400101491.

Lewis, Gilbert N. (Dec. 1912). 'THE ACTIVITY OF THE IONS AND THE DEGREE OF DISSOCIATION OF STRONG ELECTROLYTES.' In: *Journal of the American Chemical Society* 34.12, pp. 1631–1644. ISSN: 0002-7863. DOI: 10.1021/ja02213a001.

Lewis, Gilbert N. and Merle Randall (May 1921). 'THE ACTIVITY COEFFICIENT OF STRONG ELECTROLYTES. 1'. In: *Journal of the American Chemical Society* 43.5, pp. 1112–1154. ISSN: 0002-7863. DOI: 10.1021/ja01438a014.

Lewis, Gilbert Newton (1907). 'Outlines of a New System of Thermodynamic Chemistry'. In: *Proceedings of the American Academy of Arts and Sciences* 43.7, p. 259. ISSN: 01999818. DOI: 10.2307/20022322.

Lyons, Timothy W, Christopher T Reinhard and Noah J Planavsky (2014). 'The rise of oxygen in Earth's early ocean and atmosphere.' In: *Nature* 506.7488, pp. 307–15. ISSN: 1476-4687. DOI: 10.1038/nature13068. arXiv: 1402.3243.

Ma, Zheng et al. (Aug. 2018). 'Investigation of precipitation kinetics of FeCO3 by EQCM'. In: *Corrosion Science* 141.June, pp. 195–202. ISSN: 0010938X. DOI: 10.1016/j.corsci.2018.06.017.

Maliva, Robert G., Andrew H. Knoll and Bruce M. Simonson (2005). 'Secular change in the Precambrian silica cycle: Insights from chert petrology'. In: *Geological Society of America Bulletin* 117.7, p. 835. ISSN: 0016-7606. DOI: 10.1130/B25555.1.

Mallouk, Thomas E. et al. (Sept. 1984). 'Fluoride ion affinities of germanium tetrafluoride and boron trifluoride from thermodynamic and structural data for (SF3)2GeF6, ClO2GeF5, and ClO2BF4'. In: *Inorganic Chemistry* 23.20, pp. 3167–3173. ISSN: 0020-1669. DOI: 10.1021/ic00188a028.

Marcus, Yizhak (1988). 'Ionic Radii in Aqueous Solutions'. In: *Chemical Reviews* 88, pp. 1475–1498. ISSN: 00959782. DOI: 10.1007/BF00646201. arXiv: 1402.6991v1.

Marini Luigi (2006). 'Implications for CO2 solubility in concentrated aqueous solutions'. In: *Geological Sequestration of Carbon Dioxide: Thermodynamics, Kinetics, and Reaction Path Modelling*. Elsevier Science. Chap. 4. The Aqu, p. 470. ISBN: 9780080466880.

Martell, Arthur E. and Robert M. Smith (1976). *Critical Stability Constants v. 4: inorganic complexes*. New York: Plenum Press. ISBN: 0306352141.

McLennan, Scott M. (Nov. 1982). 'On the geochemical evolution of sedimentary rocks'. In: *Chemical Geology* 37.3-4, pp. 335–350. ISSN: 00092541. DOI: 10.1016/0009-2541(82)90087-0.

Milesi, Vincent et al. (Apr. 2015). 'Formation of CO2, H2 and condensed carbon from siderite dissolution in the 200–300°C range and at 50MPa'. In: *Geochimica et Cosmochimica Acta* 154, pp. 201–211. ISSN: 00167037. DOI: 10.1016/j.gca.2015.01.015.

Mohr, Peter J., David B. Newell and Barry N. Taylor (Sept. 2016). 'CODATA recommended values of the fundamental physical constants: 2014'. In: *Reviews of*

Modern Physics 88.3, p. 035009. ISSN: 0034-6861. DOI: 10.1103/RevModPhys.88.035009. arXiv: arXiv:1507.07956.

Monk, C. B. (1993). 'Controversies: Ionic strength-the final reprise?' In: *Chemistry in Britain* 29.12, pp. 1033–1034.

Monk, Cecil Bertie (1961). *Electrolytic dissociation*. London: Academic Press, p. 320.

Montes-Hernandez, German and François Renard (Dec. 2016). 'Time-Resolved in Situ Raman Spectroscopy of the Nucleation and Growth of Siderite, Magnesite, and Calcite and Their Precursors'. In: *Crystal Growth & Design* 16.12, pp. 7218–7230. ISSN: 1528-7483. DOI: 10.1021/acs.cgd.6b01406.

Mook, W.G. (Aug. 1986). '13C in atmospheric CO2'. In: *Netherlands Journal of Sea Research* 20.2-3, pp. 211–223. ISSN: 00777579. DOI: 10.1016/0077-7579(86)90043-8.

Moore, W. J. (1999). *Physical Chemistry*. 5th. Englewood Cliffes, N. J.: Prentice Hall, p. 977.

Morse, John W. and Fred T. Mackenzie (1990). *Geochemistry of Sedimentary Carbonates*. Developmen. Amsterdam-Oxford-New York-Tokyo: Elsevier, p. 705. ISBN: 0-444-87391-0.

Mucci, A. (Sept. 1983). 'The solubility of calcite and aragonite in seawater at various salinities, temperatures, and one atmosphere total pressure'. In: *American Journal of Science* 283.7, pp. 780–799. ISSN: 0002-9599. DOI: 10.2475/ajs.283.7.780.

Muhling, Janet R and Birger Rasmussen (Apr. 2020). 'Widespread deposition of greenalite to form Banded Iron Formations before the Great Oxidation Event'. In: *Precambrian Research* 339, p. 105619. ISSN: 03019268. DOI: 10.1016/j.precamres.2020.105619.

Mullin, J W (1972). *Crystallization*. 2nd. London: Butterworths, p. 600. ISBN: 0408703490.

Nancollas, G.H and M.M Reddy (Dec. 1971). 'The crystallization of calcium carbonate. II. Calcite growth mechanism'. In: *Journal of Colloid and Interface Science* 37.4, pp. 824–830. ISSN: 00219797. DOI: 10.1016/0021-9797(71)90363-8.

Nancollas, George H. (Jan. 1979). 'The growth of crystals in solution'. In: *Advances in Colloid and Interface Science* 10.1, pp. 215–252. ISSN: 00018686. DOI: 10.1016/0001-8686(79)87007-4.

Nic, M. et al. (June 2009). *IUPAC Compendium of Chemical Terminology*. Ed. by Miloslav Nič et al. Research Triagle Park, NC: IUPAC, p. 1670. ISBN: 0-9678550-9-8. DOI: 10.1351/goldbook. arXiv: ISBN:0-9678550-9-8..

Nielsen, Arne Erik (1964). *Kinetics of precipitation*. New York: Pergamon Press.

— (Jan. 1981). 'Theory of electrolyte crystal growth. The parabolic rate law'. In: *Pure and Applied Chemistry* 53.11, pp. 2025–2039. ISSN: 1365-3075. DOI: 10.1351/pac198153112025.

— (1983). 'Precipitates: formation, coprecipitation, and aging.' In: *Treatise on Analytical Chemistry*. Ed. by I. M. Kolthoff and P. J. Elving. Wiley, pp. 269–347.

— (July 1984). 'Electrolyte crystal growth mechanisms'. In: *Journal of Crystal Growth* 67.2, pp. 289–310. ISSN: 00220248. DOI: 10.1016/0022-0248(84)90189-1.

Nielsen, Arne Erik and J Christoffersen (1982). 'The Mechanisms of Chrystal Growth and Dissolution'. In: *Biological Mineralization and Demineralization*. Ed. by G H Nancollas. Berlin, Heidelberg: Springer Berlin Heidelberg, pp. 37–77. ISBN: 978-3-642-68574-3.

Nielsen, Arne Erik and O. Söhnel (Dec. 1971). 'Interfacial tensions electrolyte crystal-aqueous solution, from nucleation data'. In: *Journal of Crystal Growth* 11.3, pp. 233–242. ISSN: 00220248. DOI: 10.1016/0022-0248(71)90090-X.

Nielsen, Arne Erik and Jens M. Toft (July 1984). 'Electrolyte crystal growth kinetics'. In: *Journal of Crystal Growth* 67.2, pp. 278–288. ISSN: 00220248. DOI: 10.1016/0022-0248(84)90188-X.

Nielsen, Laura C., Donald J. DePaolo and James J. De Yoreo (June 2012). 'Self-consistent ion-by-ion growth model for kinetic isotopic fractionation during calcite precipitation'. In: *Geochimica et Cosmochimica Acta* 86, pp. 166–181. ISSN: 00167037. DOI: 10.1016/j.gca.2012.02.009.

Nielsen, Michael H., Shaul Aloni and James J. De Yoreo (Sept. 2014). 'In situ TEM imaging of CaCO3 nucleation reveals coexistence of direct and indirect path-

ways'. In: *Science* 345.6201, pp. 1158–1162. ISSN: 0036-8075. DOI: 10.1126/science.1254051.

Nordstrom, Darrell Kirk et al. (Dec. 1990). 'Revised Chemical Equilibrium Data for Major Water—Mineral Reactions and Their Limitations'. In: *Chemical Modeling of Aqueous Systems II*, pp. 398–413. DOI: 10.1021/bk-1990-0416.ch031.

O'Leary, Marion H. (Feb. 1984). 'Measurement of the isotope fractionation associated with diffusion of carbon dioxide in aqueous solution'. In: *The Journal of Physical Chemistry* 88.4, pp. 823–825. ISSN: 0022-3654. DOI: 10.1021/j150648a041.

Oelkers, E. H., S. R. Gislason and J. Matter (Oct. 2008). 'Mineral Carbonation of CO2'. In: *Elements* 4.5, pp. 333–337. ISSN: 1811-5209. DOI: 10.2113/gselements.4.5.333.

Ogundele, G. I. and W. E. White (Feb. 1986). 'Some Observations on Corrosion of Carbon Steel in Aqueous Environments Containing Carbon Dioxide'. In: *CORROSION* 42.2, pp. 71–78. ISSN: 0010-9312. DOI: 10.5006/1.3584888.

Ohmoto, Hiroshi (2004). 'Evidence from massive siderite beds for a CO 2 -rich atmosphere before , 1 . 8 billion years ago'. In: *Nature* 429.May, pp. 395–399. DOI: 10.1038/nature02572.1..

Ohtaki, Hitoshi and Tamas. Radnai (May 1993). 'Structure and dynamics of hydrated ions'. In: *Chemical Reviews* 93.3, pp. 1157–1204. ISSN: 0009-2665. DOI: 10.1021/cr00019a014.

Onsager, Lars. (Aug. 1933). 'Theories of Concentrated Electrolytes.' In: *Chemical Reviews* 13.1, pp. 73–89. ISSN: 0009-2665. DOI: 10.1021/cr60044a006.

Paris, Philip von et al. (2008). 'Warming the early earth-CO2 reconsidered'. In: *Planetary and Space Science* 56.9, pp. 1244–1259. ISSN: 00320633. DOI: 10.1016/j.pss.2008.04.008. arXiv: arXiv:0804.4134v2.

Parker, V. B. and I. L. Khodakovskii (Sept. 1995). 'Thermodynamic Properties of the Aqueous Ions (2+ and 3+) of Iron and the Key Compounds of Iron'. In: *Journal of Physical and Chemical Reference Data* 24.5, pp. 1699–1745. ISSN: 15297845. DOI: 10.1063/1.555964.

Patrick, W. A. and W. E. Thompson (1953). 'Standard Electrode Potential of the Iron-Ferrous Ion Couple at 25°'. In: *Journal of the American Chemical Society* 75.5, pp. 1184–1187. ISSN: 15205126. DOI: 10.1021/ja01101a052.

Pauling, Linus (1927). 'The size of ions and the structure of ionic crystals'. In: *Journal of the American Chemical Society* 49.3, pp. 765–790. DOI: 10.1021/ja01402a019.

Pickard, April L., Mark E. Barley and Bryan Krapež (Aug. 2004). 'Deep-marine depositional setting of banded iron formation: sedimentological evidence from interbedded clastic sedimentary rocks in the early Palaeoproterozoic Dales Gorge Member of Western Australia'. In: *Sedimentary Geology* 170.1-2, pp. 37–62. ISSN: 00370738. DOI: 10.1016/j.sedgeo.2004.06.007.

Pitzer, K. S and L. Brewer (1961). *Thermodynamics*. 2nd. New York: McGraw-Hill.

PLUMMER, L. N., D. L. PARKHURST and T. M. L. WIGLEY (Mar. 1979). 'Critical Review of the Kinetics of Calcite Dissolution and Precipitation'. In: pp. 537–573. DOI: 10.1021/bk-1979-0093.ch025.

Pokrovsky, O. S. and J. Schott (Feb. 2002). 'Surface Chemistry and Dissolution Kinetics of Divalent Metal Carbonates'. In: *Environmental Science & Technology* 36.3, pp. 426–432. ISSN: 0013-936X. DOI: 10.1021/es010925u.

Postma, D. (Oct. 1982). 'Pyrite and siderite formation in brackish and freshwater swamp sediments'. In: *American Journal of Science* 282.8, pp. 1151–1183. ISSN: 0002-9599. DOI: 10.2475/ajs.282.8.1151.

Poulton, Simon W. and Donald E. Canfeld (2011). 'Ferruginous conditions: A dominant feature of the ocean through Earth's history'. In: *Elements* 7.2, pp. 107–112. ISSN: 18115209. DOI: 10.2113/gselements.7.2.107.

Preis, Wolfgang and Heinz Gamsjäger (2002). 'Critical evaluation of solubility data: Enthalpy of formation of siderite'. In: *Physical Chemistry Chemical Physics* 4.16, pp. 4014–4019. ISSN: 14639076. DOI: 10.1039/b203626f.

Ptacek, C. J. and David W. Blowes (Dec. 1993). 'Influence of Siderite on the Pore-Water Chemistry of Inactive Mine-Tailings Impoundments'. In: pp. 172–189. DOI: 10.1021/bk-1994-0550.ch013.

Ptacek, Carol Jane (1992). 'Experimental determination of siderite solubility in high ionic-strength aqueous solutions.' PhD. University of Waterloo, Ontario, Canada.

Pufahl, Peir K. (2010). 'Bioelemental Sediments'. In: *Facies Models 4*. Ed. by N. P. James and R. W. Dalrymple. St. John's, Nfld: Geological Association of Canada. Chap. 19, pp. 477–503. ISBN: 9781897095508.

Raiswell, Rob et al. (Feb. 2011). 'Formation of syngenetic and early diagenetic iron minerals in the late Archean Mt. McRae Shale, Hamersley Basin, Australia: New insights on the patterns, controls and paleoenvironmental implications of authigenic mineral formation'. In: *Geochimica et Cosmochimica Acta* 75.4, pp. 1072–1087. ISSN: 00167037. DOI: 10.1016/j.gca.2010.11.013.

Ramsay, J.G (1963). 'Structural investigations in the Barberton Mountain Land, eastern Transvaal'. In: *Geological Society of South Africa, Transactions* 66, pp. 353–401.

Randall, Merle and Mikkel Frandsen (1932). 'The standard electrode potential of iron and the activity coefficient of ferrous chloride'. In: *Journal of the American Chemical Society* 54.1, pp. 47–54. ISSN: 15205126. DOI: 10.1021/ja01340a006.

Raoult, François-Marie (1886). 'Loi générale des tensions de vapeur des dissolvants (General law of vapour pressures of solvents)'. In: *Comptes rendus* 104, pp. 1430–1433.

Rasmussen, Birger, Bryan Krapež and Daniela B. Meier (2014). 'Replacement origin for hematite in 2.5 Ga banded iron formation: Evidence for postdepositional oxidation of iron-bearing minerals'. In: *Bulletin of the Geological Society of America* 126.3-4, pp. 438–446. ISSN: 19432674. DOI: 10.1130/B30944.1.

Rasmussen, Birger, Bryan Krapež and Janet R. Muhling (Mar. 2015a). 'Seafloor silicification and hardground development during deposition of 2.5 Ga banded iron formations'. In: *Geology* 43.3, pp. 235–238. ISSN: 1943-2682. DOI: 10.1130/G36363.1.

Rasmussen, Birger and Janet R. Muhling (Mar. 2018). 'Making magnetite late again: Evidence for widespread magnetite growth by thermal decomposition of siderite in Hamersley banded iron formations'. In: *Precambrian Research* 306.June 2017, pp. 64–93. ISSN: 03019268. DOI: 10.1016/j.precamres.2017.12.017.

Rasmussen, Birger et al. (Apr. 2013). 'Iron silicate microgranules as precursor sediments to 2.5-billion-year-old banded iron formations'. In: *Geology* 41.4, pp. 435–438. ISSN: 1943-2682. DOI: 10.1130/G33828.1.

Rasmussen, Birger et al. (2015b). 'Precipitation of iron silicate nanoparticles in early Precambrian oceans marks Earth's first iron age'. In: *Geology* 43.4, pp. 303–306. ISSN: 19432682. DOI: 10.1130/G36309.1.

Rasmussen, Birger et al. (Oct. 2016). 'Dust to dust: Evidence for the formation of "primary" hematite dust in banded iron formations via oxidation of iron silicate nanoparticles'. In: *Precambrian Research* 284, pp. 49–63. ISSN: 03019268. DOI: 10.1016/j.precamres.2016.07.003.

— (Mar. 2017). 'Greenalite precipitation linked to the deposition of banded iron formations downslope from a late Archean carbonate platform'. In: *Precambrian Research* 290, pp. 49–62. ISSN: 03019268. DOI: 10.1016/j.precamres.2016.12.005.

Rasmussen, Michael G., Bernard W. Evans and Scott M. Kuehner (1998). 'Low-temperature fayalite, greenalite, and minnesotaite from the Overlook gold deposit, Washington; phase relations in the system FeO-SiO2-H2O'. In: *The Canadian Mineralogist* 36.1, pp. 147–162.

Raymo, M. E. and W. F. Ruddiman (Sept. 1992). 'Tectonic forcing of late Cenozoic climate'. In: *Nature* 359.6391, pp. 117–122. ISSN: 0028-0836. DOI: 10.1038/359117a0.

Reiterer, F., W. Johannes and H. Gamsjäger (1981). 'Semimicro determination of solubility constants: Copper(II) carbonate and iron(II) carbonate'. In: *Mikrochimica Acta* 75.1-2, pp. 63–72. ISSN: 00263672. DOI: 10.1007/BF01198705.

Rémazeilles, C. and Ph Refait (Mar. 2009). 'Fe(II) hydroxycarbonate Fe2(OH)2CO3 (chukanovite) as iron corrosion product: Synthesis and study by Fourier Transform Infrared Spectroscopy'. In: *Polyhedron* 28.4, pp. 749–756. ISSN: 02775387. DOI: 10.1016/j.poly.2008.12.034.

Richards, Theodore William and Gustavus Edward Behr (1906). 'The electromotive force of iron under varying conditions, and the effect of occluded hydrogen.' In: *Carnegie institution of Washington* 61.

Richter, Frank M. et al. (Jan. 2006). 'Kinetic isotopic fractionation during diffusion of ionic species in water'. In: *Geochimica et Cosmochimica Acta* 70.2, pp. 277–289. ISSN: 00167037. DOI: 10.1016/j.gca.2005.09.016.

Rimstidt, J. Donald (1997). 'Quartz solubility at low temperatures'. In: *Geochimica et Cosmochimica Acta* 61.13, pp. 2553–2558. ISSN: 00167037. DOI: 10.1016/S0016-7037(97)00103-8.

Rimstidt, J.D. and H.L. Barnes (Nov. 1980). 'The kinetics of silica-water reactions'. In: *Geochimica et Cosmochimica Acta* 44.11, pp. 1683–1699. ISSN: 00167037. DOI: 10.1016/0016-7037(80)90220-3.

Robie, Richard and Bruce S. Hemingway (1995). 'Thermodynamic Properties of Minerals and Related Substances at 298.15K and 1 Bar'. In: *U.S. Geological Survey Bulletin*. ISSN: U.S. Geological Survey Bulletin, 1452. DOI: 10.3133/b2131.

Robie, Richard A., Bruce S. Hemingway and James R. Fisher (1978). 'Thermodynamic Properties of Minerals and Related Substances at 298.15K and 1 Bar Pressure and at Higher Temperatures'. In: pp. 1–464. DOI: 10.3133/b1452.

Robinson, R. A. and R. H. Stokes (2002). *Electrolyte Solutions Second Revised Edition*. New York: Dover Publications.

Rockwood, Alan L. (2015). 'Meaning and Measurability of Single-Ion Activities, the Thermodynamic Foundations of pH, and the Gibbs Free Energy for the Transfer of Ions between Dissimilar Materials'. In: *ChemPhysChem* 16.9, pp. 1978–1991. ISSN: 14397641. DOI: 10.1002/cphc.201500044.

Rodushkin, Ilia et al. (2004). 'Isotopic Fractionation during Diffusion of Transition Metal Ions in Solution'. In: *Analytical Chemistry* 76.7, pp. 2148–2151. ISSN: 00032700. DOI: 10.1021/ac035296g.

Romanek, Christopher S. et al. (Sept. 2009). 'Inorganic synthesis of Fe–Ca–Mg carbonates at low temperature'. In: *Geochimica et Cosmochimica Acta* 73.18, pp. 5361–5376. ISSN: 00167037. DOI: 10.1016/j.gca.2009.05.065.

Roobottom, Helen K et al. (Nov. 1999). 'Thermochemical Radii of Complex Ions'. In: *Journal of Chemical Education* 76.11, p. 1570. ISSN: 0021-9584. DOI: 10.1021/ed076p1570.

Rouxel, Olivier, Yves Fouquet and John N. Ludden (2004). 'Subsurface processes at the lucky strike hydrothermal field, Mid-Atlantic ridge: Evidence from sulfur, selenium, and iron isotopes'. In: *Geochimica et Cosmochimica Acta* 68.10, pp. 2295–2311. ISSN: 00167037. DOI: 10.1016/j.gca.2003.11.029.

Rouxel, Olivier et al. (2003). 'Iron isotope fractionation during oceanic crust alteration'. In: *Chemical Geology* 202.1-2, pp. 155–182. ISSN: 00092541. DOI: 10.1016/j.chemgeo.2003.08.011.

Rubey, William W (Mar. 1955). 'Development of the Hydrosphere and Atmosphere, with Special Reference to Probable Composition of the Early Atmosphere'. In: *Geological Society of America Special Papers*. Vol. 62, pp. 631–650. DOI: 10.1130/SPE62-p631.

Russel, W. B., D. A. Saville and W. R. Schowalter (1989). *Colloidal Dispersions*. Cambridge: Cambridge University Press. ISBN: 9780511608810. DOI: 10.1017/CBO9780511608810.

Rybacki, K.S. et al. (Apr. 2016). 'Weathering during the Great Oxidation Event: Fennoscandia, arctic Russia 2.06 Ga ago'. In: *Precambrian Research* 275, pp. 513–525. ISSN: 03019268. DOI: 10.1016/j.precamres.2016.01.010.

Rye, Rob, Phillip H. Kuo and Heinrich D. Holland (1995). 'Atmospheric carbon dioxide concentrations before 2.2 billion years ago'. In: *Nature* 378.6557, pp. 603–605. ISSN: 0028-0836. DOI: 10.1038/378603a0.

Sagan, Carl and George Mullen (1972). 'Earth and Mars: Evolution of Atmospheres and Surface Temperatures'. In: *Science* 177.4043, pp. 52–56. ISSN: 0036-8075. DOI: 10.1126/science.177.4043.52. arXiv: arXiv:1011.1669v3.

Saheb, M. et al. (Sept. 2008). 'Long-term corrosion behaviour of low-carbon steel in anoxic environment: Characterisation of archaeological artefacts'. In: *Journal of Nuclear Materials* 379.1-3, pp. 118–123. ISSN: 00223115. DOI: 10.1016/j.jnucmat.2008.06.019.

Saheb, M. et al. (Dec. 2010). 'Iron corrosion in an anoxic soil: Comparison between thermodynamic modelling and ferrous archaeological artefacts characterised along with the local in situ geochemical conditions'. In: *Applied Geochemistry* 25.12, pp. 1937–1948. ISSN: 08832927. DOI: 10.1016/j.apgeochem.2010.10.010.

Saldi, Giuseppe (2009). 'Les cinétiques de dissolution et précipitation de la magnesite aux conditions hydrothermales'. PhD thesis. Thèse de l'Université Paul-Sabatier, Toulouse, p. 184.

Saldi, Giuseppe D. et al. (Oct. 2009). 'Magnesite growth rates as a function of temperature and saturation state'. In: *Geochimica et Cosmochimica Acta* 73.19, pp. 5646–5657. ISSN: 00167037. DOI: 10.1016/j.gca.2009.06.035.

Sander, R. (Apr. 2015). 'Compilation of Henry's law constants (version 4.0) for water as solvent'. In: *Atmospheric Chemistry and Physics* 15.8, pp. 4399–4981. ISSN: 1680-7324. DOI: 10.5194/acp-15-4399-2015.

Sastre de Vicente, Manuel E. (May 2004). 'The Concept of Ionic Strength Eighty Years after Its Introduction in Chemistry'. In: *Journal of Chemical Education* 81.5, p. 750. ISSN: 0021-9584. DOI: 10.1021/ed081p750.

Sayles, F.L. and W.S. Fyfe (Jan. 1973). 'The crystallization of magnesite from aqueous solution'. In: *Geochimica et Cosmochimica Acta* 37.1, pp. 87–99. ISSN: 00167037. DOI: 10.1016/0016-7037(73)90246-9.

Schwab, A. P. and W. L. Lindsay (Mar. 1983). 'Effect of Redox on the Solubility and Availability of Iron'. In: *Soil Science Society of America Journal* 47.2, pp. 201–205. ISSN: 03615995. DOI: 10.2136/sssaj1983.03615995004700020005x.

Sel, Ozlem et al. (2012). 'Amorphous iron (II) carbonate: Crystallization energetics and comparison to other carbonate minerals related to CO 2 sequestration'. In: *Geochimica et Cosmochimica Acta* 87, pp. 61–68. ISSN: 00167037. DOI: 10.1016/j.gca.2012.03.011.

Seyfried, W.E. and K. Ding (May 1993). 'The effect of redox on the relative solubilities of copper and iron in Cl-bearing aqueous fluids at elevated temperatures and pressures: An experimental study with application to subseafloor hydrothermal systems'. In: *Geochimica et Cosmochimica Acta* 57.9, pp. 1905–1917. ISSN: 00167037. DOI: 10.1016/0016-7037(93)90083-9.

Seyfried, W.E.Jr. et al. (1997). 'Experimental and Theoretical Controls on the Composition of Mid-Ocean Ridge Hydrothermal Fluids'. In: *Volcanic Associated Massive Sulfide Deposits: Processes and Examples in Modern and Ancient*

Settings. Society of Economic Geologists. ISBN: 9781629490151. DOI: 10.5382/Rev.08.08.

Seyler, Clarence Arthur and Percy Vivian Lloyd (1917). 'XV. - Studies of the carbonates. Part II. Hydrolysis of sodium carbonate and bicarbonate and the ionisation constants of carbonic acid'. In: *Journal of the Chemical Society, Transactions* 111.138, pp. 138–158. ISSN: 03681645. DOI: 10.1039/CT9171100138.

Shanks, W. C. (Jan. 2001). 'Stable Isotopes in Seafloor Hydrothermal Systems: Vent fluids, hydrothermal deposits, hydrothermal alteration, and microbial processes'. In: *Reviews in Mineralogy and Geochemistry* 43.1, pp. 469–525. ISSN: 1529-6466. DOI: 10.2138/gsrmg.43.1.469.

Shaw, George H. (2008). 'Earth's atmosphere - Hadean to early Proterozoic'. In: *Chemie der Erde - Geochemistry* 68.3, pp. 235–264. ISSN: 00092819. DOI: 10.1016/j.chemer.2008.05.001.

Sheldon, Nathan D. (2006). 'Precambrian paleosols and atmospheric CO2 levels'. In: *Precambrian Research* 147.1-2, pp. 148–155. ISSN: 03019268. DOI: 10.1016/j.precamres.2006.02.004.

Shields, Graham and Ján Veizer (June 2002). 'Precambrian marine carbonate isotope database: Version 1.1'. In: *Geochemistry, Geophysics, Geosystems* 3.6, 1 of 12–12 of 12. ISSN: 15252027. DOI: 10.1029/2001GC000266.

Shiraki, Ryoji and Susan L Brantley (Apr. 1995). 'Kinetics of near-equilibrium calcite precipitation at 100°C: An evaluation of elementary reaction-based and affinity-based rate laws'. In: *Geochimica et Cosmochimica Acta* 59.8, pp. 1457–1471. ISSN: 00167037. DOI: 10.1016/0016-7037(95)00055-5.

Shock, Everett L. et al. (Dec. 1992). 'Calculation of the thermodynamic properties of aqueous species at high pressures and temperatures. Effective electrostatic radii, dissociation constants and standard partial molal properties to 1000 °C and 5 kbar'. In: *J. Chem. Soc., Faraday Trans.* 88.6, pp. 803–826. ISSN: 0956-5000. DOI: 10.1039/FT9928800803.

Siever, Raymond (Mar. 1962). 'Silica Solubility, 0°-200° C., and the Diagenesis of Siliceous Sediments'. In: *The Journal of Geology* 70.2, pp. 127–150. ISSN: 0022-1376. DOI: 10.1086/626804.

Siever, Raymond (Aug. 1992). 'The silica cycle in the Precambrian'. In: *Geochimica et Cosmochimica Acta* 56.8, pp. 3265–3272. ISSN: 00167037. DOI: 10.1016/0016-7037(92)90303-Z.

Silva, Carlos A R, Xuewu Liu and F J Millero (2002). 'Solubility of Siderite (FeCO3) in NaCl Solutions'. In: *Journal of Solution Chemistry* 31.2, pp. 97–108. ISSN: 0095-9782. DOI: 10.1023/A:1015275618138.

Simoes, Marcus C. et al. (July 2017). 'Estimation of the Thermochemical Radii and Ionic Volumes of Complex Ions'. In: *Inorganic Chemistry* 56.13, pp. 7566–7573. ISSN: 0020-1669. DOI: 10.1021/acs.inorgchem.7b01205.

Simonson, Bruce M (2003). 'Origin and evolution of large Precambrian iron formations'. In: *Geological Society, London, Special Paper* 370, pp. 231–244. DOI: 10.1130/0-8137-2370-1.231.

Singer, Philip C. and Werner Stumm (Mar. 1970). 'THE SOLUBILITY OF FERROUS IRON IN CARBONATE-BEARING WATERS'. In: *Journal - American Water Works Association* 62.3, pp. 198–202. ISSN: 0003150X. DOI: 10.1002/j.1551-8833.1970.tb03888.x.

Sizova, E. et al. (2010). 'Subduction styles in the Precambrian: Insight from numerical experiments'. In: *Lithos* 116.3-4, pp. 209–229. ISSN: 00244937. DOI: 10.1016/j.lithos.2009.05.028.

Sk, Mobbassar Hassan et al. (Sept. 2017). 'Local supersaturation and the growth of protective scales during CO2 corrosion of steel: Effect of pH and solution flow'. In: *Corrosion Science* 126.January, pp. 26–36. ISSN: 0010938X. DOI: 10.1016/j.corsci.2017.05.026.

Smith, Alexander M, Alpha A Lee and Susan Perkin (June 2016). 'The Electrostatic Screening Length in Concentrated Electrolytes Increases with Concentration'. In: *The Journal of Physical Chemistry Letters* 7.12, pp. 2157–2163. ISSN: 1948-7185. DOI: 10.1021/acs.jpclett.6b00867.

Smith, Herbert J. (June 1918). 'ON EQUILIBRIUM IN THE SYSTEM: FERROUS CARBONATE, CARBON DIOXIDE AND WATER. 1'. In: *Journal of the American Chemical Society* 40.6, pp. 879–883. ISSN: 0002-7863. DOI: 10.1021/ja02239a002.

Spencer, E. and F. G. Percival (June 1952). 'The structure and origin of the banded hematite jaspers of Singhbhum, India'. In: *Economic Geology* 47.4, pp. 365–383. ISSN: 1554-0774. DOI: 10.2113/gsecongeo.47.4.365.

Steefel, Carl I. and Philippe Van Cappellen (1990). 'A new kinetic approach to modeling water-rock interaction: The role of nucleation, precursors, and Ostwald ripening'. In: *Geochimica et Cosmochimica Acta* 54.10, pp. 2657–2677. ISSN: 00167037. DOI: 10.1016/0016-7037(90)90003-4.

Stefánsson, Andri, Pascale Bénézeth and Jacques Schott (Nov. 2013). 'Carbonic acid ionization and the stability of sodium bicarbonate and carbonate ion pairs to 200°C – A potentiometric and spectrophotometric study'. In: *Geochimica et Cosmochimica Acta* 120, pp. 600–611. ISSN: 00167037. DOI: 10.1016/j.gca.2013.04.023.

Stillinger, Frank H. and Ronald Lovett (1968). 'Ion-pair theory of concentrated electrolytes. I. Basic concepts'. In: *The Journal of Chemical Physics* 48.9, pp. 3858–3868. ISSN: 00219606. DOI: 10.1063/1.1669709.

Stokes, R. H. and R. A. Robinson (May 1948). 'Ionic Hydration and Activity in Electrolyte Solutions'. In: *Journal of the American Chemical Society* 70.5, pp. 1870–1878. ISSN: 0002-7863. DOI: 10.1021/ja01185a065.

Stumm, W. and G. F. Lee (1960). 'The chemistry of aqueous iron'. In: *Schweizerische Zeitschrift für Hydrologie* 22.1, pp. 295–319. ISSN: 00367842. DOI: 10.1007/BF02503278.

Stumm, Werner (1992). *Chemistry of the solid-water interface: processes at the mineral-water and particle-water interface in natural systems*. New York: John Wiley & Sons, p. 428. ISBN: 0471576727.

Stumm, Werner and J J Morgan (1996). 'Chemical Equilibria and Rates in Natural Waters'. In: *Aquatic chemistry*. 3rd. New York: Wiley, p. 1022. ISBN: 0471511854. arXiv: arXiv:1011.1669v3.

Sumner, Dawn Y. (1997). *Carbonate precipitation and oxygen stratification in late Archean seawater as deduced from facies and stratigraphy of the gamohaan and frisco formations, transvaal supergroup, South Africa*. DOI: 10.2475/ajs.297.5.455.

Sumner, Dawn Y. and John P. Grotzinger (2004). 'Implications for Neoarchaean ocean chemistry from primary carbonate mineralogy of the Campbellrand-Malmani Platform, South Africa'. In: *Sedimentology* 51.6, pp. 1273–1299. ISSN: 00370746. DOI: 10.1111/j.1365-3091.2004.00670.x.

Sun, Si et al. (May 2015). 'Primary hematite in Neoarchean to Paleoproterozoic oceans'. In: *Geological Society of America Bulletin* 127.5-6, pp. 850–861. ISSN: 0016-7606. DOI: 10.1130/B31122.1.

Sun, W. and S. Nešić (Apr. 2008). 'Kinetics of Corrosion Layer Formation: Part 1—Iron Carbonate Layers in Carbon Dioxide Corrosion'. In: *CORROSION* 64.4, pp. 334–346. ISSN: 0010-9312. DOI: 10.5006/1.3278477.

Sun, Wei, Srdjan Nešić and Richard C. Woollam (June 2009). 'The effect of temperature and ionic strength on iron carbonate (FeCO3) solubility limit'. In: *Corrosion Science* 51.6, pp. 1273–1276. ISSN: 0010938X. DOI: 10.1016/j.corsci.2009.03.009.

Tanger, J. C. and H. C. Helgeson (Jan. 1988). 'Calculation of the thermodynamic and transport properties of aqueous species at high pressures and temperatures; revised equations of state for the standard partial molal properties of ions and electrolytes'. In: *American Journal of Science* 288.1, pp. 19–98. ISSN: 0002-9599. DOI: 10.2475/ajs.288.1.19.

Taylor, S.R. and Scott M. McLennan (1985). *The continental crust: Its composition and evolution*. Oxford: Blackwell.

Teng, H.Henry, Patricia M. Dove and James J. De Yoreo (July 2000). 'Kinetics of calcite growth: surface processes and relationships to macroscopic rate laws'. In: *Geochimica et Cosmochimica Acta* 64.13, pp. 2255–2266. ISSN: 00167037. DOI: 10.1016/S0016-7037(00)00341-0.

Tivey, Margaret K. and Russell E. McDuff (1990). 'Mineral precipitation in the walls of black smoker chimneys: A quantitative model of transport and chemical reaction'. In: *Journal of Geophysical Research* 95.B8, p. 12617. ISSN: 0148-0227. DOI: 10.1029/JB095iB08p12617.

Tivey, Margaret Kingston (May 1995). 'The influence of hydrothermal fluid composition and advection rates on black smoker chimney mineralogy: Insights from

modeling transport and reaction'. In: *Geochimica et Cosmochimica Acta* 59.10, pp. 1933–1949. ISSN: 00167037. DOI: 10.1016/0016-7037(95)00118-2.

Tosca, Nicholas J., Stephen Guggenheim and Peir K. Pufahl (Mar. 2016). 'An authigenic origin for Precambrian greenalite: Implications for iron formation and the chemistry of ancient seawater'. In: *Geological Society of America Bulletin* 128.3-4, pp. 511–530. ISSN: 0016-7606. DOI: 10.1130/B31339.1.

Tosca, Nicholas J. et al. (Sept. 2018). 'Magnetite authigenesis and the warming of early Mars'. In: *Nature Geoscience* 11.9, pp. 635–639. ISSN: 1752-0894. DOI: 10.1038/s41561-018-0203-8.

Tosca, Nicholas J. et al. (Aug. 2019). 'Products of the iron cycle on the early Earth'. In: *Free Radical Biology and Medicine* 140.December 2018, pp. 138–153. ISSN: 08915849. DOI: 10.1016/j.freeradbiomed.2019.05.005.

Tremaine, Peter R and Jacques C Leblanc (1980). 'The Solubility of Magnetite and the Hydrolysis and Oxidation of Fe2+ in Water to 300°C'. In: *Journal of solution chemistry* 9.6, pp. 415–442. DOI: 0095-9782/80/0600-0415503.00/0.

Tremaine, Peter R., Rudi Von Masscow and G.R. Shierman (June 1977). 'A calculation of gibbs free energies for ferrous ions and the solubility of magnetite in H2O and D2O to 300°C'. In: *Thermochimica Acta* 19.3, pp. 287–300. ISSN: 00406031. DOI: 10.1016/0040-6031(77)80004-X.

Trendall, A. F. and J. G. Blockley (1970). 'The iron formations of the Precambrian Hamersley Group Western Australia'. In: *Geological Survey of Western Australia Bulletin* 119, pp. 391.

Truesdell, A H and B F Jones (1974). 'WATEQ, a Computer Program for Calculating Chemical Equilibria of Natural Waters'. In: *Journal of Research of the U.S. Geological Survey* 2.2, pp. 233–248.

Uematsu, M. and E. U. Frank (Oct. 1980). 'Static Dielectric Constant of Water and Steam'. In: *Journal of Physical and Chemical Reference Data* 9.4, pp. 1291–1306. ISSN: 0047-2689. DOI: 10.1063/1.555632.

Ulich, H. (1930). 'Ionenentropie und Solvatation.' In: *Zeitschrift für Elektrochemie und angewandte physikalische Chemie* 36.8, pp. 497–506. DOI: 10.1002/bbpc.19300360802.

Van Cappellen, P (1991). 'The Formation of Marine Apatite: A Kinetic Study'. PhD thesis. Yale University, p. 240.

van Enckevort, W. J. P., P. Bennema and W. H. van der Linden (Jan. 1981). 'On the Observation of Growth Spirals with very Low Step Heights on Potash Alum Single Crystals'. In: *Zeitschrift fur Physikalische Chemie* 124.2, pp. 171–191. ISSN: 0942-9352. DOI: 10.1524/zpch.1981.124.2.171.

van't Hoff, Jacobus Hendricus (1886). 'Lois de l'équilibre chimique dans l'état dilué, gazeux ou dissous'. In: *PA Norstedt et Söner*.

Veizer, Ján et al. (Apr. 1989). 'Geochemistry of Precambrian carbonates: I. Archean hydrothermal systems'. In: *Geochimica et Cosmochimica Acta* 53.4, pp. 845–857. ISSN: 00167037. DOI: 10.1016/0016-7037(89)90030-6.

Von Damm, K. L., J. L. Bischoff and R. J. Rosenbauer (Dec. 1991). 'Quartz solubility in hydrothermal seawater; an experimental study and equation describing quartz solubility for up to 0.5 M NaCl solutions'. In: *American Journal of Science* 291.10, pp. 977–1007. ISSN: 0002-9599. DOI: 10.2475/ajs.291.10.977.

Wagman, Donald D. et al. (1982). *The NBS Tables of Chemical Thermodynamic Properties*. Supplement. American Chemical Society for the National Bureau of Standards, p. 392.

Wagner, Rudolf (Dec. 1867). 'Ueber die Löslichkeit einiger Erd- und Metallcarbonate in kohlensäurehaltigem Wasser'. In: *Fresenius' Zeitschrift für analytische Chemie* 6.1, pp. 167–172. ISSN: 0016-1152. DOI: 10.1007/BF01347562.

Wajon, Johannes Edmund, Goen-Eng Ho and Peter J. Murphy (Jan. 1985). 'Rate of precipitation of ferrous iron and formation of mixed iron-calcium carbonates by naturally occurring carbonate materials'. In: *Water Research* 19.7, pp. 831–837. ISSN: 00431354. DOI: 10.1016/0043-1354(85)90140-X.

Walker, James C. G. (May 1984). 'Suboxic diagenesis in banded iron formations'. In: *Nature* 309.5966, pp. 340–342. ISSN: 0028-0836. DOI: 10.1038/309340a0.

— (June 1985). 'Carbon dioxide on the early earth'. In: *Origins of Life and Evolution of the Biosphere* 16.2, pp. 117–127. ISSN: 0169-6149. DOI: 10.1007/BF01809466.

Walker, James C. G., P. B. Hays and J. F. Kasting (1981). 'A negative feedback mechanism for the long-term stabilization of Earth's surface temperature'. In:

Journal of Geophysical Research 86.C10, p. 9776. ISSN: 0148-0227. DOI: 10.1029/JC086iC10p09776.

Watkins, James M., Donald J. DePaolo and E. Bruce Watson (Jan. 2017). 'Kinetic Fractionation of Non-Traditional Stable Isotopes by Diffusion and Crystal Growth Reactions'. In: *Reviews in Mineralogy and Geochemistry* 82.1, pp. 85–125. ISSN: 1529-6466. DOI: 10.2138/rmg.2017.82.4.

Wiesli, René A., Brian L. Beard and Clark M. Johnson (Nov. 2004). 'Experimental determination of Fe isotope fractionation between aqueous Fe(II), siderite and "green rust" in abiotic systems'. In: *Chemical Geology* 211.3-4, pp. 343–362. ISSN: 00092541. DOI: 10.1016/j.chemgeo.2004.07.002.

Wray, James J et al. (Apr. 2016). 'Orbital evidence for more widespread carbonate-bearing rocks on Mars'. In: *Journal of Geophysical Research: Planets* 121.4, pp. 652–677. ISSN: 21699097. DOI: 10.1002/2015JE004972.

Xu, Tianfu, John A. Apps and Karsten Pruess (June 2004). 'Numerical simulation of CO2 disposal by mineral trapping in deep aquifers'. In: *Applied Geochemistry* 19.6, pp. 917–936. ISSN: 08832927. DOI: 10.1016/j.apgeochem.2003.11.003.

— (Apr. 2005). 'Mineral sequestration of carbon dioxide in a sandstone–shale system'. In: *Chemical Geology* 217.3-4, pp. 295–318. ISSN: 00092541. DOI: 10.1016/j.chemgeo.2004.12.015.

Yamaguchi, Kosei E. et al. (2005). 'Biogeochemical cycling of iron in the Archean-Paleoproterozoic Earth: Constraints from iron isotope variations in sedimentary rocks from the Kaapvaal and Pilbara Cratons'. In: *Chemical Geology* 218.1-2 SPEC. ISS. Pp. 135–169. ISSN: 00092541. DOI: 10.1016/j.chemgeo.2005.01.020.

Zahnle, Kevin and Norman H Sleep (2002). 'Carbon dioxide cycling through the mantle and implications for the climate of ancient Earth'. In: *Geological Society, London, Special Publications* 199.1, pp. 231–257. ISSN: 0305-8719. DOI: 10.1144/GSL.SP.2002.199.01.12.

Zahnle, Kevin J. (2006). 'Earth's earliest atmosphere'. In: *Elements* 2.4, pp. 217–222. ISSN: 18115209. DOI: 10.2113/gselements.2.4.217.

Zeebe, R E and D Wolf-Gladrow (2001). *CO2 in Seawater: Equilibrium, Kinetics, Isotopes.* Ed. by David Halpern. Oceanograp. Amsterdam: Elsevier Ltd., p. 271. ISBN: 0444509461.

Zeebe, Richard E. (May 2011). 'On the molecular diffusion coefficients of dissolved , and and their dependence on isotopic mass'. In: *Geochimica et Cosmochimica Acta* 75.9, pp. 2483–2498. ISSN: 00167037. DOI: 10.1016/j.gca.2011.02.010.

Zerkle, Aubrey L. et al. (2012). 'A bistable organic-rich atmosphere on the Neoarchaean Earth'. In: *Nature Geoscience* 5.5, pp. 359–363. ISSN: 1752-0894. DOI: 10.1038/ngeo1425.

Zhang, Jingwu and G.H. Nancollas (Nov. 1990). 'Kink densities along a crystal surface step at low temperatures and under nonequilibrium conditions'. In: *Journal of Crystal Growth* 106.2-3, pp. 181–190. ISSN: 00220248. DOI: 10.1016/0022-0248(90)90062-P.

Zhang, Jingwu and George H. Nancollas (Apr. 1998). 'Kink Density and Rate of Step Movement during Growth and Dissolution of anABCrystal in a Nonstoichiometric Solution'. In: *Journal of Colloid and Interface Science* 200.1, pp. 131–145. ISSN: 00219797. DOI: 10.1006/jcis.1997.5357.

Zierenberg, Robert A. and Wayne C Shanks (1988). 'Isotopic studies of epigenetic features in metalliferous sediment Atlantis II deep, Red sea'. In: *Canadian Mineralogist* 26, pp. 737–753.

Zierenberg, Robert A. et al. (May 1988). 'Mineralization, alteration, and hydrothermal metamorphism of the ophiolite-hosted Turner-Albright sulfide deposit, southwestern Oregon'. In: *Journal of Geophysical Research: Solid Earth* 93.B5, pp. 4657–4674. ISSN: 01480227. DOI: 10.1029/JB093iB05p04657.